INFORMATION TO USERS

This manuscript has been reproduced from the microfilm master. UMI films the text directly from the original or copy submitted. Thus, some thesis and dissertation copies are in typewriter face, while others may be from any type of computer printer.

The quality of this reproduction is dependent upon the quality of the copy submitted. Broken or indistinct print, colored or poor quality illustrations and photographs, print bleedthrough, substandard margins, and improper alignment can adversely affect reproduction.

In the unlikely event that the author did not send UMI a complete manuscript and there are missing pages, these will be noted. Also, if unauthorized copyright material had to be removed, a note will indicate the deletion.

Oversize materials (e.g., maps, drawings, charts) are reproduced by sectioning the original, beginning at the upper left-hand corner and continuing from left to right in equal sections with small overlaps.

Photographs included in the original manuscript have been reproduced xerographically in this copy. Higher quality 6" x 9" black and white photographic prints are available for any photographs or illustrations appearing in this copy for an additional charge. Contact UMI directly to order.

Bell & Howell Information and Learning
300 North Zeeb Road, Ann Arbor, MI 48106-1346 USA
800-521-0600

Measuring the Second Harmonic Amplitude of an Oscillating Torsion Pendulum to Detect Small Forces

Michael Wayne Moore

A dissertation submitted in partial fulfillment of the
requirements for the degree of

Doctor of Philosophy

University of Washington

2000

Program Authorized to Offer Degree: Physics

In presenting this dissertation in partial fulfillment of the requirements for the Doctoral degree at the University of Washington, I agree that the Library shall make its copies freely available for inspection. I further agree that extensive copying of the dissertation is allowable only for scholarly purposes, consistent with "fair use" as prescribed in the U.S. Copyright Law. Requests for copying or reproduction of this dissertation may be referred to University Microfilms, 300 North Zeeb Road, Ann Arbor, MI 48106-1346, to whom the author has granted "the right to reproduce and sell (a) copies of the manuscript in microform and/or (b) printed copies of the manuscript made from microform."

Signature 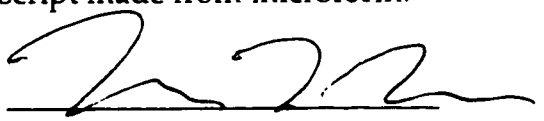

Date 2/22/00

University of Washington
Graduate School

This is to certify that I have examined this copy of a doctoral dissertation by

Michael Wayne Moore

and have found that it is complete and satisfactory in all respects,
and that any and all revisions required by the final
examining committee have been made.

Chair of the Supervisory Committee:

Paul Boynton

Reading Committee:

James Bardeen

Blayne Heckel

Date: 2/22/00

University of Washington

Abstract

Measuring the Second Harmonic Amplitude of an Oscillating Torsion Pendulum to Detect Small Forces

Michael Wayne Moore

Chairperson of the Supervisory Committee: *Professor Paul Boynton*
Physics

After more than 200 years, the torsion balance/pendulum is still one of the most precise means for measuring weak, macroscopic-range forces. Historically, two primary measurement techniques have been developed for this instrument. In one, the signal is the equilibrium angular displacement of the pendulum resulting from the presence of an external torque. In the other, this torque is detected by the associated fractional change in the natural frequency of torsion oscillations. Both techniques have been refined to the point that some experiments are now limited by temporal variations in torsion fiber temperature, despite special efforts to insure temperature stability.

We have devised and tested another torsion pendulum measurement technique for which the effect of fiber temperature variations is suppressed by more than four orders of magnitude. Our observable is the amplitude of the second harmonic of the pendulum motion. A data set of 10 runs, each approximately 3 days in duration, using a magnesium/beryllium composition-dipole pendulum yielded a variation in the second harmonic amplitude of 0.29±0.47 nanoradians which corresponds to a differential acceleration between the magnesium and beryllium of $2.5 \pm 4.0 \times 10^{-12}$ cm/sec^2. This new technique suggests that a continued improvement in the precision of these fundamental physics experiments may be realized with a moderately high Q, room-temperature apparatus.

Table of Contents

List of Figures

Page

List of Tables

Page

Acknowledgments

To my mother, who prevented me from having permanent brain damage by taking my scissors away from me when I was three years old. I had been banging my head on the floor because I couldn't cut out paper dolls that looked as good as those made by my twin sister, Mary.

To my piano teacher's husband, a physicist at Lawrence Berkeley Laboratory, who assured me over his wife's protests that I wasn't "throwing my life away" by changing my major from Music to Physics at UCLA.

To the Naval Nuclear Power School, who has allowed me to maintain the illusion that if I pursue a career in teaching that all my students will be disciplined, hard-working, and respectful.

To the National Science Foundation who has funded my Research Assistantship at the University of Washington and allowed me to afford a place to sleep and food to eat. These are two habits that I had developed in my pre-graduate-student days, and I have not been able to break them yet.

To Prof. Adelberger's group at the University of Washington and Prof. Newman's group at the University of California, Irvine whose outstanding experimental technique and professionalism convinced me that torsion balances are "serious" physics.

To the numerous other students, both graduate and undergraduate, who have worked in Prof. Boynton's lab. Several times they have saved me from my own stupidity and carelessness. They have forced me to collect my thoughts and express them clearly and to push the rigor of my arguments beyond my usual "proof by vigorous assertion". They have also done the lion's share of real work in the lab.

To Paul Boynton who has patiently waited while I write this thesis (akin to watching grass grow). He has always allowed me the freedom to pursue my ideas, no matter how hare-brained, and he has always had confidence that I can solve my problems, no matter how lost I have felt. I am also indebted to his vision of developing large-amplitude torsion pendulum techniques when no one else was doing so. Without an existing experimental apparatus with which to test and develop the second harmonic method, it is unlikely that the ideas in this thesis would have ever seen the light of day.

To my lovely wife, Andrea, for her support and understanding. Despite her deep mistrust of academics who "haven't done an honest day's work in the real world", she managed, through a severe lapse in judgment, to marry one. True love is blind.

1 Introduction

1.1 Torsion Balance Precision Force Experiments

For more than 200 years, the torsion balance/pendulum has been used to measure weak, macroscopic-range forces with ever increasing precision. The longevity of the torsion balance apparatus is due to its unrivaled raw sensitivity. In a terrestrial gravitational environment where an apparatus is required to support its own weight, the single-wire suspended torsion balance provides the largest deflection per unit force of any device. Attempts to increase this deflection by flotation, multiple-wire suspension, or magnetic suspension have invariably produced environmental couplings that were more egregious than the original problems they were intended to solve (Keyser et al. 1984).

The torsion balance has been used to measure the strength of gravity (i.e., determine the value of G, the gravitational constant in Newton's Law of Gravitation) (Luther & Towler 1984), to search for the possible composition dependence of gravity (Braginskii & Panov 1972; Su et al. 1994; Gundlach et al. 1997), to search for possible deviations from gravity's inverse square dependence on distance (Chen et al. 1984; Hoskins et al. 1985), and more recently to verify the existence of the Casimir force (Lamoreaux 1997). Currently for terrestrial length scales, it is theoretically easier to envision the addition of another very weak force to the Standard Model mediated by a very light scalar or vector boson than it is to envision a detectable modification of static gravity under General Relativity, and so most modern torsion balance/pendulum null experiments are better characterized as searches for new forces rather than precision measurements of gravity.

Fischbach's re-analysis of Eotvos' data and his hypothesis of a "Fifth Force" (Fischbach et al. 1986) spurred on many experimental groups to prove or disprove his hypothesis. Although the original hypothesis proved to be false at the level predicted, important gaps in our empirical knowledge were filled, and the performance of torsion balance/pendulum devices has been significantly improved. Even without the prompting of a "Fifth Force" search, a renewal of torsion balance/pendulum experiments would have inevitably occurred due to the rapid advancements in computers and electronics which has allowed for the implementation new techniques that previously would have been too difficult, tedious or expensive.

The main topic of this thesis is the description of the successful implementation of such a new technique in which our observable is the amplitude of the second harmonic of the pendulum motion. For this second harmonic measurement technique, the effect of fiber temperature variations is suppressed by more than four orders of magnitude relative to our earlier frequency method. To place this in context, a summary of the research program out of which this new technique evolved is required.

1.2 Use of Large Amplitude Oscillating Torsion Pendula: Index Experiments

Paul Boynton and his collaborators have conducted a series of torsion pendulum experiments at the base of a cliff face near Index, Washington in the North Cascades. Partially in response to Fischbach's conjecture, these experiments tested for the existence of a composition-dependent force using the cliff face as a source mass. The site was a man-made blind tunnel (about 15 feet in diameter and 100 feet long) carved out by the Robbins Company, a Kent, Washington based manufacturer of hard-rock boring equipment, as a test bore

for their equipment. With their cooperation, we arranged to use this granite tunnel which provided an extremely stable thermal environment for our experiment. Despite the presence of a nearby Burlington Northern railway, the overall seismic background was much quieter than at our laboratory on campus. This thesis will concentrate on the present apparatus, dubbed the Index IV experiment. The Index IV apparatus incorporated several improvements over the previous Index designs, but chief among them are the total automation of data acquisition and the movement of the pendulum and the ability to remotely start and stop runs and download data via modems here at the University of Washington. I have thus been denied the character-building experience of collecting data in a cold, dark, damp cave for 10 to 12 hours at a stretch.

Historically, two primary measurement techniques have been developed for the torsion pendulum/balance. In one, the signal is the equilibrium angular displacement of the pendulum resulting from the presence of an external torque. In the other, this torque is detected by the associated fractional change in the natural frequency of torsion oscillations. It is the latter course which the Index collaboration pursued. Although other groups had employed the frequency method (Luther & Towler 1984), the Index collaboration's effort was the first to seriously attempt high precision torque measurements with a torsion pendulum whose oscillation amplitude was greater than a small fraction of a radian. Other groups had hesitated to operate at large amplitudes due to various concerns such as the belief that the oscillations would excite complex torsion fiber processes that would obscure any attempt to detect extremely weak signals. One of our group's main achievements has been to demonstrate that, while these other experimenters' concerns were not entirely imaginary, large

amplitude fiber effects are quite manageable, and the improvements in signal-to noise obtained by operating at large amplitude far outweigh any of the method's disadvantages when trying to detect small changes in frequency. Because it would be extremely difficult to maintain the required linearity and stability of an electronic measuring device with an angular dynamic range of several radians, our data consists of the times at which the pendulum crosses through certain fiducial angles (nominally every 45 degrees) rather than a continuous time series of angular deflection.

Although large-amplitude operation reduces the effect of additive measurement noise, it does not alleviate the torsion pendulum's sensitivity to temperature drifts. The shear modulus of our beryllium-copper torsion fiber is temperature dependent, which results in a fractional change in oscillation frequency of about 1 part in 10^4 per degree Celsius. We had incorporated both active and passive temperature controls in the Index IV apparatus, but as we continued to reduce the noise budget of the experiment, we were faced with the temperature induced variations in frequency becoming an ever more prominent problem. As deflection-type torsion balance experiments approached nanoradian precision, to compete, we would have to measure the frequency to a few parts in 10^9 which translated into 10 microKelvin control over the time it took to acquire a complete cycle of data, about four hours. We had achieved frequency stability of a few parts in 10^9 on the time scale of minutes but not of hours. Whenever the support point of the fiber is rotated to a new position, fiber relaxation modes are excited that cause an exponentially decaying drift in the pendulum equilibrium position, and since these had to settle down before reasonable data could be obtained, we could not significantly shorten the time it

takes to acquire a complete cycle of data. This was unfortunate as the time scale of data acquisition (four hours) was uncomfortably close to the diurnal (i.e., 24 hour) period that has some of the largest temperature variations.

1.3 A New Large Amplitude Method: Measuring the Second Harmonic Response

It was to address these problems, that we developed a new large-amplitude torsion pendulum method: using the second harmonic response as a measure of the external torque on the pendulum. The origin of this method was my study of the fundamental thermal noise limits of torsion balance/pendulum experiments. Deflection type experiments have optimal signal-to-noise in the non-oscillating limit (i.e., 0° amplitude) whereas frequency type experiments have optimal signal-to-noise when the oscillation amplitude is about 105°, which is the amplitude used in our Index IV frequency experiments. A certain sense of conservation of information (admittedly, a somewhat dubious concept) prompted me to conjecture that if the information from all possible signals were added up, the total information about an external torque would be a constant, independent of oscillation amplitude. I must confess I have not rigorously proved or disproved this conjecture, but the idea did suggest that there might be an appreciable amount of information in the higher harmonics of the response at large amplitude. The first of these is the second harmonic, and after a few attempts I developed an algorithm that could extract the second harmonic amplitude from the raw crossing times provided that the fundamental oscillation amplitude was greater than 225°. Fortunately, this new method could be tested without having to modify any of the apparatus hardware or control and data acquisition software.

The success of the second harmonic method was immediately apparent. Even though the slow temperature drifts that had plagued the frequency method had not been removed, the Index IV apparatus could measure the amplitude of the second harmonic response to *nanoradian* precision with just one week's worth of data. Was the torsion pendulum's fundamental susceptibility to slow temperature drifts entirely removed? Not quite. Besides the existence of an external torque, the most significant physical process that can produce a second harmonic response is a cubic anharmonic term in the fiber potential energy. With our beryllium-copper torsion fiber, we observe a fiber-induced second harmonic of 5×10^{-7} radians. Presently, this is too small for us to detect any temperature dependence, but if the fractional change per °C is comparable to that of the shear modulus, then the temperature-induced change in signal is possibly a million times smaller for the second harmonic method than for the frequency method. With this suppression of temperature dependence, we can move beyond the primary limitation of the frequency method. In the near future, temperature variations could become a major limitation for deflection methods as well because the temperature coefficient of deflection is only about an order of magnitude smaller than the corresponding temperature coefficient of frequency.

2 Large Amplitude Oscillating Torsion Pendulum Detection of a Composition-Dependent Force

2.1 Characterization of a Finite-Range Composition-Dependent Force on a Torsion Balance

In order to characterize a weak, composition-dependent force (CDF) with a Yukawa-type potential, one can specify its strength relative to gravity, ξ, its characteristic range, λ, and the Lorentz-invariant quantity, q, to which the force couples. The gravitational plus CDF potential energy of two point masses is then

$$U_{12} = -\frac{Gm_1m_2}{r_{12}}\left(1 + \xi q_1 q_2 \exp\left(-\frac{r_{12}}{\lambda}\right)\right). \tag{2.1}$$

A CDF can couple to several different Lorentz-invariant quantities, but for the sake of concreteness, this section will discuss only baryon-baryon coupling for which the Lorentz-invariant quantity is the baryon number per rest mass, b, where

$$q \Rightarrow b = \frac{\text{number of baryons}}{\text{mass/(1 amu)}} = \frac{\text{mass number}}{\text{atomic mass}} \equiv 1. \tag{2.2}$$

For all known materials, b differs from 1 at most by only a few parts per thousand. Notice that both b and ξ are defined as dimensionless quantities whereas λ has units of length. Theoretically, a new force could have a finite range because it is mediated by a boson that is not massless. Experimentally, this means there could be forces on terrestrial length scales that would not be observed in lunar and planetary orbits. Precision measurements of these orbits

presently set the lowest limits on the existence of an infinite-range CDF (Muller & Nordtvedt 1998). Terrestrial length scale experiments can be futher classified as shorter-range experiments that use movable laboratory source masses and longer-range experiments that use immovable source masses such as mountains or the Earth itself. Since Index IV is of the latter variety, I will discuss only stationary source mass methods in this section.

The potential energy of a point mass interacting with a distributed source mass can be expressed in terms of a gravitational potential, V_g, and a CDF potential, V_b,

$$\begin{aligned} U(\mathbf{r}_2) &= m_2 V_g(\mathbf{r}_2) + \xi m_2 b_2 V_b(\mathbf{r}_2;\lambda) \\ &= -m_2 \iiint_{source} \frac{G\rho_1}{r_{12}} d^3\mathbf{r}_1 - \xi m_2 b_2 \iiint_{source} \frac{Gb_1\rho_1}{r_{12}} \exp\left(-\frac{r_{12}}{\lambda}\right) d^3\mathbf{r}_1. \end{aligned} \tag{2.3}$$

To predict the CDF on a torsion balance or torsion pendulum requires a calculation of the local $\nabla V_b(\lambda)$ which depends on the topography and composition of the environment, but to simplify the presentation in this section, let us invoke an ideal Earth source mass that is a perfect sphere of uniform composition with $b_{source} = 1$ exactly. In addition, let us restrict our attention to the infinite-range limit, $\lambda \to \infty$. With these simplifications, the CDF potential is directly proportional to the gravitational potential

$$V_b = \xi V_g. \tag{2.4}$$

Conceptually, the most direct way to test for the existence of such a CDF is a vertical free fall experiment. The free fall acceleration of a mass is

$$\mathbf{a} = \nabla V_g + b\nabla V_b = \mathbf{g}(1 + \xi b). \tag{2.5}$$

Thus, by comparing the differential acceleration of two masses with different b, the strength of the CDF,

$$\xi = \frac{\Delta a}{g \Delta b}, \tag{2.6}$$

can be measured. Although this method has been attempted (Carusotto et al. 1992), to date it has not achieved precision comparable to the torsion balance/pendulum experiments.

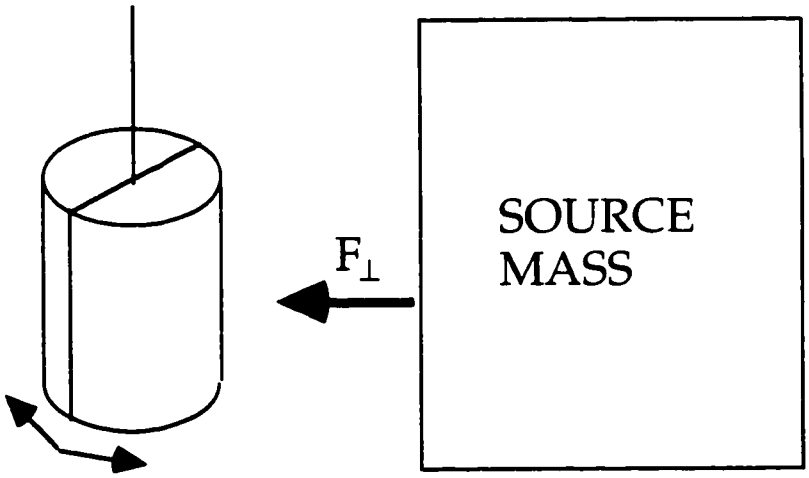

Figure 2.1. Horizontal force from source mass interacting with a two-material, composition-dipole torsion balance.

To test for a CDF with a torsion balance, a two-material mass is suspended by a torsion fiber in the proximity of a large source mass as shown in Figure 2.1, and the presence of a horizontal CDF can be detected by the slight rotation caused by the torque on the torsion balance. Since the torsion balance is sensitive only to horizontal forces, it would seem, at first glance, that our perfectly spherical, ideal Earth source mass would not exert a torque on the torsion balance. However, because of the centrifugal force due to the rotation of the Earth,

the local vertical does not generally point towards the center of the Earth, and the surface of the Earth sphere is tilted slightly from horizontal in the local frame resulting in a horizontal component to the gravitational field,

$$g_{\perp} \equiv \frac{\omega_e^2 R_e \sin 2\theta}{2}, \tag{2.7}$$

where ω_e is the rotation frequency of the Earth, R_e is the radius of the Earth, and θ is the latitude. The maximum value of the horizontal component occurs at a latitude of 45° where

$$g_{\perp} \equiv \frac{g}{582} = 1.71 \frac{\text{cm}}{\text{sec}^2}. \tag{2.8}$$

Even though a torsion balance/pendulum sacrifices a factor of roughly 600 in signal by measuring only horizontal forces, its ability of to precisely measure extremely small forces still makes it the apparatus of choice in searching for a terrestrial scale CDF.

An actual composition-dipole torsion balance is an extended mass, and it can not be treated simply as two point masses. If it is suspended by a single fiber, then its center-of-mass hangs below its support point, and it has no horizontal first moments with respect to the local vertical

$$\iiint_{balance} \rho \mathbf{r}_{\perp} dV = 0. \tag{2.9}$$

To leading order, this means the horizontal gravitational field, $\mathbf{g}_{\perp}$, does not exert a torque on the torsion balance

$$\tau_{z\,grav}\hat{\mathbf{k}} \equiv \iiint_{balance} \mathbf{r}_{\perp} \times \rho \mathbf{g}_{\perp} dV = -\mathbf{g}_{\perp} \times \iiint_{balance} \rho \mathbf{r}_{\perp} dV = 0. \tag{2.10}$$

There are significant torques that arise from higher derivatives of the gravitational field, and they will be discussed in Sections 4.4 and 5.2, but for this section they will be neglected. With that assumption, only the CDF can exert a torque on the torsion balance. In order to predict the strength of this CDF signal, let us define the composition-dipole moment of the torsion balance as

$$\mathbf{p}_b = \iiint_{balance} \mathbf{r}_\perp \rho b dV = p_b \cos(\theta)\hat{\mathbf{i}} + p_b \sin(\theta)\hat{\mathbf{j}}. \tag{2.11}$$

For a two-material torsion balance with bilateral symmetry, $\mathbf{p}_b$ points towards the higher b half of the balance, and θ will be used to specify the azimuth of the balance in the laboratory frame. The angle ψ will be used to specify the azimuth of the local horizontal gravitational field

$$\mathbf{g}_\perp = g_\perp \cos(\psi)\hat{\mathbf{i}} + g_\perp \sin(\psi)\hat{\mathbf{j}}. \tag{2.12}$$

The external torque around the vertical axis is then

$$\begin{aligned} \tau_z \hat{\mathbf{k}} &= \iiint_{balance} \mathbf{r}_\perp \times \mathbf{f}_\perp dV = \iiint_{balance} \mathbf{r}_\perp \times \rho \mathbf{g}_\perp (1 + \xi b) dV = \\ &= -\mathbf{g}_\perp \times \iiint_{balance} \rho \mathbf{r}_\perp dV - \xi \mathbf{g}_\perp \times \iiint_{balance} \mathbf{r}_\perp \rho b dV \\ &= -\xi \mathbf{g}_\perp \times \mathbf{p}_b = -\xi g_\perp p_b \sin(\theta - \psi)\hat{\mathbf{k}}. \end{aligned} \tag{2.13}$$

In static equilibrium, the above external torque is balanced against the torque exerted by the torsion fiber

$$\tau_{z\,fiber} = -\kappa(\theta - \phi) \tag{2.14}$$

where κ is the torsional fiber constant and ϕ is the azimuth of the equilibrium position of the fiber, which can be adjusted by rotating the fiber support. When using a topographic source mass (such as our ideal Earth), which can not be

moved in the lab frame, the azimuth of the external field, ψ, is a constant. Thus, the azimuth of the fiber support, ϕ, must be varied in order to change θ and thereby produce a detectable, sinusoidal variation in the external torque. The controllable input is ϕ, and the observed output is the deflection,

$$C(\phi) = \theta - \phi = \frac{\tau_{zext}(\theta)}{\kappa} = -\frac{\xi p_b g_\perp}{\kappa}\sin(\theta - \psi) \equiv -\frac{\xi p_b g_\perp}{\kappa}\sin(\phi - \psi). \quad (2.15)$$

The replacement of $\sin(\theta - \psi)$ with $\sin(\phi - \psi)$ is a valid first-order approximation provided that the external force is weak. This approximation is introduced here so that the results of this section will be consistent with the presentation of the oscillating pendulum methods in Section 2.2. Finally, by taking the difference between the maximum and minimum deflections, the strength of the CDF,

$$\xi = -\frac{\kappa\left[C(\phi = \psi + \pi/2) - C(\phi = \psi - \pi/2)\right]}{2p_b g_\perp}, \quad (2.16)$$

can be obtained.

For a finite-range CDF from a real, topographical source mass, the above derivation is essentially correct except that $\mathbf{g}_\perp$ is replaced by

$$\nabla_\perp V_b(\lambda) = |\nabla_\perp V_b(\lambda)|\cos(\psi(\lambda))\hat{\mathbf{i}} + |\nabla_\perp V_b(\lambda)|\sin(\psi(\lambda))\hat{\mathbf{j}}, \quad (2.17)$$

and therefore

$$C(\phi) = -\frac{\xi(\lambda)p_b|\nabla_\perp V_b(\lambda)|}{\kappa}\sin(\phi - \psi(\lambda)). \quad (2.18)$$

Since the azimuth of maximum torque tends to be different for different hypothesized values of λ, a continuous record of $C(\phi)$ is made, and then the ap-

propriate Fourier component is extracted to determine the strength of the CDF for each hypothesized value of λ,

$$\xi(\lambda) = -\frac{\kappa}{\pi p_b |\nabla_\perp V_b(\lambda)|} \int_0^{2\pi} C(\phi) \sin(\phi - \psi(\lambda)) d\phi. \tag{2.19}$$

Now that the traditional torsion balance method has been presented, the extension to oscillating, large-amplitude pendulum methods will be presented in Section 2.2. The composition-dipole pendulum is no longer in static equilibrium, and there are other parameters besides the time-averaged deflection, $C(\phi)$, that characterize the motion of the oscillator. Section 2.2 will explain how it is possible to obtain $\xi(\lambda)$ from those other parameters.

2.2 Oscillating Large-Amplitude Methods: Signal vs. Amplitude

Although it is physically more intuitive to describe interactions with the torsion pendulum in terms of external torques rather than the more abstract potential energy, mathematically the scalar potential energy is simpler to manipulate than axial vector torque quantities. This will be particularly true when explaining couplings to higher gravitational field derivatives in Sections 4.4 and 5.2. The azimuthal potential energy function of the pendulum is

$$U_{ext}(\theta) = \xi(\lambda) p_b |\nabla_\perp V_b(\lambda)| \cos(\theta - \psi(\lambda)). \tag{2.20}$$

For brevity, let us temporarily express this as

$$U_{ext}(\theta) = |U_{ext}| \cos(\theta - \psi). \tag{2.21}$$

As before, ϕ is the azimuth of the equilibrium position of the fiber, and the potential energy due to an ideal fiber is

$$U_{fiber}(\theta) = \kappa(\theta - \phi)^2/2, \tag{2.22}$$

but now the azimuth of the pendulum is an oscillating function of time, $\theta(t)$. If damping is neglected, and $t = 0$ is defined as one of the oscillator turning points, then in the absence of $U_{ext}(\theta)$, the nominal motion of the oscillator is

$$\theta(t) = \phi + A\cos(\omega_o t). \tag{2.23}$$

The existence of an external potential energy, $U_{ext}(\theta)$, can be detected by observing deviations from this nominal motion.

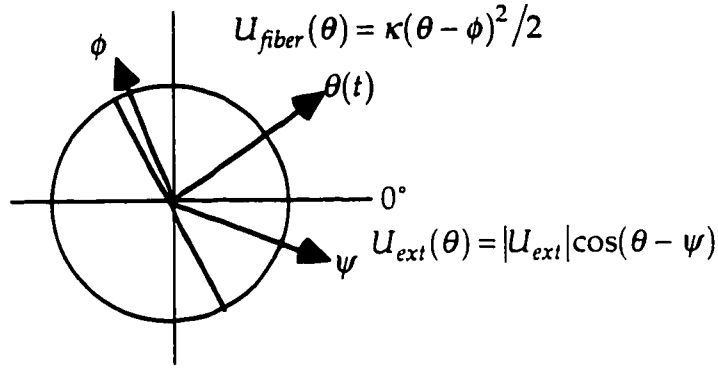

Figure 2.2. Oscillating azimuth of the composition-dipole, $\theta(t)$, and the dependence of U_{fiber} on $(\theta - \phi)$ and U_{ext} on $(\theta - \psi)$.

Figure 2.2 shows the three azimuths, ϕ, $\theta(t)$, and ψ, that are important to the description of our large-amplitude oscillating torsion pendulum method. The choice of 0° azimuth is arbitrary but is usually chosen to be the direction of photodiode detector in the lab frame. The azimuth of the equilibrium position, ϕ, is constant while data is acquired but changes whenever the fiber support is rotated. The azimuth of the composition-dipole, $\theta(t)$, oscillates with the pendulum. The azimuth of maximum potential energy, ψ, depends on the assumed value of λ, but for the case of $\lambda \to \infty$, it points North, the same direction

as the horizontal gravitational field, $\mathbf{g}_\perp$. Summary of our oscillating torsion-pendulum experimental method:

1. Rotate the fiber support to various azimuths, ϕ, and at each azimuth record several periods of free oscillation motion, $\theta(t)$.

2. At each ϕ, fit θ vs. t from the raw crossing-time data and determine the value of the frequency (old method) or second harmonic amplitude (new method).

3. From the sinusoidal variation in the frequency or the second harmonic amplitude vs. ϕ, determine $U_{ext}(\theta)$ and ultimately $\xi(\lambda)$.

Now, let us be more mathematically explicit about the response of an oscillator to an external sinusoidal potential energy, $U_{ext}(\theta)$. If damping is neglected, the periodic motion of the pendulum can be expanded in Fourier components as

$$\theta(t) = \phi + A\cos\left[(\omega_o + \Delta\omega)t\right] + C + \sum_{n=2}^{\infty} A_n \cos\left[n(\omega_o + \Delta\omega)t\right]. \tag{2.24}$$

For simplicity, one of the turning points has been chosen as $t = 0$, and thus by time-reversal symmetry, there are only cosine harmonic components. With respect to a given equilibrium-position azimuth, ϕ, $U_{ext}(\theta)$ can be split into a sine component, which is odd in $(\theta - \phi)$, and a cosine component, which is even in $(\theta - \phi)$. First, let us look at the effect of the sine component,

$$U_{ext}(\theta - \phi) = u_s \sin(\theta - \phi). \tag{2.25}$$

For a weak external potential energy ($u_s << \kappa$), u_s produces only a shift in deflection and even harmonics of motion. To first-order in u_s, the coefficients are

$$C = -\frac{J_0(A)u_s}{\kappa}, \qquad A_2 = -\frac{2J_2(A)u_s}{3\kappa}, \tag{2.26}$$

$$\text{and } A_{n\,even} = (-1)^{n/2}\frac{2J_n(A)u_s}{(n^2-1)\kappa},$$

where $J_n(A)$ are Bessel functions evaluated with A in radians. Next, consider the effect of the cosine component,

$$U_{ext}(\theta-\phi) = u_c\cos(\theta-\phi). \tag{2.27}$$

For a weak external potential energy ($u_c << \kappa$), u_c produces only a shift in frequency and odd harmonics of motion. To first-order in u_c, the coefficients are

$$\frac{\Delta\omega}{\omega_o} = -\frac{J_1(A)u_c}{A\kappa}, \qquad A_3 = \frac{2J_3(A)u_c}{8\kappa}, \tag{2.28}$$

$$\text{and } A_{n\,odd} = (-1)^{(n+1)/2}\frac{2J_n(A)u_c}{(n^2-1)\kappa}.$$

If the actual $U_{ext}(\theta)$ is now split into even and odd parts in $(\theta-\phi)$

$$\begin{aligned} U_{ext}(\theta) &= |U_{ext}|\cos(\theta-\psi) = |U_{ext}|\cos\big((\theta-\phi)+(\phi-\psi)\big) \\ &= |U_{ext}|\cos(\phi-\psi)\cos(\theta-\phi) - |U_{ext}|\sin(\phi-\psi)\sin(\theta-\phi), \end{aligned} \tag{2.29}$$

it is evident that u_c and u_s vary sinusoidally with ϕ;

$$u_c(\phi) = |U_{ext}|\cos(\phi-\psi), \text{ and } u_s(\phi) = -|U_{ext}|\sin(\phi-\psi). \tag{2.30}$$

When equations 2.30 are substituted into equations 2.26 and 2.28, one obtains the sinusoidal variation of the deflection, frequency, and higher harmonics:

$$C(\phi) = \frac{J_0(A)|U_{ext}|}{\kappa}\sin(\phi - \psi), \qquad \frac{\Delta\omega}{\omega_o}(\phi) = -\frac{J_1(A)|U_{ext}|}{A\kappa}\cos(\phi - \psi),$$

$$A_2(\phi) = \frac{2J_2(A)|U_{ext}|}{3\kappa}\sin(\phi - \psi), \qquad A_3(\phi) = \frac{2J_3(A)|U_{ext}|}{8\kappa}\cos(\phi - \psi),$$

$$A_{n\,even}(\phi) = (-1)^{(n+2)/2}\frac{2J_n(A)|U_{ext}|}{(n^2-1)\kappa}\sin(\phi - \psi), \tag{2.31}$$

$$\text{and } A_{n\,odd}(\phi) = (-1)^{(n+1)/2}\frac{2J_n(A)|U_{ext}|}{(n^2-1)\kappa}\cos(\phi - \psi).$$

Because each of the above parameters depends sinusoidally on $(\phi - \psi)$, any one of them can be used to detect the external potential energy,

$$U_{ext}(\theta) = |U_{ext}|\cos(\theta - \psi) = \xi(\lambda)p_b|\nabla_\perp V_b(\lambda)|\cos(\theta - \psi(\lambda)). \tag{2.32}$$

In particular, we are interested in the use of $C(\phi)$, $\Delta\omega(\phi)/\omega_o$, and $A_2(\phi)$ as signals to determine the strength of the CDF,

$$\xi(\lambda) = -\frac{\kappa}{\pi J_0(A)p_b|\nabla_\perp V_b(\lambda)|}\int_0^{2\pi} C(\phi)\sin(\phi - \psi(\lambda))d\phi, \tag{2.33}$$

$$\xi(\lambda) = -\frac{A\kappa}{\pi J_1(A)p_b|\nabla_\perp V_b(\lambda)|}\int_0^{2\pi} \frac{\Delta\omega}{\omega_o}(\phi)\cos(\phi - \psi(\lambda))d\phi, \tag{2.34}$$

$$\text{and } \xi(\lambda) = -\frac{3\kappa}{2\pi J_2(A)p_b|\nabla_\perp V_b(\lambda)|}\int_0^{2\pi} A_2(\phi)\sin(\phi - \psi(\lambda))d\phi. \tag{2.35}$$

Equation 2.19, which was derived for the torsion-balance deflection method, is the zero amplitude limit of Equation 2.33. Our group has used the variation in frequency (Eq. 2.34), and more recently the variation in second harmonic ampli-

tude (Eq. 2.35) to determine $\xi(\lambda)$. To be rigorously correct, the Fourier integrals should be replaced with discrete sums for methods, such as ours, that rotate ϕ in discrete steps rather than continuously. The magnitudes of these three signals–$|C(\phi)|$, $|\Delta\omega(\phi)/\omega_o|$, and $|A_2(\phi)|$–are plotted in Figure 2.3 as functions of the oscillation amplitude, A.

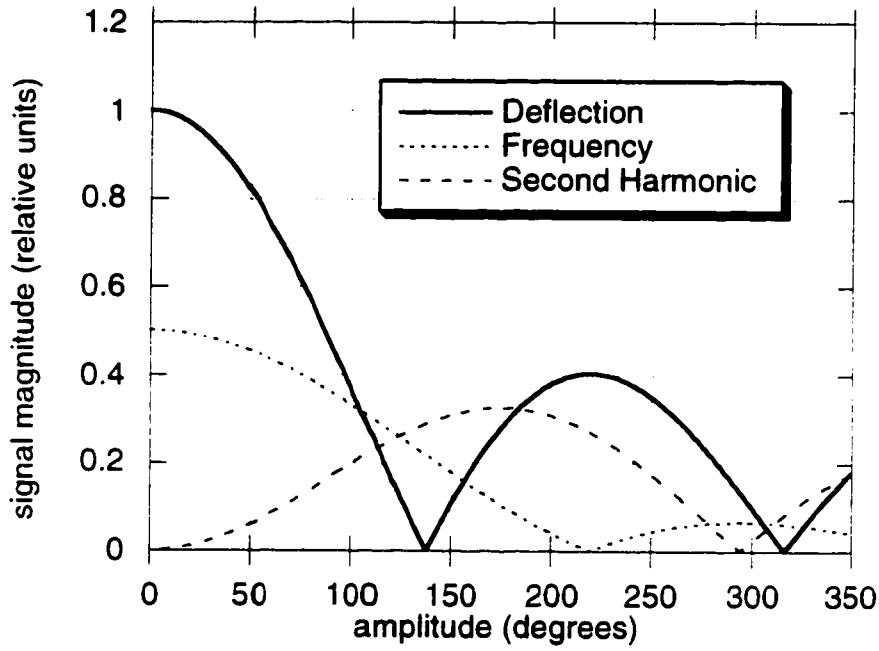

Figure 2.3. Magnitude of deflection signal, frequency signal and second harmonic signal as a function of torsion pendulum oscillation amplitude.

For the traditional deflection method ($C(\phi)$ as signal), the maximum signal occurs at 0° amplitude, and there is no reason to use an oscillating pendulum. Looking at Figure 2.3 , it would seem that the small amplitude limit would be optimal for the frequency method as well, but signal-to-noise considerations (discussed in Sections 2.4 and 3.1) define an optimal amplitude of 105°. For our

second harmonic method, the maximum signal-to-noise occurs at 175°, but in order to get a sufficient number of crossings to fit for all relevant parameters, it turns out we must operate at 230° amplitude. This particular second harmonic fit method (the "10-parameter fit") is presented in Section 2.3; and for comparison, our older frequency fit method (the "5-parameter fit") is presented in Section 2.4.

2.3 Description of Second Harmonic Method (10-parameter Fit)

The equation of motion,

$$\theta(t) = \phi + A\exp\left[-\gamma\left(t - t_{eq}\right)\right]\sin\left[\omega\left(t - t_{eq}\right)\right] + A_2\cos\left[2\omega\left(t - t_{eq}\right)\right] + B_3\sin\left[3\omega\left(t - t_{eq}\right)\right] + C + D\left(t - t_{eq}\right), \tag{2.36}$$

used in our actual second harmonic fit method is slightly different from the equation of motion (Eq. 2.24) presented in Section 2.2. The individual fits are centered in time on a crossing of the equilibrium position rather than at a turning point, and therefore sine is used for the fundamental of oscillation rather than cosine. Because the exact phase of oscillation is not known *a priori*, the parameter t_{eq} is introduced to parameterize the phase. The damping of the fundamental is not negligible so the parameter γ is introduced to parameterize the exponential decay in amplitude, and A is defined as the instantaneous amplitude at t_{eq}. Of the higher harmonics, only the second and third (A_2 and B_3) are included in the fit, and they are small enough that no exponential decay factors are needed. The secular drift term, $D\left(t - t_{eq}\right)$, is introduced to parameterize the slow unwinding that is observed in a torsion fiber under tension. Although the fiber is nominally a perfect cylinder, the extrusion process in manufacture creates right-handed or left-handed helical stresses that slowly relax.

Eight parameters of the 10-parameter fit, $\{A, \gamma, \omega, t_{eq}, A_2, B_3, C, D\}$, appear in Eq. 2.36. The equilibrium position of the fiber, ϕ, does not count as a parameter because it is a controlled input. It is only $A_2(\phi)$, however, that is used to determine the strength of the external CDF, $\xi(\lambda)$ (see Eq. 2.35 in Section 2.2). The ninth and tenth parameters, θ_1 and θ_2, fit for angles between the faces of the eight-sided edge-reflector attached to the pendulum. These mirror angles are nominally 45 degrees but differ by a few tenths of a degree due to imperfections in the edge-reflector's manufacture. In our present Index IV apparatus, a visible-light semiconductor laser shines a beam on the eight-sided edge-reflector which is attached to the rotating torsion pendulum, and a split photodiode detects the reflected beam. A crossing time (to the nearest 0.5 microsecond) is thus recorded approximately every 45° of pendulum motion. In collecting data, the fiber support is rotated to positions for which the azimuth of the fiber equilibrium position, ϕ, is nominally aligned with one of the eight mirror faces. A 10-parameter fit is carried out for each period of free oscillation data.

The term "fit" usually implies an over-determined fit that optimizes some measure of goodness-of-fit such as minimizing the squares of the residues. Historically, our initial data analysis step has consisted of exactly determined fits of n parameters to n data points that are then averaged. In general, this method is less optimal than the least-squares fitting method, but for the 10-parameter fit, the difference is quite small, and therefore we have not yet modified our analysis software to support least-squares fitting. For each period of data, we select two sets of ten crossings designated crossing set I and crossing set II. The mirror angles θ_1 and θ_2 and the crossing times used in the two crossings sets of the 10-parameter fit are shown in Figure 2.4.

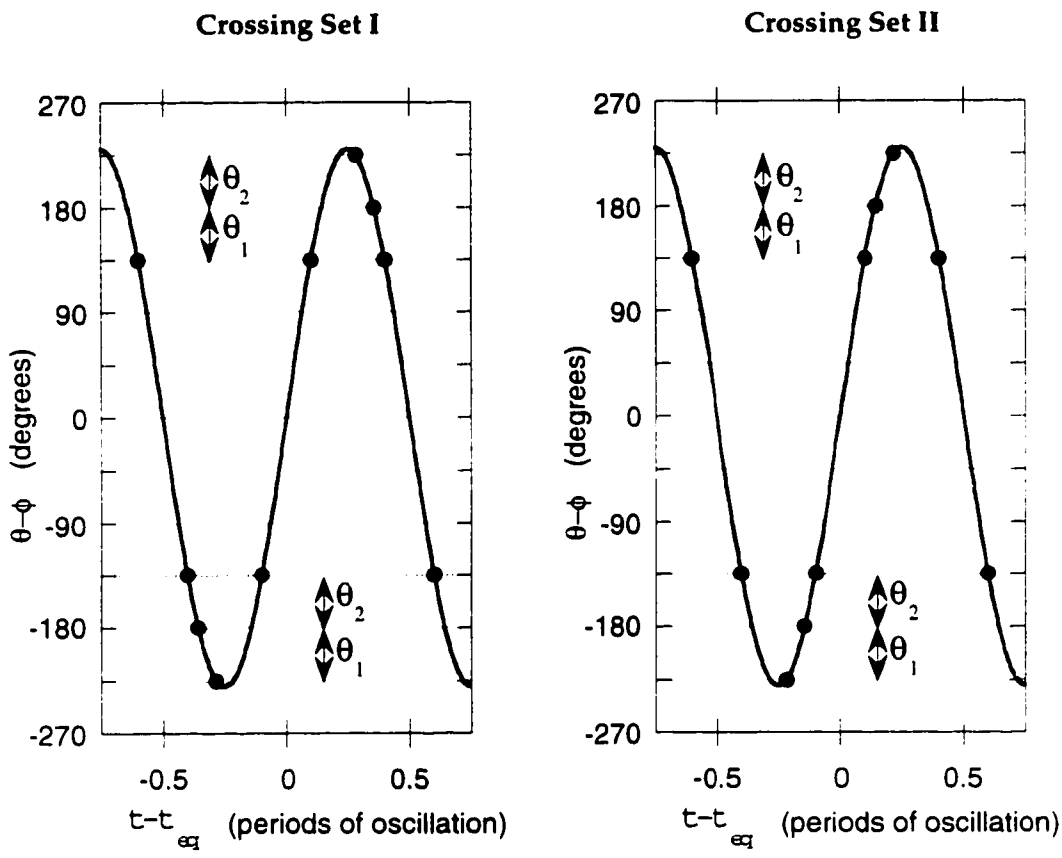

Figure 2.4. Black dots indicate crossing times of crossing set I and crossing set II. The parameter estimates of the 10-parameter fit are defined as the average of the solutions obtained from crossing set I and from crossing set II.

The ten parameters, $\{A, \gamma, \omega, t_{eq}, A_2, B_3, C, D, \theta_1, \theta_2\}$, are fit to the ten time crossings of crossing set I, and the ten parameters are also fit to the ten time crossings of crossing set II. These solutions are not independent as they share six of their ten crossings. For each period of data, the solution for $\{A, \gamma, \omega, t_{eq}, A_2, B_3, C, D, \theta_1, \theta_2\}$ from crossing set I is averaged with that from crossing set II and is printed to an output file. In Sections 3 and 4, the error

propagation of a "10-parameter fit" will refer to this average which is effectively a fit of ten parameters to fourteen crossings.

A 10-parameter fit uses crossings from just three mirrors, the 135°, 180°, and 225° mirrors which are identical to the -225°, -180°, and -135° mirrors except that they are separated by a 360° rotation. Unlike θ_1 and θ_2, these 360° rotations are known to be exact *a priori*, and this knowledge is essential to making the 10-parameter fit non-degenerate. Thus, although the variation in the second harmonic, $|A_2(\phi)|$, is largest for $A = 175°$, we need $A > 225°$ to get enough crossings from the eight-sided edge reflector for the fit to all ten parameters to be non-degenerate. Data is collected at $A = 230°$ to provide a margin of safety so that no crossings will be missed. The amplitude of oscillation is controlled by choosing the speed and time at which the automatic move software rotates the fiber support to a new position.

Crossings with negative velocity (i.e., $d\theta/dt < 0$) are designated as "1" type crossings in the data log while positive velocity crossings are designated as "2" type crossings. Those fits that are centered in time on a "1" type equilibrium crossing are called a 212 type fit, and those fits that are centered in time on a "2" type equilibrium crossing are called a 121 type fit. For the 212 type 10-parameter fit, minus signs are placed before A and B_3 in the equation of motion

$$\begin{aligned}\theta(t) = \phi - A\exp\left[-\gamma\left(t - t_{eq}\right)\right]\sin\left[\omega\left(t - t_{eq}\right)\right] + \\ A_2\cos\left[2\omega\left(t - t_{eq}\right)\right] - B_3\sin\left[3\omega\left(t - t_{eq}\right)\right] + C + D\left(t - t_{eq}\right)\end{aligned} \tag{2.37}$$

so that the values of all the parameters from 212 type fits are consistent in sign with those from 121 type fits. Doing both 121 and 212 type fits is useful because

the error propagation of certain systematic effects is equal and opposite for 121 and 212 fits and therefore cancels out to first order upon averaging. Most notable of these effects is the local linear drift of frequency caused by drifts in the fiber temperature as will be discussed further in Sections 3.6.

2.4 Description of Frequency Method (5-parameter Fit)

Prior to using the variation in second harmonic amplitude as our signal, our group used the variation in frequency, $\Delta\omega(\phi)$, to determine the strength of the external CDF, $\xi(\lambda)$ (see Eq. 2.34 in Section 2.2). The equation of motion was simpler,

$$\theta(t) = \phi + A\exp(-\gamma t)\sin\left[\omega\left(t - t_{eq}\right)\right] + C, \tag{2.38}$$

using only the five parameters of a damped sine wave, $\left\{A, \gamma, \omega, t_{eq}, C\right\}$. We therefore refer to this frequency method as the 5-parameter fit. To properly describe the 5-parameter fit requires some further elaboration of our optical system. Above in Section 2.3, it was stated that a crossing occurs approximately once every 45° of pendulum rotation, but in fact a diagonal mirror in the return path of the laser beam has been split into two halves and tilted, forming a slight dihedral angle. This results in two separate crossings rather than one as each face of the eight-sided edge-reflector passes by. The angular separation of the two crossings is 3.10° on each of the eight faces, and the two types of crossings are designated "fixed mirror" and "movable mirror" crossings because one of the split diagonal mirrors is adjustable for optical alignment purposes. The 10-parameter fit treats the fixed and movable mirror crossings as separate data sets and does independent fits to each whereas the 5-parameter fit uses both

types of crossings in a single fit. The crossings used in the 5-parameter are shown in Figure 2.5.

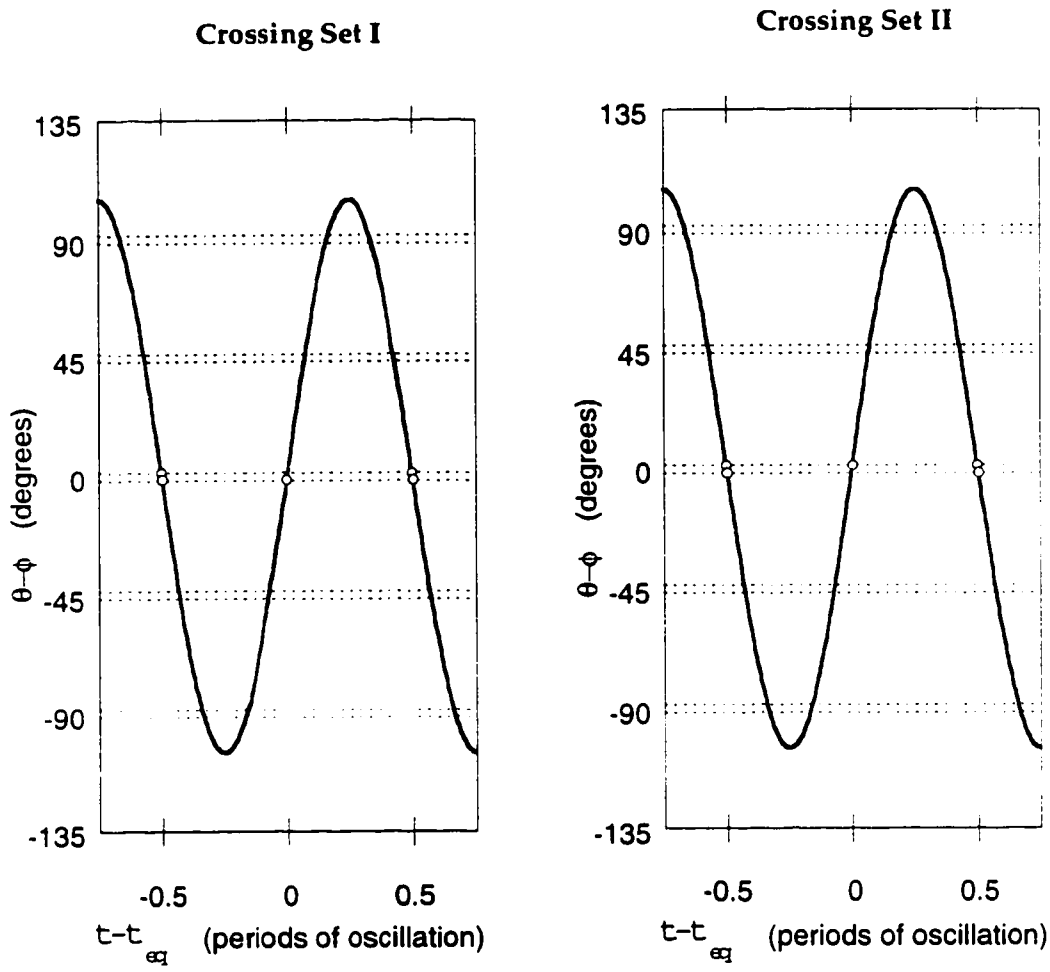

Figure 2.5 Circles indicate crossing times used in crossing set I and crossing set II of 5-parameter fit.

Similar to the 10-parameter fit, the 5-parameter fit is the average of exactly determined fit of n parameters to n data points. The six crossings of the 5-parameter fit are grouped into overlapping sets of five, and a exactly determined fit of 5 parameters to 5 crossings is carried out for both crossing set I and

crossing set II. The parameter estimates of the 5-parameter fit are defined as the average of the solutions obtained from crossing set I and from crossing set II.

As depicted in Figure 2.5, our group uses an oscillation amplitude, A, of 105° for the frequency method. Although the signal strength of $|\Delta\omega(\phi)|$ is proportional to $J_1(A)/A$ (where A is in radians), the error propagation of most noise processes scales as $1/A$ for frequency, and thus the signal-to-noise is optimum at the maximum of $J_1(A)$, which occurs for $A = 1.84$ radians = 105 degrees. Unlike the 10-parameter fit, the 5-parameter fit must use an assumed value for the mirror angle rather than fitting for it directly. This does not affect the estimates of ω, γ, or t_{eq}, but the estimates of A and C will be directly proportional to that assumed value. Since the variation in frequency is the signal, this uncertainty in A is not a leading problem, but it can cause complications in fine-tuned amplitude corrections of the frequency used in later stages of data analysis (see Section 5.3).

Another parameter not in the 5-parameter fit is the linear drift in the fiber due to unwinding. This is subtracted out by averaging 121 and 212 type fits. The sign of A in the equation of motion,

$$\theta(t) = \phi - A\exp(-\gamma t)\sin\left[\omega\left(t - t_{eq}\right)\right] + C, \tag{2.39}$$

is reversed so that the 212 estimates of A will have the same sign as 121 estimates of A. For the 10-parameter fit, averaging of 121 and 212 type fits is used to remove the linear drift in frequency, but for the 5-parameter fit, no such easy remedy is at hand because the frequency is the signal for the 5-parameter fit. Ultimately, it was the temperature induced drifts in frequency that prompted

our group to adopt the 10-parameter fit second harmonic method over the 5-parameter fit frequency method.

3 Error Propagation and Noise Comparison of the 10-parameter Fit and the 5-parameter Fit

3.1 Error Propagation of the 10-parameter Fit and the 5-parameter Fit

Both the 10-parameter fit and the 5-parameter fit are simple averages of exactly determined fits. Since these fits are unique, no choice between various fits is required, and a goodness-of-fit criteria doesn't need to be specified in order to discuss the error propagation of these fits. Formally, consider a linear fit of n parameters, $\mathbf{p} = \{p_1, p_2, \ldots p_n\}$, to n observations, $\mathbf{y} = \{y_1, y_2, \ldots y_n\}$. In the absence of noise, the pure signal, $\mathbf{y_o}$, would be observed. The true values of the parameters to be determined, $\mathbf{p_o}$, are directly related to this signal by an $n \times n$ design matrix,

$$\mathbf{y_o} = \mathbf{M} \bullet \mathbf{p_o}, \tag{3.1}$$

where it is assumed that $\mathbf{M}$ is known *a priori*. The actual data, of course, includes errors due to noise,

$$\mathbf{y} = \mathbf{y_o} + \Delta\mathbf{y} = \mathbf{M} \bullet \mathbf{p_o} + \Delta\mathbf{y}. \tag{3.2}$$

Because these unknown errors, $\Delta\mathbf{y}$, can not be accounted for, they propagate into errors in the parameter estimates,

$$\mathbf{y} = \mathbf{M} \bullet \mathbf{p} = \mathbf{M} \bullet (\mathbf{p_o} + \Delta\mathbf{p}). \tag{3.3}$$

In order for the fit to be non-degenerate, the square design matrix, $\mathbf{M}$, must have a non-zero determinant, and it is therefore invertible. The inverse of the design matrix, $\mathbf{M}^{-1}$, provides an exact solution for how the data errors propagate into the parameter estimates,

$$\begin{aligned}\Delta\mathbf{p} &= \mathbf{M}^{-1}\bullet\mathbf{y}-\mathbf{p_o} = \mathbf{M}^{-1}\bullet(\mathbf{y}-\mathbf{M}\bullet\mathbf{p_o}) = \mathbf{M}^{-1}\bullet(\mathbf{y}-\mathbf{y_o}) \\ &= \mathbf{M}^{-1}\bullet(\Delta\mathbf{y}).\end{aligned} \tag{3.4}$$

If one is interested in the i^{th} parameter, p_i, in particular, then the contraction of i^{th} row of the inverse design matrix with the data,

$$\hat{p}_i = \sum_{j=1}^{n}\left(M^{-1}\right)_{ij} y_j, \tag{3.5}$$

is the estimator of p_i, and the expected variance of that estimator can be calculated from the i^{th} row of the inverse design matrix and the data covariance matrix,

$$\mathrm{var}(\hat{p}_i) = \sum_{j=1}^{n}\sum_{k=1}^{n}\left(M^{-1}\right)_{ij}\mathrm{cov}\left(y_j,y_k\right)\left(M^{-1}\right)_{ik}. \tag{3.6}$$

Although the form of the estimator (Eq. 3.5) is independent of the noise process, a calculation of the variance of the estimator (Eq. 3.6) does require a knowledge of the noise process because of the dependence on $\mathrm{cov}\left(y_j,y_k\right)$.

Above, I have intentionally used the generic variable $\mathbf{y}=\{y_1,y_2,\ldots y_n\}$ to denote the observations because I do not wish to treat the crossing times, $\mathbf{t}=\{t_1,t_2,\ldots t_n\}$, as the observations in this section. Although the raw data are indeed crossing times at given angles, it will be less awkward to consider the observations as angular positions of the pendulum recorded at specific times,

$$\mathbf{y}=\theta=\{\theta(t_1),\theta(t_2),\ldots\theta(t_n)\}, \tag{3.7}$$

and to treat the noise as angle errors, $\Delta\theta=\{\Delta\theta(t_1),\Delta\theta(t_2),\ldots\Delta\theta(t_n)\}$, rather than timing errors, $\Delta\mathbf{t}=\{\Delta t_1,\Delta t_2,\ldots\Delta t_n\}$. For large signal-to-noise, a first-order ap-

proximation is valid, and a set of equivalent angle errors can be defined in terms of the crossing-time errors as

$$\Delta\theta(t_j) = -\left.\frac{d\theta}{dt}\right|_{t=t_j} \Delta t_j. \tag{3.8}$$

The parameter vector for the 10-parameter fit is,

$$\mathbf{p} = \{A, \gamma, \omega, t_{eq}, A_2, B_3, C, D, \theta_1, \theta_2\}, \tag{3.9}$$

and for the 5-parameter fit is,

$$\mathbf{p} = \{A, \gamma, \omega, t_{eq}, C\}. \tag{3.10}$$

Because of their dependence on γ and ω, both the 10-parameter fit and the 5-parameter fit are non-linear. The exact value of the design matrix, $\mathbf{M}$, is therefore not known *a priori*, and the fit must be repeated iteratively. The linearization of non-linear fits is covered in more depth in Section A.3 of the Appendix, but for this section the important fact is that the equation for the variance in the estimator,

$$\mathrm{var}(\hat{p}_i) = \sum_{j=1}^{n}\sum_{k=1}^{n}\left(M^{-1}\right)_{ij} \mathrm{cov}\left(\theta(t_j), \theta(t_k)\right)\left(M^{-1}\right)_{ik}, \tag{3.11}$$

is still valid to first-order. For the 10-parameter fit, the parameter of interest is A_2, the amplitude of the second harmonic, and for the 5-parameter fit, the parameter of interest is the oscillation frequency, ω. In a non-linear, iterative fit, the inverse of the design matrix, $\mathbf{M}^{-1}$, is contracted with the residue of the data to provide a correction to the initial parameter estimates,

$$\begin{aligned}\hat{\mathbf{p}}_2 &= \hat{\mathbf{p}}_1 + \mathbf{M}_1^{-1} \bullet (\mathbf{y} - \mathbf{y}_1) \\ \hat{\mathbf{p}}_3 &= \hat{\mathbf{p}}_2 + \mathbf{M}_2^{-1} \bullet (\mathbf{y} - \mathbf{y}_2). \\ &\vdots\end{aligned} \tag{3.12}$$

The design matrix, $\mathbf{M}$, is not a constant matrix, but is more properly thought of as the Jacobian matrix of the functions $\{\theta(t_1), \theta(t_2), \ldots \theta(t_n)\}$ with respect to the parameters $\{p_1, p_2, \ldots p_n\}$,

$$M_{ij} = \frac{\partial \theta(t_i)}{\partial p_j}. \tag{3.13}$$

In order to calculate the expected variance in the estimator, $\text{var}(\hat{p}_i)$, in Eq. 3.11, the nominal value of the signal parameters, $\mathbf{p_o}$, at which the first derivatives in the Jacobian are evaluated must be specified. For this section, the nominal signal parameters for the 10-parameter fit will be

$$\begin{aligned}\mathbf{p_o} = \{&A = 230°, \gamma = 0, \omega = \omega_o, t_{eq} = 0, A_2 = 0, \\ &B_3 = 0, C = 0, D = 0, \theta_1 = 45°, \theta_2 = 45°\},\end{aligned} \tag{3.14}$$

and for the 5-parameter fit, they will be

$$\mathbf{p_o} = \{A = 105°, \gamma = 0, \omega = \omega_o, t_{eq} = 0, C = 0\}. \tag{3.15}$$

As discussed in Sections 2.3 and 2.4, the parameter estimates written to output files by our analysis software are averages of exactly determined fits to crossing sets I and exactly determined fits to crossing sets II. That is,

$$\hat{p}_{iAvg} = (\hat{p}_{iI} + \hat{p}_{iII})/2. \tag{3.16}$$

The variances of $\hat{p}_{iI}$ and $\hat{p}_{iII}$ can not be simply added together because they have crossings in common and their errors are therefore correlated, but the di-

rect calculation of the variance in Eq. 3.11 can be extended to averages of exactly determined fits,

$$\mathrm{var}\left(\hat{p}_{i\,Avg}\right)=\sum_{j=1}^{n'}\sum_{k=1}^{n'}\left(\frac{M_I^{-1'}+M_{II}^{-1'}}{2}\right)_{ij}\mathrm{cov}\left(\theta(t_j),\theta(t_k)\right)\left(\frac{M_I^{-1'}+M_{II}^{-1'}}{2}\right)_{ik}. \quad (3.17)$$

Here, n' is the total number of crossings which is now greater than n, the number of parameters. For the 10-parameter fit, $n=10$ and $n'=14$ while for the 5-parameter fit, $n=5$ and $n'=6$. The primes on the inverse design matrices, $\mathbf{M}_I^{-1'}$ and $\mathbf{M}_{II}^{-1'}$, indicate that they have been modified from square $n\times n$ matrices to rectangular $n\times n'$ matrices by the insertion of zero's into the appropriate columns. From now on, the "avg" subscript will be dropped from $\hat{p}_i$, and the average of the i^{th} rows of $\mathbf{M}_I^{-1'}$ and $\mathbf{M}_{II}^{-1'}$ will be designated as the sampling function of $\hat{p}_i$,

$$\mathbf{s}(\hat{p}_i)=\left\{\left(\frac{M_I^{-1'}+M_{II}^{-1'}}{2}\right)_{i1},\left(\frac{M_I^{-1'}+M_{II}^{-1'}}{2}\right)_{i2},\ldots\left(\frac{M_I^{-1'}+M_{II}^{-1'}}{2}\right)_{in'}\right\}. \quad (3.18)$$

The variance in the estimator can then be more simply expressed as

$$\mathrm{var}(\hat{p}_i)=\sum_{j=1}^{n'}\sum_{k=1}^{n'}s_j(\hat{p}_i)\mathrm{cov}\left(\theta(t_j),\theta(t_k)\right)s_k(\hat{p}_i). \quad (3.19)$$

Let us define $\partial\theta/\partial p_i$ as the n' component vector of the partial derivatives of the signal with respect to the i^{th} parameter,

$$\frac{\partial\theta}{\partial p_i}=\left\{\frac{\theta(t_1)}{\partial p_i},\frac{\theta(t_2)}{\partial p_i},\ldots\frac{\theta(t_{n'})}{\partial p_i}\right\}. \quad (3.20)$$

Then the contraction of a sampling function vector with a partial derivative vector obeys an orthonormality condition,

$$\mathbf{s}(\hat{p}_i) \bullet \frac{\partial \theta}{\partial p_j} = \delta_{ij}. \tag{3.21}$$

That is, each sampling function is only sensitive to variations in its own parameter and is insensitive (orthogonal) to variations in all the other parameters.

More specifically, the sampling function of $\hat{A}_2$ for the 10-parameter fit at 230° amplitude (see $\mathbf{p_o}$ in Eq. 3.14) is

$$\begin{aligned}\mathbf{s}(\hat{A}_2) = \{&-0.068,\ 0.272,\ 0.000,\ -0.204,\ -0.204,\ 0.000,\ 0.204,\\ &0.204,\ 0.000,\ -0.204,\ -0.204,\ 0.000,\ 0.272,\ -0.068\}.\end{aligned} \tag{3.22}$$

These 14 components of $\mathbf{s}(\hat{A}_2)$ are displayed pictorially in Figure 3.1.

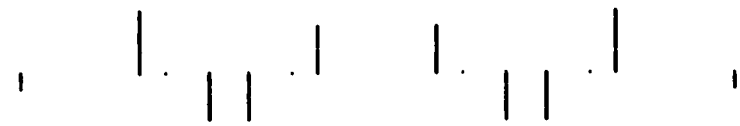

Figure 3.1. The sampling function for the second harmonic amplitude, $\mathbf{s}(\hat{A}_2)$. The horizontal axis is time, and the vertical height of each line is proportional to the weight with which the error in each of the 14 crossings propagates into the estimate of the second harmonic amplitude, $\hat{A}_2$. Note that the errors on the 180° mirror have zero weight (i.e., to first order, they do not propagate into the parameter estimate).

For comparison, the 14 components of the partial derivative vector are

$$\frac{\partial\theta}{\partial A_2} = \{0.311,\ 0.311,\ -0.225,\ -0.914,\ -0.914,\ -0.225,\ 0.311,\ 0.311,\ -0.225,\ -0.914,\ -0.914,\ -0.225,\ 0.311,\ 0.311\}, \tag{3.23}$$

and they are displayed pictorially in Figure 3.2.

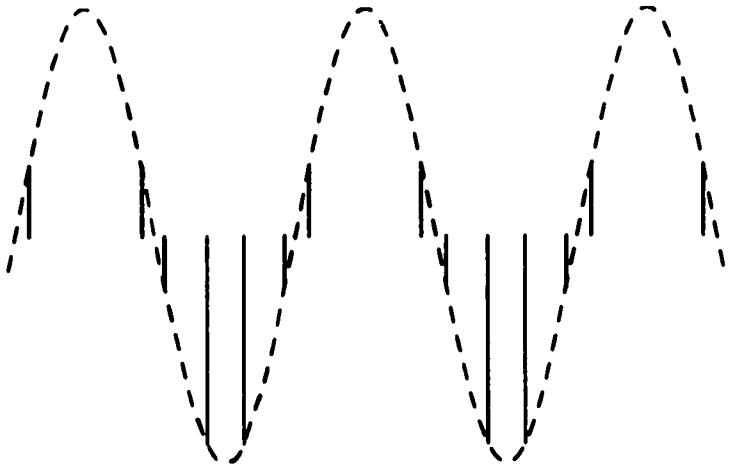

Figure 3.2. The 14 components of $\partial\theta/\partial A_2$. The dashed curve traces out $\cos(2\omega t)$ and is there to guide the eye.

The dashed curve in Figure 3.2 is proportional to the second harmonic component of the pendulum motion, $A_2\cos(2\omega t)$, and it should not be confused with the sine waves in Figure 2.4 which correspond to the much larger fundamental oscillation of the pendulum, $A\sin(\omega t)$. In Figure 3.3, $\partial\theta/\partial A_2$ is shown without the dashed curve and with $\mathbf{s}(\hat{A}_2)$ directly below it.

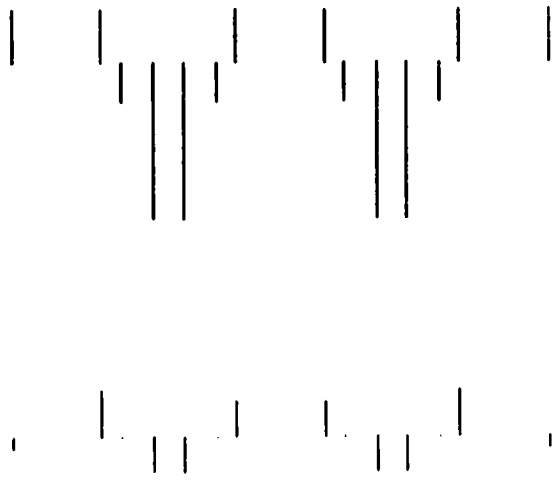

Figure 3.3. The 14 components of $\partial\theta/\partial A_2$ (without dashed lines) and $\mathbf{s}(\hat{A}_2)$ directly underneath it. The horizontal axis is time, and the vertical scales, although offset, are the same for both vectors. Both $\partial\theta/\partial A_2$ and $\mathbf{s}(\hat{A}_2)$ are dimensionless.

Although the two vectors, $\partial\theta/\partial A_2$ and $\mathbf{s}(\hat{A}_2)$, are roughly similar in shape, they are by no means identical. One might have thought that the zero weights on the 180° mirrors in $\mathbf{s}(\hat{A}_2)$ were due to $\cos(2\omega t)$ being zero on those mirrors, but a closer inspection of $\partial\theta/\partial A_2$ reveals that $\cos(2\omega t) = -0.225$ on the 180° mirrors; the zero weights in $\mathbf{s}(\hat{A}_2)$ are due to some deeper symmetry of the overall 10-parameter fit. The vector of partial derivatives with respect to A_2 sets the normalization of the sampling function because $(\partial\theta/\partial A_2)\bullet\mathbf{s}(\hat{A}_2) = 1$, but the overall shape of $\mathbf{s}(\hat{A}_2)$ is much more strongly determined by the requirement that it be orthogonal to any variation in the nine other parameters than it is by

the shape of $\partial\theta/\partial A_2$. Because large, multi-parameter fits tend to defy intuitive comprehension, the shape of $\mathbf{s}(\hat{A}_2)$ rather than that of $\partial\theta/\partial A_2$ is a better guide to understanding the error propagation into the estimate of the second harmonic amplitude, $\hat{A}_2$. For a given noise process, the variance in $\hat{A}_2$ will be identical to that of an equal-weighted, least-squares fit to a single-parameter function of the shape of $\mathbf{s}(\hat{A}_2)$.

Now let's look at the 5-parameter fit and $\mathbf{s}(\hat{\omega})$. If we were to proceed in the same manner as the 10-parameter fit, the data vector would consist of the 6 crossings that comprise the union of crossing set I and crossing set II in Section 2.4,

$$\mathbf{y} = \{\theta(t_1), \theta(t_2), \theta(t_3), \theta(t_4), \theta(t_5), \theta(t_6)\}, \tag{3.24}$$

but since the 3.1° angle which separates the pairs of crossings is so small, it will make the presentation more clear to change to a position/velocity basis obtained by combining the pairs as sums and differences. That is,

$$\{\theta(t_1), \theta(t_2)\} \Rightarrow \{\theta(t_i), \dot{\theta}(t_i)\} \equiv \left\{\frac{\theta(t_1)+\theta(t_2)}{2}, \frac{\theta(t_2)-\theta(t_1)}{t_2-t_1}\right\},$$

$$\{\theta(t_3), \theta(t_4)\} \Rightarrow \{\theta(t_o), \dot{\theta}(t_o)\} \equiv \left\{\frac{\theta(t_3)+\theta(t_4)}{2}, \frac{\theta(t_4)-\theta(t_3)}{t_4-t_3}\right\}, \text{ and} \tag{3.25}$$

$$\{\theta(t_5), \theta(t_6)\} \Rightarrow \{\theta(t_f), \dot{\theta}(t_f)\} \equiv \left\{\frac{\theta(t_5)+\theta(t_6)}{2}, \frac{\theta(t_6)-\theta(t_5)}{t_6-t_5}\right\},$$

so that the new, 5-parameter-fit data vector is

$$\mathbf{y} = \{\theta(t_i), \dot{\theta}(t_i), \theta(t_o), \dot{\theta}(t_o), \theta(t_f), \dot{\theta}(t_f)\}. \tag{3.26}$$

In this basis, the sampling function for frequency is

$$\mathbf{s}(\hat{\omega}) = \left\{+\frac{\omega}{2\pi A}, 0, 0, 0, -\frac{\omega}{2\pi A}, 0\right\}, \tag{3.27}$$

where A is in radians. To justify our choice of $A = 105°$ for the frequency method, it was asserted in Section 2.4 that the error propagation of the frequency estimate scaled as $1/A$. From Eq. 3.27, it can be seen explicitly that this is true, and for any stationary noise process, $\mathrm{var}(\hat{\omega})$ will therefore scale as $1/A^2$. Once again, the sampling function differs from the partial derivative vector, which is

$$\frac{\partial \mathbf{y}}{\partial \omega} = \left\{+\frac{\pi A}{\omega}, -A, 0, +A, -\frac{\pi A}{\omega}, -A\right\}. \tag{3.28}$$

Note that $(\partial \mathbf{y}/\partial \omega) \bullet \mathbf{s}(\hat{\omega}) = 1$ as it should. Both Eqs. 3.27 and 3.28 are for a 121-type fit. The 212-type fit vectors can be arrived at by an $A \Rightarrow -A$ transformation, which changes the sign of each component. For the 10-parameter fit, there was no difference between the 121-type and 212-type vectors, and so it was not an issue. When Eq. 3.27 is evaluated numerically for $A = 105°$ (see $\mathbf{p_o}$ in Eq. 3.15), one gets

$$\frac{\mathbf{s}(\hat{\omega})}{\omega_o} = \{+0.086, 0.000, 0.000, 0.000, -0.086, 0.000\}. \tag{3.29}$$

Because $\mathbf{s}(\hat{\omega})$ has non-zero components only for $\left\{\theta(t_i), \theta(t_f)\right\}$, Eq. 3.19 can be directly used to calculate $\mathrm{var}(\hat{\omega})$, and no knowledge of the position/velocity or velocity/velocity covariance function is required. Conceptually, it is useful to note that $\mathbf{s}(\hat{\omega})$ has the same structure as a naive least-squares, single-parameter zero-crossing determination of the period–that is, fitting $\mathbf{p} = \{\omega\}$ to

$\mathbf{y} = \left\{\theta(t_i), \theta(t_f)\right\}$–but similar to the zero's in $\mathbf{s}(\hat{A}_2)$, this feature is due to deeper symmetries in the overall, multi-parameter fit, which would have been difficult to guess *a priori*.

3.2 "White" Noise Comparison

Now that the general error propagation of the 5-parameter fit and the 10-parameter fit has been presented, the remaining portion of Section 3 will compare the two methods' signal-to-noise ratios for various noise processes. Section 3.2 considers one of the simplest noise models, additive "white" noise, for which the covariance function is

$$\mathrm{cov}_{wh}\left(\theta(t_j), \theta(t_k)\right) = \theta_{rms}^2 \delta_{jk}. \tag{3.30}$$

The angular root-mean-square error per crossing, θ_{rms}, is the same for all crossings, and the Kronecker delta indicates the errors have no correlation with one another. Electronic noise in the photo-diode amplifiers, for example, produces "white" noise in the crossings, but for the Index IV apparatus a much more serious source of "white" noise is the seismically-induced swinging, rocking, and bouncing modes of the pendulum which tilt and translate the edge-reflector attached to the pendulum. In order to see and subtract off these modes, another graduate student in our group, Richard Horn, is working on replacing the simple split photo-diode with a 512 pixel photo-diode array for the next generation apparatus that we are currently building, but that is beyond the scope of this thesis.

Substituting Eqs. 3.30, 3.22, and 3.29 into Eq. 3.19, one gets the "white" noise variance in $\hat{A}_2$ for a single-period, 10-parameter fit,

$$\mathrm{var}_{wh}\left(\hat{A}_2\right) = (0.407)\theta_{rms}^2 \qquad \mathrm{stddev}_{wh}\left(\hat{A}_2\right) = (0.638)\theta_{rms}, \quad (3.31)$$

and the "white" noise variance in $\hat{\omega}$ for a single-period, 5-parameter fit,

$$\frac{\mathrm{var}_{wh}(\hat{\omega})}{\omega_o^2} = (0.015)\theta_{rms}^2 \qquad \frac{\mathrm{stddev}_{wh}(\hat{\omega})}{\omega_o} = (0.122)\theta_{rms}, \quad (3.32)$$

where in Eq. 3.32 θ_{rms} must be expressed in radians. The two methods' signal strengths, the variation in second harmonic amplitude,

$$|A_2(\phi)| = \left|\frac{2J_2(A)}{3}\right|\frac{|U_{ext}|}{\kappa} = (0.240)\frac{|U_{ext}|}{\kappa} \quad (3.33)$$

and the fractional variation in oscillation frequency,

$$\left|\frac{\Delta\omega}{\omega_o}(\phi)\right| = \left|\frac{J_1(A)}{A}\right|\frac{|U_{ext}|}{\kappa} = (0.316)\frac{|U_{ext}|}{\kappa} \quad (3.34)$$

are obtained by substituting the appropriate oscillation amplitudes (in radians) into Eq. 2.31. Thus, the signal-to-noise ratio is

$$(S/N)_{wh}[A_2] = (0.376)\frac{|U_{ext}|}{\kappa\theta_{rms}} \quad (3.35)$$

for the 10-parameter fit and

$$(S/N)_{wh}[\omega] = (2.586)\frac{|U_{ext}|}{\kappa\theta_{rms}} \quad (3.36)$$

for the 5-parameter fit. One can quibble about decreasing these values by a factor of $\sqrt{2}$ because $|U_{ext}|$ is the peak amplitude of a sinusoidal variation or about increasing these values by a factor of $\sqrt{2}$ because the fixed and movable mirror crossings are averaged, but for the purpose of comparing the two methods,

these factors will cancel. Therefore regardless of convention, the ratio of the two methods' signal-to-noise is

$$\frac{(S/N)_{wh}[\omega]}{(S/N)_{wh}[A_2]} = 6.88 \qquad \frac{(S/N)^2_{wh}[\omega]}{(S/N)^2_{wh}[A_2]} = 47.3. \tag{3.37}$$

Not being a natural salesman, this was the first comparison that I presented to my Professor, and needless to say, he was not impressed. For a "white" noise limited experiment, the old frequency method could measure a force 6.88 times smaller than the new second harmonic method given the same amount of time, or alternatively, it would take the new method 47.3 times longer to measure the same force.

But wait. It gets worse. The factor of 47.3 in time assumes that uncorrelated fits are being averaged so that the signal-to-noise increases with integration time, τ, as $\tau^{1/2}$, and for the second harmonic fits, this is a very good approximation. The error propagation of the 5-parameter frequency fits, however, is weighted entirely on the initial and final crossings, and since final crossing of one period is the initial crossing of the period immediately following, adjacent frequency fits will be highly correlated–and in quite a favorable manner. A little inspection shows that for a simple average of a series of adjacent 5-parameter frequency fits, the signal-to-noise increases as τ, and if you fit in an optimal least-square manner over several periods, it can be shown that the signal-to-noise increases as $\tau^{3/2}$. The number of adjacent periods you can average is only limited by the number of free oscillation periods you are willing to stay centered on each mirror face before rotating the fiber support to a new position. Hence, the signal-to-noise of the frequency method is actually better by a factor of $6.88 \times$(number of periods per face).

If the frequency method is so much better, why switch to the second harmonic method? The answer is that, for the Index IV apparatus, the frequency method is not "white" noise limited, but instead temperature induced variations in frequency dominate the error budget. A more explicit comparison of the error propagation of slow frequency drifts for the two methods will be presented in Section 3.6.

3.3 Thermal Noise Comparison

If you lived in an ideal world without additive "white" noise or temperature drifts, what would be your noise limitation? The azimuthal Brownian rotation of the pendulum, or more simply thermal noise, would be the fundamental limitation, and the proper design goal of a torsion pendulum experiment is to become thermal-noise limited. In contrast to "white" noise, the error per crossing, θ_{rms}, for thermal noise is a fundamental, physical property of the pendulum instead of an engineering specification of the measuring device, and the magnitude of that crossing error can be derived quickly from the Equipartition Theorem for a harmonic oscillator,

$$\langle P.E. \rangle = \frac{1}{2}\kappa\theta_{rms}^2 = \frac{1}{2}k_bT \quad \Rightarrow \quad \theta_{rms} = \sqrt{\frac{k_bT}{\kappa}}. \tag{3.38}$$

Here, a "b" subscript has been added to Boltzmann's constant to avoid confusion with κ, the fiber torsion constant. The Fluctuation-Dissipation Theorem states that thermal noise fluctuations and macroscopic damping are two manifestations of the same physical phenomena, and so we can no longer use the undamped, $\gamma = 0$, approximation. For a damped oscillator, there are three different frequencies–ω_o, ω_d, and ω_r–that are commonly used. The undamped natural frequency,

$$\omega_o = \sqrt{\kappa / I}, \tag{3.39}$$

depends only on the fiber torsion constant, κ, and the rotational inertia of the pendulum, I. The free oscillation frequency of a damped oscillator,

$$\omega_d = \sqrt{\omega_o^2 - \gamma^2}, \tag{3.40}$$

is the frequency parameter used in the 10-parameter fit and the 5-parameter fit. For an externally driven damped oscillator, the resonant frequency,

$$\omega_r = \sqrt{\omega_o^2 - 2\gamma^2}, \tag{3.41}$$

is the frequency that has maximum response, and the dimensionless quality factor of the pendulum, Q, is defined as

$$Q = \frac{\omega_r}{2\gamma}. \tag{3.42}$$

For thermal noise, the errors of two different crossings can be highly correlated or anti-correlated depending on the time interval between them. The exact thermal-noise auto-covariance function for two crossings at t_j and t_k is (Helstrom 1968)

$$\begin{aligned} \mathrm{cov}_{th}\left(\theta(t_j), \theta(t_k)\right) = {} & \theta_{rms}^2 \exp\left(-\gamma|t_k - t_j|\right)\cos\left(\omega_d\left(t_k - t_j\right)\right) \\ & + \left(\frac{\gamma}{\omega_d}\right)\theta_{rms}^2 \exp\left(-\gamma|t_k - t_j|\right)\sin\left(\omega_d|t_k - t_j|\right), \end{aligned} \tag{3.43}$$

and the auto-correlation function (the auto-covariance function divided by the variance, θ_{rms}^2) is plotted for a pendulum with a Q of 10 in Figure 3.4.

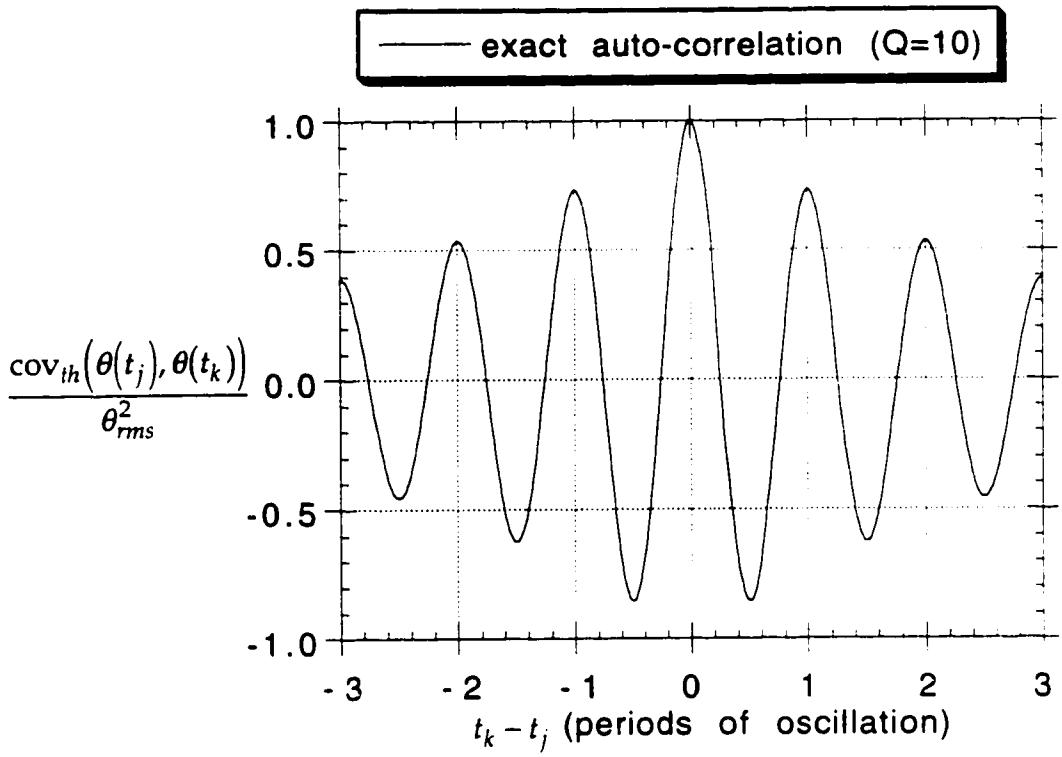

Figure 3.4. Exact thermal-noise auto-correlation for $Q = 10$ plotted as a function of the time difference between the two crossings in periods of oscillation.

Note that crossings separated by an integer number of periods are correlated while those separated by a half-integer number of periods are anti-correlated, and the overall magnitude of correlation slowly dies away with an $\exp\left(-\gamma\left|t_k - t_j\right|\right)$ envelope.

At Index, however, the pendulum oscillates in a vacuum with a Q of 4000, and so Figure 3.4 greatly exaggerates the rate of decoherence in the noise process. In this high Q regime, it will be more useful to expand the auto-covariance function in powers of $1/Q$,

$$\begin{aligned}\mathrm{cov}_{th}\left(\theta(t_j),\theta(t_k)\right) = {} & \theta_{rms}^2 \mathrm{corr}_{th}\left(\theta(t_j),\theta(t_k)\right)_0 + \\ & \theta_{rms}^2 \mathrm{corr}_{th}\left(\theta(t_j),\theta(t_k)\right)_1 + \\ & \theta_{rms}^2 \mathrm{corr}_{th}\left(\theta(t_j),\theta(t_k)\right)_2 + \ldots,\end{aligned} \tag{3.44}$$

where the zero-order, first-order, second-order, etc. auto-correlation functions are uniquely defined such that

$$\begin{aligned}\mathrm{corr}_{th}\left(\theta(t_j),\theta(t_k)\right)_0 &\propto \frac{1}{Q^0} \\ \mathrm{corr}_{th}\left(\theta(t_j),\theta(t_k)\right)_1 &\propto \frac{1}{Q^1} \\ \mathrm{corr}_{th}\left(\theta(t_j),\theta(t_k)\right)_2 &\propto \frac{1}{Q^2}. \\ &\vdots\end{aligned} \tag{3.45}$$

Under this scheme, the zero-order auto-correlation is

$$\mathrm{corr}_{th}\left(\theta(t_j),\theta(t_k)\right)_0 = \cos\left(\omega_o\left(t_k - t_j\right)\right), \tag{3.46}$$

and it is plotted in Figure 3.5.

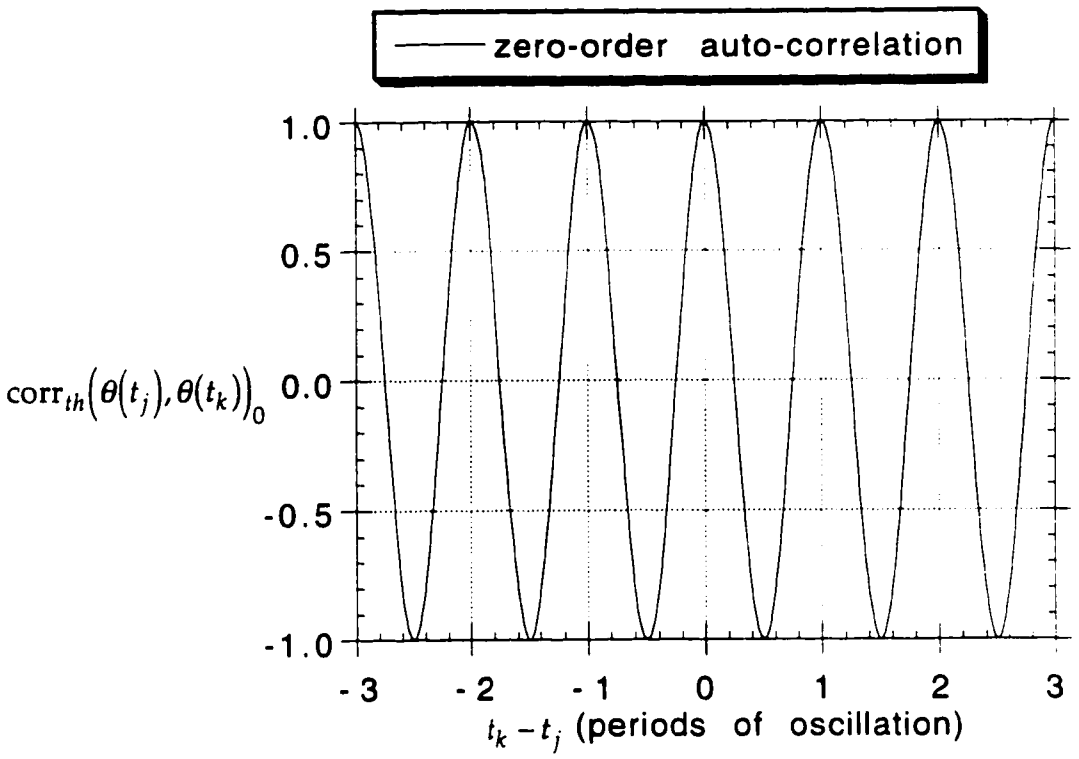

Figure 3.5. Thermal-noise auto-correlation zero-order in $1/Q$ (i.e., undamped limit).

In this non-physical, undamped limit, a particular realization of thermal noise is simply coherent ringing at the natural frequency with some arbitrary phase and amplitude chosen from the canonical ensemble. When the zero-order approximation of the covariance function is substituted into Eq. 3.19,

$$\mathrm{var}_{th}(\hat{p}_i) \equiv \sum_{j=1}^{n'}\sum_{k=1}^{n'} s_j(\hat{p}_i)\theta_{rms}^2 \cos\left(\omega_o\left(t_k - t_j\right)\right)s_k(\hat{p}_i), \tag{3.47}$$

and the expected variances in the signal parameters are calculated, one gets $\mathrm{var}_{th}\left(\hat{A}_2\right) = 0$ for the 10-parameter fit and $\mathrm{var}_{th}(\hat{\omega}) = 0$ for the 5-parameter fit. This is obviously wrong, but it should not be surprising because the parameters

A and t_{eq}, which appear in both the 10-parameter fit and the 5-parameter fit, can fit for a fundamental sine wave of arbitrary phase and amplitude. Thus the zero-order thermal noise propagates entirely into the parameter estimates $\hat{A}$ and $\hat{t}_{eq}$, and the other parameter estimates, being orthogonal to the sine wave, remain unaffected.

To calculate the thermal-noise variances in $\hat{A}_2$ and $\hat{\omega}$, it is necessary to go to at least first-order in $1/Q$. The first-order auto-correlation function is

$$\mathrm{corr}_{th}\left(\theta(t_j),\theta(t_k)\right)_1 = \frac{\sin\left(\omega_o|t_k - t_j|\right) - \omega_o|t_k - t_j|\cos\left(\omega_o(t_k - t_j)\right)}{2Q}, \qquad (3.48)$$

and it is plotted in Figure 3.6.

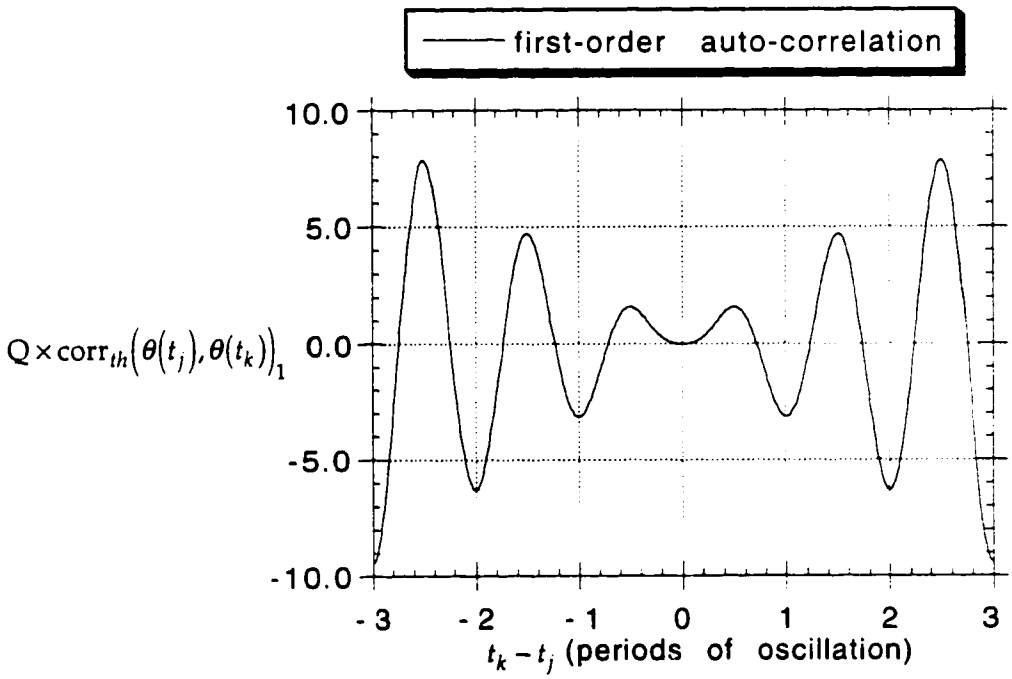

Figure 3.6. Thermal-noise auto-correlation first-order in $1/Q$. For a high-Q oscillator's auto-covariance function, this represents the small, leading-order deviation from a pure sine wave.

Although this first-order component is roughly $1/Q$ smaller than the zero-order component, it is the first-order component that does all the damage to your parameter estimates because it creates the decoherence in the thermal noise process. Note the envelope is proportional to $|t_k - t_j|$, which is similar to a random walk. If the fundamental oscillation of the pendulum is demodulated, then the effect of the thermal noise can be fairly well approximated as a two-dimensional random walk in amplitude and phase–at least for time scales shorter than $1/\gamma$ for which the first-order $1/Q$ approximation is valid. When the first-order auto-correlation is substituted into Eq. 3.19, one gets the thermal-noise variance in $\hat{A}_2$ for a single-period, 10-parameter fit,

$$\mathrm{var}_{th}\left(\hat{A}_2\right) = (0.0699)\frac{\theta_{rms}^2}{Q} \qquad \mathrm{stddev}_{th}\left(\hat{A}_2\right) = (0.264)\frac{\theta_{rms}}{Q^{1/2}} \quad (3.49)$$

and the thermal-noise variance in $\hat{\omega}$ for a single-period, 5-parameter fit,

$$\frac{\mathrm{var}_{th}(\hat{\omega})}{\omega_o^2} = (0.0474)\frac{\theta_{rms}^2}{Q} \qquad \frac{\mathrm{stddev}_{th}(\hat{\omega})}{\omega_o} = (0.218)\frac{\theta_{rms}}{Q^{1/2}} \quad (3.50)$$

where in Eq. 3.50 θ_{rms} must be expressed in radians. The signal strengths are the same as before (Eqs. 3.33 and 3.34), and so the signal-to-noise ratio is

$$(S/N)_{th}[A_2] = (0.909)\frac{|U_{ext}|Q^{1/2}}{\kappa\theta_{rms}} = (0.909)|U_{ext}|\sqrt{\frac{Q}{\kappa k_b T}} \quad (3.51)$$

for a thermal-noise limited 10-parameter fit and

$$(S/N)_{th}[\omega] = (1.450)\frac{|U_{ext}|Q^{1/2}}{\kappa\theta_{rms}} = (1.450)|U_{ext}|\sqrt{\frac{Q}{\kappa k_b T}} \quad (3.52)$$

for a thermal-noise limited 5-parameter fit. The ratio of the two methods' signal-to-noise is therefore

$$\frac{(S/N)_{th}[\omega]}{(S/N)_{th}[A_2]} = 1.60 \qquad \frac{(S/N)^2_{th}[\omega]}{(S/N)^2_{th}[A_2]} = 2.54, \tag{3.53}$$

which still favors the frequency method, but the second harmonic method looks much better than it did in the "white" noise comparison of Section 3.2 (see Eq. 3.37). If one has to pay a price to be immune to the temperature-induced frequency drifts, a factor of 1.60 is more acceptable than a factor of $6.88 \times$(number of periods per face).

One might ask does averaging adjacent frequency fits increase the advantage of the 5-parameter fit as it did for the "white" noise case. The answer is no. The thermal noise causes a random walk in the phase of the oscillator such that adjacent frequency fits are uncorrelated. For averaging thermal-noise limited fits, the signal-to-noise of the 10-parameter fit and the 5-parameter fit both increase with integration time as $\tau^{1/2}$. The optimal, thermal-noise, minimum-variance, 5-parameter fit to an ideal (i.e., no additive "white" noise), continuous data set is derived in the Appendix. The thermal-noise variance in the 5-parameter frequency estimate (Eq. 3.50) is identical to the minimum-variance frequency estimate of that optimal 5-parameter fit (Eq. A.112). Thus for a thermal-noise limited experiment using frequency as the signal, the optimal signal-to-noise can be obtained with just four crossings per period. From an engineering standpoint, this is good news because building a continuous, multi-radian angular readout with the required linearity and stability would be extremely difficult. I have not yet worked out the optimal, thermal-noise fit for the second harmonic method, but if the frequency method is any guide, there is

not that much to be gained in signal-to-noise by increasing the number of crossings per period once the experiment has become thermal-noise limited.

Since C, the deflection, is another of the 5 parameters in the optimal, thermal-noise fit derived in the Appendix, we can compare the thermal-noise limited signal-to-noise ratio of the deflection method to the signal-to-noise ratios of the frequency method (5-parameter fit) and the second harmonic method (10-parameter fit). A similar, quantitative comparison between the continuous-sampling, deflection method and large-amplitude, crossing-time methods is not possible for "white"-noise limited experiments without specifying the bandwidth of the crossing-time measurements, or equivalently the effective integration time of the crossing-time measurements. However, a quantitative comparison is not necessary for the "white" noise case because it is evident that a continuous-sampling method should have a much lower "white" noise limit than a crossing-time method.

Given a continuous time series of an oscillator in thermal equilibrium, one straightforward method to estimate the true equilibrium position, C, is to take a "boxcar" average of the data. To make the estimate immune to the zero-order auto-correlation function, the data should be averaged for an integer number of periods. Define a single-period, "boxcar" estimate as

$$\hat{C}_{box} = \frac{\omega_d}{2\pi} \int_{-\pi/\omega_d}^{+\pi/\omega_d} \theta(t)dt. \tag{3.54}$$

Using the Fourier methods described in the Appendix, the leading, first-order variance of the "boxcar" estimate is

$$\mathrm{var}_{th}\left(\hat{C}_{box}\right) = (0.477)\frac{\theta_{rms}^2}{Q} \qquad \mathrm{stddev}_{th}\left(\hat{C}_{box}\right) = (0.691)\frac{\theta_{rms}}{Q^{1/2}} \tag{3.55}$$

where $\theta_{rms} = (k_b T/\kappa)^{1/2}$ as in defined in Eq. 3.38. The signal strength of the deflection method,

$$|C(\phi)| = |J_0(A)|\frac{|U_{ext}|}{\kappa} = (1.000)\frac{|U_{ext}|}{\kappa}, \tag{3.56}$$

is the zero-amplitude limit of Eq. 2.31. The signal-to-noise ratio of the "boxcar" average is therefore

$$(S/N)_{th}[C_{box}] = (1.447)\frac{|U_{ext}|Q^{1/2}}{\kappa\theta_{rms}} = (1.447)|U_{ext}|\sqrt{\frac{Q}{\kappa k_b T}}, \tag{3.57}$$

and when it is compared to the second harmonic method,

$$\frac{(S/N)_{th}[C_{box}]}{(S/N)_{th}[A_2]} = 1.59 \qquad \frac{(S/N)^2_{th}[C_{box}]}{(S/N)^2_{th}[A_2]} = 2.54, \tag{3.58}$$

the comparison is almost identical to that of the 5-parameter fit frequency method (see Eqs. 3.52 and 3.53).

However, the "boxcar" average is not the optimal estimator of the true equilibrium position, C, in the presence of thermal noise. In the Appendix, it is shown that the optimal estimator,

$$\hat{C}_{opt} = \frac{\omega_d}{2\pi}\int_{-\pi/\omega_d}^{+\pi/\omega_d}\theta(t)dt + \frac{\dot{\theta}(+\pi/\omega_d) - \dot{\theta}(-\pi/\omega_d)}{2\pi\omega_d}, \tag{3.59}$$

uses the initial velocity measurement, $\dot{\theta}(-\pi/\omega_d)$, and the final velocity measurement, $\dot{\theta}(+\pi/\omega_d)$, in addition to the "boxcar" average. This reduces the variance in C by a factor 2/3 to

$$\mathrm{var}_{th}\left(\hat{C}_{opt}\right) = (0.318)\frac{\theta^2_{rms}}{Q} \qquad \mathrm{stddev}_{th}\left(\hat{C}_{opt}\right) = (0.564)\frac{\theta_{rms}}{Q^{1/2}}, \tag{3.60}$$

and the optimal signal-to-noise ratio is

$$(S/N)_{th}[C_{opt}] = (1.772)\frac{|U_{ext}|Q^{1/2}}{\kappa\theta_{rms}} = (1.772)|U_{ext}|\sqrt{\frac{Q}{\kappa k_b T}}. \qquad (3.61)$$

A large-amplitude method that assembles the information from all available channels (deflection, frequency, second harmonic, third harmonic, etc.) can equal but not surpass the above signal-to-noise ratio. Only in the zero-amplitude limit is all the signal concentrated into one channel—the deflection. When compared to the 10-parameter fit,

$$\frac{(S/N)_{th}[C_{opt}]}{(S/N)_{th}[A_2]} = 1.95 \qquad \frac{(S/N)^2_{th}[C_{box}]}{(S/N)^2_{th}[A_2]} = 3.80, \qquad (3.62)$$

the optimal, thermal-noise deflection method is almost a factor of two better in signal-to-noise, but as with the frequency method comparison, this may be a reasonable price to pay in order to be immune to some of the problems that plague deflection methods. Slow temperature variations cause variations in deflection either through the properties of the fiber or due to small changes in the optical path of the laser. These temperature problems are typically a smaller problem for the deflection method than for the frequency method, but they are not entirely insignificant. Bigger in magnitude is the coupling of the tilt of the fiber support point into the deflection. A more detailed comparison of the various physical sources of error for the different methods will be made in Section 5. For Section 3, we will simply assume that slow drifts in deflection and frequency exist, and we will investigate the error propagation of these drifts for the various methods. Only the second harmonic method is relatively immune to both types of drift.

3.4 "Red" Noise (Random Walk) Comparison

Mathematically, the simplest type of noise process that illustrates the problems associated with low frequency noise is "red" noise, also known as a random-walk process. In analogy to optical color, the noise is called "red" because it has more power at lower frequencies whereas "white" noise has equal power at all frequencies. The term "red" is often loosely applied to any noise process with a large low-frequency component, but in this section, it will specifically denote noise with a $1/f^2$ frequency power spectrum in deflection. As a time series, the "red" noise process is a random walk: the continuous limit of an infinite number of infinitesimal, random, and uncorrelated steps. To be somewhat more precise, the deflection time series, $\theta(t)$, is the integrated motion of a velocity time series, $\dot{\theta}(t)$, that is a "white" noise process. One mathematical difficulty of a "red" noise process is that the equilibrium position is constantly wandering away, and thus the expected variance in a particular crossing,

$$\mathrm{var}_{red}\left(\theta\left(t_j\right)\right) \rightarrow \infty, \tag{3.63}$$

becomes infinite if you attempt to treat the "red" noise as a stationary process.

The solution to this dilemma is to calculate all quantities in a difference basis because the "red" noise variance of the difference of two crossings,

$$\mathrm{var}_{red}\left(\theta(t_k) - \theta\left(t_j\right)\right) = \left(\theta_{red}^2 \omega_o / 2\pi\right)\left|t_k - t_j\right|, \tag{3.64}$$

is finite. Here, I have expressed the normaliztion of the "red" noise process in terms of the angle θ_{red}, the standard deviation in the angular displacement that the random walk will wander in one period of pendulum oscillation. The derivation of Equation 3.64 follows directly from the fact that "red" noise is inte-

grated "white" noise. The difference in Eq. 3.64 can be expressed as a definite integral of the velocity,

$$\theta(t_k)-\theta(t_j)=\int_{t_j}^{t_k}\dot{\theta}(s)ds, \tag{3.65}$$

and the "white" noise covariance of the velocity,

$$\mathrm{cov}_{red}\left(\dot{\theta}(s),\dot{\theta}(u)\right)=\left(\theta_{red}^2\omega_o/2\pi\right)\delta(u-s), \tag{3.66}$$

can then be used to calculate the variance in the difference of two crossings,

$$\begin{aligned}
&\mathrm{var}_{red}\left(\theta(t_k)-\theta(t_j)\right)=\mathrm{var}_{red}\left(\int_{t_j}^{t_k}\dot{\theta}(s)ds\right)\\
&=\int_{t_j}^{t_k}\int_{t_j}^{t_k}\mathrm{cov}_{red}\left(\dot{\theta}(s),\dot{\theta}(u)\right)dsdu=\int_{t_j}^{t_k}\int_{t_j}^{t_k}\left(\theta_{red}^2\omega_o/2\pi\right)\delta(u-s)dsdu\\
&=\left(\theta_{red}^2\omega_o/2\pi\right)\left|t_{j+1}-t_j\right|. \qquad \text{Q.E.D.}
\end{aligned} \tag{3.67}$$

The covariance of two different crossing differences, $\theta(t_k)-\theta(t_j)$ and $\theta(t_m)-\theta(t_l)$, can be similarly calculated. However, the covariance is simplified if you restrict the difference basis to differences of temporally adjacent crossings because then two crossing differences, $\theta(t_{j+1})-\theta(t_j)$ and $\theta(t_{k+1})-\theta(t_k)$, are either identical $(j=k)$, in which case the covariance is the variance above in Eq. 3.67, or they are non-overlapping $(j\neq k)$, and the covariance is zero because the integrated velocities are not correlated. Thus,

$$\mathrm{cov}_{red}\left(\theta(t_{j+1})-\theta(t_j),\theta(t_{k+1})-\theta(t_k)\right)=\left(\theta_{red}^2\omega_o/2\pi\right)\left|t_{j+1}-t_j\right|\delta_{jk}. \tag{3.68}$$

Going to an adjacent difference basis nicely resolves a lot of problems with handling "red" noise calculations, but it can only be used if the sampling function of interest can be decomposed into adjacent differences. This requires that

$$\sum_{j=1}^{n'} s_j(\hat{p}_i) = 0, \tag{3.69}$$

and so at first glance, it would seem this method could only be applied in special cases. Upon inspection, however, it can be seen that Equation 3.69 is mathematically equivalent to the statement

$$\mathbf{s}(\hat{p}_i) \bullet \frac{\partial \boldsymbol{\theta}}{\partial C} = 0, \tag{3.70}$$

and therefore the orthonormality condition discussed in Section 3.1 (see Eq. 3.21) guarantees that both $\mathbf{s}\left(\hat{A}_2\right)$ of the 10-parameter fit and $\mathbf{s}(\hat{\omega})$ of the 5-parameter fit can be decomposed into adjacent differences. More specifically, the decomposition

$$\sum_{j=1}^{n'} s_j(\hat{p}_i)\theta\left(t_j\right) = \sum_{j=1}^{n'-1}\left(-\sum_{l=1}^{j} s_l(\hat{p}_i)\right)\left(\theta\left(t_{j+1}\right) - \theta\left(t_j\right)\right) \tag{3.71}$$

works provided that Equation 3.69 is satisfied. If the decomposition of Equation 3.71 is then substituted into Equation 3.19, the "red" noise variance of the parameter estimate,

$$\mathrm{var}_{red}(\hat{p}_i) = \mathrm{var}_{red}\left(\sum_{j=1}^{n'} s_j(\hat{p}_i)\theta(t_j)\right) =$$

$$\mathrm{var}_{red}\left(\sum_{j=1}^{n'-1}\left(-\sum_{l=1}^{j} s_l(\hat{p}_i)\right)\left(\theta(t_{j+1})-\theta(t_j)\right)\right) =$$

$$\sum_{j=1}^{n'-1}\sum_{k=1}^{n'-1}\left(-\sum_{l=1}^{j} s_l(\hat{p}_i)\right)\mathrm{cov}_{red}\left(\theta(t_{j+1})-\theta(t_j),\theta(t_{k+1})-\theta(t_k)\right)\left(-\sum_{m=1}^{k} s_m(\hat{p}_i)\right) =$$

$$\sum_{j=1}^{n'-1}\sum_{k=1}^{n'-1}\left(-\sum_{l=1}^{j} s_l(\hat{p}_i)\right)\left(-\sum_{m=1}^{k} s_m(\hat{p}_i)\right)\left(\theta_{red}^2\omega_o/2\pi\right)\left|t_{j+1}-t_j\right|\delta_{jk} = \qquad (3.72)$$

$$\left(\theta_{red}^2\omega_o/2\pi\right)\sum_{j=1}^{n'-1}\left(\sum_{l=1}^{j} s_l(\hat{p}_i)\right)^2\left|t_{j+1}-t_j\right|,$$

can be calculated.

When this method is applied to the second harmonic estimate of a single-period, 10-parameter fit, one gets

$$\mathrm{var}_{red}\left(\hat{A}_2\right) = (0.0213)\theta_{red}^2 \qquad \mathrm{stddev}_{red}\left(\hat{A}_2\right) = (0.146)\theta_{red}, \quad (3.73)$$

and for the frequency estimate of a single-period, 10-parameter fit, one gets

$$\frac{\mathrm{var}_{red}(\hat{\omega})}{\omega_o^2} = (0.0075)\theta_{red}^2 \qquad \frac{\mathrm{stddev}_{red}(\hat{\omega})}{\omega_o} = (0.086)\theta_{red}. \quad (3.74)$$

The corresponding signal-to-noise ratios are

$$(S/N)_{red}[A_2] = (1.64)\frac{|U_{ext}|}{\kappa\theta_{red}} \qquad (3.75)$$

and

$$(S/N)_{red}[\omega] = (3.66)\frac{|U_{ext}|}{\kappa\theta_{red}}. \qquad (3.76)$$

The ratio of the two methods' signal-to-noise ratios is then

$$\frac{(S/N)_{red}[\omega]}{(S/N)_{red}[A_2]} = 2.23 \qquad \frac{(S/N)^2_{red}[\omega]}{(S/N)^2_{red}[A_2]} = 4.98. \tag{3.77}$$

Once again, the frequency method is somewhat superior to the second harmonic method, and similar to the thermal noise case, the signal-to-noise increases with integration time as $\tau^{1/2}$ for both the 10-parameter fit and the 5-parameter fit, and so the ratio of the two methods does not change with increased integration time.

What is not similar to the thermal noise case is the comparison to the deflection method. The simple "boxcar" average estimate, $\hat{C}_{box}$, does not work because

$$\mathrm{var}_{red}\left(\hat{C}_{box}\right) \to \infty \tag{3.78}$$

in the presence of "red" noise. In fact, any arbitrary estimator of C,

$$\hat{C}_{arb} = \int_{-\pi/\omega_o}^{+\pi/\omega_o} w_{arb}(t)\theta(t)dt, \tag{3.79}$$

will suffer the same fate because proper normalization requires that

$$\int_{-\pi/\omega_o}^{+\pi/\omega_o} w_{arb}(t)\frac{\partial\theta(t)}{\partial C}dt = \int_{-\pi/\omega_o}^{+\pi/\omega_o} w_{arb}(t)dt = 1 \tag{3.80}$$

whereas the continuous generalization of Equation 3.69 requires that

$$\int_{-\pi/\omega_o}^{+\pi/\omega_o} w_{arb}(t)\frac{\partial\theta(t)}{\partial C}dt = \int_{-\pi/\omega_o}^{+\pi/\omega_o} w_{arb}(t)dt = 0 \tag{3.81}$$

if $\mathrm{var}_{red}\left(\hat{C}_{box}\right)$ is to be finite. The only way Equation 3.81 can be satisfied so that a deflection method can be used with "red" noise present is to physically modulate the signal. As described in Section 2.1, however, this is typically what is done in a torsion balance experiment.

Consider a non-oscillating, torsion balance experiment in which the source mass slowly rotates around the instrument with a modulation frequency of ω_{mod}. The nominal pendulum motion is then

$$\theta(t) = C_o + C_{mod}\cos(\omega_{mod}t) + Dt, \tag{3.82}$$

where the linear Dt term has been included to model the natural unwinding of the fiber. The signal is now in the sinusoidal amplitude, C_{mod}, rather than the dc amplitude, C_o. In general, there would also be a $\sin(\omega_{mod}t)$ term, but for simplicity in presentation, let us assume that the phase of the signal is known. For a data set one period of modulation in duration, the ideal estimator of C_{mod} is

$$\hat{C}_{mod} = \frac{\omega_{mod}}{\pi}\int_0^{2\pi/\omega_{mod}} \theta(t)\cos(\omega_{mod}t)dt. \tag{3.83}$$

Since Equation 3.81 is now satisfied, Equation 3.72 can be generalized from the case of discrete crossing data to the case of continuous, time-series data, and the variance in C_{mod},

$$\begin{aligned}\mathrm{var}_{red}\left(\hat{C}_{mod}\right) &= \frac{\theta_{red}^2\omega_o}{2\pi}\int_0^{2\pi/\omega_{mod}}\left(\frac{\omega_{mod}}{\pi}\int_0^t \cos(\omega_{mod}u)du\right)^2 dt \\ &= \frac{\theta_{red}^2}{2\pi^2}\left(\frac{\omega_o}{\omega_{mod}}\right),\end{aligned} \tag{3.84}$$

can be calculated and shown to be finite. Before it can be compared to the 10-parameter fit and 5-parameter fit, however, the "red" noise variance in C_{mod} must be normalized to the same time period because it is fitting to a data set that is one modulation period in duration whereas the 10-parameter fit and 5-parameter fit are fitting to a data set that is one pendulum oscillation period in duration. Since the variance scales as $1/\tau$, let us divide the variance by the ratio of the duration times,

$$\mathrm{var}_{red}^{nor}\left(\hat{C}_{mod}\right) = \frac{(2\pi/\omega_{mod})}{(2\pi/\omega_o)}\mathrm{var}_{red}\left(\hat{C}_{mod}\right) = \frac{\theta_{red}^2}{2\pi^2}\left(\frac{\omega_o}{\omega_{mod}}\right)^2, \tag{3.85}$$

and use a "nor" superscript to designate that it has been normalized. Numerically, this is

$$\mathrm{var}_{red}^{nor}\left(\hat{C}_{mod}\right) = (0.0507)\theta_{red}^2\left(\frac{\omega_o}{\omega_{mod}}\right)^2$$

$$\mathrm{stddev}_{red}^{nor}\left(\hat{C}_{mod}\right) = (0.225)\theta_{red}\left(\frac{\omega_o}{\omega_{mod}}\right). \tag{3.86}$$

The signal-to-noise ratio is then

$$(S/N)_{red}^{nor}[C_{mod}] = (4.44)\frac{|U_{ext}|}{\kappa\theta_{red}}\left(\frac{\omega_{mod}}{\omega_o}\right). \tag{3.87}$$

Note how it decreases with modulation frequency.

The signal-to-noise of the 10-parameter fit in Equation 3.75 has not accounted for the modulation of the signal; it has assumed the signal is always at maximum amplitude. To have a fair comparison, the sinusoidally modulated

deflection, C_{mod}, should compared to a sinusoidally modulated second harmonic signal, $A_{2_{mod}}$, whose signal-to-noise,

$$(S/N)_{red}[A_{2mod}] = \frac{(S/N)_{red}[A_2]}{\sqrt{2}} = (1.16)\frac{|U_{ext}|}{\kappa\theta_{red}}, \tag{3.88}$$

is reduced by a factor of $1/2^{1/2}$, the ratio of the root-mean-square to peak signal amplitude. The ratio of the two signal-to-noise ratios is

$$\frac{(S/N)^{nor}_{red}[C_{mod}]}{(S/N)_{red}[A_{2mod}]} = 3.83\left(\frac{\omega_{mod}}{\omega_o}\right)$$

$$\frac{(S/N)^{nor^2}_{red}[C_{mod}]}{(S/N)^2_{red}[A_{2mod}]} = 14.66\left(\frac{\omega_{mod}}{\omega_o}\right)^2. \tag{3.89}$$

Unless the source mass is rotated faster than once every four oscillation periods, the modulated second harmonic method will be superior to the modulated deflection method for a "red" noise limited experiment. As a severe example, consider using the sun as a source mass as both Dicke and Braginskii have done (Braginskii & Panov 1972; Roll et al. 1964). The advantage to this method is that the instrument does not have to be moved in the lab frame in order to modulate the signal, but as (ω_{day}/ω_o) is typically on the order of 1/200, the "red" noise limit is roughly 50 times larger in amplitude and 2500 times longer in time for the deflection method compared to a second harmonic experiment using the same fiber and pendulum.

3.5 Very Low Frequency Noise Comparison

The results of the previous "red" noise section are informative, but low frequency variations do not always have a $1/f^2$ frequency power spectrum.

One approach would be to continue investigating the error propagation of other power-law noise ensembles because their lack of a characteristic time scale makes them fairly tractable mathematically. There are difficulties, however, arising from their singularities at $f = 0$ which make them non-stationary, and it is not clear that an arbitrary noise process can be reasonably modeled as a composition of power-law processes. A more basic approach is to consider the error propagation of a single frequency component of noise. In particular, I will look at very low frequency noise, $\omega_n << \omega_o$, for which an approximation to leading order in ω_n/ω_o will be sufficient. Also, since the additive noise of slow drifts in deflection is a simpler concept than the frequency modulation that arises from slow drifts in frequency, the discussion in this section will provide a good introduction to Section 3.6.

Let us determine the effect of a single, low frequency component of noise in angular displacement with amplitude, a_n, frequency, ω_n, and phase, δ_n. It will be convenient to expand this sine wave as a power series in time around $t = 0$,

$$\begin{aligned} a_n \cos(\omega_n t - \delta_n) &= a_n \cos(\omega_n t)\cos(\delta_n) - a_n \sin(\omega_n t)\sin(\delta_n) \\ &= a_n \cos(\delta_n) - a_n \sin(\delta_n)(\omega_n t) - \\ &\quad \frac{a_n \cos(\delta_n)}{2}(\omega_n t)^2 + \frac{a_n \sin(\delta_n)}{6}(\omega_n t)^3 \ldots, \end{aligned} \tag{3.90}$$

and it will also be convenient to define vectors of the nominal crossing-times taken to various powers,

$$\begin{aligned} \mathbf{t}^0 &= \{t_1^0, t_2^0, \ldots t_{n'}^0\} = \{1,1,\ldots 1\} \\ \mathbf{t}^1 &= \{t_1, t_2, \ldots t_{n'}\} \\ \mathbf{t}^2 &= \{t_1^2, t_2^2, \ldots t_{n'}^2\} \\ \mathbf{t}^3 &= \{t_1^3, t_2^3, \ldots t_{n'}^3\}. \end{aligned} \tag{3.91}$$

The error in the parameter estimate, $\Delta\hat{p}_i$, can then be expanded as

$$\begin{aligned}
\Delta\hat{p}_i &= \mathbf{s}(\hat{p}_i)\bullet\Big[a_n\cos(\delta_n)\mathbf{t}^0 - a_n\sin(\delta_n)\omega_n\mathbf{t}^1 \\
&\quad -\frac{a_n\cos(\delta_n)}{2}\omega_n^2\mathbf{t}^2 + \frac{a_n\sin(\delta_n)}{6}\omega_n^3\mathbf{t}^3\ldots\Big] \\
&= a_n\cos(\delta_n)\Big(\mathbf{s}(\hat{p}_i)\bullet\mathbf{t}^0\Big) - a_n\sin(\delta_n)\Big(\mathbf{s}(\hat{p}_i)\bullet\omega_n\mathbf{t}^1\Big) \\
&\quad -\frac{a_n\cos(\delta_n)}{2}\Big(\mathbf{s}(\hat{p}_i)\bullet\omega_n^2\mathbf{t}^2\Big) + \frac{a_n\sin(\delta_n)}{6}\Big(\mathbf{s}(\hat{p}_i)\bullet\omega_n^3\mathbf{t}^3\Big)\ldots \\
&= a_n\cos(\delta_n)\Big(\mathbf{s}(\hat{p}_i)\bullet\mathbf{t}^0\Big) - a_n\sin(\delta_n)\left(\frac{\omega_n}{\omega_o}\right)\Big(\mathbf{s}(\hat{p}_i)\bullet\omega_o\mathbf{t}^1\Big) \\
&\quad -\frac{a_n\cos(\delta_n)}{2}\left(\frac{\omega_n}{\omega_o}\right)^2\Big(\mathbf{s}(\hat{p}_i)\bullet\omega_o^2\mathbf{t}^2\Big) + \\
&\quad \frac{a_n\sin(\delta_n)}{6}\left(\frac{\omega_n}{\omega_o}\right)^3\Big(\mathbf{s}(\hat{p}_i)\bullet\omega_o^3\mathbf{t}^3\Big)\ldots.
\end{aligned} \tag{3.92}$$

Now consider a statistical ensemble of sine waves, all with the frequency ω_n but with random phases and normally distributed amplitudes. Let us designate the spectral power, which is the variance of the noise amplitude, as

$$\mathrm{var}_n(a_n) = \theta_n^2. \tag{3.93}$$

The variance in each quadrature component,

$$\mathrm{var}_n\big(a_n\cos(\delta_n)\big) = \mathrm{var}_n\big(a_n\sin(\delta_n)\big) = \theta_n^2/2, \tag{3.94}$$

is then half of that. Substituting Equation 3.94 into the variance of Equation 3.92, the variance of the parameter estimate can be expanded in powers of (ω_n/ω_o). The leading variance, due to the zeroth-order error, is

$$\mathrm{var}_n(\hat{p}_i)_0 = \frac{\theta_n^2}{2}\Big(\mathbf{s}(\hat{p}_i)\bullet\mathbf{t}^0\Big)^2. \tag{3.95}$$

If the zeroth-order term is zero, then the next leading-order variance,

$$\mathrm{var}_n(\hat{p}_i)_1 = \frac{\theta_n^2}{2}\left(\frac{\omega_n}{\omega_o}\right)^2 \left(\mathbf{s}(\hat{p}_i)\bullet\omega_o\mathbf{t}^1\right)^2, \tag{3.96}$$

is due to the error first-order in (ω_n/ω_o), and if that is also zero, then the variance is

$$\mathrm{var}_n(\hat{p}_i)_2 = \frac{\theta_n^2}{8}\left(\frac{\omega_n}{\omega_o}\right)^4 \left(\mathbf{s}(\hat{p}_i)\bullet\omega_o^2\mathbf{t}^2\right)^2. \tag{3.97}$$

And similarly, if that is zero, the variance due to the third-order error is

$$\mathrm{var}_n(\hat{p}_i)_3 = \frac{\theta_n^2}{72}\left(\frac{\omega_n}{\omega_o}\right)^6 \left(\mathbf{s}(\hat{p}_i)\bullet\omega_o^3\mathbf{t}^3\right)^2. \tag{3.98}$$

For a single-period, "boxcar" deflection estimate, the variance

$$\begin{aligned}\mathrm{var}_n\left(\hat{C}_{box}\right) \equiv \mathrm{var}_n\left(\hat{C}_{box}\right)_0 &= \frac{\theta_n^2}{2}\left(\frac{\omega_d}{2\pi}\int_{-\pi/\omega_d}^{+\pi/\omega_d} 1dt\right)^2 = \frac{\theta_n^2}{2} \\ \mathrm{stddev}_n\left(\hat{C}_{box}\right) &\equiv (0.707)\theta_n\end{aligned} \tag{3.99}$$

is dominated by the zero-order term. In Equation 3.99, the term in parentheses is the continuous generalization of $\left(\mathbf{s}(\hat{p}_i)\bullet\mathbf{t}^0\right)$, and that term is 1 because

$$\mathbf{t}^0 = \partial\boldsymbol{\theta}/\partial\mathbf{C}. \tag{3.100}$$

On the other hand, Equation 3.100 and the orthnormality condition of Equation 3.21 ensures that the zero-order variance,

$$\mathrm{var}_n\left(\hat{A}_2\right)_0 = \frac{\theta_n^2}{2}\left(\mathbf{s}\left(\hat{A}_2\right)\bullet\frac{\partial\theta}{\partial\mathbf{C}}\right)^2 = 0$$

$$\frac{\mathrm{var}_n(\hat{\omega})_0}{\omega_o^2} = \frac{\theta_n^2}{2}\left(\frac{\mathbf{s}(\hat{\omega})}{\omega_o} \bullet \frac{\partial \boldsymbol{\theta}}{\partial C}\right)^2 = 0, \tag{3.101}$$

will vanish for both the 10-parameter fit and the 5-parameter fit. The variance of the frequency estimate of the 5-parameter fit,

$$\begin{aligned} \frac{\mathrm{var}_n(\hat{\omega})}{\omega_o^2} \equiv \frac{\mathrm{var}_n(\hat{\omega})_1}{\omega_o^2} &= \frac{\theta_n^2}{2}\left(\frac{\omega_n}{\omega_o}\right)^2\left(\frac{\mathbf{s}(\hat{\omega})}{\omega_o} \bullet \omega_o \mathbf{t}^1\right)^2 = (0.147)\theta_n^2\left(\frac{\omega_n}{\omega_o}\right)^2 \\ \frac{\mathrm{stddev}_n(\hat{\omega})}{\omega_o} &= (0.384)\theta_n\left(\frac{\omega_n}{\omega_o}\right), \end{aligned} \tag{3.102}$$

is dominated by the first-order error, but since

$$\mathbf{t}^1 = \partial \boldsymbol{\theta} / \partial D, \tag{3.103}$$

the first-order error of the 10-parameter fit,

$$\mathrm{var}_n\left(\hat{A}_2\right)_1 = \frac{\theta_n^2 \omega_n^2}{2}\left(\mathbf{s}\left(\hat{A}_2\right) \bullet \frac{\partial \boldsymbol{\theta}}{\partial D}\right)^2 = 0, \tag{3.104}$$

will vanish. The variance of the 10-parameter fit,

$$\begin{aligned} \mathrm{var}_n\left(\hat{A}_2\right) \equiv \mathrm{var}_n\left(\hat{A}_2\right)_2 &= \frac{\theta_n^2}{8}\left(\frac{\omega_n}{\omega_o}\right)^4\left(\mathbf{s}\left(\hat{A}_2\right) \bullet \omega_o^2 \mathbf{t}^2\right)^2 = (0.0181)\theta_n^2\left(\frac{\omega_n}{\omega_o}\right)^4 \\ \mathrm{stddev}_n\left(\hat{A}_2\right) &= (0.135)\theta_n\left(\frac{\omega_n}{\omega_o}\right)^2, \end{aligned} \tag{3.105}$$

is dominated by the second-order error.

It would seem from comparing Equations 3.102 and 3.105 that I finally have a noise process for which the 10-parameter fit is superior to the 5-parameter fit, but Equation 3.104 seems to suggest that the 10-parameter fit

has an unfair advantage because it explicitly fits for a linear, Dt term whereas the 5-parameter fit does not. If the 5-parameter fit were modified to include a Dt term, then its variance would also be second-order dominated. However, there is an even easier method to make the frequency estimate immune to linear drifts. The error propagation of the Dt term is equal and opposite for 121-type 5-patameter fits as compared to 212-type 5-parameter fits, and so a simple average of the two will eliminate the effect of the Dt term. Let us define $\hat{\omega}_{lf}$ (the "lf" subscript is short for "linear filter") as such an average,

$$\hat{\omega}_{lf} = \frac{\hat{\omega}_{121}\left(t_{eq} = 0\right) + \hat{\omega}_{212}\left(t_{eq} = \pi/\omega_o\right)}{2}. \tag{3.106}$$

The weighting function, $\mathbf{s}\left(\hat{\omega}_{lf}\right)$, for such a frequency estimate is graphically depicted in Figure 3.7, and its variance,

$$\begin{aligned}
\frac{\mathrm{var}_n\left(\hat{\omega}_{lf}\right)}{\omega_o^2} \cong \frac{\mathrm{var}_n\left(\hat{\omega}_{lf}\right)_2}{\omega_o^2} &= \frac{\theta_n^2}{8}\left(\frac{\omega_n}{\omega_o}\right)^4\left(\frac{\mathbf{s}\left(\hat{\omega}_{lf}\right)}{\omega_o} \bullet \omega_o^2 \mathbf{t}^2\right)^2 \\
&= (0.364)\theta_n^2\left(\frac{\omega_n}{\omega_o}\right)^4 \\
\frac{\mathrm{stddev}_n\left(\hat{\omega}_{lf}\right)}{\omega_o} &= (0.603)\theta_n\left(\frac{\omega_n}{\omega_o}\right)^2,
\end{aligned} \tag{3.107}$$

is dominated by the second-order error just as $\mathrm{var}_n\left(\hat{A}_2\right)$ of the 10-parameter fit is.

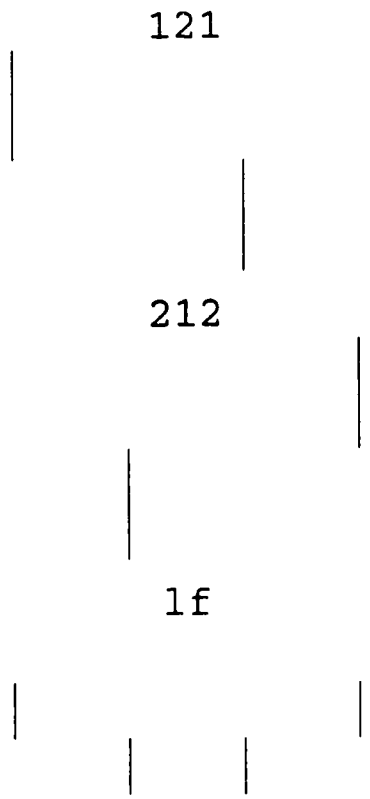

Figure 3.7. The sampling function of the frequency estimate of a 5-parameter fit centered on a clockwise zero-crossing, $\mathbf{s}(\hat{\omega}_{121})$ (see Eq. 3.29), the sampling function of the frequency estimate of a 5-parameter fit centered on a counterclockwise zero-crossing one-half period later, $\mathbf{s}(\hat{\omega}_{212})$, and the sampling function the average of the two estimates, $\mathbf{s}(\hat{\omega}_{lf})$. The horizontal axis is time, and the vertical height is proportional to the weight with which error propagates into the frequency estimate.

Can this trick be repeated in order to make the frequency estimate dominated by third-order errors? Yes, if you define the "quadratic filter" estimate as

$$\hat{\omega}_{qf} = \frac{\hat{\omega}_{121}\left(t_{eq}=0\right) + 2\hat{\omega}_{212}\left(t_{eq}=\pi/\omega_o\right) + \hat{\omega}_{121}\left(t_{eq}=2\pi/\omega_o\right)}{4}, \tag{3.108}$$

then

$$\mathbf{s}\left(\hat{\omega}_{qf}\right)\bullet \mathbf{t}^0 = 0, \quad \mathbf{s}\left(\hat{\omega}_{qf}\right)\bullet \mathbf{t}^1 = 0, \quad \text{and} \quad \mathbf{s}\left(\hat{\omega}_{qf}\right)\bullet \mathbf{t}^2 = 0, \tag{3.109}$$

and the variance,

$$\begin{aligned}\frac{\mathrm{var}_n\left(\hat{\omega}_{qf}\right)}{\omega_o^2} \cong \frac{\mathrm{var}_n\left(\hat{\omega}_{qf}\right)_3}{\omega_o^2} &= \frac{\theta_n^2}{72}\left(\frac{\omega_n}{\omega_o}\right)^6\left(\frac{\mathbf{s}\left(\hat{\omega}_{qf}\right)}{\omega_o}\bullet \omega_o^3\mathbf{t}^3\right)^2 \\ &= (0.898)\theta_n^2\left(\frac{\omega_n}{\omega_o}\right)^6 \\ \frac{\mathrm{stddev}_n\left(\hat{\omega}_{qf}\right)}{\omega_o} &= (0.948)\theta_n\left(\frac{\omega_n}{\omega_o}\right)^3,\end{aligned} \tag{3.110}$$

is dominated by third-order errors. The sampling function of the "quadratic filter" estimate, $\mathbf{s}\left(\hat{\omega}_{qf}\right)$, is graphically depicted in Figure 3.8.

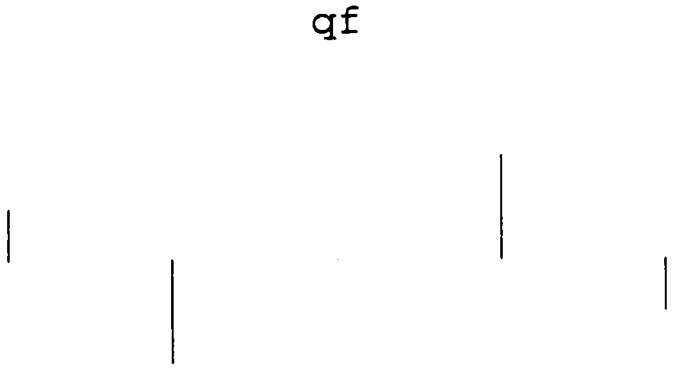

Figure 3.8. Pictorial representation of $\mathbf{s}\left(\hat{\omega}_{qf}\right)$. The horizontal axis is time, and the vertical height is proportional to the weight with which error propagates into the frequency estimate. The weights were uniquely chosen so that $\mathbf{s}\left(\hat{\omega}_{qf}\right)\bullet \mathbf{t}^0 = 0$, $\mathbf{s}\left(\hat{\omega}_{qf}\right)\bullet \mathbf{t}^1 = 0$, and $\mathbf{s}\left(\hat{\omega}_{qf}\right)\bullet \mathbf{t}^2 = 0$.

In Section 3.4, the variance in the estimate of C_{mod} was normalized to an equivalent value corresponding to one oscillation period of data. Since both $\hat{\omega}_{lf}$

and $\hat{\omega}_{qf}$ utilize more than one oscillation period of crossing data, it would seem that it would be appropriate to normalize the variances in Eqs. 3.107 and 3.110 before comparing their signal-to-noise to the 10-parameter fit and the 5-parameter fit. However, the underlying assumption that the errors of adjacent fits are uncorrelated and therefore decrease when averaged together does not hold for low frequency noise. A more conservative estimate of the effect of low frequency noise is to assume that it will not be decreased by averaging adjacent fits. Under this assumption, the signal-to-noise ratios for the five methods discussed in this section are

$$(S/N)_n[C_{box}] = (1.414)\frac{|U_{ext}|}{\kappa\theta_n}, \tag{3.111}$$

$$(S/N)_n[\omega] = (0.823)\frac{|U_{ext}|}{\kappa\theta_n}\left(\frac{\omega_o}{\omega_n}\right), \tag{3.112}$$

$$(S/N)_n[\omega_{lf}] = (0.524)\frac{|U_{ext}|}{\kappa\theta_n}\left(\frac{\omega_o}{\omega_n}\right)^2, \tag{3.113}$$

$$(S/N)_n[A_2] = (1.778)\frac{|U_{ext}|}{\kappa\theta_n}\left(\frac{\omega_o}{\omega_n}\right)^2, \text{ and} \tag{3.114}$$

$$(S/N)_n[\omega_{qf}] = (0.333)\frac{|U_{ext}|}{\kappa\theta_n}\left(\frac{\omega_o}{\omega_n}\right)^3. \tag{3.115}$$

And expressed as ratios relative to the 10-parameter fit, they are

$$\frac{(S/N)_n[C_{box}]}{(S/N)_n[A_2]} = (0.795)\left(\frac{\omega_n}{\omega_o}\right)^2, \tag{3.116}$$

$$\frac{(S/N)_n[\omega]}{(S/N)_n[A_2]} = (0.463)\left(\frac{\omega_n}{\omega_o}\right), \tag{3.117}$$

$$\frac{(S/N)_n[\omega_{lf}]}{(S/N)_n[A_2]} = 0.295, \text{ and} \tag{3.118}$$

$$\frac{(S/N)_n[\omega_{qf}]}{(S/N)_n[A_2]} = (0.187)\left(\frac{\omega_o}{\omega_n}\right). \tag{3.119}$$

Since the low-frequency noise error does not decrease with averaging adjacent fits, the ratios of the squares of the $(S/N)_n$'s have not been presented because they are only useful to compare the time required by the various methods to integrate the error down to some specified level.

Looking at the equations above, the most striking feature is the deflection method's inability to filter out low-frequency noise. It suffers a $(\omega_n/\omega_o)^2$ disadvantage in signal-to-noise relative to the 10-parameter fit. Following the discussion of C_{mod} in Section 3.4, it should seem that modulating the signal would provide some relief from low-frequency noise, and it does, but only for frequencies below the modulation frequency. The other methods, however, can gain the same advantage by modulating the signal because their errors are also correlated. Thus, although the signal-to-noise ratios in Equations 3.111 through 3.115 will be increased by modulation, they are all increased by the same amount so the relative performance in Equations 3.116 through 3.119 remain unaffected and are essentially correct.

The second most striking feature of the above equations is the relative ease with which the frequency method can be made immune to low-frequency noise, to arbitrary order, by simple weighted averages of adjacent fits. One must keep

in mind that for "white" noise these weightings are not optimal, and you will therefore suffer some moderate degradation in signal-to-noise if the "white" noise error is larger than the low-frequency noise error. Although there is not simple average that can make the 10-parameter fit immune to quadratic drifts, one can modify the fit to explicitly include an eleventh parameter, a quadratic Et^2 term. When this is done, however, the degradation of the "white" noise signal-to-noise ratio for A_2 is severe, and since our present Index experiment is limited by rocking motion errors which behave like "white" noise, such a modification of the 10-parameter fit would be counterproductive. The simple weighted averages of adjacent frequency fits is possible because the error propagation of the 5-parameter fit frequency estimate changes sign every half-period. In the next section, it will be shown that the error propagation of frequency drifts into the second harmonic estimate also changes sign every half-period, and so the second harmonic estimate can be made immune to slow frequency drifts, to arbitrary order, by simple weighted averages of adjacent 10-parameter fits.

3.6 Slow Drifts in Frequency

In Section 3.5, we looked at the error propagation of a single low-frequency noise component of deflection variation, $a_n \cos(\omega_n t - \delta_n)$. In this section, we look at the error propagation of a single low-frequency noise component of frequency variation. More specifically, we assume there is a physical process, such as fiber temperature variation, that alters the shear modulus of the fiber so that the torsion fiber constant,

$$\kappa(t) = \kappa_o + \kappa_n \cos(\omega_n t - \delta_n), \tag{3.120}$$

varies sinusoidally with amplitude κ_n and frequency ω_n. As in Section 2, we will neglect damping in order to simplify the presentation. The motion of the pendulum then obeys the equation,

$$\frac{d^2\theta(t)}{dt^2} = \left(1 + \frac{\kappa_n \cos(\omega_n t - \delta_n)}{\kappa_o}\right)\omega_o^2 \theta(t). \tag{3.121}$$

It should be emphasized that ω_n is not the magnitude of the frequency shift but rather the rate at which the frequency is modulated. For a diurnal variation, $\omega_n = 2\pi/(1\ \text{day})$, and ω_n/ω_o would typically be about 1/200. The magnitude of the fractional variation in frequency will be determined by κ_n/κ_o, which in a well-regulated experiment is no larger than $1/10^6$. Since κ_n/κ_o is so small, results in this section are all approximated to first-order in κ_n/κ_o. To first order, one would guess that the $\kappa_n \cos(\omega_n t - \delta_n)$ term would modify the basic $\theta(t) = A\sin(\omega_o t)$ motion to include low-frequency, sinusoidal variations in the amplitude and phase of the fundamental pendulum oscillation. That is, assume

$$\begin{aligned}\theta(t) &\equiv \left(A + a_1\cos(\omega_n t) + b_1 \sin(\omega_n t)\right)\sin\left(\omega_o t + p_1\cos(\omega_n t) + q_1\cos(\omega_n t)\right) \\ &\equiv A\sin(\omega_o t) + a_1\cos(\omega_n t)\sin(\omega_o t) + b_1\sin(\omega_n t)\sin(\omega_o t) - \\ &\quad Ap_1\cos(\omega_n t)\cos(\omega_o t) + Aq_1\sin(\omega_n t)\cos(\omega_o t)\end{aligned} \tag{3.122}$$

to be a solution to 3.121. Upon substitution, it is in fact a solution provided that

$$\begin{aligned} a_1 &= -A\left(\frac{\kappa_n}{\kappa_o}\right)\frac{\omega_o^2\cos(\delta_n)}{4\omega_o^2 - \omega_n^2}, & b_1 &= -A\left(\frac{\kappa_n}{\kappa_o}\right)\frac{\omega_o^2\sin(\delta_n)}{4\omega_o^2 - \omega_n^2}, \\ p_1 &= \left(\frac{\kappa_n}{\kappa_o}\right)\frac{2\omega_o^3\sin(\delta_n)}{\omega_n\left(4\omega_o^2 - \omega_n^2\right)}, \quad \text{and} & q_1 &= \left(\frac{\kappa_n}{\kappa_o}\right)\frac{2\omega_o^3\cos(\delta_n)}{\omega_n\left(4\omega_o^2 - \omega_n^2\right)}. \end{aligned} \tag{3.123}$$

Next we would like to substitute Eq. 3.123 into Eq. 3.122 and expand in powers of ω_n/ω_o. Expanded through third-order in ω_n/ω_o (but still only first-order in κ_n/κ_o), Eq. 3.122 becomes

$$\begin{aligned}\theta(t) \equiv & A\sin(\omega_o t) + A\left(\frac{\kappa_n}{\kappa_o}\right)\left(\frac{\omega_n}{\omega_o}\right)^{-1}\sin(\delta_n)\left[-\frac{1}{2}\cos(\omega_o t)\right] + \\ & A\left(\frac{\kappa_n}{\kappa_o}\right)\cos(\delta_n)\left[-\frac{1}{4}\sin(\omega_o t) + \frac{1}{2}\omega_o t\cos(\omega_o t)\right] + \\ & A\left(\frac{\kappa_n}{\kappa_o}\right)\left(\frac{\omega_n}{\omega_o}\right)\sin(\delta_n)\left[-\frac{1}{8}\cos(\omega_o t) - \frac{1}{4}\omega_o t\sin(\omega_o t) + \right. \\ & \left.\frac{1}{4}\omega_o^2 t^2\cos(\omega_o t)\right] + \\ & A\left(\frac{\kappa_n}{\kappa_o}\right)\left(\frac{\omega_n}{\omega_o}\right)^2\cos(\delta_n)\left[-\frac{1}{16}\sin(\omega_o t) + \frac{1}{8}\omega_o t\cos(\omega_o t) + \right. \\ & \left.\frac{1}{8}\omega_o^2 t^2\sin(\omega_o t) - \frac{1}{12}\omega_o^3 t^3\cos(\omega_o t)\right] + \\ & A\left(\frac{\kappa_n}{\kappa_o}\right)\left(\frac{\omega_n}{\omega_o}\right)^3\sin(\delta_n)\left[-\frac{1}{32}\cos(\omega_o t) - \frac{1}{16}\omega_o t\sin(\omega_o t) + \right. \\ & \left.\frac{1}{16}\omega_o^2 t^2\cos(\omega_o t) + \frac{1}{24}\omega_o^3 t^3\sin(\omega_o t) - \frac{1}{48}\omega_o^4 t^4\cos(\omega_o t)\right].\end{aligned} \tag{3.124}$$

In Section 3.5, expansion in powers of ω_n/ω_o led to terms that were simple powers of t whereas here the terms are powers of t multiplied by either $\sin(\omega_o t)$ or $\cos(\omega_o t)$. So it is useful to define new vectors of powers of crossing times multiplied by $\sin(\omega_o t)$,

$$\begin{aligned}\mathbf{t}_{\sin}^0 &= \left\{\sin(\omega_o t_1), \sin(\omega_o t_2), \ldots \sin(\omega_o t_{n'})\right\} \\ \mathbf{t}_{\sin}^1 &= \left\{t_1\sin(\omega_o t_1), t_2\sin(\omega_o t_2), \ldots t_{n'}\sin(\omega_o t_{n'})\right\} \\ \mathbf{t}_{\sin}^2 &= \left\{t_1^2\sin(\omega_o t_1), t_2^2\sin(\omega_o t_2), \ldots t_{n'}^2\sin(\omega_o t_{n'})\right\} \\ \mathbf{t}_{\sin}^3 &= \left\{t_1^3\sin(\omega_o t_1), t_2^3\sin(\omega_o t_2), \ldots t_{n'}^3\sin(\omega_o t_{n'})\right\},\end{aligned} \tag{3.125}$$

and similarly new vectors of powers of crossing times multiplied by $\cos(\omega_o t)$,

$$\begin{aligned}
\mathbf{t}^0_{\cos} &= \left\{\cos(\omega_o t_1), \cos(\omega_o t_2), \ldots \cos(\omega_o t_{n'})\right\} \\
\mathbf{t}^1_{\cos} &= \left\{t_1 \cos(\omega_o t_1), t_2 \cos(\omega_o t_2), \ldots t_{n'} \cos(\omega_o t_{n'})\right\} \\
\mathbf{t}^2_{\cos} &= \left\{t_1^2 \cos(\omega_o t_1), t_2^2 \cos(\omega_o t_2), \ldots t_{n'}^2 \cos(\omega_o t_{n'})\right\} \\
\mathbf{t}^3_{\cos} &= \left\{t_1^3 \cos(\omega_o t_1), t_2^3 \cos(\omega_o t_2), \ldots t_{n'}^3 \cos(\omega_o t_{n'})\right\} \\
\mathbf{t}^4_{\cos} &= \left\{t_1^4 \cos(\omega_o t_1), t_2^4 \cos(\omega_o t_2), \ldots t_{n'}^4 \cos(\omega_o t_{n'})\right\}.
\end{aligned} \tag{3.126}$$

The $\mathbf{t}^0_{\sin}$ and $\mathbf{t}^0_{\cos}$ terms can be dropped, however, because it is only deviations from pure sinusoidal motion that can cause errors in the signal parameter. Or couched in terms of the orthnormality condition of Equation 3.21,

$$\mathbf{s}(\hat{p}_i) \bullet \mathbf{t}^0_{\sin} = \mathbf{s}(\hat{p}_i) \bullet \frac{\partial \boldsymbol{\theta}}{\partial A} = 0 \quad \text{and}$$

$$\mathbf{s}(\hat{p}_i) \bullet \mathbf{t}^0_{\cos} = -\frac{1}{A\omega_o}\left(\mathbf{s}(\hat{p}_i) \bullet \frac{\partial \boldsymbol{\theta}}{\partial t_{eq}}\right) = 0 \tag{3.127}$$

provided that there are two parameters, such as A and teq, that fit for the amplitude and phase of the fundamental oscillation. With those terms dropped, the error in the parameter estimate, $\Delta\hat{p}_i$, can then be expanded as

$$\begin{aligned}
\Delta p_i = {} & A\left(\frac{\kappa_n \cos(\delta_n)}{\kappa_o}\right)\left[\frac{1}{2}\mathbf{s}(\hat{p}_i)\bullet\omega_o\mathbf{t}^1_{\cos}\right]+ \\
& A\left(\frac{\kappa_n \sin(\delta_n)}{\kappa_o}\right)\left(\frac{\omega_n}{\omega_o}\right)\left[-\frac{1}{4}\mathbf{s}(\hat{p}_i)\bullet\omega_o\mathbf{t}^1_{\sin}+\frac{1}{4}\mathbf{s}(\hat{p}_i)\bullet\omega_o^2\mathbf{t}^2_{\cos}\right]+ \\
& A\left(\frac{\kappa_n \cos(\delta_n)}{\kappa_o}\right)\left(\frac{\omega_n}{\omega_o}\right)^2\left[\frac{1}{8}\mathbf{s}(\hat{p}_i)\bullet\omega_o\mathbf{t}^1_{\cos}+\frac{1}{8}\mathbf{s}(\hat{p}_i)\bullet\omega_o^2\mathbf{t}^2_{\sin}-\right. \\
& \left.\frac{1}{12}\mathbf{s}(\hat{p}_i)\bullet\omega_o^3\mathbf{t}^3_{\cos}\right]+ \\
& A\left(\frac{\kappa_n \sin(\delta_n)}{\kappa_o}\right)\left(\frac{\omega_n}{\omega_o}\right)^3\left[-\frac{1}{16}\mathbf{s}(\hat{p}_i)\bullet\omega_o\mathbf{t}^1_{\sin}+\frac{1}{16}\mathbf{s}(\hat{p}_i)\bullet\omega_o^2\mathbf{t}^2_{\cos}+\right. \\
& \left.\frac{1}{24}\mathbf{s}(\hat{p}_i)\bullet\omega_o^3\mathbf{t}^3_{\sin}-\frac{1}{48}\mathbf{s}(\hat{p}_i)\bullet\omega_o^4\mathbf{t}^4_{\cos}\right]+\ldots.
\end{aligned} \tag{3.128}$$

Equation 3.128 is equivalent to Equation 3.92 in Section 3.5. Once again, we want to consider an ensemble of random phases and determine the corresponding variance in the parameter estimate. Designate the spectral power of the torsion fiber constant variation as

$$\mathrm{var}_{\kappa n}(\kappa_n) = (\delta\kappa)^2_{\kappa n}. \tag{3.129}$$

Here I have used the subscript "κn" on the variance to avoid confusion with the variances due to low-frequency deflection noise in Section 3.5. The fractional variance of each quadrature component,

$$\frac{\mathrm{var}_{\kappa n}\left(\kappa_n \cos(\delta_n)\right)}{\kappa_o^2} = \frac{\mathrm{var}_{\kappa n}\left(\kappa_n \sin(\delta_n)\right)}{\kappa_o^2} = \frac{1}{2}\left(\frac{\delta\kappa}{\kappa_o}\right)^2_{\kappa n} = 2\left(\frac{\delta\omega}{\omega_o}\right)^2_{\kappa n}, \tag{3.130}$$

is half of the fractional spectral power of the torsion fiber constant variation which is twice the fractional spectral power of the frequency variation. This last

relationship arises from the frequency being proportional to the square root of the torsion fiber constant,

$$\omega = \left(\frac{\kappa}{I}\right)^{1/2} \quad \Rightarrow \quad \frac{\delta\omega}{\omega_o} = \frac{1}{2}\frac{\delta\kappa}{\kappa_o} \quad \Rightarrow \quad \left(\frac{\delta\omega}{\omega_o}\right)^2_{\kappa m} = \frac{1}{4}\left(\frac{\delta\kappa}{\kappa_o}\right)^2_{\kappa m}. \tag{3.131}$$

Substituting Equation 3.130 into the variance of Equation 3.128, the variance of the parameter estimate can be expanded in powers of (ω_n/ω_o). The leading variance, due to the zeroth-order error, is

$$\mathrm{var}_{\kappa m}(\hat{p}_i)_0 = \frac{A^2}{2}\left(\frac{\delta\omega}{\omega_o}\right)^2_{\kappa m}\left(\mathbf{s}(\hat{p}_i)\bullet\omega_o\mathbf{t}^1_{\cos}\right)^2. \tag{3.132}$$

If the zeroth-order term is zero, then the next leading-order variance,

$$\mathrm{var}_{\kappa m}(\hat{p}_i)_1 = \frac{A^2}{8}\left(\frac{\delta\omega}{\omega_o}\right)^2_{\kappa m}\left(\frac{\omega_n}{\omega_o}\right)^2\left(\mathbf{s}(\hat{p}_i)\bullet\omega_o\mathbf{t}^1_{\sin} - \mathbf{s}(\hat{p}_i)\bullet\omega_o^2\mathbf{t}^2_{\cos}\right)^2, \tag{3.133}$$

is due to the first-order error; and if that is also zero, the leading error is second-order, and the variance is

$$\mathrm{var}_{\kappa m}(\hat{p}_i)_2 = \frac{A^2}{288}\left(\frac{\delta\omega}{\omega_o}\right)^2_{\kappa m}\left(\frac{\omega_n}{\omega_o}\right)^4\left(3\mathbf{s}(\hat{p}_i)\bullet\omega_o^2\mathbf{t}^2_{\sin} - 2\mathbf{s}(\hat{p}_i)\bullet\omega_o^3\mathbf{t}^3_{\cos}\right)^2. \tag{3.134}$$

The above expression (Eq. 3.134) was simplified by dropping the $\mathbf{s}(\hat{p}_i)\bullet\mathbf{t}^1_{\cos}$ term because we are assuming $\mathrm{var}_{\kappa m}(\hat{p}_i)_0$ (Eq. 3.132) is zero. Continuing on in a similar manner, if the leading error is third-order, the variance is

$$\mathrm{var}_{\kappa m}(\hat{p}_i)_3 = \frac{A^2}{1152}\left(\frac{\delta\omega}{\omega_o}\right)^2_{\kappa m}\left(\frac{\omega_n}{\omega_o}\right)^6\left(2\mathbf{s}(\hat{p}_i)\bullet\omega_o^3\mathbf{t}^3_{\sin} - \mathbf{s}(\hat{p}_i)\bullet\omega_o^4\mathbf{t}^4_{\cos}\right)^2. \tag{3.135}$$

One feature that stands out about the above errors and variances is that they increase with oscillation amplitude. This makes sense since the variations in the fiber torsion constant directly affect the motion of the pendulum, and the larger the fundamental motion of the pendulum, the larger the effect will be. In order to reduce these errors, why doesn't one simply reduce the amplitude? Or better yet, don't let it oscillate at all? Then the effects would disappear altogether. This argument is valid, and it is one of the strongest reasons for using a non-oscillating deflection method, and if there were no other sources of noise to contend with, there would be no justification to pursue oscillating methods. However, as pointed out in Section 3.5, deflection methods are sensitive to low-frequency noise drifts in deflection to which the oscillating methods are much more immune. In pursuing an oscillating method, the question is whether the "price" of increased sensitivity to temperature drifts in the fiber is worth the "purchase" increased immunity to deflection drifts. At present, we feel that for the frequency method the answer is probably no whereas for the second harmonic method the answer is probably yes. The only way to find out for sure is to build the apparatus and see if it performs as expected; when pushing the performance of the instrument into uncharted territory, it is not easy to predict what systematic effect or noise process is going to be a "show stopper". Having made a tentative determination on which method is superior, that answer is not set in stone. Any new technology or clever idea can completely change the relative importance of the various noise processes requiring a new assessment of the various methods. The purpose of Section 3 has been to provide an exposition on the various, competing noise processes so that the reader can independently evaluate their relative importance.

In that spirit of full disclosure, what is the "price" the oscillating methods have to pay in increased sensitivity to temperature drifts? The frequency estimate of the 5-parameter fit is dominated by the zero-order error, and so its variance is

$$\frac{\mathrm{var}_{KT}(\hat{\omega})}{\omega_o^2} \equiv \frac{\mathrm{var}_{KT}(\hat{\omega})_0}{\omega_o^2} = \frac{A^2}{2\omega_o^2}\left(\frac{\delta\omega}{\omega_o}\right)_{KT}^2 \left(\mathbf{s}(\hat{\omega}) \bullet \omega_o \mathbf{t}^1_{\cos}\right)^2 = 0.500\left(\frac{\delta\omega}{\omega_o}\right)_{KT}^2$$

$$\frac{\mathrm{stddev}_{KT}(\hat{\omega})}{\omega_o} \equiv 0.707\left(\frac{\delta\omega}{\omega_o}\right)_{KT}. \tag{3.136}$$

Because $\mathbf{t}^1_{\cos}$ is directly related to $\partial\boldsymbol{\theta}/\partial\omega$,

$$\frac{\partial(A\sin(\omega t))}{\partial\omega} = At\cos(\omega t) \quad \Rightarrow \quad \frac{\partial\boldsymbol{\theta}}{\partial\omega} = A\mathbf{t}^1_{\cos}, \tag{3.137}$$

the variance in Equation 3.136 is not specific to the 5-parameter fit; any method which fits for the frequency will get the same result,

$$\frac{A^2}{2\omega_o^2}\left(\mathbf{s}(\hat{\omega}) \bullet \omega_o \mathbf{t}^1_{\cos}\right)^2 = \frac{A^2}{2\omega_o^2}\left(\mathbf{s}(\hat{\omega}) \bullet \frac{\omega_o}{A}\frac{\partial\boldsymbol{\theta}}{\partial\omega}\right)^2 = \frac{1}{2}\left(\mathbf{s}(\hat{\omega}) \bullet \frac{\partial\boldsymbol{\theta}}{\partial\omega}\right)^2 = \frac{1}{2}. \tag{3.138}$$

Thus, there is no modification to the frequency fit that can decrease the error. This situation is analogous to Section 3.5 where

$$\mathrm{var}_n(\hat{C}) = \frac{\theta_n^2}{2}\left(\mathbf{s}(\hat{C}) \bullet \mathbf{t}^0\right)^2 = \frac{\theta_n^2}{2}\left(\mathbf{s}(\hat{C}) \bullet \frac{\partial\boldsymbol{\theta}}{\partial C}\right)^2 = \frac{\theta_n^2}{2} \tag{3.139}$$

regardless of the fit method used to determine the offset, C. There is a qualitative difference between noise processes that physically alter the signal parameter, which therefore can not be filtered out, and those that merely contaminate the fit and can be filtered out with an appropriate modification of the fit

method. For the 10-parameter fit, the frequency noise is of the latter, "contamination" variety, and in fact, the orthnormality condition and Equation 3.137 ensure that the zero-order variance of the second harmonic estimate,

$$\mathrm{var}_{KM}\left(\hat{A}_2\right)_0 = \frac{A^2}{2}\left(\frac{\delta\omega}{\omega_o}\right)_{KM}^2\left(\mathbf{s}\left(\hat{A}_2\right)\bullet\frac{\omega_o}{A}\frac{\partial\boldsymbol{\theta}}{\partial\omega}\right)^2 = 0, \tag{3.140}$$

is zero. The second harmonic variance,

$$\begin{aligned}\mathrm{var}_{KM}\left(\hat{A}_2\right) &\equiv \mathrm{var}_{KM}\left(\hat{A}_2\right)_1 \\ &= \frac{A^2}{8}\left(\frac{\delta\omega}{\omega_o}\right)_{KM}^2\left(\frac{\omega_n}{\omega_o}\right)^2\left(\mathbf{s}\left(\hat{A}_2\right)\bullet\omega_o\mathbf{t}^1_{\sin} - \mathbf{s}\left(\hat{A}_2\right)\bullet\omega_o^2\mathbf{t}^2_{\cos}\right)^2 \\ &= 1.93\left(\frac{\delta\omega}{\omega_o}\right)_{KM}^2\left(\frac{\omega_n}{\omega_o}\right)^2\end{aligned}$$

$$\mathrm{stddev}_{KM}\left(\hat{A}_2\right) \equiv 1.39\left(\frac{\delta\omega}{\omega_o}\right)_{KM}\left(\frac{\omega_n}{\omega_o}\right), \tag{3.141}$$

is dominated by the first-order error. This is a definite improvement over the frequency method, but typical values of $\left(\delta\omega/\omega_o\right)_{KM} = 10^{-6}$ and $\left(\omega_n/\omega_o\right) = 1/200$ can still produce errors in $\hat{A}_2$ which are on the order of 10 nanoradians—still too large for us to be comfortable with.

To achieve higher-order immunity to frequency drifts, we average 121-type 10-parameter fits and 212-type 10-parameter fits, similar to what we did with the 5-parameter fits in Section 3.5. Let us define a "linear filter" second harmonic estimate as

$$\hat{A}_{2\ lf} = \left(\hat{A}_{2\,121}\left(t_{eq}=0\right) + \hat{A}_{2\,212}\left(t_{eq}=\pi/\omega_o\right)\right)/2. \tag{3.142}$$

The sampling function vector of this estimate, $\mathbf{s}\left(\hat{A}_{2lf}\right)$, is simply the average of the 121-type and 212-type sampling functions, and the variance of this averaged estimate,

$$\begin{aligned}\mathrm{var}_{km}\left(\hat{A}_{2lf}\right) &\equiv \mathrm{var}_{km}\left(\hat{A}_{2lf}\right)_2 \\ &= \frac{A^2}{288}\left(\frac{\delta\omega}{\omega_o}\right)_{km}^2\left(\frac{\omega_n}{\omega_o}\right)^4\left(3\mathbf{s}\left(\hat{A}_{2lf}\right)\bullet\omega_o^2\mathbf{t}_{\sin}^2 - 2\mathbf{s}\left(\hat{A}_{2lf}\right)\bullet\omega_o^3\mathbf{t}_{\cos}^3\right)^2 \\ &= 4.77\left(\frac{\delta\omega}{\omega_o}\right)_{km}^2\left(\frac{\omega_n}{\omega_o}\right)^4\end{aligned}$$

$$\mathrm{stddev}_{km}\left(\hat{A}_{2lf}\right) \equiv 2.18\left(\frac{\delta\omega}{\omega_o}\right)_{km}\left(\frac{\omega_n}{\omega_o}\right)^2, \tag{3.143}$$

is dominated by the second-order error rather than the first-order error. Because the slow drifts in frequency produce correlated errors in adjacent fits, we are using the same conservative assumption as in Section 3.5 that the errors do not decrease with integration, and therefore the variances in this section are not normalized to unit time for comparison to other methods. The "linear filter" average eliminates the first-order error because the error propagations of the 121-type and 212-type fits are equal and opposite to leading order. The sign of the error propagation changes as t_{eq} is incremented a half-period because the effect of the frequency variations are proportional to the amplitude of oscillation and the effective amplitude changes from 230 degrees for the 121-type fit to –230 degrees for the 212-type fit. If desired, this can be repeated to eliminate the second-order error of $\hat{A}_{lf}$. Define a "quadratic filter" second harmonic estimate as

$$\hat{A}_{2\ qf} = \left(\hat{A}_{2\ 121}\left(t_{eq}=0\right) + 2\hat{A}_{2\ 212}\left(t_{eq}=\pi/\omega_o\right) + \hat{A}_{2\ 121}\left(t_{eq}=2\pi/\omega_o\right)\right)/4. \tag{3.144}$$

The variance,

$$\begin{aligned}\mathrm{var}_{KM}\left(\hat{A}_{2qf}\right) &\equiv \mathrm{var}_{KM}\left(\hat{A}_{2qf}\right)_3 \\ &= \frac{A^2}{1152}\left(\frac{\delta\omega}{\omega_o}\right)_{KM}^2\left(\frac{\omega_n}{\omega_o}\right)^6\left(2\mathbf{s}\left(\hat{A}_{2qf}\right)\bullet\omega_o^3\mathbf{t}_{\sin}^3 - \mathbf{s}\left(\hat{A}_{2qf}\right)\bullet\omega_o^4\mathbf{t}_{\cos}^4\right)^2 \\ &= 11.77\left(\frac{\delta\omega}{\omega_o}\right)_{KM}^2\left(\frac{\omega_n}{\omega_o}\right)^6\end{aligned}$$

$$\mathrm{stddev}_{KM}\left(\hat{A}_{2qf}\right) \equiv 3.43\left(\frac{\delta\omega}{\omega_o}\right)_{KM}\left(\frac{\omega_n}{\omega_o}\right)^3, \tag{3.145}$$

is then dominated by the third-order error. In theory, this can be repeated to provide immunity to an arbitrarily high order, but at some point, signal-to-noise will suffer as one becomes limited by some other noise process such as "white" noise. At present, we feel that the "linear filter" average provides sufficient immunity to slow frequency drifts for our experiment at Index, and so we have not implemented the "quadratic filter" average in our data analysis.

The signal-to-noise ratios for the methods discussed here in Section 3.6 are

$$(S/N)_{KM}[\omega] = (0.447)\frac{|U_{ext}|}{\kappa_o(\delta\omega/\omega_o)_{KM}}, \tag{3.146}$$

$$(S/N)_{KM}[A_2] = (0.173)\frac{|U_{ext}|}{\kappa_o(\delta\omega/\omega_o)_{KM}}\left(\frac{\omega_o}{\omega_n}\right), \tag{3.147}$$

$$(S/N)_{KM}\left[A_{2lf}\right] = (0.110)\frac{|U_{ext}|}{\kappa_o(\delta\omega/\omega_o)_{KM}}\left(\frac{\omega_o}{\omega_n}\right)^2, \text{ and} \tag{3.148}$$

$$(S/N)_{km}\left[A_{2qf}\right] = (0.092)\frac{|U_{ext}|}{\kappa_o(\delta\omega/\omega_o)_{km}}\left(\frac{\omega_o}{\omega_n}\right)^3. \tag{3.149}$$

As was the case for the deflection method in Section 3.5, the poor signal-to noise of the frequency method can be improved by physically modulating the signal although only for noise frequencies below the modulation frequency. The second harmonic methods can also be improved in the same manner, however, and so ratios of the above signal-to-noise ratios,

$$\frac{(S/N)_{km}[\omega]}{(S/N)_{km}\left[A_{2lf}\right]} = 4.06\left(\frac{\omega_n}{\omega_o}\right)^2, \tag{3.150}$$

$$\frac{(S/N)_{km}[A_2]}{(S/N)_{km}\left[A_{2lf}\right]} = 1.57\left(\frac{\omega_n}{\omega_o}\right), \text{ and} \tag{3.151}$$

$$\frac{(S/N)_{km}\left[A_{2qf}\right]}{(S/N)_{km}\left[A_{2lf}\right]} = 0.84\left(\frac{\omega_o}{\omega_n}\right), \tag{3.152}$$

are a fair comparison of the methods. The signal-to-noise of each method is compared to that of the A_{2lf} estimate because that is the method we are presently using.

4 Systematic Error Theory

4.1 Fiber Non-Linearities

Having discussed the error propagation of random noise processes in Section 3, Section 4 will discuss the error propagation of systematic effects which produce reproducible errors. Since these systematic effect don't vary, they can be potentially more limiting than noise processes to an experiment's performance because no amount of integration will reduce their effect, and they are more easy to mistake for a constant signal.

For the deflection method, tilt in the fiber support can create a false deflection. For the frequency method, a change in fiber temperature can create a false change the frequency of oscillation. For the second harmonic method, what besides an external torque can create a second harmonic component to the pendulum motion? It is the non-linear behavior of the torsion fiber. For an external potential, which is periodic every 360 degrees, an oscillation amplitude of $A = 230°$ is considered "large", and a power series expansion in A does not converge quickly. The results Section 2.2 were therefore expressed in closed form in terms of Bessel functions. For a torsion fiber with a typical diameter-to-length ratio of $1/10^5$, however, an amplitude of $A = 230° \approx 4$ radians results in shear stresses in the fiber of only a few parts in 10^5. Thus the amplitude is "small", and one would expect a power series expansion to leading order in A to be a very good approximation.

The first anharmonic term in a power series expansion is the cubic term in the fiber potential energy,

$$U_{fiber}(\theta-\phi)=\frac{\kappa}{2}(\theta-\phi)^2+\lambda_3(\theta-\phi)^3. \tag{4.1}$$

As in Section 2, θ is the angular position in the lab frame, and ϕ is equilibrium position which changes whenever the fiber support point is rotated to a new azimuth. For simplicity, damping and any external potential energy are neglected in this derivation. To leading order, the anharmonic potential causes a small deflection, C, from the natural equilibrium position, ϕ, and a second harmonic amplitude, A_2. That is,

$$\theta(t)=\phi+A\sin\left(\omega_o\left(t-t_{eq}\right)\right)+A_2\cos\left(2\omega_o\left(t-t_{eq}\right)\right)+C, \tag{4.2}$$

where, to first order in λ_3,

$$A_2=-\frac{\lambda_3}{2\kappa}A^2 \quad \text{and} \qquad C=-\frac{3\lambda_3}{2\kappa}A^2. \tag{4.3}$$

Note that A_2 is independent of ϕ, and although λ_3 produces a second harmonic amplitude, it is the same at each fiber support position so there is no sinusoidal variation in $A_2(\phi)$ to produce a false signal provided that the oscillation amplitude, A, is the same for each fiber support position for which data is taken. But, if there is a variation in A when the fiber support is moved to different positions, particularly if it is a reproducible function of ϕ, then raw estimates of A_2 will show some false sinusoidal variation. To prevent this, the extremely precise estimates of A from the 10-parameter fit and the known A^2 dependence of A_2 should be used to normalize all the raw estimates of A_2 to the same nominal value of A before looking for any sinusoidal variation in $A_2(\phi)$.

This amplitude correction scheme becomes more complicated if the experiment is not a true null experiment. Ideally, one would like $|U_{ext}|=0$ if only

Newtonian gravity is present, but often it is difficult to physically remove all external torques on the pendulum. In that case, one tries the next best approach which is to take data in two different configurations where the systematic torques have opposite signs and then the systematic error can be subtracted away from the signal. However, since the second harmonic amplitude from an external potential energy has a $J_2(A)$ variation whereas the second harmonic amplitude from the fiber non-linearity has an A^2 dependence, the proper amplitude normalization of A_2 is more complex than the simple A^2 normalization described above. In fact, it requires a global fit to the entire data set to properly disentangle the effects. In addition, as will be described in Section 4.3, an external potential energy, $U_{ext}(\theta)$, that has a $\cos(m\theta)$ or $\sin(m\theta)$ dependence will have a $J_2(mA)$ amplitude dependence, further complicating the situation. The data analysis methods subsequent to the basic 10-parameter fit that correct for all these various amplitude induced variations will be discussed in more detail in Section 5.3.

Although the amplitude dependence of A_2 complicates the data analysis, it does not pose a real limitation to extracting the signal. A more fundamental problem would be variations in A_2 caused by slow, random, temporal drifts in the value of λ_3. These variations would go straight into signal, and since they physically alter the second harmonic, there would be no way improve the fit method to make it more immune. This is analogous to slow drifts in deflection for a deflection method (see Section 3.5) or slow drifts in frequency for a frequency method (see Section 3.6). The similarity, however, is only qualitative rather that quantitative. For the Index IV apparatus, we observe a fiber-induced second harmonic amplitude of 1 microradian or less at $A = 230°$, and

we have not observed any perceptible dependence on temperature variation or tilt of the fiber support. For comparison, the temperature coefficient of our Index IV fibers is a fractional change in frequency of $2\times10^{-4}/°C$ and the Eot-Wash group (Su et al. 1994) has reported typical tilt coefficients of 0.05 radian torsional deflection/radian of fiber support tilt. Thus, the temperature and tilt-induced variations in our second harmonic signal are several orders of magnitude below the other methods. We do observe a slow, constant, increase in A_2 with time, and we believe this results from some work hardening or slow relaxation process in the fiber. It may be related to the process that creates the constant linear drift in deflection after the pendulum is hung. The values of ω and γ also show a slow, secular drift. Similar to the linear drift in deflection, though, the linear drift in the second harmonic is easy to filter out because it occurs on time scales of weeks and months rather than hours. In fact, it is a much smaller problem because the drift in A_2 is on the order of 1 microradian/month whereas the drift in deflection is on the order of 1 microradian/hour.

After the cubic anharmonic term, the next term is the quartic term in the fiber potential energy,

$$U_{fiber}(\theta-\phi)=\frac{\kappa}{2}(\theta-\phi)^2+\lambda_4(\theta-\phi)^4. \tag{4.4}$$

We consider it independently of the cubic term because to first-order in λ_3 and λ_4 the effects are additive. To leading order, the quartic term produces a shift in oscillation frequency, $\Delta\omega=\omega-\omega_o$, and a third harmonic amplitude, B_3. That is,

$$\theta(t)=\phi+A\sin\Big((\omega_o+\Delta\omega)\big(t-t_{eq}\big)\Big)+B_3\sin\Big(3(\omega_o+\Delta\omega)\big(t-t_{eq}\big)\Big), \tag{4.5}$$

where, to first order in λ_4,

$$\frac{\Delta\omega}{\omega_o} = \frac{3\lambda_4}{2\kappa}A^2 \quad \text{and} \qquad B_3 = -\frac{\lambda_4}{8\kappa}A^3. \tag{4.6}$$

From a naïve, mathematical perspective, one would expect the second harmonic, $A_2 \propto A^2$, to be larger than the third harmonic, $B_3 \propto A^3$, because the shear stresses in the fiber are so small, but that ignores the physical difference between odd and even potential energy terms. Odd terms, such as $\lambda_3(\theta-\phi)^3$, break the left/right handed helicity symmetry of the fiber, and they would not be present in a "perfect" fiber with no internal stress. We know from the observed second harmonic and the linear drift in deflection that real fibers do have a particular handedness, but that is a remnant of the extrusion process in their manufacture. The even terms, such as $\lambda_4(\theta-\phi)^4$, result from the fundamental, non-linear, bulk properties of the fiber material, and therefore tend to be larger than the incidental odd terms. At Index, we observe the third harmonic amplitude to be several microradians, which is large enough to justify the inclusion of B_3 in the 10-parameter fit. Since the third harmonic motion is odd about t_{eq} and the second harmonic motion is even about t_{eq}, the "white" noise error in A_2 is uncorrelated with that of B_3, and so the inclusion of B_3 is "free" and does not reduce the signal-to-noise of the second harmonic signal.

The fourth and higher harmonics due to fiber non-linearites are of negligible amplitude for $A = 230° \approx 4$ radians. This has been empirically verified by Newman's group at UC Irvine (Bantel & Newman 1998), who has looked at the higher harmonic motions for oscillation amplitudes up to 100 radians using beryllium-copper fibers. They also verified that A_2 follows an A^2 dependence up to $A = 100$ radians. The fourth and higher harmonics from the external poten-

tial energy, $U_{ext}(\theta)$, are not necessarily negligible, and their error propagation will be discussed in Section 4.3. The magnitudes of the higher harmonics due to $U_{ext}(\theta)$ are directly related to the observed $A_2(\phi)$ and $B_3(\phi)$, and with proper modeling their effects can be subtracted without adding additional degrees of freedom to the fit. These data analysis methods are explained in detail in Section 5.3.

As a last note, the A^2 amplitude dependence of the frequency shift, $\Delta\omega$, in Equation 4.6 is not the amplitude dependence actually observed. Although the $\Delta\omega$ from the quartic term, $\lambda_4(\theta-\phi)^4$, is present, it is dominated by another process with a $\Delta\omega \propto |A|$ dependence. The damping constant, γ, also displays an $|A|$ dependence. Our group had observed this several years ago, and we were unable to determine what sort of process could produce such non-analytic behavior. We had observed that the effect is larger in tungsten fibers than it is in beryllium-copper fibers, and being somewhat nervous about this unexplained phenomenon, we opted to use beryllium-copper fibers in our Index IV apparatus. Later, a student of Peter Saulson (Huang & Saulson 1998) developed a toy mathematical model of blocks connected by springs sliding on a surface with Coulomb friction that produced an $|A|$ dependence in $\Delta\omega$ and γ. This conjecture is consistent with the fibrous structure of tungsten fiber which would have more internal sliding friction than beryllium-copper. Newman's group has observed this process in their very large amplitude studies, and from the higher harmonics it produces, they have even been able to reconstruct the hysterisis loop in the shear stress-strain plot of the material. For our second harmonic method, however, their most important finding is that this non-analytic friction process does not appear to affect the A^2 dependence of A_2.

4.2 Fiber Relaxation Transients

At the vacuum in which we oscillate the torsional pendulum in the Index IV apparatus, about 10^{-6} torr, the damping of the oscillation motion is due primarily to internal fiber losses rather than air friction on the pendulum. Although, as mentioned in Section 4.1, there is tiny portion of the fiber damping which is non-linear and non-analytic, the vast majority of the fiber damping is perfectly linear at the amplitudes that we oscillate the pendulum. However, this "perfectly linear" damping is more complex than a simple mass-spring-dashpot system, and it can produce relaxation transients whenever the free oscillation of the pendulum is disturbed by rotating the fiber support to a new position. In Figure 4.1, 10-parameter fit estimates of the offset, C, are plotted versus the number of oscillation periods elapsed since the fiber support was rotated to a new position. These fits are to a sample of actual data taken from the Index IV apparatus with an oscillation amplitude of $A = 230° \approx 4$ radians.

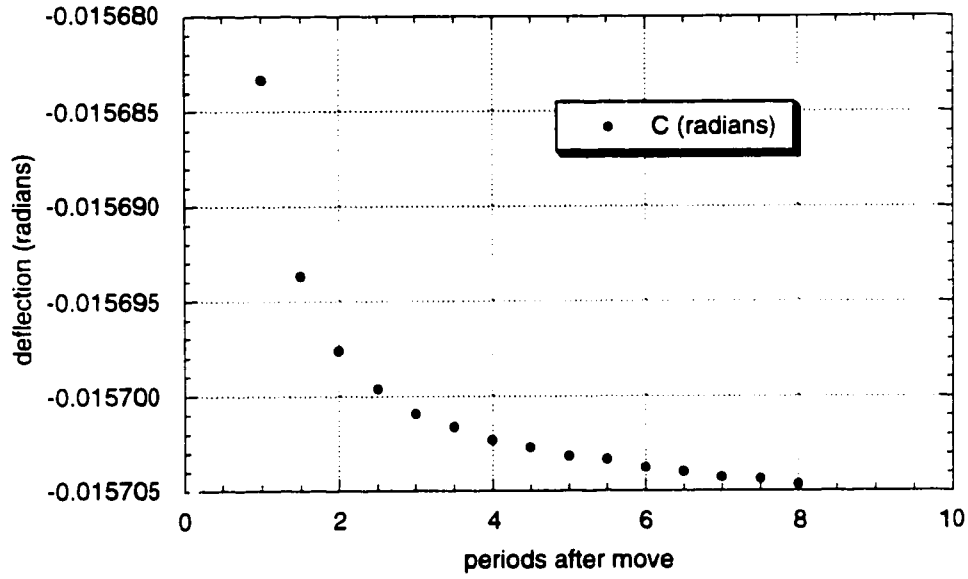

Figure 4.1. A sample relaxation transient of the fiber induced by rotating the support point to a new position. Single-period estimates of the offset are plotted versus the time elapsed after the end of the move.

The fits that are an integer number of periods after the end of the move are 121-type fits whereas the fits that are half-integer number of periods after the end of the move are 212-type fits. Looking at the tail end of the fits, one can see the fiber settling down into a constant rate of unwinding. One can also just barely perceive the "bouncing up and down" of the estimates caused by the linear drift in frequency which propagates with opposites signs into the 121-type and 212-type fits. This is similar to the effect of the linear drift in frequency on the 10-parameter fit estimate of the second harmonic discussed in Section 3.6. However, the most noticeable feature in Figure 4.1 is the exponentially decaying transient, whose initial amplitude is about 2×10^{-5} radians. This kind of

transient is consistently reproduced each time the fiber support is rotated to a new position, and it results from excitations of slowly-relaxing internal degrees of freedom in the fiber.

To derive the effect of these internal degrees of freedom, let us start with just a single internal degree of freedom. Figure 4.2 depicts a mass suspended by a vertical, linear spring in parallel with a smaller spring-and-dashpot combination that is commonly referred to as a Maxwell unit in elasticity theory. This spring-mass oscillator provides a visually simpler presentation of the Maxwell unit than a torsion pendulum does.

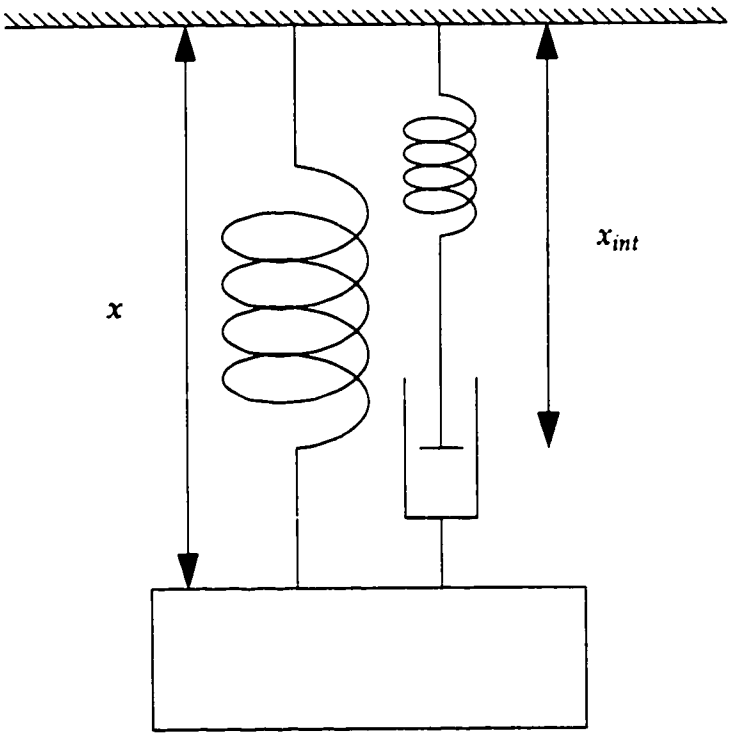

Figure 4.2. Linear, vertical spring-mass system with a single, internal degree of freedom modeled as a Maxwell unit, an elastic and a resistive element in series. The Maxwell unit has a characteristic relaxation time, τ_{int}.

The function, $x(t)$, describes the observed motion of the pendulum mass while $x_{int}(t)$ describes the time evolution of an "invisible" internal degree of freedom with no inertia. This is only a toy mathematical model, and so in reality $x_{int}(t)$ need not describe a displacement as $x(t)$ does. For example, $x_{int}(t)$ could be a temperature if the relaxation process were thermo-elastic. The main spring has a spring constant, k_o, and in the absence of the Maxwell unit, the nominal oscillation frequency is $\omega_o = (k_o/m)^{1/2}$. The spring constant of the internal spring in the Maxwell unit, k_{int}, is assumed to be much smaller than k_o, and so results in this section are only calculated to first-order in k_{int}/k_o. The frictional force in the dashpot is directly proportional to velocity, and its strength is usually expressed in terms of a friction constant, b_{int},

$$F_{fr} = -b_{int}(\dot{x}_{int} - \dot{x}) = -\tau_{int}k_{int}(\dot{x}_{int} - \dot{x}), \tag{4.7}$$

but for our purposes, it is more convenient to express b_{int} as the product of the spring constant, k_{int}, and a characteristic time, τ_{int}. The equations of motion are therefore

$$\left.\begin{aligned} m\ddot{x} &= -k_o x - \tau_{int}k_{int}(\dot{x} - \dot{x}_{int}) \\ 0 &= -k_{int}x_{int} - \tau_{int}k_{int}(\dot{x}_{int} - \dot{x}) \end{aligned}\right\} \Rightarrow \left\{\begin{aligned} \ddot{x} &= -\omega_o^2 x - \left(\frac{k_{int}}{k_o}\right)\omega_o^2\tau_{int}(\dot{x} - \dot{x}_{int}) \\ 0 &= -x_{int} - \tau_{int}(\dot{x}_{int} - \dot{x}). \end{aligned}\right. \tag{4.8}$$

First, let us look at the limit as $k_{int} \to 0$, but instead of keeping b_{int} constant, let us increase $b_{int} \to \infty$ so that $\tau_{int} = \text{constant}$. In this zero-coupling limit, the motion of the mass,

$$x_o(t) = B\sin(\omega_o t), \tag{4.9}$$

is a simple, undamped sine wave unaffected by the Maxwell unit. Here, the amplitude of oscillation, B, can assume any value, and for simplicity, the phase has been chosen so that there is no $\cos(\omega_o t)$ component. The motion of the internal degree of freedom,

$$x_{int}(t) = A_{int}\cos(\omega_o t) + B_{int}\sin(\omega_o t) + C_{int}\exp(-t/\tau_{int}) \tag{4.10}$$

includes both oscillatory and exponentially-decaying components in the zero-coupling limit, and somewhat surprisingly, the quadrature amplitudes of the oscillatory component,

$$A_{int} = -\frac{\omega_o \tau_{int}}{1+\omega_o^2\tau_{int}^2}B \quad \text{and} \qquad B_{int} = \frac{1}{1+\omega_o^2\tau_{int}^2}B, \tag{4.11}$$

have a well-defined zero-coupling limit which is independent of k_{int} and depends only on B and the dimensionless quantity $\omega_o\tau_{int}$. The exponential amplitude, C_{int}, is independent of B and can assume any value. With no external disturbance, the exponential component will die away with time, and only the oscillatory component will remain.

Next, let us look at the weak-coupling limit when k_{int} is small but non-zero. The motion of the mass is altered by its coupling to oscillatory and exponential components of $x_{int}(t)$. Specifically, the oscillation becomes lightly damped, the oscillation frequency is shifted from its nominal value, and the pendulum motion acquires a small exponential component, or mathematically,

$$x(t) = B\exp(-\gamma t)\sin\big((\omega_o + \Delta\omega)t\big) + C\exp(-t/\tau_{int}). \tag{4.12}$$

When Equations 4.8 are solved to first order in k_{int}/k_o, one gets,

$$\frac{\Delta\omega}{\omega_o} = \frac{1}{2}\left(\frac{k_{int}}{k_o}\right)\frac{\omega_o^2\tau_{int}^2}{1+\omega_o^2\tau_{int}^2}, \tag{4.13}$$

$$\frac{\gamma}{\omega_o} = \frac{1}{2}\left(\frac{k_{int}}{k_o}\right)\frac{\omega_o\tau_{int}}{1+\omega_o^2\tau_{int}^2}, \text{ and} \tag{4.14}$$

$$C = \left(\frac{k_{int}}{k_o}\right)\frac{\omega_o^2\tau_{int}^2}{1+\omega_o^2\tau_{int}^2}C_{int}. \tag{4.15}$$

There are also first-order shifts in A_{int}, B_{int}, and τ_{int}, but these are not important to the following discussion.

The frequency shift, $\Delta\omega$, for a given k_{int} is plotted versus $\log_{10}(\omega_o\tau_{int})$ in Figure 4.3.

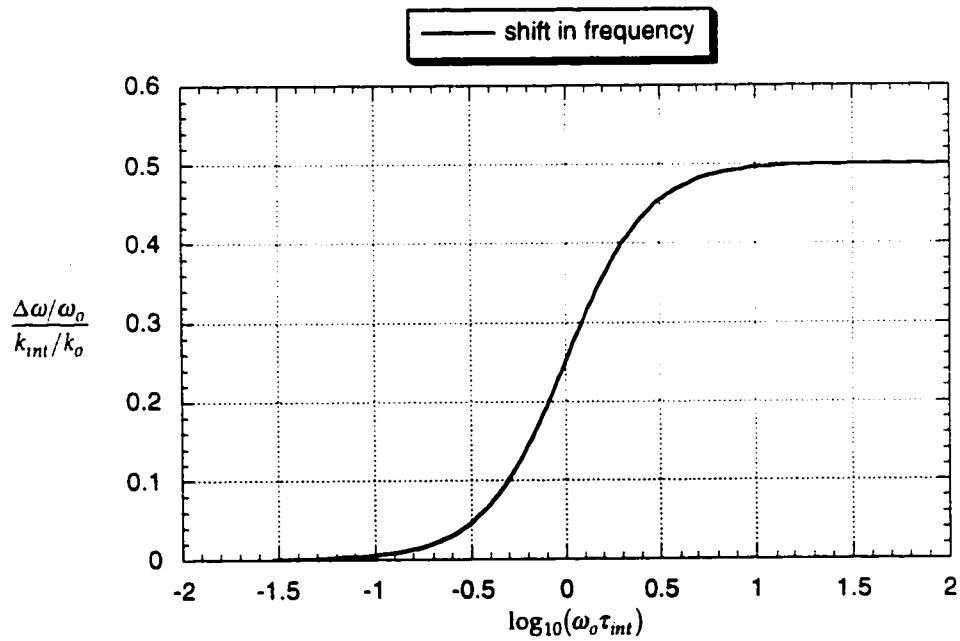

Figure 4.3. First-order frequency shift, $\Delta\omega$, is plotted versus relaxation time for an oscillator with a single Maxwell unit.

Qualitatively, Figure 4.3 is easy to understand. In the short τ_{int} regime where the dashpot is weak, the small spring is hardly compressed at all and $\omega = (k_o/m)^{1/2} = \omega_o$ whereas as $\tau_{int} \to \infty$, the dashpot becomes increasingly viscous until both springs are compressed in parallel and $\omega = ((k_o + k_{int})/m)^{1/2} \equiv \omega_o + 0.5(k_{int}/k_o)\omega_o$. For a thermo-elastic relaxation process, the change in frequency around $\tau_{int} = \omega_o$ corresponds to the transition from the isothermal regime to the adiabatic regime. Figure 4.4 displays the damping constant, γ, for a given k_{int} versus $\log_{10}(\omega_o \tau_{int})$.

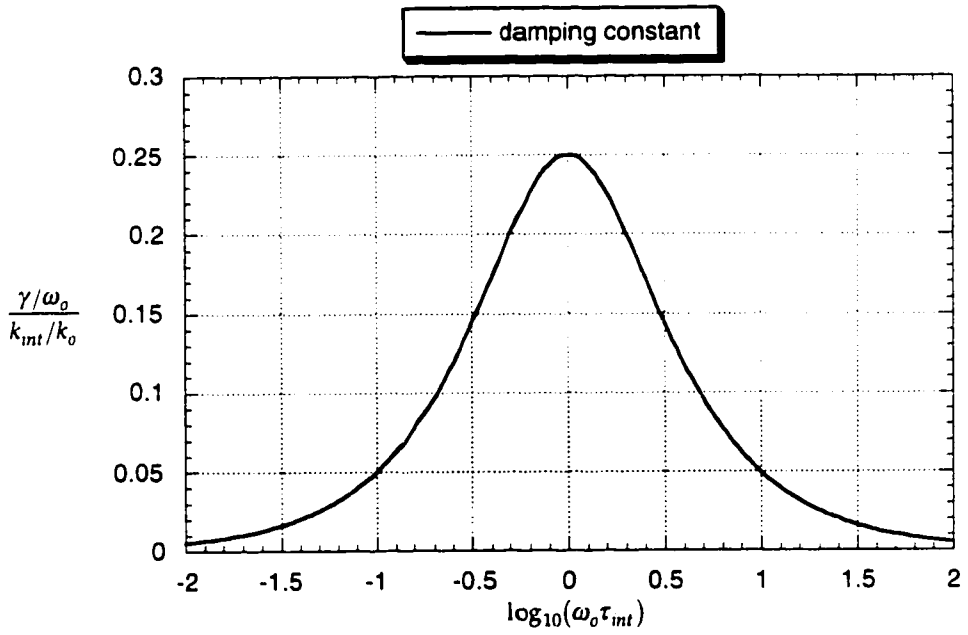

Figure 4.4. First-order damping constant, γ, is plotted versus relaxation time for an oscillator with a single Maxwell unit.

The power dissipation being proportional to the product of the dashpot's velocity and frictional force, the damping constant is small in the short τ_{int} regime because there is very little frictional force in the dashpot whereas the damping

constant is small in the long τ_{int} regime because there is very little motion in the dashpot. Thus, only for τ_{int} around ω_o can the force-velocity product become large enough to produce significant losses. For the thermo-elastic example, both isothermal and adiabatic oscillations are reversible, quasi-static processes, and it is only for τ_{int} around ω_o that there is appreciable amount of irreversible heat transfer.

The most direct evidence of the internal degree of freedom is the exponential component of the pendulum motion, $C\exp(-t/\tau_{int})$. Unlike $\Delta\omega$ and γ, whose magnitude is well-determined, C can assume any arbitrary magnitude depending on the value of C_{int}. However, what can be well specified is, ΔC_{move}, the change in C excited by moving the support point. Specifically, we are concerned about the effect of a vertical, constant-speed move that displaces the support point a distance, Δx_{move}, at a speed of $\dot{x}_{move}$. Because of Gallilean invariance, the same equations of motion apply during the constant-speed move as when the support is stationary, and so by matching boundary conditions at the beginning and and of the move, one gets

$$\Delta C_{move} = -\left(\frac{k_{int}}{k_o}\right)\frac{\dot{x}_{move}}{\omega_o}\left(1-\exp\left(-\frac{\Delta x_{move}}{\dot{x}_{move}\tau}\right)\right)\frac{2\omega_o^3\tau_{int}^3}{\left(1+\omega_o^2\tau_{int}^2\right)^2}. \tag{4.16}$$

This change in C is the same regardless of the phase of oscillation at which the move begins. Using Equation 4.14, k_{int}/k_o can be replaced with γ/ω_o,

$$\Delta C_{move} = -\left(\frac{\gamma}{\omega_o}\right)\frac{\dot{x}_{move}}{\omega_o}\left(1-\exp\left(-\frac{\Delta x_{move}}{\dot{x}_{move}\tau}\right)\right)\frac{2\omega_o^2\tau_{int}^2}{1+\omega_o^2\tau_{int}^2}. \tag{4.17}$$

For numerical predictions, Equation 4.17 is more useful than Equation 4.16 because γ/ω_o can be determined by simple observation of the free oscillation

whereas *a priori* knowledge of the magnitude of k_{int}/k_o is more difficult to obtain. For us, an even more important quantity is the size of the exponential transient,

$$C_{move}(t_{wait}) = \Delta C_{move} \exp\left(-\frac{t_{wait}}{\tau_{int}}\right), \tag{4.18}$$

that remains after waiting a time, t_{wait}, after the end of the move.

With a substitution of $\Delta x_{move} \rightarrow \Delta\theta_{move}$ and $\dot{x}_{move} \rightarrow \dot{\theta}_{move}$, the above results can be applied to a constant-rotational-speed move of the fiber support of our Index IV torsion pendulum. A typical move is $\Delta\theta_{move} = -225$ degrees (the minus sign signifies a clockwise rotation viewed from above) and $\dot{\theta}_{move} = -230 \text{ degrees} \times \omega_o$. The speed of the move is chosen to match the maximum speed of the pendulum as it passed through its equilibrium position. The ratio γ/ω_o for our oscillator is about 1/8000. For these values and assuming just a single Maxwell unit, the size of the transient, ΔC_{move}, is plotted as funtion of $\log(\omega_o \tau_{int})$ in Figure 4.5. For comparison, the size of the transient after one period of oscillation, $C_{move}(t_{wait} = 2\pi/\omega_o)$, is also plotted.

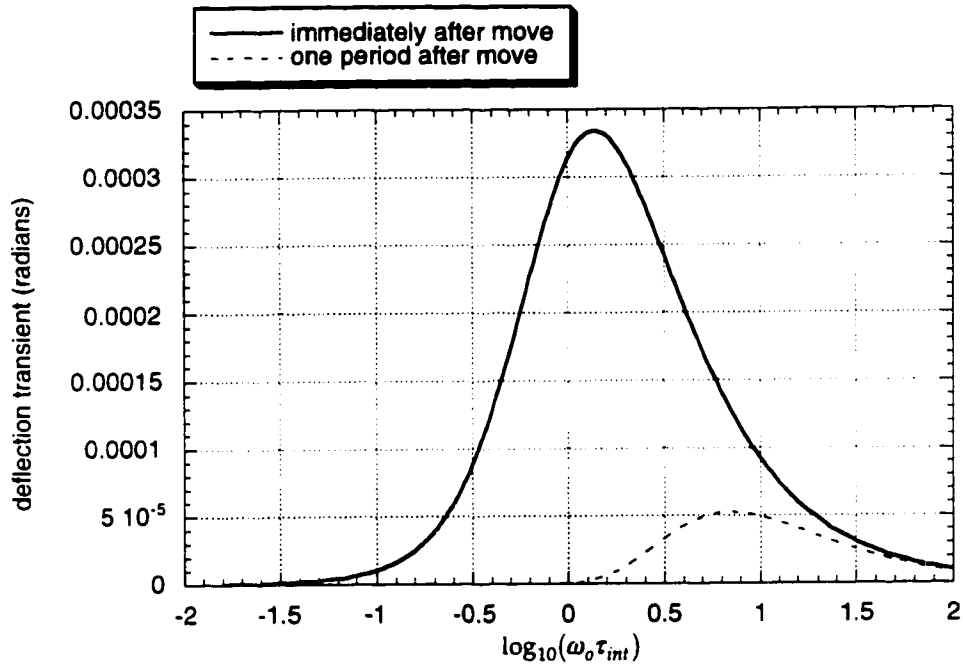

Figure 4.5. Predicted size of move-induced transient, ΔC_{move}, for our Index IV experiment assuming a single Maxwell unit of relaxation time, τ_{int}. The solid line is the size immediately after the move, the dashed line is one period after the move.

For a single Maxwell unit, ΔC_{move} can be as large as 3×10^{-4} radians depending on the value of τ_{int}. In reality, there is not a single Maxwell unit but a whole spectrum Maxwell units with different k_{int}'s and τ_{int}'s, and their contributions to γ and ΔC_{move} are additive to first-order. Since the contributions to γ must sum up to $\omega_o/8000$, the actual ΔC_{move} must be some weighted average of the values in Figure 4.5 and therefore is somewhere between 0 and 3×10^{-4} radians. Without a more detailed knowledge of the Maxwell unit spectrum, a more precise prediction can not be made. The first empirical measurement of C_{move} we can make is one period after the end of the move. From Figure 4.5, a value between 0 and 5×10^{-5} radians is predicted for $C_{move}(t_{wait} = 1 \text{ period})$. Looking

at the empircal estimates in Figure 4.1, one can see the actual value of $C_{move}(t_{wait} = 1 \text{ period})$ is about 2×10^{-5} radians. This is well within the range of expected values which gives one confidence that the Maxwell unit model provides an appropriate description of the observed transient.

Although we have described the transient, a magnitude of 2×10^{-5} radians is disturbingly large when one wants to measure parameters to nanoradian precision. Given that the transients die away exponentially, it would seem waiting a few more periods should significantly reduce the size of the transient. In the analysis of our data, we do in fact throw out the first 5 periods after each move. The predicted size of $C_{move}(t_{wait})$ for 1 through 6 periods after move is plotted in Figure 4.6.

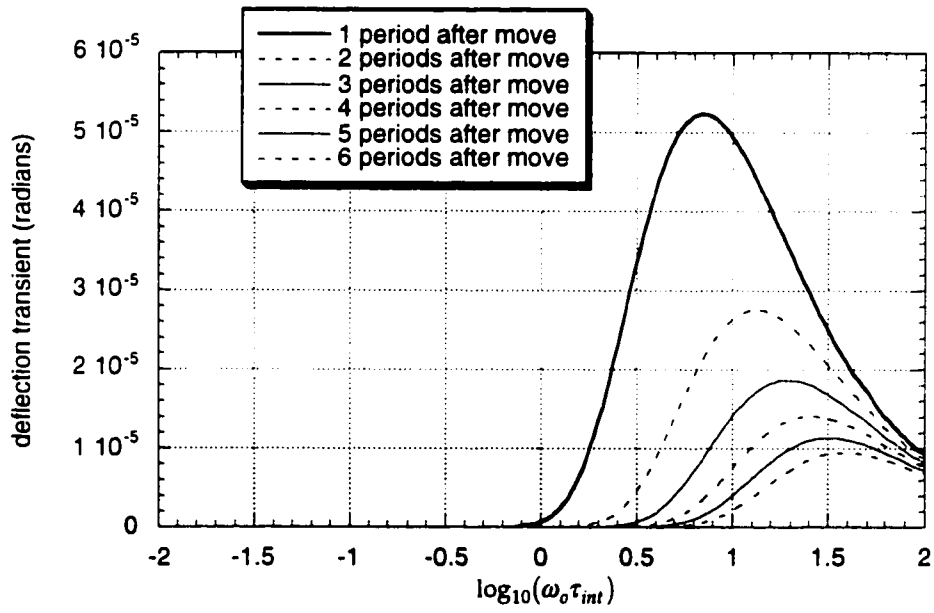

Figure 4.6. Decrease in size of move-induced transient with time for our Index IV experiment assuming a single Maxwell unit of relaxation time, τ_{int}. $C_{move}(t_{wait})$ is plotted for 1, 2, 3, 4, 5, and 6 periods after the end of the move.

The decrease in $C_{move}(t_{wait})$ is not as rapid as one might hope. Although the $C_{move}(t_{wait})$ for a particular value of τ_{int} dies away exponentially, the worst-case τ_{int} keeps increasing to larger values of τ_{int} that die away more slowly so that the worst-case $C_{move}(t_{wait})$ decreases as roughly $1/t_{wait}$. The actual $C_{move}(t_{wait})$ most likely does decrease much faster than the worst-case value, but without a more detailed of the knowledge of the Maxwell unit spectrum, one can not be sure.

However, we are less concerned with the size of $C_{move}(t_{wait})$ than we are with how it propagates into the estimates of the second harmonic, A_2. In Section 3.5, it was demonsrated that the quadratic drift in C produces the leading-order error in A_2 for low-frequency drifts. By relating the second time derivative of $C_{move}(t_{wait}) = \Delta C_{move} \exp(-t/\tau_{int})$ to the second time derivative's of $\sin(\omega_n t)$ and $\cos(\omega_n t)$ in Section 3.5, Equation 3.105 can be readily modified,

$$A_{2move}(t_{wait}) = \frac{0.135\sqrt{2}}{\omega_o^2 \tau_{int}^2} C_{move}(t_{wait}), \tag{4.19}$$

to express the move-induced error in the second harmonic, $A_{2move}(t_{wait})$, in terms of $C_{move}(t_{wait})$. The predicted $A_{2move}(t_{wait} = 1 \text{ period})$ for the Index IV pendulum is plotted in Figure 4.7.

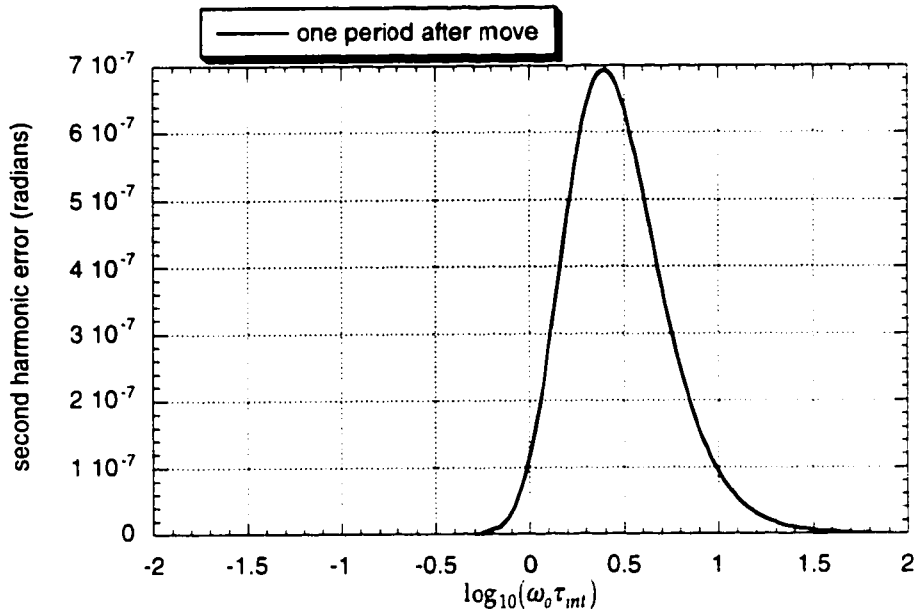

Figure 4.7. The predicted size of the move-induced error in the second harmonic estimate one period after the end of the move, $A_{2move}(t_{wait} = 1 \text{ period})$.

The worst-case $A_{2move}(t_{wait} = 1 \text{ period})$ of 7×10^{-7} radians is smaller than the worst-case $C_{move}(t_{wait} = 1 \text{ period})$ of 2×10^{-5} radians, and furthermore the contribution of longer τ_{int} exponentials is attenauted by a factor of $1/\omega_o^2 \tau_{int}^2$ because their second time deriavtives are proportionally smaller. Thus, one would expect that waiting more periods after the move produces a more dramatic decrease in the worst-case $A_{2move}(t_{wait})$ than for it does $C_{move}(t_{wait})$, and in fact the worst-case $A_{2move}(t_{wait})$ falls off as roughly $1/t_{wait}^3$. Since we throw away the first 5 periods of data after a move, the sixth period second harmonic estimate is the first used in our data analysis. The predicted size of $A_{2move}(t_{wait} = 6 \text{ period})$ is plotted in Figure 4.8.

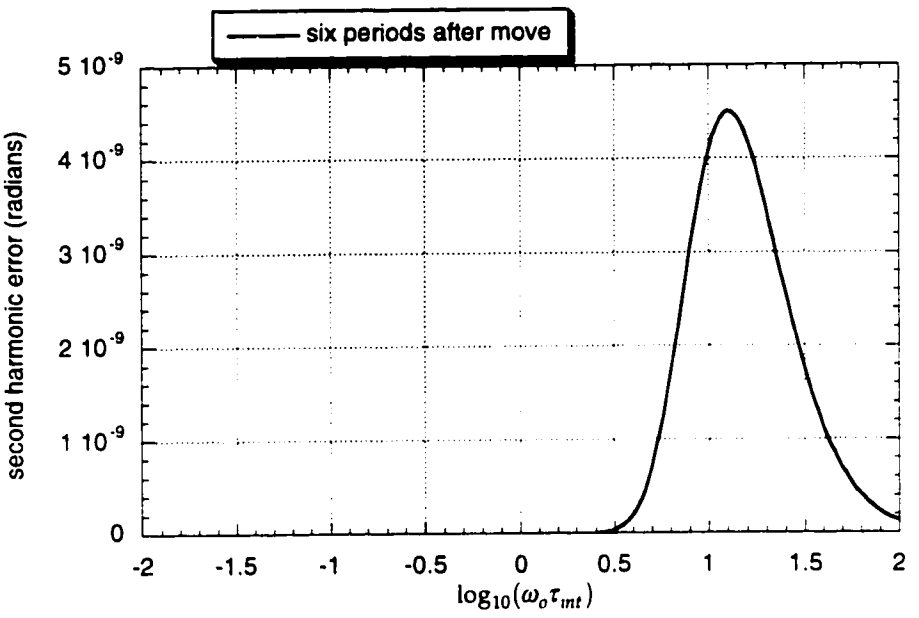

Figure 4.8. The predicted size of the move-induced error in the second harmonic estimate six periods after the end of the move, $A_{2move}(t_{wait} = 6 \text{ period})$. This is the first period used in the data anlysis for our Index IV experiment.

The worst-case $A_{2move}(t_{wait} = 6 \text{ period})$ is less than 5 nanoradians. This is larger than the sub-nanoradian signals we want to be able to detect, but it is only the variation in $A_{2move}(t_{wait} = 6 \text{ period})$ from one move to the next that can cause a false signal. Maintaining reproducibility of the move at the 1% level is not a very stringent requirement. We occaisonally have been plagued with the lubricant of the fiber support bushing causing a viscous recoil after moving the pendulum. This relaxation process is slower and less reproducible than the fiber relaxation processes, but it is also a less fundamental problem, resulting from sloppy experimental technique rather than from intrinsic properties of the fiber material.

A final comment on Maxwell-unit fiber relaxations and non-null frequency method experiments such as Luther and Towler's measurement of the gravitational constant, G (Luther & Towler 1984). Kuroda (Kuroda 1995) has noted that a Maxwell unit makes the torsion fiber constant frequency dependent. In a frequency method measurement, most of the change in frequency is produced by the external potential energy interaction, $U_{ext}(\theta)$, (see Section 2.2) but there will also be a small change due to the change in the torsion fiber constant as the pendulum oscillates at a different frequency. Kuroda has shown that if one naively ignores this small effect when calculating the strength of the signal, a percentage bias will result, which expressed in the notation of this section is

$$\%\text{bias} = \left(\frac{k_{int}}{k_o}\right)\frac{\omega_o^2\tau_{int}^2}{\left(1+\omega_o^2\tau_{int}^2\right)^2}. \tag{4.20}$$

Newman (Newman & Bantel 1999) has re-expressed this in terms of (γ/ω_o),

$$\%\text{bias} = \left(\frac{\gamma}{\omega_o}\right)\frac{2\omega_o\tau_{int}}{1+\omega_o^2\tau_{int}^2} \quad \Rightarrow \quad 0 \le \%\text{bias} \le (\gamma/\omega_o), \tag{4.21}$$

and thereby shown that the worst-case %bias for a distribution of Maxwell-units is (γ/ω_o). But what if one wants to push the precision beyond (γ/ω_o)? How can one determine the actual %bias for a particular fiber so that one can correct for it? Let us look at the first time derivative of the transient immediately after the move,

$$\Delta D_{move} = \left(\frac{\gamma}{\omega_o}\right)v_{move}\left(1-\exp\left(-\frac{\Delta x_{move}}{v_{move}\tau}\right)\right)\frac{2\omega_o\tau_{int}}{1+\omega_o^2\tau_{int}^2}. \tag{4.22}$$

If one takes the limit as $\Delta x_{move} \to \infty$, which corresponds to an infinitely long constant-speed move that allows all the Maxwell units to come into equilibrium, then when one stops it,

$$\Delta D_{move} = \left(\frac{\gamma}{\omega_o}\right) v_{move} \frac{2\omega_o \tau_{int}}{1+\omega_o^2 \tau_{int}^2}. \tag{4.23}$$

This is directly proportional to the %bias (Eq. 4.20) regardless of the value of γ, ω_o, or τ_{int}. Thus, even for a spectrum of Maxwell units,

$$\%\text{bias} = \lim_{\Delta x_{move} \to \infty} \left(\frac{\Delta D_{move}}{v_{move}}\right). \tag{4.24}$$

By measuring ΔD_{move} to just 1% accuracy, one can surpass the Kuroda effect accuracy limit by two orders of magnitude.

4.3 Higher Harmonics of Oscillation

The 10-parameter fit includes the parameters A_2 and B_3 to fit for the second and third harmonic amplitudes, but it does not include parameters to fit for the fourth or higher harmonic amplitudes even though the derivation in Section 2.2 demonstrated that an external sinusoidal potential produces those higher harmonics. What are the consequences of leaving those higher harmonics out of the 10-parameter model? To answer this, let's first review the notation used in Section 2.2. Neglecting damping and non-linearites of the fiber, the potential energy is

$$U(\theta) = U_{fiber}(\theta - \phi) + U_{ext}(\theta) = \frac{\kappa(\theta-\phi)^2}{2} + |U_{ext}|\cos(\theta - \psi). \tag{4.25}$$

In the derivation of Section 2.2, $t = 0$ was chosen to be a turning point of oscillation and all the harmonics of motion were cosine components, $\cos(n\omega t)$. Be-

cause the 10-parameter fits are centered on equilibrium crossings, the equilibrium crossing will be defined as $t = 0$ in this section. This changes the odd harmonics of motion from cosine to sine components so that Equation 2.24 becomes

$$\theta(t) = \phi + A\sin(\omega t) + C + \sum_{\substack{n=2 \\ \text{even}}}^{\infty} A_n \cos(n\omega t) + \sum_{\substack{n=3 \\ \text{odd}}}^{\infty} B_n \sin(n\omega t). \tag{4.26}$$

The frequency shift, $\omega = \omega_0 + \Delta\omega$, is not explicitly written out since it won't be important in this section's discussion. Using the convention of Equation 4.26, the amplitudes of the higher harmonics are

$$A_{n\,even}(\phi) = -\frac{2J_n(A)|U_{ext}|}{(n^2-1)\kappa}\sin(\phi - \psi) \tag{4.27}$$

for the even harmonics, and

$$B_{n\,odd}(\phi) = -\frac{2J_n(A)|U_{ext}|}{(n^2-1)\kappa}\cos(\phi - \psi) \tag{4.28}$$

for the odd harmonics where the arguments of the Bessel functions, $J_n(A)$, are expressed in radians. For an oscillation amplitude of $A = 230° = 4.014$ radians, the second through seventh harmonics are

$$A_2(\phi) = -0.240\frac{|U_{ext}|}{\kappa}\sin(\phi - \psi), \qquad B_3(\phi) = -0.108\frac{|U_{ext}|}{\kappa}\cos(\phi - \psi),$$

$$A_4(\phi) = -0.038\frac{|U_{ext}|}{\kappa}\sin(\phi - \psi), \qquad B_5(\phi) = -0.011\frac{|U_{ext}|}{\kappa}\cos(\phi - \psi), \tag{4.29}$$

$$A_6(\phi) = -0.003\frac{|U_{ext}|}{\kappa}\sin(\phi - \psi), \text{ and} \qquad B_7(\phi) = -0.001\frac{|U_{ext}|}{\kappa}\cos(\phi - \psi).$$

To determine the precise effect of the higher harmonics on the 10-parameter fit, we need not only their amplitudes but also their error propagation. Define the vectors of the higher harmonics evaluated at the 14 crossings of the 10-parameter fit as

$$\begin{aligned}\cos(n\omega_o\mathbf{t}) &= \{\cos(n\omega_o t_1), \cos(n\omega_o t_2), \ldots \cos(n\omega_o t_{14})\} \text{ and} \\ \sin(n\omega_o\mathbf{t}) &= \{\sin(n\omega_o t_1), \sin(n\omega_o t_2), \ldots \sin(n\omega_o t_{14})\}.\end{aligned} \tag{4.30}$$

We are primarily concerned with the error propagation into the estimate of the signal parameter, $\hat{A}_2$. The weighting function, $\mathbf{s}(\hat{A}_2)$, is even under time reversal whereas the odd harmonics are odd under time reversal, and so their contraction,

$$\mathbf{s}(\hat{A}_2) \bullet \sin(n_{odd}\omega_o\mathbf{t}) = 0, \tag{4.31}$$

is zero, and the odd harmonics do not propagate into $\hat{A}_2$. The error caused by the fourth and higher even harmonics,

$$\begin{aligned}\Delta\hat{A}_2(\phi) &= A_4(\phi)\mathbf{s}(\hat{A}_2) \bullet \cos(4\omega_o\mathbf{t}) + A_6(\phi)\mathbf{s}(\hat{A}_2) \bullet \cos(6\omega_o\mathbf{t}) + \ldots \\ &= \frac{0.038}{0.240} A_2(\phi)(-1.206) + \frac{0.003}{0.240} A_2(\phi)(-0.409) + \ldots \\ &= -0.196 A_2(\phi),\end{aligned} \tag{4.32}$$

is directly proportional to the signal, $A_2(\phi)$, and therefore effectively reduces the signal by about 20%. This means that all the signal-to-noise ratios calculated in Section 3 for the second harmonic method are 20% too high because they assumed a signal strength of $|A_2(\phi)| = 0.240|U_{ext}|/\kappa$ whereas the measured value is $|A_2(\phi)|_{meas} = 0.193|U_{ext}|/\kappa$. These coefficients are valid only for the nominal oscillation amplitude of $A = 230° = 4.014$ radians. If the amplitude is some other value, then both the ratios $A_n(\phi)/A_2(\phi)$ and the scalar products

$\mathbf{s}(\hat{A}_2) \bullet \cos(n\omega_o \mathbf{t})$ in Equation 4.32 need to be re-evaluated at that amplitude. This makes the effective amplitude dependence of $|A_2(\phi)|_{meas}$ different from the $J_2(A)$ amplitude dependence of $|A_2(\phi)|$.

The above presentation has assumed that the external potential energy, $U_{ext}(\theta)$, is a simple sinusoidal function of θ, the form which the CDF signal would take. In general, however, the external potential energy,

$$U_{ext}(\theta) = \sum_{m=1}^{\infty} |U_m| \cos(m(\theta - \psi_m)), \tag{4.33}$$

can have higher azimuthal Fourier components of magnitude, $|U_m|$, and phase ψ_m. The higher harmonics of motion due to these higher Fourier components of $U_{ext}(\theta)$ have a $J_n(mA)$ amplitude dependence so that the total contribution to an even harmonic is

$$A_{n\,even}(\phi) = -\sum_{m=1}^{\infty} \frac{2mJ_n(mA)|U_m|}{(n^2-1)\kappa} \sin(m(\phi - \psi_m)), \tag{4.34}$$

and the total contribution to an odd harmonic is

$$B_{n\,odd}(\phi) = -\sum_{m=1}^{\infty} \frac{2mJ_n(mA)|U_m|}{(n^2-1)\kappa} \cos(m(\phi - \psi_m)). \tag{4.35}$$

For example, with a pure $m = 2$ potential energy and an oscillation amplitude of $A = 230° = 4.014$ radians, the second through seventh harmonics are

$$A_2(\phi) = 0.141\frac{|U_2|}{\kappa}\sin(2(\phi-\psi_2)), \qquad B_3(\phi) = 0.146\frac{|U_2|}{\kappa}\cos(2(\phi-\psi_2)),$$

$$A_4(\phi) = 0.030\frac{|U_2|}{\kappa}\sin(2(\phi-\psi_2)), \qquad B_5(\phi) = -0.030\frac{|U_2|}{\kappa}\cos(2(\phi-\psi_2)), \quad (4.36)$$

$$A_6(\phi) = -0.038\frac{|U_2|}{\kappa}\sin(2(\phi-\psi_2)), \qquad B_7(\phi) = -0.027\frac{|U_2|}{\kappa}\cos(2(\phi-\psi_2)).$$

Comparing Equation 4.36 to Equation 4.29, one sees that the ratio of the even harmonics to each other are different for an $m = 2$potential than for an $m = 1$ potential, and thus the fractional error in the measured second harmonic, $\Delta\hat{A}_2(\phi)/A_2(\phi)$, is different for an m=2 potential than for an $m = 1$ potential. In general, we are not directly concerned with the higher azimuthal Fourier components of the external potential, and if all the data were collected at precisely the same amplitude, A, then the Fourier components could be separated simply by their angular dependence on ϕ. However, because all the data is not collected at precisely the same amplitude, amplitude corrections must be made, and a knowledge of the exact amplitude dependence of the higher Fourier components is required to prevent them from "bleeding" into the $m = 1$ signal.

4.4 Multipole Expansion of Pendulum Interactions

As a systematic error, gravitational interactions are both important and unimportant. As far as this thesis is concerned, they are unimportant because they are not specific to the second harmonic method. Gravitational interactions produce a false signal because they apply torques to the pendulum, and any method that measures the torque on the pendulum will see the same false signal. So unlike the systematic errors discussed in Sections 4.1, 4.2, and 4.3, the

gravitational interactions have nothing to do with the fact that the torsion pendulum is oscillating. This also means that other groups who use non-oscillating deflection methods have written extensively on gravitational interactions and the design strategies used to minimize them. Most notably, Adelberger and his Eot-Wash collaborators (Stubbs et al. 1987) were the first to fully develop the spherical harmonic multipole expansion analysis methods and apply them to torsion balance experiments. On the other hand, gravitational interactions are a very important systematic error that can not be ignored, and unlike electromagnetic interactions, there are no effective shields to gravitational fields. The physical design of our Index IV apparatus is largely dictated by gravitational considerations. These will be discussed in Section 5.2.

I would like to use this section to present an alternate formulation of the spherical harmonic multipole expansion that our group has found useful. It was developed to analyze the third moment/third potential derivative coupling of a Yukawa potential interaction for the Inverse Square Law Violation experiment which our group is currently constructing (Moore et al. 1994). The details of that experiment are beyond the scope of this thesis, but suffice it to say that the non-Newtonian third moment/third potential derivative couplings required a more formal mathematical development than the non-Newtonian first moment/first potential derivative couplings of the CDF Index IV experiment (see Section 2.1). This generalized multipole expansion is not restricted to $1/r$ potentials for it can be applied to any potential provided it is analytic over the extent of the pendulum. A second feature of this method is that the various mass moments, potential derivatives, and energies can be calculated without factors i, π, or square roots, and the tilt and translation coefficients can be de-

rived directly from the Cartesian transformations without having to explicitly use spherical harmonic rotation matrices or Clebsch-Gordan coefficients. Mathematically this method is equivalent to the traditional multipole expansion, but psychologically it's easier to comprehend and use, particularly for undergraduates who may not be as experienced in the mathematical methods of quantum mechanics.

First, however, let me present the traditional multipole expansion. The pendulum is expanded in mass moments as

$$q_{\ell m} = \iiint \rho_p(\vec{r}) r^{\ell} Y_{\ell m}(\theta,\phi) d^3\vec{r} \tag{4.37}$$

where the $Y_{\ell m}(\theta,\phi)$ are spherical harmonic functions. Actually, Adelberger's convention is to define the mass moments with the complex conjugate, $Y^*_{\ell m}(\theta,\phi)$, but I have defined them in Equation 4.37 to be consistent with later notation. The complex conjugate will appear in a moment as I go to bra-ket notation and take the adjoint of the ket mass moment vector. The source mass is expanded as

$$Q_{\ell m} = \iiint \rho_s(\vec{r}') \frac{Y_{\ell m}(\theta',\phi')}{r'^{\ell+1}} d^3\vec{r}'. \tag{4.38}$$

These correspond to the various field derivatives to which the mass moments couple. The total potential energy of the pendulum in the source mass potential can then be expressed as

$$\begin{aligned} U &= \sum_{\ell=0}^{\infty} \sum_{m=-\ell}^{\ell} q^*_{\ell m} \frac{-4\pi G}{2\ell+1} Q_{\ell m} = \sum_{\ell m, \ell' m'} q^*_{\ell m} \frac{-4\pi G \delta_{\ell m, \ell' m'}}{2\ell+1} Q_{\ell' m'} \\ &= \sum_{\ell m, \ell' m'} q^*_{\ell m} K_{\ell m, \ell' m'} Q_{\ell' m'} = \langle q | \mathbf{K} | Q \rangle. \end{aligned} \tag{4.39}$$

The diagonal matrix, **K**, is introduced for use in derivations later in this section.

As a specific example of the traditional method, let us write out the calculation of the leading gravitational systematic error, the $\ell = 2$, $m = \pm 1$ interaction. The mass moments are

$$q_{21} = -\sqrt{\frac{15}{8\pi}} \iiint \rho_p(\vec{r}) r^2 \sin\theta\cos\theta(\cos\phi + i\sin\phi) d^3\vec{r} \quad \text{and}$$
$$q_{2-1} = \sqrt{\frac{15}{8\pi}} \iiint \rho_p(\vec{r}) r^2 \sin\theta\cos\theta(\cos\phi - i\sin\phi) d^3\vec{r}. \tag{4.40}$$

The fields are

$$Q_{21} = -\sqrt{\frac{15}{8\pi}} \iiint \rho_s(\vec{r}') \frac{\sin\theta'\cos\theta'(\cos\phi' + i\sin\phi')}{r'^3} d^3\vec{r}' \quad \text{and}$$
$$Q_{2-1} = \sqrt{\frac{15}{8\pi}} \iiint \rho_s(\vec{r}') \frac{\sin\theta'\cos\theta'(\cos\phi' - i\sin\phi')}{r'^3} d^3\vec{r}'. \tag{4.41}$$

And finally, the energies are

$$U_{21} = -\frac{4\pi G}{5} q_{21}^* Q_{21} \quad \text{and} \qquad U_{2-1} = -\frac{4\pi G}{5} q_{2-1}^* Q_{2-1}. \tag{4.42}$$

The same calculation can also be done with Cartesian xz and yz second mass moments and second derivatives of the potential.

$$M_{xz} = \iiint \rho_p(\vec{r}) xz d^3\vec{r} \qquad M_{yz} = \iiint \rho_p(\vec{r}) yz d^3\vec{r} \tag{4.43}$$

$$V_{xz} = \left.\frac{\partial^2 V(\vec{r})}{\partial x \partial z}\right|_{\vec{r}=0} = -G \iiint \rho_s(\vec{r}') \frac{3x'z'}{r'^5} d^3\vec{r}'$$
$$V_{yz} = \left.\frac{\partial^2 V(\vec{r})}{\partial y \partial z}\right|_{\vec{r}=0} = -G \iiint \rho_s(\vec{r}') \frac{3y'z'}{r'^5} d^3\vec{r}' \tag{4.44}$$

$$U_{xz} = M_{xz} V_{xz} \qquad U_{yz} = M_{yz} V_{yz} \tag{4.45}$$

The two methods are equivalent in that

$$U_{21} + U_{2-1} = U_{xz} + U_{yz}, \tag{4.46}$$

but the spherical harmonic moments, fields and energies are complex quantities whereas as the Cartesian ones are real and easier to remember.

Can the entire multipole expansion be done in Cartesian moments? Yes, it can be done for any potential interaction,

$$U = \iiint \rho_p(\vec{r}) V(\vec{r}) d^3\vec{r}, \tag{4.47}$$

provided $V(\vec{r})$ is analytic over the extent of the pendulum. Define the Cartesian mass moments as

$$M_{ijk} = \iiint \rho_p(\vec{r}) x^i y^j z^k d^3\vec{r}. \tag{4.48}$$

The potential, being analytic, can be expanded in a Taylor series in terms of its derivatives at the origin,

$$V_{ijk} = \left. \frac{\partial^{i+j+k} V(\vec{r})}{\partial x^i \partial y^j \partial z^k} \right|_{\vec{r}=0}. \tag{4.49}$$

The total potential energy of the pendulum in the potential can then be expressed as

$$\begin{aligned} U &= \sum_{i=0}^{\infty} \sum_{j=0}^{\infty} \sum_{k=0}^{\infty} M_{ijk} \frac{1}{i!\,j!\,k!} V_{ijk} = \sum_{ijk,i'j'k'} M_{ijk} \frac{\delta_{ijk,i'j'k'}}{i!\,j!\,k!} V_{i'j'k'} \\ &= \sum_{ijk,i'j'k'} M_{ijk} C_{ijk,i'j'k'} V_{i'j'k'} = \langle M | \mathbf{C} | V \rangle. \end{aligned} \tag{4.50}$$

The matrix **C** of Taylor series coefficients, analogous to the matrix **K** for the spherical harmonic decomposition, is also diagonal. Does the Cartesian basis

provide a reasonable alternative to the spherical harmonic basis for calculating pendulum interactions? No, not really. Ultimately, one wants the Fourier components of the azimuthal dependence of the potential energy as the pendulum rotates in the external potential (see Eq. 4.33). The m eigenvalues of the spherical harmonic basis naturally provide such a Fourier decomposition while the Cartesian basis does not, and the Cartesian basis is therefore a poor substitute for the spherical harmonic basis.

Is there perhaps a compromise? Is there some basis that combines the best qualities of both the spherical harmonic and Cartesian bases? Let us start by making the spherical harmonic basis complete by allowing the ℓ eigenvalue to assume other values besides n, the order of the mass moment. Specifically, define

$$q_{n\ell m} = \iiint \rho_p(\vec{r}) r^n Y_{\ell m}(\theta,\phi) d^3\vec{r} \qquad \ell = \{n, n-2, \ldots\} \geq 0, \quad -\ell \leq m \leq \ell. \tag{4.51}$$

When this is done, the spherical harmonic basis has $(n+1)(n+2)/2$ linearly independent moments for each order n just as the Cartesian basis does. Next, define mass moments,

$$\begin{aligned}
(q_N)_{n\ell 0\cos} &= N_{n\ell 0\cos, n\ell 0\cos} \iiint \rho_p(\vec{r}) r^n \,\mathrm{Re}(Y_{\ell m}(\theta,\phi)) d^3\vec{r} \qquad m = 0 \\
(q_N)_{n\ell m\cos} &= N_{n\ell m\cos, n\ell m\cos} \sqrt{2} \iiint \rho_p(\vec{r}) r^n \,\mathrm{Re}(Y_{\ell m}(\theta,\phi)) d^3\vec{r} \qquad 1 \leq m \leq \ell \\
(q_N)_{n\ell m\sin} &= N_{n\ell m\sin, n\ell m\sin} \sqrt{2} \iiint \rho_p(\vec{r}) r^n \,\mathrm{Im}(Y_{\ell m}(\theta,\phi)) d^3\vec{r} \qquad 1 \leq m \leq \ell,
\end{aligned} \tag{4.52}$$

that are real ($\cos(m\phi)$and $\sin(m\phi)$ rather than $\exp(im\phi)$ and $\exp(-im\phi)$) and have arbitrary normalization. The factors of $\sqrt{2}$ are elements of a unitary matrix so that the real, unnormalized, spherical harmonic moments can be related to the traditional spherical harmonic moments as

$$|q_N\rangle = \mathbf{NU}|q\rangle \tag{4.53}$$

where **N** is a diagonal, real matrix and **U** is a unitary matrix. Let us also define the real transformation matrix,

$$|q_N\rangle = \mathbf{S}_N|M\rangle \tag{4.54}$$

that relates the Cartesian mass moments to the real, unnormalized spherical harmonic moments. Can the total potential energy be calculated with these mass moments? Yes,

$$U = \langle q_N \| K_N Q_N \rangle = \langle M|\mathbf{S}_N^T|K_N Q_N\rangle = \langle M|\mathbf{C}|V\rangle, \tag{4.55}$$

provided that the dual fields are defined as

$$|K_N Q_N\rangle = \mathbf{S}_N^{-1^T}\mathbf{C}|V\rangle. \tag{4.56}$$

Here, the new method appears to lose its charm, at least for calculating gravitational interactions. With the traditional spherical harmonic multipoles, one only needs the specific $Y_{lm}(\theta,\phi)$ in order to calculate the field, Q_{lm}, that couples to a particular mass moment q_{lm}. With the real, unnormalized harmonics, it seems one needs all $(n+1)(n+2)/2$ unnormalized harmonics of order n arranged in a square matrix $\mathbf{S}_N$ that then needs to be inverted in order the determine the dual field that couples to $(q_N)_{nlmtrig}$. That appears to be a high price to pay just to avoid using complex numbers and square roots. Nevertheless, let us look at a specific example and see what happens. Use the quadratic Cartesian polynomials,

$$
\begin{aligned}
&n=2,\ell=0,m=0,\cos: && x^2+y^2+z^2\\
&n=2,\ell=2,m=0,\cos: && -x^2-y^2+2z^2\\
&n=2,\ell=2,m=1,\cos: && xz\\
&n=2,\ell=2,m=1,\sin: && yz\\
&n=2,\ell=2,m=2,\cos: && x^2-y^2\\
&n=2,\ell=2,m=2,\sin: && 2xy
\end{aligned}
\tag{4.57}
$$

to define the second moments of our real, unnormalized spherical harmonic basis. The factor of 2 is added to the xy polynomial so that the $m=2$ moments can be added in quadrature. That is, the quantity $\sqrt{(q_N)^2_{222\cos}+(q_N)^2_{222\sin}}$ remains invariant as the pendulum rotates around the z-axis. This is not necessary, but it is convenient, and it is not difficult to do. In general, sine and cosine moments can be added in quadrature provided the corresponding polynomials are of the form

$$
\mathrm{Re}\left((x+iy)^m\right)f\left(z,x^2+y^2\right) \quad \text{and} \quad \mathrm{Im}\left((x+iy)^m\right)f\left(z,x^2+y^2\right). \tag{4.58}
$$

The matrix $\mathbf{S}_N$ defined by the polynomials in Eq. 4.57 is

$$
|q_N\rangle=\begin{pmatrix}(q_N)_{200\cos}\\(q_N)_{220\cos}\\(q_N)_{221\cos}\\(q_N)_{221\sin}\\(q_N)_{222\cos}\\(q_N)_{222\sin}\end{pmatrix}=\begin{pmatrix}1&0&0&1&0&1\\-1&0&0&-1&0&2\\0&0&1&0&0&0\\0&0&0&0&1&0\\1&0&0&-1&0&0\\0&2&0&0&0&0\end{pmatrix}\begin{pmatrix}M_{xx}\\M_{xy}\\M_{xz}\\M_{yy}\\M_{yz}\\M_{zz}\end{pmatrix}=\mathbf{S}_N|M\rangle, \tag{4.59}
$$

and the matrix of Taylor series coefficients is

$$\mathbf{C}=\begin{pmatrix} 1/2 & 0 & 0 & 0 & 0 & 0 \\ 0 & 1 & 0 & 0 & 0 & 0 \\ 0 & 0 & 1 & 0 & 0 & 0 \\ 0 & 0 & 0 & 1/2 & 0 & 0 \\ 0 & 0 & 0 & 0 & 1 & 0 \\ 0 & 0 & 0 & 0 & 0 & 1/2 \end{pmatrix}. \tag{4.60}$$

The dual fields can then be expressed in terms of the Cartesian field derivatives as

$$|K_N Q_N\rangle = \left(\mathbf{S}_N^{-1^T}\mathbf{C}\right)|V\rangle = \begin{pmatrix} 1/6 & 0 & 0 & 1/6 & 0 & 1/6 \\ -1/12 & 0 & 0 & -1/12 & 0 & 1/12 \\ 0 & 0 & 1 & 0 & 0 & 0 \\ 0 & 0 & 0 & 0 & 1 & 0 \\ 1/4 & 0 & 0 & -1/4 & 0 & 0 \\ 0 & 1/2 & 0 & 0 & 0 & 0 \end{pmatrix} \begin{pmatrix} V_{xx} \\ V_{xy} \\ V_{xz} \\ V_{yy} \\ V_{yz} \\ V_{zz} \end{pmatrix}. \tag{4.61}$$

Upon closer inspection, one sees that

$$\mathbf{S}_N^{-1^T}\mathbf{C} = \begin{pmatrix} 1/6 & 0 & 0 & 0 & 0 & 0 \\ 0 & 1/12 & 0 & 0 & 0 & 0 \\ 0 & 0 & 1 & 0 & 0 & 0 \\ 0 & 0 & 0 & 1 & 0 & 0 \\ 0 & 0 & 0 & 0 & 1/4 & 0 \\ 0 & 0 & 0 & 0 & 0 & 1/4 \end{pmatrix} \mathbf{S}_N = \mathbf{K}_N \mathbf{S}_N. \tag{4.62}$$

Since this is true, you can define fields using the same transformation matrix used for the mass moments,

$$|Q_N\rangle = \mathbf{S}_N|V\rangle \quad \text{rather than} \quad |K_N Q_N\rangle = \mathbf{S}_N^{-1^T}\mathbf{C}|V\rangle, \tag{4.63}$$

and the total potential energy can be calculated as

$$U = \langle M|\mathbf{C}|V\rangle = \langle q_N|\mathbf{S}_N^{-1^T}\mathbf{C}\mathbf{S}_N^{-1}|Q_N\rangle$$
$$= \langle q_N|\mathbf{K}_N|Q_N\rangle \text{ where } \mathbf{K}_N \text{ is diagonal.} \tag{4.64}$$

This is great if it is true in general because if both $\mathbf{K}_N$ and $\mathbf{C}$ are diagonal then

$$(K_N)_{n\ell mtrig,n\ell mtrig} = \frac{1}{\left(K_N^{-1}\right)_{n\ell mtrig,n\ell mtrig}} = \frac{1}{\left(S_N C^{-1} S_N^T\right)_{n\ell mtrig,n\ell mtrig}}$$
$$= \frac{1}{\sum_{ijk} i!j!k!(S_N)^2_{n\ell mtrig,ijk}}, \tag{4.65}$$

and one only needs one row of $\mathbf{S}_N$ to calculate a particular energy. For example, from Equation 4.59,

$$\langle (S_N)_{220\cos}| = (-1 \quad 0 \quad 0 \quad -1 \quad 0 \quad 2). \tag{4.66}$$

One can then apply Equations 4.64 and 4.65, to get

$$U_{220\cos} = (q_N)_{220\cos}(K_N)_{220\cos}(Q_N)_{220\cos}$$
$$= (q_N)_{220\cos}\left(\frac{1}{(-1)^2 2! + (-1)^2 2! + (2)^2 2!}\right)(Q_N)_{220\cos} \tag{4.67}$$
$$= \frac{\left(-M_{xx} - M_{yy} + 2M_{zz}\right)\left(-V_{xx} - V_{yy} + 2V_{zz}\right)}{12}.$$

Notice one doesn't need to know that $(q_N)_{220\cos} = (16\pi/5)^{1/2} q_{220}$ to do the above calculation; one just needs Equation 4.66. Speaking of which, I can more clearly describe a particular row of $\mathbf{S}_N$ by contracting it with $|X\rangle$, the column vector of Cartesian monomials, such as

$$\langle (S_N)_{220\cos}|X\rangle = -x^2 - y^2 + 2z^2. \tag{4.68}$$

The above scheme only works, however, if $\mathbf{K}_N$ is truly a diagonal matrix, and so far I have only proved it is for $n = 2$. First I shall prove it for $n = 1$, but instead of doing an explicit calculation, I shall invoke general properties of the spherical harmonic and Cartesian bases that are true for all orders of n so that the proof can be generalized. What can we say in general about the $n = 1$ spherical harmonic mass moments $|q\rangle$ and fields $|Q\rangle$? Well, we know they have the same $\ell = 1$ rotation matrices, $\{\mathbf{D}_1\}$. That is,

$$|\tilde{q}\rangle = \mathbf{D}_1|q\rangle \quad \text{and} \qquad \left|\tilde{Q}\right\rangle = \mathbf{D}_1|Q\rangle \tag{4.69}$$

where $|\tilde{q}\rangle$ and $\left|\tilde{Q}\right\rangle$ are the row vectors of moments and fields that result from rotating the pendulum or source mass respectively. The $\{\mathbf{D}_1\}$ can be parameterized by three Euler angles, but that level of detail is not necessary for this derivation. What we do need to know is that these 3x3 matrices are unitary,

$$\mathbf{D}_1^\dagger = \mathbf{D}_1^{-1} \text{ for all } \mathbf{D}_1, \tag{4.70}$$

and that $\{\mathbf{D}_1\}$ is an irreducible representation of the rotation group. For us, the most important property of an irreducible representation is a corollary of Schur's lemma which states

$$\text{if} \quad \mathbf{D}_1\mathbf{A}\mathbf{D}_1^{-1} = \mathbf{A} = \mathbf{D}_1^{-1}\mathbf{A}\mathbf{D}_1 \quad \text{for all } \mathbf{D}_1, \text{ then} \quad \mathbf{A} = \lambda\mathbf{I}, \tag{4.71}$$

where $\mathbf{I}$ is the identity matrix, and λ is some scalar.

The total potential energy is rotationally invariant, and so it should make no difference whether it is calculated with rotated vectors or not,

$$U = \langle\tilde{q}|\mathbf{K}\left|\tilde{Q}\right\rangle = \langle q|\mathbf{D}_1^{-1}\mathbf{K}\mathbf{D}_1|Q\rangle = \langle q|\mathbf{K}|Q\rangle. \tag{4.72}$$

Since

$$\mathbf{D}_1^{-1}\mathbf{K}\mathbf{D}_1 = \mathbf{K} \quad \text{for all } \mathbf{D}_1 \quad \Rightarrow \quad \mathbf{K} = k_1\mathbf{I}_1 \tag{4.73}$$

where k_1 is some scalar. The "1" subscripts are added to make the notation consistent with notation used later in this section. Thus simply knowing that the rotation matrices are the same for both spherical harmonic fields and mass moments and that those rotation matrices form an irreducible group is enough to prove that $\mathbf{K}$ must be a multiple of the identity matrix, which in fact it is. $\mathbf{K} = (-4\pi G/3)\mathbf{I}_1$. For the first moments, the same argument can be applied to the Cartesian representation whose rotation matrices are $\{\mathbf{R}\}$.

$$\left|\tilde{M}\right\rangle = \mathbf{R}|M\rangle \quad \text{and} \qquad \left|\tilde{V}\right\rangle = \mathbf{R}|V\rangle. \tag{4.74}$$

$$U = \left\langle \tilde{M}\middle|\mathbf{C}\middle|\tilde{V}\right\rangle = \langle M|\mathbf{R}^{-1}\mathbf{C}\mathbf{R}|V\rangle = \langle M|\mathbf{C}|V\rangle \tag{4.75}$$

Since

$$\mathbf{R}^{-1}\mathbf{C}\mathbf{R} = \mathbf{C} \quad \text{for all } \mathbf{R} \quad \Rightarrow \quad \mathbf{C} = c_1\mathbf{I}_1. \tag{4.76}$$

And in fact it does, $\mathbf{C} = \mathbf{I}_1$.

Now let us define the the transformation matrices between the Cartesian and traditional spherical harmonic mass moments and fields as

$$|q\rangle = \mathbf{S}_M|M\rangle \quad \text{and} \qquad |Q\rangle = \mathbf{S}_V|V\rangle. \tag{4.77}$$

We know the rows of $\mathbf{S}_M$ are the coefficients of $rY_{1m}(\theta,\phi)$ expressed as Cartesian polynomials. What can we say about $\mathbf{S}_V$? First let us relate $\mathbf{D}_1$ and $\mathbf{R}$,

$$\begin{aligned} &|\tilde{q}\rangle = \mathbf{D}_1|q\rangle \\ &\mathbf{S}_M\left|\tilde{M}\right\rangle = \mathbf{D}_1\mathbf{S}_M|M\rangle \\ &\mathbf{S}_M\mathbf{R}|M\rangle = \mathbf{D}_1\mathbf{S}_M|M\rangle \quad \Rightarrow \quad \mathbf{R} = \mathbf{S}_M^{-1}\mathbf{D}_1\mathbf{S}_M. \end{aligned} \tag{4.78}$$

Similarly,

$$\begin{aligned}
&\left|\tilde{Q}\right\rangle = \mathbf{D}_1|Q\rangle \\
&\mathbf{S}_V\left|\tilde{V}\right\rangle = \mathbf{D}_1\mathbf{S}_V|V\rangle \\
&\mathbf{S}_V\mathbf{R}|V\rangle = \mathbf{D}_1\mathbf{S}_V|V\rangle \quad \Rightarrow \quad \mathbf{R} = \mathbf{S}_V^{-1}\mathbf{D}_1\mathbf{S}_V = \mathbf{S}_M^{-1}\mathbf{D}_1\mathbf{S}_M.
\end{aligned} \tag{4.79}$$

Since

$$\begin{aligned}
&(\mathbf{S}_V)\mathbf{S}_V^{-1}\mathbf{D}_1\mathbf{S}_V\left(\mathbf{S}_M^{-1}\mathbf{D}_1^{-1}\right) = (\mathbf{S}_V)\mathbf{S}_M^{-1}\mathbf{D}_1\mathbf{S}_M\left(\mathbf{S}_M^{-1}\mathbf{D}_1^{-1}\right) \\
&\mathbf{D}_1\left(\mathbf{S}_V\mathbf{S}_M^{-1}\right)\mathbf{D}_1^{-1} = \mathbf{S}_V\mathbf{S}_M^{-1} \quad \text{for all } \mathbf{D}_1 \\
&\Rightarrow \quad \mathbf{S}_V\mathbf{S}_M^{-1} = s_1\mathbf{I}_1 \quad \Rightarrow \quad \mathbf{S}_V = s_1\mathbf{S}_M.
\end{aligned} \tag{4.80}$$

Thus $\mathbf{S}_V$ is a multiple of $\mathbf{S}_M$, and indeed it is. $\mathbf{S}_V = (-1/G)\mathbf{S}_M$.

The matrices $\mathbf{N}$, $\mathbf{U}$, $\mathbf{S}_N$, and $\mathbf{S}_M$ have been defined above (see Eqs. 4.53, 4.54, and 4.77) so that

$$|q_N\rangle = \mathbf{S}_N|M\rangle = \mathbf{NU}|q\rangle = \mathbf{NUS}_M|M\rangle \quad \Rightarrow \quad \mathbf{S}_N = \mathbf{NUS}_M. \tag{4.81}$$

Similarly, using Equation 4.80,

$$|Q_N\rangle = \mathbf{S}_N|V\rangle = \mathbf{NUS}_M|V\rangle = \mathbf{NU}s_1^{-1}\mathbf{S}_V|V\rangle = \mathbf{NU}s_1^{-1}|Q\rangle. \tag{4.82}$$

By comparing the potential energy calculated in the traditional and the real, unnormalized spherical harmonic bases,

$$\begin{aligned}
U &= \langle q|\mathbf{K}|Q\rangle = \langle q|k_1\mathbf{I}_1|Q\rangle \\
&= \langle q_N|\mathbf{N}^{-1}\mathbf{U}k_1\mathbf{I}_1s_1\mathbf{U}^{-1}\mathbf{N}^{-1}|Q_N\rangle = \langle q_N|k_1s_1\mathbf{N}^{-2}|Q_N\rangle = \langle q_N|\mathbf{K}_N|Q_N\rangle
\end{aligned} \tag{4.83}$$

one sees that

$$\mathbf{K}_N = k_1s_1\mathbf{N}^{-2} \quad \text{is diagonal.} \quad \text{Q.E.D.} \tag{4.84}$$

Next I want to prove that $\mathbf{K}_N$ is diagonal for $n=2$ from the same general properties used to prove the $n=1$ case above. The rotation matrices, $\{\mathbf{D}\}$, that rotate the second moments and fields,

$$|\tilde{q}\rangle = \mathbf{D}|q\rangle \quad \text{and} \qquad |\tilde{Q}\rangle = \mathbf{D}|Q\rangle, \tag{4.85}$$

are unitary 6x6 matrices. Once again, the potential energy is rotationally invariant,

$$\begin{aligned} &U = \langle\tilde{q}|\mathbf{K}|\tilde{Q}\rangle = \langle q|\mathbf{D}^{-1}\mathbf{K}\mathbf{D}|Q\rangle = \langle q|\mathbf{K}|Q\rangle \\ &\mathbf{D}^{-1}\mathbf{K}\mathbf{D} = \mathbf{K} \quad \text{for all } \mathbf{D}, \\ &\text{but } \{\mathbf{D}\} \text{ is not an irreducible representation.} \end{aligned} \tag{4.86}$$

Thus Schur's lemma can not be immediately applied. $\{\mathbf{D}\}$ is a direct sum representation of the irreducible $\ell=0$ representation, $\{\mathbf{D}_0\}$ (1x1 matrix), and the irreducible $\ell=2$ representation, $\{\mathbf{D}_2\}$ (5x5 matrices). Each matrix $\mathbf{D}$ is block diagonal in $\mathbf{D}_0$ and $\mathbf{D}_2$. That is,

$$\mathbf{D} = \begin{pmatrix} \mathbf{D}_0 & {}^{15}\mathbf{0} \\ {}^{51}\mathbf{0} & \mathbf{D}_2 \end{pmatrix} \tag{4.87}$$

where ${}^{15}\mathbf{0}$ represents a 1x5 null matrix and ${}^{51}\mathbf{0}$ represents a 5x1 null matrix. In general, it will be useful to break up any 6x6 matrix $\mathbf{A}$ into submatices

$$\mathbf{A} = \begin{pmatrix} {}^{11}\mathbf{A} & {}^{15}\mathbf{A} \\ {}^{51}\mathbf{A} & {}^{55}\mathbf{A} \end{pmatrix}. \tag{4.88}$$

It will also be useful to define the $\ell=0$ identity matrix and the $\ell=2$ identity matrix as

$$\mathbf{I}_0 = \begin{pmatrix} {}^{11}\mathbf{I} & {}^{15}\mathbf{0} \\ {}^{51}\mathbf{0} & {}^{55}\mathbf{0} \end{pmatrix} \quad \text{and} \quad \mathbf{I}_2 = \begin{pmatrix} {}^{11}\mathbf{0} & {}^{15}\mathbf{0} \\ {}^{51}\mathbf{0} & {}^{55}\mathbf{I} \end{pmatrix}. \tag{4.89}$$

$$\mathbf{I}_0 + \mathbf{I}_2 = \mathbf{I} \quad \mathbf{I}_0\mathbf{I}_0 = \mathbf{I}_0 \quad \mathbf{I}_2\mathbf{I}_2 = \mathbf{I}_2 \quad \mathbf{I}_0\mathbf{I}_2 = \mathbf{I}_2\mathbf{I}_0 = \mathbf{0}$$

These can be used to extract the submatrices of $\mathbf{A}$.

$$\mathbf{A} = (\mathbf{I}_0 + \mathbf{I}_2)\mathbf{A}(\mathbf{I}_0 + \mathbf{I}_2) = \mathbf{I}_0\mathbf{A}\mathbf{I}_0 + \mathbf{I}_0\mathbf{A}\mathbf{I}_2 + \mathbf{I}_2\mathbf{A}\mathbf{I}_0 + \mathbf{I}_2\mathbf{A}\mathbf{I}_2$$

$$\mathbf{I}_0\mathbf{A}\mathbf{I}_0 = \begin{pmatrix} {}^{11}\mathbf{A} & {}^{15}\mathbf{0} \\ {}^{51}\mathbf{0} & {}^{55}\mathbf{0} \end{pmatrix} \quad \mathbf{I}_0\mathbf{A}\mathbf{I}_2 = \begin{pmatrix} {}^{11}\mathbf{0} & {}^{15}\mathbf{A} \\ {}^{51}\mathbf{0} & {}^{55}\mathbf{0} \end{pmatrix} \tag{4.90}$$

$$\mathbf{I}_2\mathbf{A}\mathbf{I}_0 = \begin{pmatrix} {}^{11}\mathbf{0} & {}^{15}\mathbf{0} \\ {}^{51}\mathbf{A} & {}^{55}\mathbf{0} \end{pmatrix} \quad \mathbf{I}_2\mathbf{A}\mathbf{I}_2 = \begin{pmatrix} {}^{11}\mathbf{0} & {}^{15}\mathbf{0} \\ {}^{51}\mathbf{0} & {}^{55}\mathbf{A} \end{pmatrix}$$

In this notation, $\mathbf{D}$ being block diagonal can be expressed as

$$\mathbf{D} = \begin{pmatrix} \mathbf{D}_0 & {}^{15}\mathbf{0} \\ {}^{51}\mathbf{0} & \mathbf{D}_2 \end{pmatrix} \quad \Leftrightarrow \quad \mathbf{D} = \mathbf{I}_0\mathbf{D}\mathbf{I}_0 + \mathbf{I}_2\mathbf{D}\mathbf{I}_2. \tag{4.91}$$

Now, let's try once again to apply Schur's lemma to Equation 4.86. First re-write it as

$$\begin{aligned} &\mathbf{D}\mathbf{K} = \mathbf{K}\mathbf{D} \quad \text{for all } \mathbf{D} \\ &(\mathbf{I}_0\mathbf{D}\mathbf{I}_0 + \mathbf{I}_2\mathbf{D}\mathbf{I}_2)\mathbf{K} = \mathbf{K}(\mathbf{I}_0\mathbf{D}\mathbf{I}_0 + \mathbf{I}_2\mathbf{D}\mathbf{I}_2). \end{aligned} \tag{4.92}$$

Multiply both sides of the equation on the left and on the right by $\mathbf{I}_0$.

$$\begin{aligned} &\mathbf{I}_0(\mathbf{I}_0\mathbf{D}\mathbf{I}_0 + \mathbf{I}_2\mathbf{D}\mathbf{I}_2)\mathbf{K}\mathbf{I}_0 = \mathbf{I}_0\mathbf{K}(\mathbf{I}_0\mathbf{D}\mathbf{I}_0 + \mathbf{I}_2\mathbf{D}\mathbf{I}_2)\mathbf{I}_0 \\ &(\mathbf{I}_0\mathbf{D}\mathbf{I}_0)(\mathbf{I}_0\mathbf{K}\mathbf{I}_0) = (\mathbf{I}_0\mathbf{K}\mathbf{I}_0)(\mathbf{I}_0\mathbf{D}\mathbf{I}_0) \\ &\mathbf{D}_0\,{}^{11}\mathbf{K} = {}^{11}\mathbf{K}\mathbf{D}_0 \quad \text{for all } \mathbf{D}_0 \quad \Rightarrow \quad {}^{11}\mathbf{K} = k_0\,{}^{11}\mathbf{I} \quad \Leftrightarrow \quad \mathbf{I}_0\mathbf{K}\mathbf{I}_0 = k_0\mathbf{I}_0. \end{aligned} \tag{4.93}$$

Similarly, by multiplying both sides of the equation on the left and on the right by $\mathbf{I}_2$, one gets

$$\begin{aligned}
&\mathbf{I}_2(\mathbf{I}_0\mathbf{D}\mathbf{I}_0 + \mathbf{I}_2\mathbf{D}\mathbf{I}_2)\mathbf{K}\mathbf{I}_2 = \mathbf{I}_2\mathbf{K}(\mathbf{I}_0\mathbf{D}\mathbf{I}_0 + \mathbf{I}_2\mathbf{D}\mathbf{I}_2)\mathbf{I}_2 \\
&(\mathbf{I}_2\mathbf{D}\mathbf{I}_2)(\mathbf{I}_2\mathbf{K}\mathbf{I}_2) = (\mathbf{I}_2\mathbf{K}\mathbf{I}_2)(\mathbf{I}_2\mathbf{D}\mathbf{I}_2) \\
&\mathbf{D}_2\,{}^{22}\mathbf{K} = {}^{22}\mathbf{K}\mathbf{D}_2 \quad \text{for all } \mathbf{D}_2 \quad \Rightarrow \quad {}^{22}\mathbf{K} = k_2\,{}^{22}\mathbf{I} \quad \Leftrightarrow \quad \mathbf{I}_2\mathbf{K}\mathbf{I}_2 = k_2\mathbf{I}_2.
\end{aligned} \tag{4.94}$$

To complete the proof, we need another part of Schur's lemma which concerns rectangular transformation matrices between representations of different dimensions such as $\{\mathbf{D}_0\}$ and $\{\mathbf{D}_2\}$.

$$\begin{aligned}
&\text{If} \quad \mathbf{D}_0\mathbf{A} = \mathbf{A}\mathbf{D}_2 \quad \text{for all } \mathbf{D}_0 \text{ and } \mathbf{D}_2 \text{ then} \quad \mathbf{A} = {}^{15}\mathbf{0}. \\
&\text{If} \quad \mathbf{D}_2\mathbf{A} = \mathbf{A}\mathbf{D}_0 \quad \text{for all } \mathbf{D}_0 \text{ and } \mathbf{D}_2 \text{ then} \quad \mathbf{A} = {}^{51}\mathbf{0}.
\end{aligned} \tag{4.95}$$

Essentially this states that inequivalent representations can not be mapped into each other using linear operators. Multiply both sides of Equation 4.92 on the left by $\mathbf{I}_0$ and on the right by $\mathbf{I}_2$.

$$\begin{aligned}
&\mathbf{I}_0(\mathbf{I}_0\mathbf{D}\mathbf{I}_0 + \mathbf{I}_2\mathbf{D}\mathbf{I}_2)\mathbf{K}\mathbf{I}_2 = \mathbf{I}_0\mathbf{K}(\mathbf{I}_0\mathbf{D}\mathbf{I}_0 + \mathbf{I}_2\mathbf{D}\mathbf{I}_2)\mathbf{I}_2 \\
&(\mathbf{I}_0\mathbf{D}\mathbf{I}_0)(\mathbf{I}_0\mathbf{K}\mathbf{I}_2) = (\mathbf{I}_0\mathbf{K}\mathbf{I}_2)(\mathbf{I}_2\mathbf{D}\mathbf{I}_2) \\
&\mathbf{D}_0\,{}^{15}\mathbf{K} = {}^{15}\mathbf{K}\mathbf{D}_2 \quad \text{for all } \mathbf{D}_0, \mathbf{D}_2 \quad \Rightarrow \quad {}^{15}\mathbf{K} = {}^{15}\mathbf{0} \quad \Leftrightarrow \quad \mathbf{I}_0\mathbf{K}\mathbf{I}_2 = \mathbf{0}.
\end{aligned} \tag{4.96}$$

Then multiply both sides of Equation 4.92 on the left by $\mathbf{I}_2$ and on the right by $\mathbf{I}_0$.

$$\begin{aligned}
&\mathbf{I}_2(\mathbf{I}_0\mathbf{D}\mathbf{I}_0 + \mathbf{I}_2\mathbf{D}\mathbf{I}_2)\mathbf{K}\mathbf{I}_0 = \mathbf{I}_2\mathbf{K}(\mathbf{I}_0\mathbf{D}\mathbf{I}_0 + \mathbf{I}_2\mathbf{D}\mathbf{I}_2)\mathbf{I}_0 \\
&(\mathbf{I}_2\mathbf{D}\mathbf{I}_2)(\mathbf{I}_2\mathbf{K}\mathbf{I}_0) = (\mathbf{I}_2\mathbf{K}\mathbf{I}_0)(\mathbf{I}_0\mathbf{D}\mathbf{I}_0) \\
&\mathbf{D}_2\,{}^{51}\mathbf{K} = {}^{51}\mathbf{K}\mathbf{D}_0 \quad \text{for all } \mathbf{D}_0, \mathbf{D}_2 \quad \Rightarrow \quad {}^{51}\mathbf{K} = {}^{51}\mathbf{0} \quad \Leftrightarrow \quad \mathbf{I}_2\mathbf{K}\mathbf{I}_0 = \mathbf{0}.
\end{aligned} \tag{4.97}$$

By combining the results, one has

$$\mathbf{K} = \mathbf{I}_0\mathbf{K}\mathbf{I}_0 + \mathbf{I}_2\mathbf{K}\mathbf{I}_2 = k_0\mathbf{I}_0 + k_2\mathbf{I}_2. \tag{4.98}$$

Notice that for the $n=2$ case, the class of rotationally invariant matrices is a two-parameter family (k_0 and k_2) whereas for the $n=1$ case (see Eq. 4.73), the class of rotationally invariant matrices is a one-parameter family (k_1).

Once again the Cartesian rotation matrices, $\{\mathbf{R}\}$, are the same for both the mass moments, $|M\rangle$, and the potential derivatives, $|V\rangle$, so that the relationship in Equation 4.79,

$$\mathbf{R} = \mathbf{S}_V^{-1}\mathbf{D}\mathbf{S}_V = \mathbf{S}_M^{-1}\mathbf{D}\mathbf{S}_M, \tag{4.99}$$

still holds, and by applying the same type of argument as we did to the matrix $\mathbf{K}$ above, one can show that

$$\begin{aligned} &\mathbf{D}\left(\mathbf{S}_V\mathbf{S}_M^{-1}\right) = \left(\mathbf{S}_V\mathbf{S}_M^{-1}\right)\mathbf{D} \quad \text{for all } \mathbf{D} \quad \Rightarrow \quad \mathbf{S}_V\mathbf{S}_M^{-1} = s_0\mathbf{I}_0 + s_2\mathbf{I}_2 \\ &\mathbf{S}_V = (s_0\mathbf{I}_0 + s_2\mathbf{I}_2)\mathbf{S}_M \quad \text{and} \quad \mathbf{S}_M = \left(s_0^{-1}\mathbf{I}_0 + s_2^{-1}\mathbf{I}_2\right)\mathbf{S}_V. \end{aligned} \tag{4.100}$$

From which we can get the relationships

$$|q_N\rangle = \mathbf{N}\mathbf{U}|q\rangle \quad \text{and} \qquad |Q_N\rangle = \mathbf{N}\mathbf{U}\left(s_0^{-1}\mathbf{I}_0 + s_2^{-1}\mathbf{I}_2\right)|Q\rangle. \tag{4.101}$$

Here, however, the matrix $\mathbf{U}$ must not only be unitary but also block diagonal,

$$\mathbf{U} = \mathbf{I}_0\mathbf{U}\mathbf{I}_0 + \mathbf{I}_2\mathbf{U}\mathbf{I}_2,$$

so that $\ell=0$ and $\ell=2$ spherical harmonics are not mixed together. An important property of a block diagonal matrix is that

$$\begin{aligned} &\text{if} \quad \mathbf{A} = \mathbf{I}_0\mathbf{A}\mathbf{I}_0 + \mathbf{I}_2\mathbf{A}\mathbf{I}_2, \\ &\text{then} \quad \mathbf{A}(\lambda_0\mathbf{I}_0 + \lambda_2\mathbf{I}_2) = (\lambda_0\mathbf{I}_0 + \lambda_2\mathbf{I}_2)\mathbf{A}. \end{aligned} \tag{4.102}$$

Finally, by comparing the potential energy calculated in the traditional and the real, unnormalized spherical harmonic bases,

$$
\begin{aligned}
U &= \langle q|\mathbf{K}|Q\rangle = \langle q|(k_0\mathbf{I}_0 + k_2\mathbf{I}_2)|Q\rangle \\
&= \langle q_N|\mathbf{N}^{-1}\mathbf{U}(k_0\mathbf{I}_0 + k_2\mathbf{I}_2)(s_0\mathbf{I}_0 + s_2\mathbf{I}_2)\mathbf{U}^{-1}\mathbf{N}^{-1}|Q_N\rangle \\
&= \langle q_N|(k_0s_0\mathbf{I}_0 + k_2s_2\mathbf{I}_2)\mathbf{N}^{-2}|Q_N\rangle = \langle q_N|\mathbf{K}_N|Q_N\rangle,
\end{aligned}
\tag{4.103}
$$

one sees that

$$
\mathbf{K}_N = (k_0s_0\mathbf{I}_0 + k_2s_2\mathbf{I}_2)\mathbf{N}^{-2} \quad \text{is diagonal.} \quad \text{Q.E.D.} \tag{4.104}
$$

If the above proof is repeated for higher order moments,

$$
\begin{aligned}
n = 3\text{:}\ \ \mathbf{K}_N &= (k_1s_1\mathbf{I}_1 + k_3s_3\mathbf{I}_3)\mathbf{N}^{-2} \quad \text{is diagonal.} \\
n = 4\text{:}\ \ \mathbf{K}_N &= (k_0s_0\mathbf{I}_0 + k_2s_2\mathbf{I}_2 + k_4s_4\mathbf{I}_4)\mathbf{N}^{-2} \quad \text{is diagonal.} \\
&\ \ \vdots
\end{aligned}
\tag{4.105}
$$

it can be shown that $\mathbf{K}_N$ is always diagonal.

When designing precision gravity experiments, one not only needs to know the energies from the planned moments and fields, but also what interactions will arise from the pendulum or source mass being tilted from their nominal design position. This tells you what tilt tolerances must be maintained if the gravitational interactions are to remain negligible. Typically, only first-order tilts need to be calculated as errors resulting from second-order tilts are generally much smaller than fabrication errors resulting from machining imperfections and density inhomogeneities. Let us define the rotation matrix of the real, unnormalized harmonics as $\mathbf{D}_N$.

$$
|\tilde{q}_N\rangle = \mathbf{D}_N|q_N\rangle \quad \text{and} \qquad |\tilde{Q}_N\rangle = \mathbf{D}_N|Q_N\rangle. \tag{4.106}
$$

One can obtain $\mathbf{D}_N$ from the traditional spherical harmonic rotation matrix, $\mathbf{D}$, by means of the similarity transformation

$$
\mathbf{D}_N = \mathbf{NUDU}^{-1}\mathbf{N}^{-1} = \mathbf{K}_N^{-1/2}\mathbf{UDU}^{-1}\mathbf{K}_N^{+1/2}. \tag{4.107}
$$

Note that one does not need to know the normalization matrix, $\mathbf{N}$; simply knowing $\mathbf{K}_N$ and $\mathbf{U}$ will suffice. If one uses $\mathbf{K}_N$, however, there are ambiguities of sign that result from taking the square root of the diagonal matrix $\mathbf{K}_N$, but often one is only concerned with the magnitude of the tilt coefficients and not their sign so this is not a severe handicap. Still one does have to deal with the factors of $\sqrt{2}$ and i in $\mathbf{U}$, and there are a lot of square roots in the calculation that end up canceling in the final result. I prefer to derive the tilt coefficients from the Cartesian rotation matrix,

$$\mathbf{D}_N = \mathbf{S}_N \mathbf{R} \mathbf{S}_N^{-1} = \mathbf{S}_N \mathbf{R} \mathbf{C}^{-1} \mathbf{S}_N^T \mathbf{K}_N. \tag{4.108}$$

For first-order tilts, $\mathbf{D}_N$ is a sparse matrix (i.e., most of its matrix elements are zero), and it is best not to do a full matrix calculation. Rather, from a qualitative knowledge of $\mathbf{D}$, one can predict *a priori* which elements of $\mathbf{D}_N$ are zero and then calculate only the few non-zero elements. To calculate a specific matrix element of $\mathbf{D}_N$ from Equation 4.108,

$$\begin{aligned}&(D_N)_{nlmtrig,n'l'm'trig'} = \\ &\sum_{ijk,i'j'k'} (S_N)_{nlmtrig,ijk} R_{ijk,i'j'k'} C^{-1}_{i'j'k',i'j'k'} \left(S_N^T\right)_{i'j'k',n'l'm'trig'} (K_N)_{n'l'm'trig',n'l'm'trig'},\end{aligned} \tag{4.109}$$

one only needs two rows of $\mathbf{S}_N$. This can be expressed more succinctly in braket form.

$$(D_N)_{nlmtrig,n'l'm'trig'} = \left\langle (S_N R)_{nlmtrig} \middle\| \left(C^{-1} S_N^T K_N\right)_{n'l'm'trig'} \right\rangle. \tag{4.110}$$

As an example, consider all the mass moments that mix under first-order tilts into the third moment $(q_N)_{331\cos}$. Because tilts can not change the n or ℓ

eigenvalues and first-order tilts can change the m eigenvalue by at most ± 1, the only moments we need to be concerned with are

$$\begin{aligned}
\langle (S_N)_{330\cos} | X \rangle &= -3(x^2+y^2)z + 2z^3 & (K_N)_{330\cos,330\cos} &= 1/60 \\
\langle (S_N)_{331\cos} | X \rangle &= x(-x^2-y^2+4z^2) & (K_N)_{331\cos,331\cos} &= 1/40 \\
\langle (S_N)_{331\sin} | X \rangle &= y(-x^2-y^2+4z^2) & (K_N)_{331\sin,331\sin} &= 1/40 \\
\langle (S_N)_{332\cos} | X \rangle &= (x^2-y^2)z & (K_N)_{332\cos,332\cos} &= 1/4 \\
\langle (S_N)_{332\sin} | X \rangle &= 2xyz & (K_N)_{332\sin,332\sin} &= 1/4.
\end{aligned} \tag{4.111}$$

Under rotation around the z-axis, θ_z, the m eigenvalue doesn't change so only the $(q_N)_{331\sin}$ moment mixes into the $(q_N)_{331\cos}$ moment. The two row and column vectors we need for the calculation are

$$\begin{aligned}
&\langle (S_N)_{331\cos} | X \rangle = -x^3 - xy^2 + 4xz^2 \quad \text{and} \\
&\langle X | (S_N^T)_{331\sin} \rangle = -x^2y - y^3 + 4yz^2.
\end{aligned} \tag{4.112}$$

The effect of the first-order rotation matrix, $\mathbf{R}$, acting to the left,

$$\langle (S_N R)_{331\cos} | X \rangle = -x^3 - xy^2 + 4xz^2 + (x^2y + y^3 - 4yz^2)\theta_z, \tag{4.113}$$

is equivalent to the substitution

$$\{x \to x - y\theta_z, \quad y \to y + x\theta_z, \quad z \to z\}. \tag{4.114}$$

The result of the diagonal matrices $\mathbf{C}^{-1}$ and $\mathbf{K}_N$ acting on the ket vector is

$$\langle X | (C^{-1} S_N^T K_N)_{331\sin} \rangle = -\frac{x^2y}{20} - \frac{3y^3}{20} + \frac{yz^2}{5}. \tag{4.115}$$

The tilt coefficient is then found by taking the inner product,

$$
\begin{aligned}
(D_N)_{331\cos,331\sin} &= \left\langle (S_N R)_{331\cos} \middle\| \left(C^{-1} S_N^T K_N\right)_{331\sin} \right\rangle \\
&= \left((1)\left(-\frac{1}{20}\right) + (1)\left(-\frac{3}{20}\right) + (-4)\left(\frac{1}{5}\right) \right) \theta_z = -\theta_z ,
\end{aligned}
\tag{4.116}
$$

or

$$
(\tilde{q}_N)_{331\cos} = (q_N)_{331\cos} - (q_N)_{331\sin}\theta_z . \tag{4.117}
$$

This result is not surprising since we knew that the coefficient would have to be ± 1 for rotation of $m = 1$ moments around the z-axis.

Now, let's perform a calculation whose result is harder to predict, the first-order rotation around the x-axis, θ_x. Since mathematically the $(q_N)_{330\sin}$ moment does not exist, only the $(q_N)_{332\sin}$ moment mixes into the $(q_N)_{331\cos}$ moment. The effect of the first-order rotation matrix, $\mathbf{R}$, acting on the ket vector,

$$
\left\langle (S_N R)_{331\cos} \middle| X \right\rangle = -x^3 - xy^2 + 4xz^2 + (10xyz)\theta_x , \tag{4.118}
$$

is equivalent to the substitution

$$
\left\{ x \to x, \quad y \to y - z\theta_x, \quad z \to z + y\theta_x \right\}. \tag{4.119}
$$

The result of the diagonal matrices $\mathbf{C}^{-1}$ and $\mathbf{K}_N$ acting on the ket vector is

$$
\left\langle X \middle\| \left(C^{-1} S_N^T K_N\right)_{332\sin} \right\rangle = \frac{xyz}{2}. \tag{4.120}
$$

The tilt coefficient can then found by taking the inner product of Equations 4.118 and 4.120, and one gets

$$
(\tilde{q}_N)_{331\cos} = (q_N)_{331\cos} + 5(q_N)_{332\sin}\theta_x . \tag{4.121}
$$

For the first-order rotation around the y-axis, θ_y, it is the $(q_N)_{330\cos}$ and $(q_N)_{332\cos}$ moments that mix into the $(q_N)_{331\cos}$ moment. The effect of the first-order rotation matrix, $\mathbf{R}$, acting on the ket vector,

$$\langle (S_N R)_{331\cos} \| X \rangle = -x^3 - xy^2 + 4xz^2 + \left(-11x^2 z - y^2 z + 4z^3\right)\theta_y, \tag{4.122}$$

is equivalent to the substitution

$$\left\{ x \to x + z\theta_y, \quad y \to y, \quad z \to z - x\theta_y \right\}. \tag{4.123}$$

There are now two ket vectors,

$$\begin{aligned} \langle X \| \left(C^{-1} S_N^T K_N\right)_{330\cos} \rangle &= -\frac{x^2 z}{10} - \frac{y^2 z}{10} + \frac{z^3}{5} \quad \text{and} \\ \langle X \| \left(C^{-1} S_N^T K_N\right)_{332\cos} \rangle &= \frac{x^2 z}{2} - \frac{y^2 z}{2}, \end{aligned} \tag{4.124}$$

which results in the relationship

$$(\tilde{q}_N)_{331\cos} = (q_N)_{331\cos} + \left(2(q_N)_{330\cos} - 5(q_N)_{332\cos}\right)\theta_y. \tag{4.125}$$

If the above calculations are repeated for the $(q_N)_{331\sin}$ moment, one gets

$$\begin{aligned} (\tilde{q}_N)_{331\sin} = (q_N)_{331\sin} &+ \left(-2(q_N)_{330\cos} - 5(q_N)_{332\cos}\right)\theta_x \\ &-5(q_N)_{332\sin}\theta_y + (q_N)_{331\cos}\theta_z. \end{aligned} \tag{4.126}$$

Since the potential derivatives have the same rotation matrices,

$$\begin{aligned} \left(\tilde{Q}_N\right)_{331\cos} = (Q_N)_{331\cos} &+ 5(Q_N)_{332\sin}\theta_x \\ &+\left(2(Q_N)_{330\cos} - 5(Q_N)_{332\cos}\right)\theta_y - (Q_N)_{331\sin}\theta_z \end{aligned} \tag{4.127}$$

and

$$\begin{aligned}\left(\tilde{Q}_N\right)_{331\sin} = (Q_N)_{331\sin} + \left(-2(Q_N)_{330\cos} - 5(Q_N)_{332\cos}\right)\theta_x \\ -5(Q_N)_{332\sin}\theta_y + (Q_N)_{331\cos}\theta_z.\end{aligned} \tag{4.128}$$

Besides rotations, one also needs to determine the effects of translations of the pendulum or source mass from their nominal design positions. Define the translation matrices as

$$\left|\tilde{M}\right\rangle = \mathbf{T}_M|M\rangle \quad \text{and} \qquad \left|\tilde{V}\right\rangle = \mathbf{T}_V|V\rangle \tag{4.129}$$

where $\left|\tilde{M}\right\rangle$ and $\left|\tilde{V}\right\rangle$ are the mass moments and potential derivatives of a translated pendulum or source mass. Let us look at first-order translations of mass moments that mix into $(q_N)_{331\cos}$. We will need the following second moments:

$$\begin{aligned}
\left\langle (S_N)_{220\cos}\middle\| X\right\rangle &= -x^2 - y^2 + 2z^2 & (K_N)_{220\cos,220\cos} &= 1/12 \\
\left\langle (S_N)_{221\cos}\middle\| X\right\rangle &= xz & (K_N)_{221\cos,221\cos} &= 1 \\
\left\langle (S_N)_{221\sin}\middle\| X\right\rangle &= yz & (K_N)_{221\sin,221\sin} &= 1 \\
\left\langle (S_N)_{222\cos}\middle\| X\right\rangle &= x^2 - y^2 & (K_N)_{222\cos,222\cos} &= 1/4 \\
\left\langle (S_N)_{222\sin}\middle\| X\right\rangle &= 2xy & (K_N)_{222\sin,222\sin} &= 1/4.
\end{aligned} \tag{4.130}$$

For the first-order z translation, Δz, only the moment $(q_N)_{221\cos}$ will mix into $(q_N)_{331\cos}$. The effect of the translation matrix, $\mathbf{T}_M$, acting to the left is

$$\begin{aligned}\left\langle (S_N T_M)_{331\cos}\middle\| X\right\rangle &= \left\langle (S_N)_{331\cos}\middle\| X\right\rangle + \Delta z \frac{\partial\left\langle (S_N)_{331\cos}\middle\| X\right\rangle}{\partial z} \\ &= -x^3 - xy^2 + 4xz^2 + (8xz)\Delta z.\end{aligned} \tag{4.131}$$

The result of the diagonal matrices $\mathbf{C}^{-1}$ and $\mathbf{K}_N$ acting on the ket vector is

$$\left\langle X\middle\|\left(C^{-1}S_N^T K_N\right)_{221\cos}\right\rangle = xz. \tag{4.132}$$

The translated moment is then

$$(\tilde{q}_N)_{331\cos} = (q_N)_{331\cos} + \left\langle (S_N T_M)_{331\cos} \middle\| \left(C^{-1} S_N^T K_N\right)_{221\cos} \right\rangle (q_N)_{221\cos} \quad (4.133)$$
$$= (q_N)_{331\cos} + 8(q_N)_{221\cos} \Delta z.$$

For the first-order horizontal translations, the m eigenvalue can change by ± 1. Thus for the Δx translation, we have

$$\left\langle (S_N T_M)_{331\cos} \middle| X \right\rangle = -x^3 - xy^2 + 4xz^2 + \left(-3x^2 - y^2 + 4z^2\right)\Delta x. \quad (4.134)$$

$$\left\langle X \middle\| \left(C^{-1} S_N^T K_N\right)_{220\cos} \right\rangle = -\frac{x^2}{6} - \frac{y^2}{6} + \frac{z^2}{3} \quad \text{and}$$
$$\left\langle X \middle\| \left(C^{-1} S_N^T K_N\right)_{222\cos} \right\rangle = \frac{x^2}{2} - \frac{y^2}{2}. \quad (4.135)$$

$$(\tilde{q}_N)_{331\cos} = (q_N)_{331\cos} + \left(2(q_N)_{220\cos} - (q_N)_{222\cos}\right)\Delta x. \quad (4.136)$$

And similarly, for the Δy translation, we have

$$\left\langle (S_N T_M)_{331\cos} \middle| X \right\rangle = -x^3 - xy^2 + 4xz^2 + (-2xy)\Delta y. \quad (4.137)$$

$$\left\langle X \middle\| \left(C^{-1} S_N^T K_N\right)_{222\cos} \right\rangle = \frac{xy}{2}. \quad (4.138)$$

$$(\tilde{q}_N)_{331\cos} = (q_N)_{331\cos} - (q_N)_{222\sin} \Delta y. \quad (4.139)$$

If the above calculations are repeated for the $(q_N)_{331\sin}$ moment, one gets

$$(\tilde{q}_N)_{331\sin} = (q_N)_{331\sin} - (q_N)_{222\sin} \Delta x$$
$$+\left(2(q_N)_{220\cos} + (q_N)_{222\cos}\right)\Delta y + 8(q_N)_{221\sin} \Delta z. \quad (4.140)$$

Next, we would like to calculate the potential derivatives that mix into $(Q_N)_{331\cos}$ under first-order translations of the source mass. From dimensional

considerations, we know that fourth derivatives mix into third derivatives under translation. Specifically,

$$\begin{aligned}
\langle (S_N)_{440\cos} \| X\rangle &= 3\left(x^2+y^2\right)^2 - 24\left(x^2+y^2\right)z^2 + 8z^4 & (K_N)_{440\cos,440\cos} &= 1/6720 \\
\langle (S_N)_{441\cos} \| X\rangle &= x\left(-3\left(x^2+y^2\right)z + 4z^3\right) & (K_N)_{441\cos,441\cos} &= 1/168 \\
\langle (S_N)_{441\sin} \| X\rangle &= y\left(-3\left(x^2+y^2\right)z + 4z^3\right) & (K_N)_{441\sin,441\sin} &= 1/168 \\
\langle (S_N)_{442\cos} \| X\rangle &= \left(x^2-y^2\right)\left(-x^2-y^2+6z^2\right) & (K_N)_{442\cos,442\cos} &= 1/336 \\
\langle (S_N)_{442\sin} \| X\rangle &= 2xy\left(-x^2-y^2+6z^2\right) & (K_N)_{442\sin,442\sin} &= 1/336.
\end{aligned} \tag{4.141}$$

For a non-Newtonian interaction, the $n=4$, $\ell=2$ derivatives,

$$\begin{aligned}
\langle (S_N)_{420\cos} \| X\rangle &= \left(-x^2-y^2+2z^2\right)\left(x^2+y^2+z^2\right) & (K_N)_{420\cos,420\cos} &= 1/168 \\
\langle (S_N)_{421\cos} \| X\rangle &= xz\left(x^2+y^2+z^2\right) & (K_N)_{421\cos,421\cos} &= 1/14 \\
\langle (S_N)_{421\sin} \| X\rangle &= yz\left(x^2+y^2+z^2\right) & (K_N)_{421\sin,421\sin} &= 1/14 \\
\langle (S_N)_{422\cos} \| X\rangle &= \left(x^2-y^2\right)\left(x^2+y^2+z^2\right) & (K_N)_{422\cos,422\cos} &= 1/56 \\
\langle (S_N)_{422\sin} \| X\rangle &= 2xy\left(x^2+y^2+z^2\right) & (K_N)_{422\sin,422\sin} &= 1/56,
\end{aligned} \tag{4.142}$$

also need to be considered. Since these $n=4$, $\ell=2$ derivatives are second derivatives of the Laplacian, they are identically zero for gravitational fields, but they shall be included in the calculation as an example of how the method is generalized to non-Newtonian potentials.

Under a first-order z translation, Δz, it is the $(Q_N)_{421\cos}$ and $(Q_N)_{441\cos}$ derivatives that mix into the $(Q_N)_{331\cos}$ derivative. The effect of the translation matrix, $\mathbf{T}_M$, acting to the left,

$$\langle (S_N T_V)_{331\cos} \| X\rangle = -x^3 - xy^2 + 4xz^2 + \left(-x^3z - xy^2z + 4xz^3\right)\Delta z, \tag{4.143}$$

is to multiply the polynomial by z. The result of the diagonal matrices $\mathbf{C}^{-1}$ and $\mathbf{K}_N$ acting on the ket vectors is

$$\begin{aligned}\langle X\|\left(C^{-1}S_N^T K_N\right)_{421\cos}\rangle &= \frac{3x^3z}{7}+\frac{xy^2z}{7}+\frac{3xz^3}{7} \quad \text{and}\\ \langle X\|\left(C^{-1}S_N^T K_N\right)_{441\cos}\rangle &= -\frac{3x^3z}{28}-\frac{xy^2z}{28}+\frac{xz^3}{7},\end{aligned} \tag{4.144}$$

and so when the inner products are taken, one gets

$$\left(\tilde{Q}_N\right)_{331\cos} = (Q_N)_{331\cos}+\left(\frac{8}{7}(Q_N)_{421\cos}+\frac{5}{7}(Q_N)_{441\cos}\right)\Delta z. \tag{4.145}$$

Similarly, for the Δx translation, one gets

$$\langle (S_N T_V)_{331\cos}\|X\rangle = -x^3-xy^2+4xz^2+\left(-x^4-x^2y^2+4x^2z^2\right)\Delta x. \tag{4.146}$$

$$\begin{aligned}\langle X\|\left(C^{-1}S_N^T K_N\right)_{420\cos}\rangle &= -\frac{x^4}{7}-\frac{x^2y^2}{21}-\frac{y^4}{7}+\frac{x^2z^2}{42}+\frac{y^2z^2}{42}+\frac{2z^4}{7},\\ \langle X\|\left(C^{-1}S_N^T K_N\right)_{422\cos}\rangle &= \frac{3x^4}{7}-\frac{3y^4}{7}+\frac{x^2z^2}{14}-\frac{y^2z^2}{14},\\ \langle X\|\left(C^{-1}S_N^T K_N\right)_{440\cos}\rangle &= \frac{3x^4}{280}+\frac{x^2y^2}{280}+\frac{3y^4}{280}-\frac{x^2z^2}{70}-\frac{y^2z^2}{70}+\frac{z^4}{35}, \text{ and}\\ \langle X\|\left(C^{-1}S_N^T K_N\right)_{442\cos}\rangle &= -\frac{x^4}{14}+\frac{y^4}{14}+\frac{x^2z^2}{14}-\frac{y^2z^2}{14}.\end{aligned} \tag{4.147}$$

$$\begin{aligned}\left(\tilde{Q}_N\right)_{331\cos} = (Q_N)_{331\cos}+\Big(&\frac{2}{7}(Q_N)_{420\cos}-\frac{1}{7}(Q_N)_{422\cos}\\ &-\frac{1}{14}(Q_N)_{440\cos}+\frac{5}{14}(Q_N)_{442\cos}\Big)\Delta x\end{aligned} \tag{4.148}$$

And for the Δy translation, one gets

$$\left\langle (S_N T_V)_{331\cos} \middle| X \right\rangle = -x^3 - xy^2 + 4xz^2 + \left(-x^3 y - xy^3 + 4xyz^2\right)\Delta y. \tag{4.149}$$

$$\begin{aligned} \left\langle X \middle| \left(C^{-1} S_N^T K_N\right)_{422\sin} \right\rangle &= \frac{3x^3 y}{14} + \frac{3xy^3}{14} + \frac{xyz^2}{14} \quad \text{and} \\ \left\langle X \middle| \left(C^{-1} S_N^T K_N\right)_{442\sin} \right\rangle &= -\frac{x^3 y}{28} - \frac{xy^3}{28} + \frac{xyz^2}{14}. \end{aligned} \tag{4.150}$$

$$\left(\tilde{Q}_N\right)_{331\cos} = (Q_N)_{331\cos} + \left(-\frac{1}{7}(Q_N)_{422\sin} + \frac{5}{14}(Q_N)_{442\sin}\right)\Delta y. \tag{4.151}$$

If the above calculations are repeated for the $(Q_N)_{331\sin}$ derivative, the result is

$$\begin{aligned} \left(\tilde{Q}_N\right)_{331\sin} = (Q_N)_{331\sin} &+ \left(-\frac{1}{7}(Q_N)_{422\sin} + \frac{5}{14}(Q_N)_{442\sin}\right)\Delta x \\ &+ \left(\frac{2}{7}(Q_N)_{420\cos} + \frac{1}{7}(Q_N)_{422\cos}\right. \\ &\left. - \frac{1}{14}(Q_N)_{440\cos} - \frac{5}{14}(Q_N)_{442\cos}\right)\Delta y \\ &+ \left(\frac{8}{7}(Q_N)_{421\sin} + \frac{5}{7}(Q_N)_{441\sin}\right)\Delta z. \end{aligned} \tag{4.152}$$

5 Design of Index IV Apparatus and Preliminary Results

5.1 Basic Description

Having made only cursory references to the design of the Index IV apparatus so far, I should like to describe the instrument in more detail before presenting the results of the initial data runs using the second harmonic method in Section 5.3. In simplified form, Figure 5.1 depicts the major components of the Index IV apparatus. Of these, the components most essential to the detection of weak forces are the pendulum mass and the torsion fiber. The design of the composition-dipole pendulum and the compensating lead stacks will be discussed in Section 5.2. The main beryllium-copper torsion fiber is 30 microns in diameter, and the weight of the 60 gram pendulum is approximately 75% of the fiber's tensile strength. As κ, the torsion fiber constant, scales as the diameter to the fourth power, there is a strong incentive to use a fiber that is as thin as possible. The main torsion fiber is suspended from an aluminum disk which is suspended by a shorter, thicker beryllium-copper fiber 150 microns in diameter. Rare-earth magnets surround but do not touch the aluminum disk. This type of arrangement, used by Luther and Towler (Luther & Towler 1984), damps out the swinging and rocking modes of the pendulum by means of eddy currents in the aluminum disk without degrading the torsional Q because the thick fiber is torsionally stiff. The top fiber support rotates inside the vacuum chamber in a silicon carbide bushing , and it is driven by a dc motor outside the vacuum chamber and thermal wall by means of pin-and-slot couplings. This allows the pins to be backed off between moves for better thermal and seismic isolation, but it also

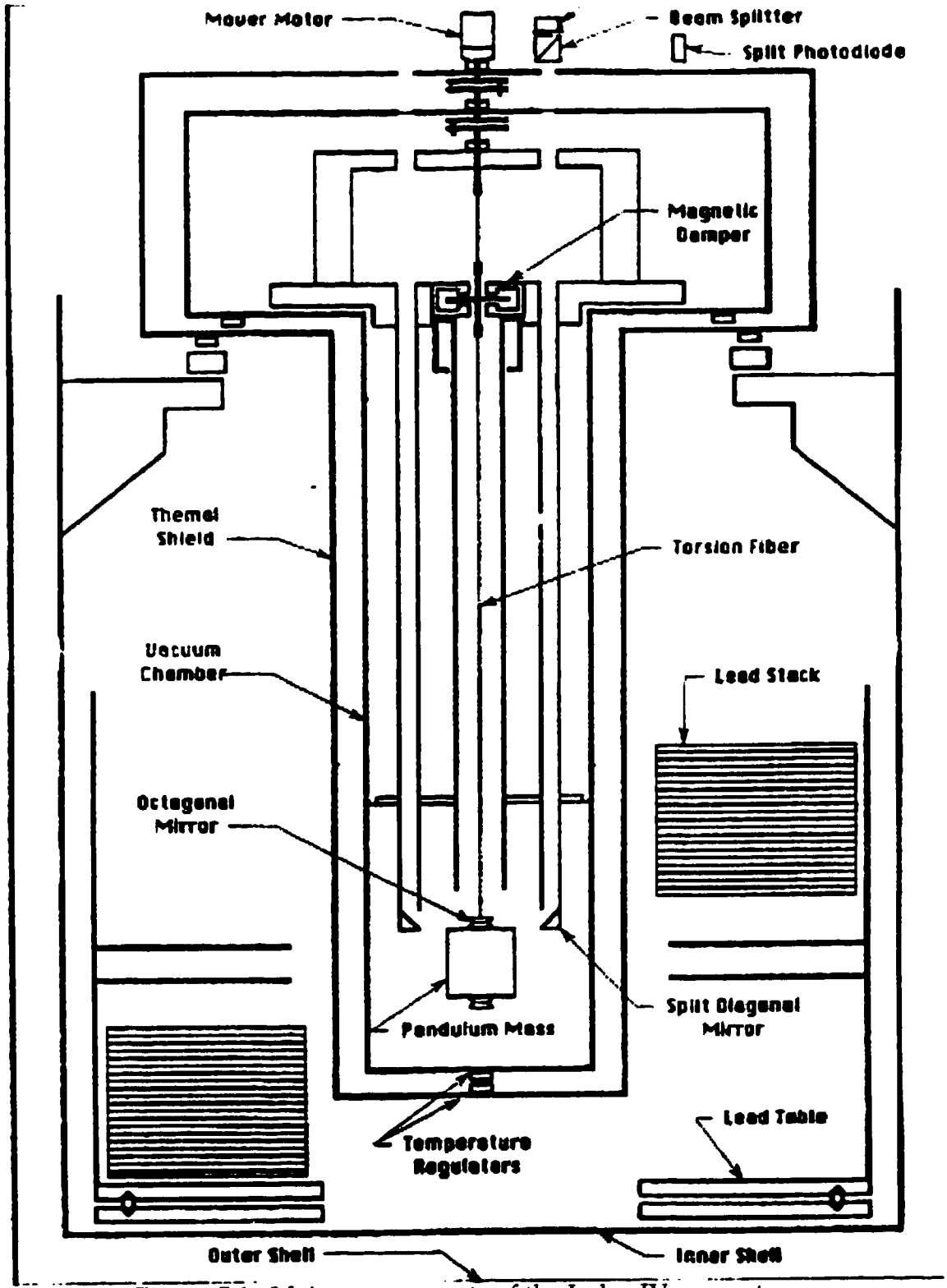

Figure 5.1. Major components of the Index IV apparatus.

prevents us from using move profiles that require a controlled reversal of rotation of the fiber support.

The azimuthal free oscillation of the pendulum mass is detected by the optical system. A visible red light, semiconductor laser emits a beam downward that passes through a 4 mm aperture, a convex focusing lens, and a beam splitter. The beam then enters the vacuum chamber, goes down a brass tube, bounces off a 45 degree diagonal mirror, bounces off one of the top and then bottom mirrors of the eight-sided edge reflector mounted on top of the pendulum mass, and then it returns via the diagonal mirror to the beam splitter where part of the beam is directed to a split photodiode to be detected. The total optical path is about 2 meters long. In order to maintain gravitational symmetry, there is a dummy optical path on the opposite side of the vacuum chamber which has neither a laser nor a photodiode. The laser beam is focused in the plane of the photodiode to a diameter of approximately 0.5 mm. The size of the beam is limited by both the diffraction off the 4 mm aperture and by the image size of the active element of the laser magnified by the 36 mm focal length convex lens. As mentioned in Section 2.4, the diagonal mirror is vertically split with a dihedral angle between the mirror halves that is slightly less than 180 degrees. This results in two crossings, separated by about 0.05 radians, off each face of the eight-sided edge reflector as the pendulum oscillates back and forth.

As the reflected beam sweeps across the split photodiode, each half generates a current proportional to the total illumination falling on that half. These currents are then converted into voltage signals by transimpedance amplifiers, and both a sum and difference voltage are generated. When the sum signal exceeds a certain threshold, the microprocessor is "armed" to record the next

crossing, and the next time that the difference signal passes through equality (i.e., when the laser spot is perfectly centered between the two halves of the photodiode), the crossing time is captured to the nearest 0.5 microsecond and stored in memory. By noting whether the difference signal passes through equality from above or below, the microprocessor can determine the direction of the crossing as either counter-clockwise (a "1" type crossing) or clockwise (a "2" type crossing). For a typical crossing speed of 0.025 radians/sec, the duration of the 0 to 5 volt transition of the difference signal is about 5 milliseconds. This is far too short to be able to filter out any errors from the swinging, rocking or bouncing modes of the pendulum which unfortunately are presently the largest source of additive noise even with the first-order tilt immunity provided by the edge reflector and the passive suppression of these modes by the magnetic damper.

The measurement of the crossing time is not instantaneous because capacitors are placed in the electronics to filter out high frequency electronic noise and reduce the photon shot noise limit. Thus the effective integration time of the crossing is approximately 0.1 millisecond, and the measured time of the crossing is delayed from the true physical time of the crossing also by about 0.1 millisecond. As long as the delay is identical for each of the crossings, the phase parameter t_{eq} absorbs all of these errors in the 10-parameter fit, and the signal parameter A_2 remains unaffected. In order for all the delays to be identical, the difference voltage vs. time should be perfectly linear as it passes through equality. If higher order curvatures are not negligible over the effective integration time, then velocity-dependent time lags can result. The 0.1 millisecond integration time is sufficiently short to make the velocity-dependent time lags

negligible yet sufficiently long so that the crossing error is neither electronic noise nor shot noise limited. The measured angular rms error per crossing is about 30 nanoradians which results from the swinging, rocking, and bouncing modes of the pendulum, and so increasing the integration time will not further reduce the error per crossing.

The inside of the vacuum chamber is maintained at a pressure of 10^{-6} torr by an ion pump. Prior to starting the ion pump, bake-out heating coils are used overnight to accelerate the outgassing of water vapor and other volatiles from the vacuum chamber surfaces, and the vacuum chamber is then evacuated by a mechanical fore pump. At 10^{-6} torr, the mean free path of the air molecules is larger than the dimensions of the chamber, and as the gas proceeds from the hydrodynamic to the ballistic regime, the viscosity drops making the air damping negligible compared to the internal losses in the fiber (see Section 4.2). Reducing the density of the air also reduces torques resulting from temperature gradients from one side of the chamber to the other. Molecules bouncing off the "hot" side recoil on average at a greater velocity than those bouncing of the "cold" side of the chamber.

Since the Index IV apparatus was originally designed to utilize the frequency method, great care was taken to ensure temperature stability of the fiber. The apparatus is inside a room with fiberglass insulation inside a man-made granite cave that is sealed off by a cinderblock wall. The diurnal temperature variation inside the room is on the order of 10 milliKelvin. The apparatus is constructed with alternating metallic shells and insulating layers. There are ten small actively controlled heaters placed throughout the apparatus whose temperature setpoints are individually adjustable by means of thermis-

tors and potentiometers placed in resistance bridges. By measuring the frequency of thermistors in RC circuits, the microprocessor can monitor the temperature at 15 locations in the apparatus, 10 of which are coincident with the temperature controllers. Because the torsion fiber is so thin, its radiative coupling to the environment is comparable to the conduction heat transfer down the fiber. A hollow copper cylinder has been placed inside the vacuum chamber around most of the length of the torsion fiber in order to provide a thermal mass whose temperature is more stable than the vacuum chamber wall. Our best measure of the change in fiber temperature is the change in the fitted frequency of pendulum oscillation. From this, we have determined that the effective time constant of the response of the fiber temperature to changes in the ambient room temperature is on the order of 14 hours.

In order to reduce the magnetic field inside the vacuum chamber, three sets of Helmholtz coils cancel the local magnetic field of the Earth, and compensating magnets are placed around the ion pump to reduce the stray field from the ion pump's permanent magnet. In addition, a single-layer, high-permeability metallic shield is placed just outside of the vacuum chamber. A diminishing 60 Hz current is run through annealing coils around the shield any time the shield is rotated or the Helmholtz coils are turned off and on in order to remove residual magnetization in the shield. We have measured the magnetic field inside the shield after annealing, and the horizontal component is less than 20 microGauss. The magnetometer can not reliably measure fields smaller than this because of currents in the wires that supply it power.

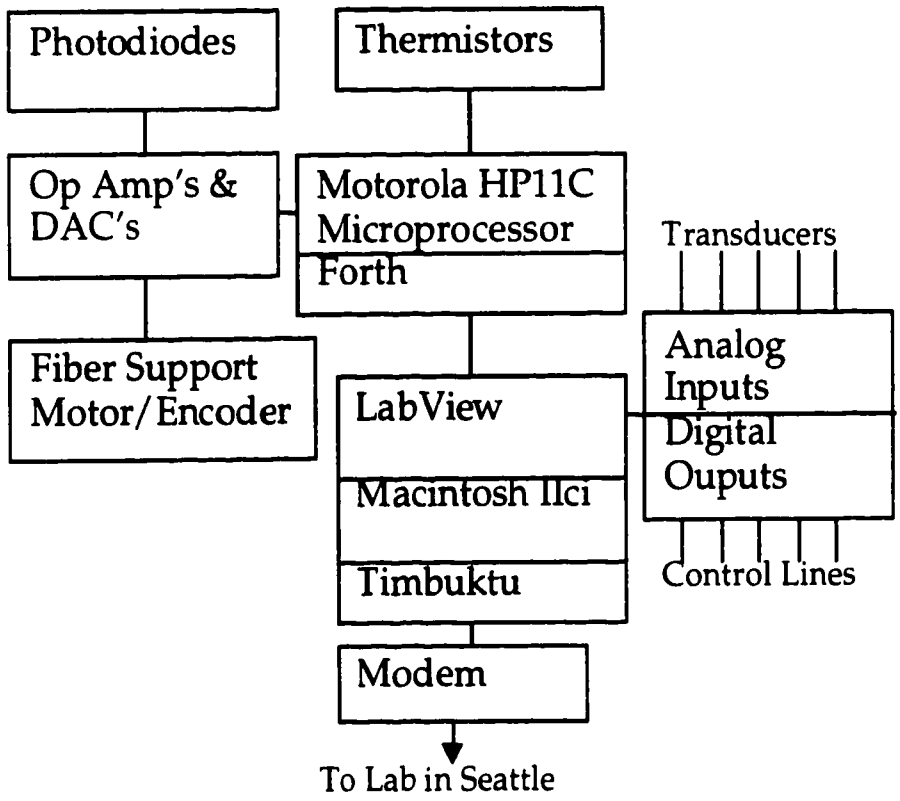

Figure 5.2. Block diagram of computer and electronic systems of Index IV.

The basic interconnections of the computer and electronic systems at Index are shown in Figure 5.2. The two major components are a Motorola HP11C microprocessor and a Macintosh IIci personal computer. Not having the computational overhead of an operating system, the Motorola HP11C is fast, simple, and reliable, and it is tasked with real-time control and data acquisition. We programmed the Motorola HP11C using the Forth programming language which is a step up from assembly code but it lacks such niceties as floating-point arithmetic. The higher level programming is done on the Macintosh IIci using LabView virtual instrument software, and it communicates its requests for fiber support moves, recent photodiode crossing times, or thermistor readings to the

Forth software on the Motorola HP11C via a serial line. The time-critical tasks of the Motorola HP11C are performed on interrupts so that the communications with the Macintosh do not interfere with them. These time-critical tasks are very basic, and so the Forth software is rarely modified. Most modifications are made to the LabView software, and since the LabView software uses an intuitive icon-based wiring diagram approach, no specialized programming knowledge is required, and undergraduates can start modifying programs very quickly after joining the research group. Another nice feature of LabView is its interactive operating environment. The operator can display as many or as few of the sub-virtual-instrument panels of a program that he wishes while the program is running. These sub-virtual-instrument panels can also be run as main programs by themselves. This aids debugging and is conducive to both bottom-up or top-down styles of programming.

The speed of the dc motor that rotates the fiber support is varied by the voltage from an 8-bit DAC controlled by the Motorola HP11C. The rotation of the motor is monitored by a 4096-step encoder. Using the encoder output, the speed of the motor is controlled during moves by a closed feedback loop that is updated every 4 milliseconds. Although all data used for analysis is acquired between moves during the free oscillation periods, having reasonable control of the motor is important so that the oscillation amplitude immediately after the move is close to the target value. This ensures that the oscillation amplitude in the eight different fiber support positions is nearly identical, and this in turn reduces one's dependence on the amplitude correction software (see Sections 4.3 and 5.3). Although our control in stopping the motor is only 1/4096 circle = 0.0015 radian, the precision with which we can determine the equilibrium posi-

tion of the oscillator is much greater. From the C, θ_1, and θ_2 parameter estimates of a 10-parameter fit, the equilibrium position of the pendulum can be measured to better than 10^{-7} radians–much better precision than is required.

We use a phone line at the Index cave that was put in by the Robbins Company when they were actively boring the tunnel. The Macintosh IIci has Timbuktu Pro software installed which allows us to call up via modem and control the Macintosh IIci at Index from a Macintosh in our laboratory in Seattle. The screen of the Index Macintosh is reproduced on the screen of the Seattle Macintosh, and the Seattle Macintosh's keyboard strokes and mouse movements are transmitted up to the Index Macintosh. Thus we can start data runs remotely and transfer the data back down to the lab. The Macintosh IIci also has a LabNB board installed that is controlled by the LabView software. The LabNB board has TTL digital out put lines that allows us to remotely switch various components off and on such as the Motorola microprocessor's reset line and a dehumidifier in the room that is cycled on and off overnight prior to opening up the vacuum chamber. The LabNB board also has a multiplexed 12-bit ADC that allows us to read various external transducers. During data acquisition, the most important transducer is the seismometer because there is a Burlington Northern rail line that runs about 500 feet away from the experiment. Needless to say, the ground motion during the passage of a train is excessive, and the seismometer data is used to reject from the data set those periods of pendulum oscillation that occur during the train passage.

5.2 Gravitational Pendulum and Lead Mass Design

In designing a torsion pendulum experiment to detect a composition-dependent force due to baryon-baryon coupling, one wants to choose materials

for the two halves of the pendulum that have a large contrast in baryon number per unit mass, Δb. As the choice of materials is not specific to the second harmonic method, the relative merits of various pairs of materials have been discussed by others (Stubbs et al. 1990; Nelson et al. 1990), and I shall not go into extensive detail on this topic. Rather I shall simply try to motivate our choice of beryllium and magnesium for the two halves of our composition-dipole pendulum. We had a strong preference for metals because they are strong, hard, easy to machine, and generally have good density homogeneity. They are electrically conductive, which alleviates electrostatic effects, and they can be electroplated or evaporated with other even less reactive metals such as gold. They have low volatility and are therefore suitable for high vacuum conditions. The elements with the greatest variation in baryon number per unit mass are the lighter elements, and this is helpful since we want to use low-density materials to reduce gravitational systematic errors. Many of the leading gravitational interactions result from second and higher moments of the pendulum due to machining errors, and so there is an advantage to using low-density materials so that a machining tolerance of a given thickness results in smaller machining-error mass moments. Another advantage of the lighter elements is that they are not ferro-magnetic and they tend to have very small magnetic susceptibilities. This is essential in order to reduce systematic errors due to magnetic interactions.

The metallic element with the lowest baryon per unit mass, $b = 0.99770$, is lithium, but as with the other alkali metals, it is too reactive to be used in pure, metallic form in ordinary laboratory conditions. The next metallic element, beryllium, $b = 0.99865$, is more stable. Its primary disadvantage is that if it is in-

haled in particulate form, it is highly toxic (ultimately fatal) to a small percentage of the population. The machining of beryllium is therefore expensive since it can only be done at specialized shops that can properly handle airborne hazardous materials. Despite this, our group felt that the low baryon per unit mass of beryllium justified its expense. Which light metals have a contrasting high baryon per unit mass? The natural candidates are magnesium and aluminum. We settled on magnesium for the second metal because its density is closer to that of beryllium, and this simplifies the gravitational design of the pendulum. The contrast in baryon per unit mass for our Index IV pendulum is therefore

$$\Delta b = b_{Mg} - b_{Be} = 1.00062 - 0.99865 = 0.00197. \tag{5.1}$$

Another important consideration is the choice of torsion fiber material. For a fiber that can support a given weight pendulum, one would like the largest deflection per torque possible. The figure of merit for fibers is therefore

$$\frac{(tensile\ strength)^2}{shear\ modulus}. \tag{5.2}$$

Our group has chosen beryllium-copper for the torsion fiber at Index IV. Two other commonly use materials, tungsten and quartz, have superior figures of merit. Tungsten, however, displays more non-linear behavior than beryllium-copper, and so we are reluctant to use it for an oscillating torsion pendulum experiment, and the tensile strength of quartz fibers degrade well below their theoretical value when stressed in the presence of moisture. In order to use quartz, the apparatus must be designed so that the fiber is not placed under tension until it is in a vacuum. Newman (Beilby et al. 1994) has achieved quality factors as high as 300,000 with bare quartz fibers, but bare quartz is not elec-

trically conductive and thus does not provide a good grounding path to prevent electrostatic charges from building up. He has tried several types of conductive coatings, but they all degrade the quality factor of the fiber to less than 1000. Our group is considering quartz fibers for future generations of experiments, but until these problems are solved, they are not feasible for use with our present Index IV apparatus.

The deflection per unit torque can also be increased by making the torsion fiber longer. The torsion fiber of the Index IV apparatus is 70 centimeters long, and it can not be lengthened without constructing a new vacuum chamber. The length of the fiber belongs to a class of design parameters for which there is no fundamental limit or well-defined optimum. The limit is placed by one's ability, one's patience, one's funding, or simply reaching a point of diminishing returns. Similarly, the optimal value for the machining tolerance in fabricating the pendulum, or the optimal value for temperature variations of the fiber, or the optimal value for ambient gravity gradient variations due to changes in the local water table are all the same: make them as small as possible. In order to have a well-posed optimization problem, one must assume that easy methods for reducing these quantities have been exhausted, and one should therefore treat them has hard constraints within which one tries to maximize the signal strength by varying the remaining free design parameters.

When we were designing the pendulum for the Index IV apparatus, the materials for the two halves of the pendulum, the fiber material, and the length of the fiber were chosen. The general construction of the pendulum also had been determined. The basic mass distribution was essentially equivalent to two thick rings enclosed in a thin cylindrical can with small, eight-sided edge reflec-

tors on the top (to reflect the laser beam) and bottom (to match the top mirror for gravitational symmetry). This left four free design parameters–the mass of the pendulum, the radius of the pendulum, the height of the pendulum, and the diameter of the fiber–that could be adjusted to maximize the signal. The height/radius ratio of the pendulum is constrained by the requirement that the cylindrically symmetric second moment, $M_{220\cos} = -M_{xx} - M_{yy} + 2M_{zz}$, be made zero. This ensures that there are no second moments in the design that can mix into the offending "2-1" moments, M_{xz} and M_{yz}, if the pendulum is hung slightly off-center causing its axis of symmetry to tilt away from true vertical. Since most of the mass is concentrated in the two rings that determine the height and radius of the cylinder,

$$height \equiv \sqrt{2}\ radius \quad \Rightarrow \quad size \propto height \propto radius, \tag{5.3}$$

and the two free parameters "height" and "radius" are replaced by a single linear dimension "size".

Because the composition-dipole moment of the pendulum, $\mathbf{p}_b$, increases with size (see Eq. 2.11), one might naively assume that the pendulum should be as large as possible. However, the mass moments that couple to gravitational field gradients also increase with size. The leading "2-1" moments, M_{xz} and M_{yz}, result primarily from machining errors, and so they increase by two factors of "size" because of the increase in machined surface area and another two factors of "size" because they are second moments. Thus

$$\text{"2-1" } signal \propto \frac{\sqrt{M_{xz}^2 + M_{yz}^2}}{\kappa} \propto \frac{size^4}{\kappa}. \tag{5.4}$$

Obviously, the gravity interactions get bigger much faster with size than the signal does. One is inclined therefore to go to the other extreme and try to make the pendulum as small as possible. When we were designing the Index IV pendulum, we intended to use the frequency method, and so we were concerned about the limit imposed by temperature variations in the fiber. These variations are solely a function of the temperature coefficient of the shear modulus of the fiber and are independent of the diameter of the fiber or the mass and size of the pendulum. It does not make sense to reduce the size of the pendulum to further reduce the gravity gradient couplings once the frequency variations have become the dominant systematic error. Although we did not have exact numbers for what those variations were, we had some rough estimates, and the optimal pendulum size for a given fiber diameter is that which makes the gravitational and temperature variations roughly equal in size. This constraint imposes the relationship

$$\text{"2 - 1" } signal \equiv \left(\frac{\Delta\omega}{\omega_o}\right)_{temperature} \quad \Rightarrow \quad size \propto \kappa^{1/4}. \tag{5.5}$$

The above relationship (Eq. 5.5) only limits the size of the pendulum, not its mass. For a given diameter fiber, the upper limit on the mass is set by the tensile strength of the fiber, and this imposes the relationship

$$mass \propto weight \propto diameter^2 \quad \text{and} \quad \kappa \propto diameter^4 \quad \Rightarrow \quad \kappa \propto mass^2. \tag{5.6}$$

Having been constrained by the relationships in Equations 5.5 and 5.6, the signal strength scales with pendulum mass as

$$CDF\ signal \propto \frac{mass * size}{\kappa} \propto \frac{mass * mass^{1/2}}{mass^2} = \frac{1}{mass^{1/2}}, \tag{5.7}$$

and it appears that the optimum pendulum mass is zero. This is not correct because we have assumed that the composition-dipole moment is proportional to the total mass of the pendulum when in fact it is only proportional to the "active" portion of the mass comprised of he beryllium and magnesium halves. There is also a "dead" portion of the mass, the eight-sided edge reflectors, which neither contribute to the signal nor scale with size. Given the optical design, the eight-sided edge reflectors must be able to reflect 2 mm diameter laser spots, and therefore they can not be made smaller. The weight of these mirrors (about 2 grams each) has to be supported by the fiber, and so the diameter of the fiber can not be made arbitrarily small. A more realistic scaling of the signal strength is

$$CDF\ signal \propto \frac{(mass - mirror\ mass)size}{\kappa} \propto \frac{(mass - mirror\ mass)}{mass^{3/2}}. \qquad (5.8)$$

This scaling of CDF signal versus mass is plotted in relative units in Figure 5.3, and the maximum signal is obtained for a mass that is three times the mirror mass.

The actual mass of the Index IV CDF pendulum is 60 grams, and the total mass to mirror mass ratio, $60/(2+2) = 15$, results in a signal strength that is roughly 63% of optimal. To be totally honest, our original design process was not as systematic as the optimization presented above, and we erroneously relied on a more intuitive sense of what constituted a reasonable total mass to mirror mass ratio. Hindsight, of course, is 20-20. Here, our decision to use beryllium in the Index IV CDF pendulum has come back to haunt us because it becomes much more expensive to make small revisions to the pendulum design. Even if we had made a new pendulum, it would have been a wasted ef-

fort once we switched from the frequency method to the second harmonic method because then the temperature variations are no longer a leading problem, and the rocking modes of the pendulum therefore replace the temperature variations as a constraint in

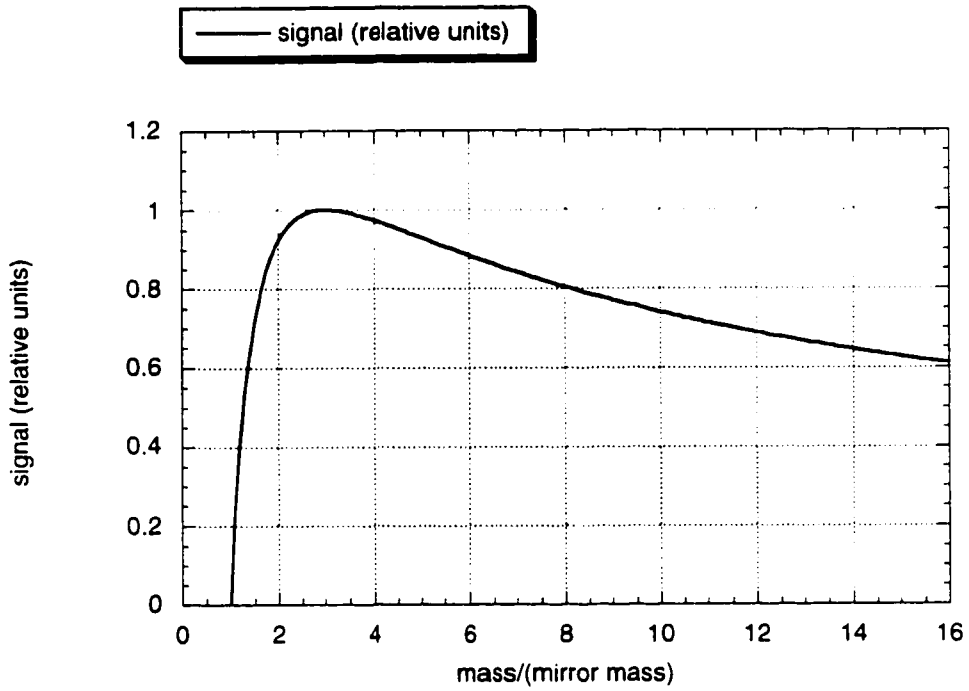

Figure 5.3. Plot of how CDF signal strength scales with the mass of the pendulum. The pendulum design is constrained by gravity gradient interactions, variations in the fiber temperature, and the "dead" mass of the mirrors that don't contribute to the signal. Theoretically, the total pendulum mass should be three times the mirror mass.

the optimization problem. Even designing to those new criteria could have been a mistake because as I am writing this section (April 99), we have looked more closely at the error propagation of the optical system once again, and there are indications that the additive error per crossing due to the rocking modes can be reduced by more stringent optical alignment. Although this has

yet to be confirmed, there is hope that the Index IV experiment could become thermal-noise limited, and that would change the optimization problem yet again. This experience emphasizes that it is not the details of a particular optimization which are important since the optimization problem will change as improvements are made, but rather it is more important to have a firm theoretical grasp of all the various noise processes and systematic errors so that the design can be altered as conditions change. That is why I have dedicated the majority of this thesis to presenting my best understanding of those noise processes and systematic errors.

Besides the CDF Index IV pendulum, our group has also constructed a null pendulum that is made entirely of magnesium and therefore has zero composition-dipole moment. By getting a null result with the null pendulum, we feel more confident that we have truly suppressed most systematic errors which makes the results from the CDF pendulum much more credible. The magnesium end caps, which form the top and bottom of the cylinder in both the CDF pendulum and null pendulum design, each have eight circular holes cut out of them to reduce their mass. Since the edge-reflectors also have eight-fold rotation symmetry and all the other pieces of the null pendulum are cylindrically symmetric, the only intentional mass moments in the null pendulum design are $m = \{0,8,16...\}$. As there are no $m = 8$ mass moments below eighth moments, the null pendulum design is cylindrically symmetric through seventh moments. We have also made the null pendulum top-bottom symmetric about the horizontal mid-plane which makes all the $\ell = \text{odd}$, $m = 0$ moments zero. This leaves only the $\ell = \text{even}$, $m = 0$ moments to consider. Because our fiber can not safely support a mass greater than 60 grams, the total mass, the $M_{000\cos}$

moment, is designed to be 60 grams by choosing an appropriate cross-sectional area for the main top and bottom rings of the pendulum. In order to provide tilt insensitivity, the $M_{220\cos}$ moment is designed to be zero by choosing the appropriate vertical separation between the top and bottom rings of the pendulum. The couplings to a tilted $M_{440\cos}$ moment are small enough to be ignored.

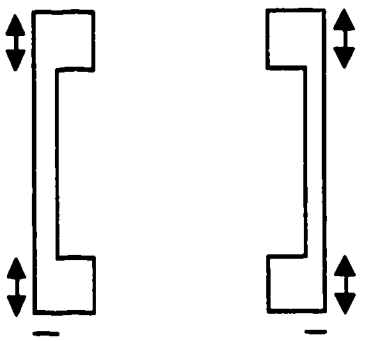

Figure 5.4. Cross-section of CDF pendulum half-cylinders. In the CDF pendulum, the two dimensions indicated by the arrow and dashes are slightly different on the two sides to compensate for the different densities of the magnesium and beryllium.

The design of the CDF pendulum is very similar to the null pendulum, but with one small complication: the density of the beryllium and magnesium halves are not identical. In fact, the "magnesium" half is not actually pure magnesium but a magnesium alloy chosen because its density is close to that of beryllium. Even so, the densities differ by 1%, and some of the gravitational symmetries that were present in the null pendulum design have been broken. In particular, if the density difference were ignored and both halves were made with identical dimensions, all the $\ell = \text{odd}$, $m = \text{odd}$ moments of the CDF pendulum would fail to be exactly zero. The two most disturbing of these moments are the $M_{110\cos}$ moment because it will shift the center-of-mass and cause

the pendulum to tilt and the M_{310cos} moment because it can interact directly with the V_{310cos} and V_{310sin} components of the local gravitational potential and produce a false $m = 1$ signal. Figure 5.4 displays a cross-section through the magnesium and beryllium halves of the CDF pendulum (the endcaps and other pieces of the pendulum are not shown). The thickness of the 180 degree arcs of the top and bottom ring masses (indicated by arrows in Figure 5.4) are made slightly different in the magnesium and beryllium halves. Similarly, the thickness of the cylindrical walls (indicated by dashes in Figure 5.4) are made slightly different in the magnesium and beryllium halves. These two degrees of freedom in the design allow the M_{110cos} and M_{330cos} to be re-zeroed.

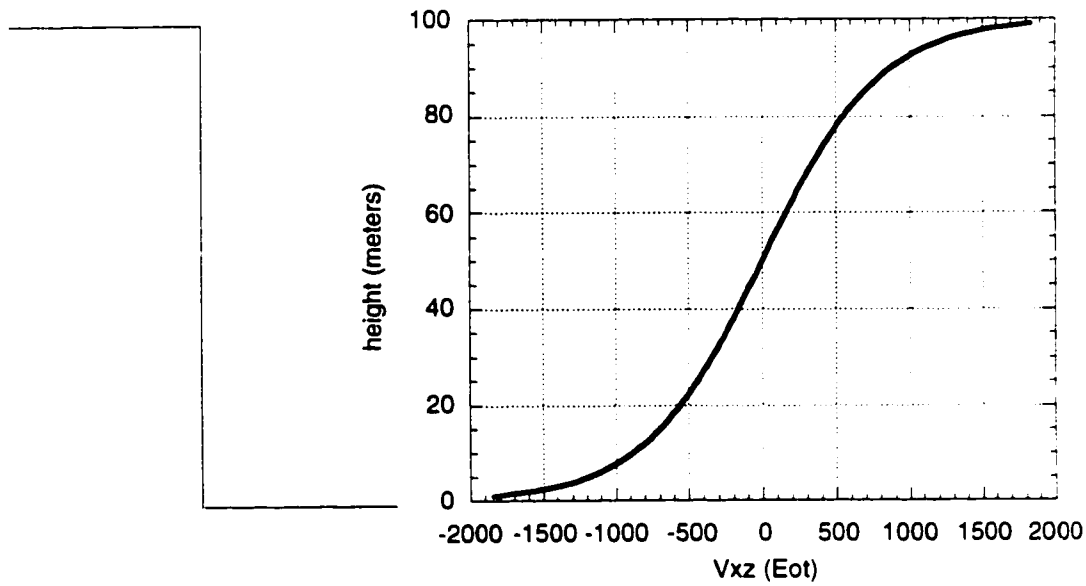

Figure 5.5. Side view of an ideal, 100-meter, semi-infinite granite cliff and the V_{xz} gravitational potential at the cliff face as a function of height.

Although all the important gravitational mass moments have been designed to be zero, there remain the mass moments due to machining errors. The most significant of these are the "2-1" mass moments which produce the largest contribution to a false $\cos(\phi)$ or $\sin(\phi)$ signal. In a Cartesian basis, these moments are M_{xz} and M_{yz}, and they couple to V_{xz} and V_{yz} derivatives of the local gravitational potential. This is unfortunate considering the placement of the Index IV apparatus, which is at the bottom of a cliff face. Figure 5.5 illustrates the problem for an ideal, semi-infinite, 100-meter granite cliff face, a reasonable first approximation of the cliff face at Index. The ideal placement for a torsion pendulum experiment would be half way up the cliff face where V_{xz} is zero. Needless to say, the Robbins Company did not find 50 meters up the cliff face the most convenient location to drill a test tunnel, and so the actual locaition of the tunnel is at the base of the cliff where the V_{xz} reaches a maximum, and actually becomes infinite for a cliff with idealized, perfectly sharp corners. The actual V_{xz} inside the tunnel is on the order of 1000 Eot = $10^{-6}\,\mathrm{sec}^{-2}$. If no attempt is made to cancel this gravitational potential derivative from the cliff, we see a false signal of 400 nanoradians of second harmonic due to couplings to the M_{xz} and M_{yz} moments of the CDF Index IV pendulum.

Since the goal of the Index IV experiment is to measure the $m = 1$ signal to sub-nanoradian accuracy, this is clearly unacceptable and the local V_{xz} potential must be cancelled. The concept for canceling the V_{xz} potential is similar to the field compensators used by the Eot-Wash group (Su et al. 1994), but since we have a much larger initial potential, our compensator is more massive—about 1000 pounds of lead. Although the magnitude of the uncancelled V_{xz} potential is larger at the Index IV site than the Eot-Wash site, the time variation in the V_{xz}

potential is actually smaller because the granite cliff is less porous and the effect of changes in the water table due to seasonal rainfall is therefore less. The goal of the compensator is to reduce V_{xz} and V_{yz} to less than 1 Eot, a factor of 1000 reduction, and thereby reduce the false $m = 1$ signal to less than 0.4 nanoradians of second harmonic. This factor of 1000 reduction in $\sqrt{V_{xz}^2 + V_{yz}^2}$ can be empirically verified using a pendulum with an exaggerated M_{xz} mass moment. The ratio of the exaggerated M_{xz} mass moment to the CDF pendulum M_{xz} mass moment is about 500. This has been empirically determined by taking data with both pendula in the uncompensated cliff V_{xz} potential, and then taking the ratio of their $m = 1$ signals.

The next $m = 1$ potentials to worry about are the "3-1" third derivatives of the potential. We have constructed a pendulum with an exaggerated "3-1" mass moment, and we empirically measure an $m = 1$ signal of 50 nanoradians of second harmonic in the uncompensated cliff field. At first glance, this seems remarkably small considering that the exaggerated "2-1" pendulum produces an $m = 1$ signal of 20,000 nanoradians. The mystery is solved by looking at how the various potential derivatives integrate. If you have an arbitrary density function that depends only on the spherical co-ordinates θ and ϕ and is independent of r, and you then integrate over that density distribution between $r = a$ and $r = b$, the "3-1" potential,

$$\int_{r=a}^{r=b} \oiint \frac{\rho(\theta,\phi) Y_1^3(\theta,\phi)}{r^4} d\Omega r^2 dr = \text{const} \times \left(\frac{1}{a} - \frac{1}{b} \right), \tag{5.9}$$

is finite even in the limit as $b \to \infty$. Its magnitude is dominated by the value of the inner radius, a. Similarly, the "4-1" potential,

$$\int_{r=a}^{r=b}\oiint\frac{\rho(\theta,\phi)Y_1^4(\theta,\phi)}{r^5}d\Omega r^2dr = \text{const}\times\left(\frac{1}{a^2}-\frac{1}{b^2}\right) \tag{5.10}$$

is also finite in the limit as $b\to\infty$. The "2-1" potential, however,

$$\int_{r=a}^{r=b}\oiint\frac{\rho(\theta,\phi)Y_1^2(\theta,\phi)}{r^3}d\Omega r^2dr = \text{const}\times\ln\left(\frac{b}{a}\right) \tag{5.11}$$

diverges logarithmically, and therefore can become arbitrarily large. Although we have not empirically verified the ratio of the exaggerated "3-1" mass moment to the "3-1" mass moment of the CDF pendulum, we believe it greater than 100, and so the "3-1" potential from the cliff does not have to be compensated in order to achieve sub-nanoradian accuracy with the CDF pendulum.

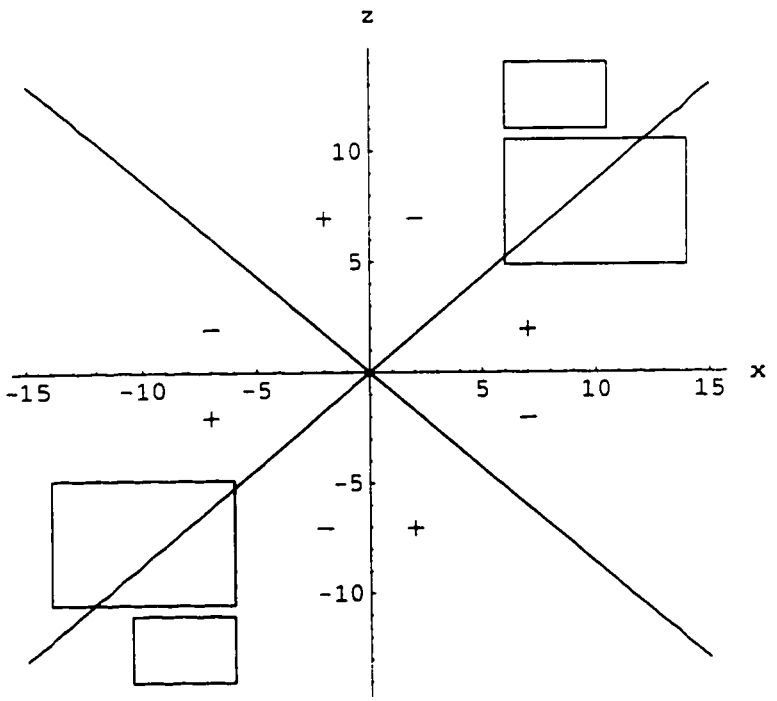

Figure 5.6. Cross-section of lead compensator mass in the vertical xz-plane. All of the mass is placed in the positive xz quadrants to maximize the "2-1" potential, V_{xz}. The positive and negative regions of the "4-1" potential are indicated. The "4-1" potential of the compensator is designed to be zero. The scale is in inches.

The "3-1" potentials and "4-1" potentials from the cliff are negligible because of its distance from the pendulum. If care is not taken, however, the "2-1" compensator can inadvertently create "3-1" potentials and "4-1" potentials because the inner radius of the compensator is only 6 inches. The lead plates of the compensator are designed with point inversion symmetry about the pendulum. This naturally produces a large V_{xz} by only placing mass in the quadrants for which V_{xz} is positive, but it also has the advantage of making all the $\ell = \text{odd}$ potentials zero. Most importantly, the "3-1" and "5-1" potentials are made zero. The "4-1" potential is made zero by choosing the appropriate height for the lower edge of the stack (see Figure 5.6). The stacks then straddle the "4-1" potential nodes and have mass in both the positive and negative regions. Similarly, the exaggerated "2-1" pendulum is also designed with point inversion symmetry, and the height of the half-rings is chosen to make the "4-1" mass moment zero. The first $m = 1$ interaction between the lead compensator and the exaggerated "2-1" pendulum after $\ell = 2$ is the "6-1" interaction which is a factor of 24,000 weaker than the "2-1" interaction. Since we only need to trim V_{xz} by a factor of 1000, this "6-1" interaction can safely be ignored.

In fact, both components of the "2-1" potential, V_{xz} and V_{yz}, need to be cancelled to 1 Eot, and this requires two degrees of freedom in the lead compensator. The lead compensator can be rotated to an arbitrary azimuth, but changing the magnitude of its "2-1" potential requires unstacking and restacking the lead plates in order to preserve inversion symmetry. That process is too tedious to be used for the final steps of trimming the "2-1" potential. The lead compensator mass was therefore designed to compensate for 98% of the cliff field, and the final 2% of the field (20 Eot) is trimmed by a stack of 6 lead bricks

placed a distance of 24 inches from the pendulum. To trim both V_{xz} and V_{yz} to 1 Eot, the azimuthal and radial position of the stack is moved iteratively and data is taken with the exaggerated "2-1" pendulum until the cancellation of the "2-1" potential is verified. The stack of lead bricks is placed on cinder blocks so that the vertical extension of the stack straddles the "3-1" node line and thus does not significantly alter the "3-1" potential. The stack is small enough and far enough away to not be a concern for the "4-1" potential.

5.3 Preliminary Index IV Results

Now that the theory of the second harmonic method and the design of the Index IV apparatus has been presented, I am ready to answer a question would naturally be posed by many experimentalists. "When the method is applied to a real apparatus, does it actually work?" To answer this, I will present a set of ten data runs, each approximately 3 days in duration, which comprise our group's best data set to date with the Index IV apparatus. The results are designated "preliminary" because the set of data was a diagnostic set of runs taken after we had placed a cylindrical copper insert inside the vacuum chamber to see if it would reduce the slow temporal variations in signal that our group had observed in out initial set of runs. We believed this wandering signal resulted from ballistic molecules outgassing from the aluminum surface of the vacuum chamber and then striking the surface of the composition-dipole pendulum. Since the average momentum transferred from the gas molecules to the pendulum depends upon the surface roughness, there was a differential torque applied to the outer magnesium and beryllium surfaces because the roughness of their machined surfaces differed even though they were geometrically identical on a macroscopic scale. Our group believed that the majority of the outgassing

molecules came from a weld site in the vacuum chamber. If our conjecture were true, then placing a cylindrical copper insert inside the vacuum chamber between the weld and the pendulum should remove the observed slow variation in signal due to the outgassing, and the results from the different runs in the data set should be statistically consistent with one another unlike those of the initial data set. The purpose of this set of ten data runs was to prove or disprove this hypothesis. As it turned out, the cylindrical copper insert did indeed remove the problem.

In terms of how the data is analyzed, there is no difference between diagnostic runs and true data runs that are to be published, and at first glance, this emphasis on what appears to be a merely psychological distinction may seem to be overly fastidious. All statistical measures of significance, however, demand that an *a priori* decision be made as to size of the data set and the criteria for rejection of data. Deciding these things after "peeking" at the data is a dangerous game that can open the door to unintentional bias. The capacity of the human mind to see the patterns it wants to see in data is truly phenomenal, and without the straightjacket of rigorous statistical protocols, all sorts of mischief can result. This is particularly true of null experiments where one "knows" what the result should be, and one's psychological reaction to a null and a non-null result are distinctly different. So for the sake of truth in advertising, I want to emphasize that decisions about the size of the data set and rejection criteria were not consciously made prior to taking this data set of 10 runs. Our sole purpose was to determine the efficacy of the cylindrical copper insert. If it was successful, we were then going to go ahead and take a true set of data runs for publication. Unfortunately, there have been other systematic effects that we

have been busy identifying and eliminating. All of these subsequent systematics, however, appear to rotate with the vacuum can and can therefore be subtracted off from the true couplings to the cliff and Earth. Let me put off further discussion of these systematic effects until I have presented the results of the set of 10 data runs.

Although this data set is a little suspect for the purposes of making an entirely unbiased claim about the existence or non-existence of a composition-dependent force of a given magnitude, it is perfectly adequate to meet the less stringent requirements of this thesis. Namely, does the data demonstrate that the second harmonic method is a useful torsion pendulum method with sufficient promise to merit further application? My admittedly biased opinion is that it does.

I shall now concentrate on one of the 10 data runs, 2/27/97.1, as representative of the data set.

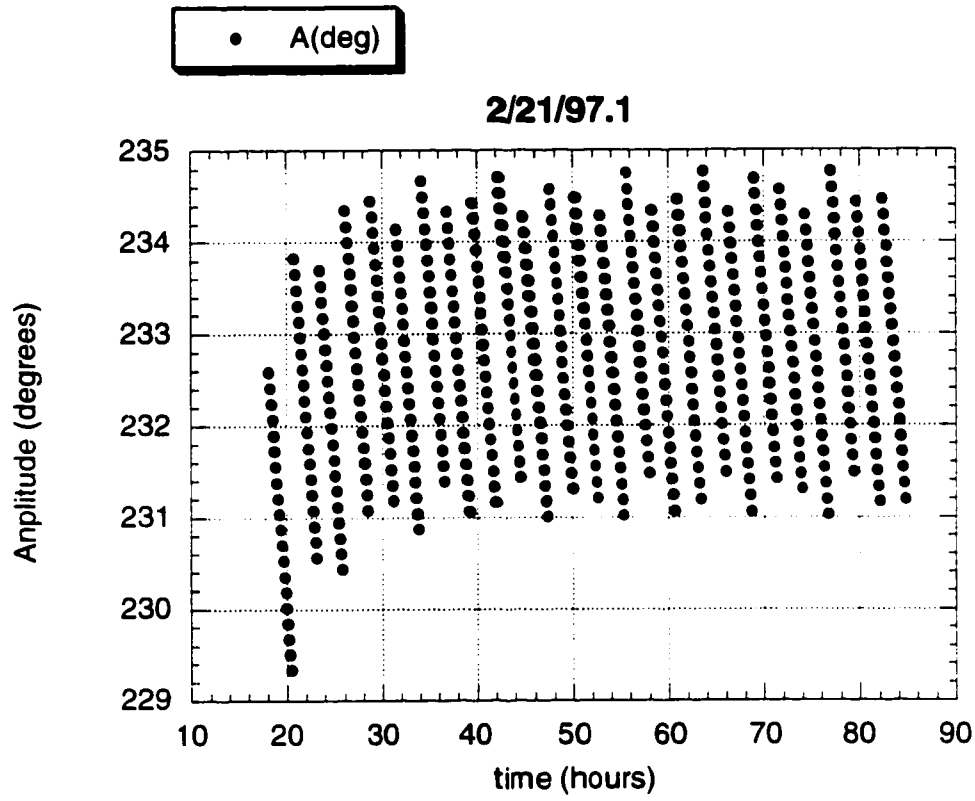

Figure 5.7. Plot of 10-parameter estimates of oscillation amplitude versus time. There is one fit per oscillation period. The slow decreases in oscillation amplitude are caused by internal losses in the fiber. The sudden increases in amplitude occur when the fiber support is rotated to a new position.

During 2/27/97.1, the fiber support was rotated 24 times, and after the end of each move, the pendulum was allowed to freely oscillate for 21 oscillation periods (about 2 hours and 40 minutes) before the next move was begun. For each of these 21-period strings of data, parameter estimates from 20 separate 121-type 10-parameter fits could be obtained. The parameter estimates of $\hat{A}$ versus $\hat{t}_{eq}$ (i.e., oscillation amplitude versus time) are plotted in Figure 5.7. Looking at Figure 5.7, one can see the oscillation amplitude is mostly constrained to a fairly narrow range between 231° and 234.5°. This is desirable because it reduces the

dependence on amplitude correction software to normalize all the results to a nominal amplitude. The amplitude range could be restricted even further by moving more often, but this reduces the effective duty cycle of data collection because there is no useful data collected during the moves and also a portion of the data immediately after each move has to be rejected to allow for the fiber relaxation transients to sufficiently attenuate (see Section 4.2). In order to have the same oscillation amplitude after the move as before the move, the nominal move strategy is to start a uniform speed move just as the pendulum is passing clockwise through the fiber equilibrium position, match the rotation rate of the fiber support to the angular speed of the pendulum so that the rotation speed of the pendulum is constant during the move, and then stop the rotation of the fiber support when the desired new equilibrium position is reached. Since the angular kinetic energy of the pendulum is the same at the end of the move as it was at the beginning, the pendulum will resume its original oscillation amplitude when the move ends. When the damping due to internal fiber losses is taken into account, the goal is to have the amplitude after the move to be slightly greater than at the beginning of the move, and so the move is begun slightly earlier than the pendulum's passage through the equilibrium position so that energy is imparted to the pendulum during the move.

Data need to be acquired with the equilibrium position of the fiber centered on each of the eight mirror faces of the edge-reflector. Since we want to spend as little time as possible moving the pendulum, one might think that we simply rotate the fiber support by 45° to the next mirror face during each move. In fact, we rotate it 225° (5 mirror faces) during each move. There are two reasons for this. Looking at Figure 5.7, one can see that the amplitude range of the

first few positions is somewhat lower than the subsequent positions; it takes a few moves before the amplitude range settles into a steady-state value. This convergence towards a steady-state amplitude range is more rapid for 225° moves than it would be for 45° moves. The second advantage of 225° moves is that they "chop" an $m = 1$ signal at a higher effective frequency than do 45° moves, and therefore we gain greater immunity to whatever slow drifts in the second harmonic amplitude may exist.

Of all the parameter estimates of the 10-parameter fit, it is the second harmonic amplitude estimates, $\hat{A}_2$, that are most important because they are used to detect the existence of any external potential coupling, $U_{ext}(\theta)$. The raw 121-type 10-parameter estimates of the second harmonic amplitude for the data run 2/21/97.1 are plotted versus time in Figure 5.8.

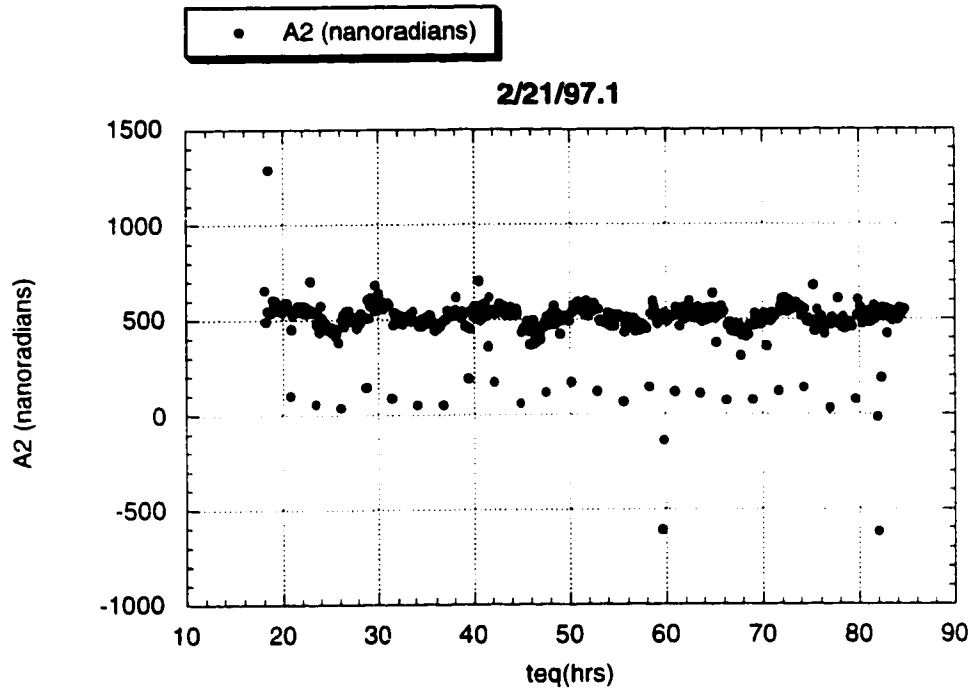

Figure 5.8. Plot of raw 10-parameter fit estimates of the second harmonic amplitude, A_2, versus time.

At first glance, this data appears fairly ugly when one considers that we want to achieve sub-nanoradian precision. However, we know that fiber relaxation transients distort the second harmonic estimate, so we uniformly strip out the first five periods of data after each move. Simultaneous seismic data was recorded during the run, and this allows us also to strip out the data that occurred during train passages since these data have an excessive amount of noise. There are a few extreme outliers that do not occur during train passages which we believe are due to spontaneous "fiber quakes". Since the additive noise process is quite gaussian, these outliers are very easy to identify and reject at the 3σ level. When all of these data are rejected, the remaining data appear much better (see Figure 5.9).

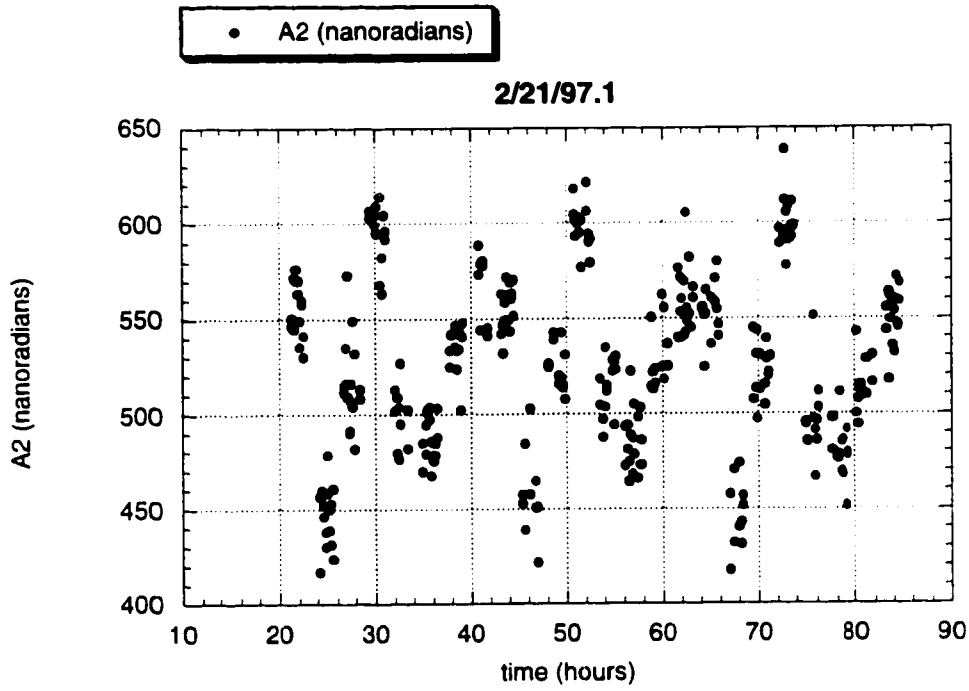

Figure 5.9. Plot of second harmonic estimates after the data has been "cleaned up". The first five oscillation periods after each move were stripped out, the data during train passages move were stripped out, and extreme outliers due to fiber quakes were rejected. In addition, 121-type and 212-type fits were averaged to eliminate errors due to linear drifts in oscillation frequency.

In addition to throwing out fits we have deemed unacceptable, we have also averaged the remaining 121-type fits (i.e., fits centered on a clockwise zero-crossing) and 212-type fits (i.e., fits centered on a counter-clockwise zero-crossing) to produce $\hat{A}_{2lf}$ estimates. All the fits plotted in Figure 5.9 are $\hat{A}_{2lf}$ estimates whereas the fits plotted in Figure 5.8 are all simple 121-type $\hat{A}_2$ estimates. As discussed in Section 3.6, these $\hat{A}_{2lf}$ fits are immune to first-order to drifts in oscillation frequency. Figure 5.10 depicts the specific manner in which we average the fits from each 21-period span of free oscillation data.

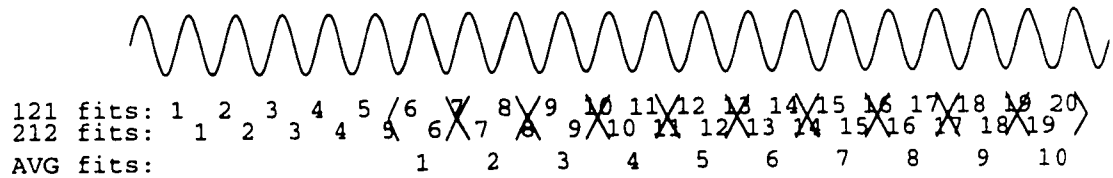

Figure 5.10. For each 21-period stretch of data between moves, 20 of the 121-type 10-parameter fits and 19 of the 212-type 10-parameter fits can be obtained. The first 5 periods of data are thrown out, and the remaining fits are averaged as indicated above to produce 10 $\hat{A}_{2lf}$ estimates that are immune to linear drifts in frequency.

Note that for the manner in which the fits are averaged, the 10 $\hat{A}_{2lf}$ fits are non-overlapping. This is done so that the 10 $\hat{A}_{2lf}$ fits are statistically independent for additive "white" noise, and therefore the residues of the overall second harmonic amplitude versus angular equilibrium position (A_2 vs. ϕ) fit that is to be done (see Eqs. 5.12 and 5.13) will provide a statistically reliable estimate of the error in the $m=1$ signal. The observant reader might notice that for each 21-period stretch of data corresponding to a single equilibrium position, there are more than 10 $\hat{A}_{2lf}$ estimates plotted in Figure 5.9. In fact, before the stripping of outliers and train passage data, there are 20 $\hat{A}_{2lf}$ estimates per equilibrium position, 10 from the "fixed mirror" crossings and 10 from the "movable mirror" crossings (see Section 2.4), and both are used in the overall A_2 vs. ϕ fit. For clarity, only "fixed mirror" estimates were plotted in Figure 5.8.

I have indicated that we use $\hat{A}_{2lf}$ estimates in our data analysis to gain immunity to first-order drifts in the oscillation frequency. How serious a problem are these frequency drifts? To demonstrate the magnitude of the problem, the 121-type 10-parameter estimates of the frequency, $\hat{\omega}$, for the data run 2/21/97.1 are plotted versus time in Figure 5.11.

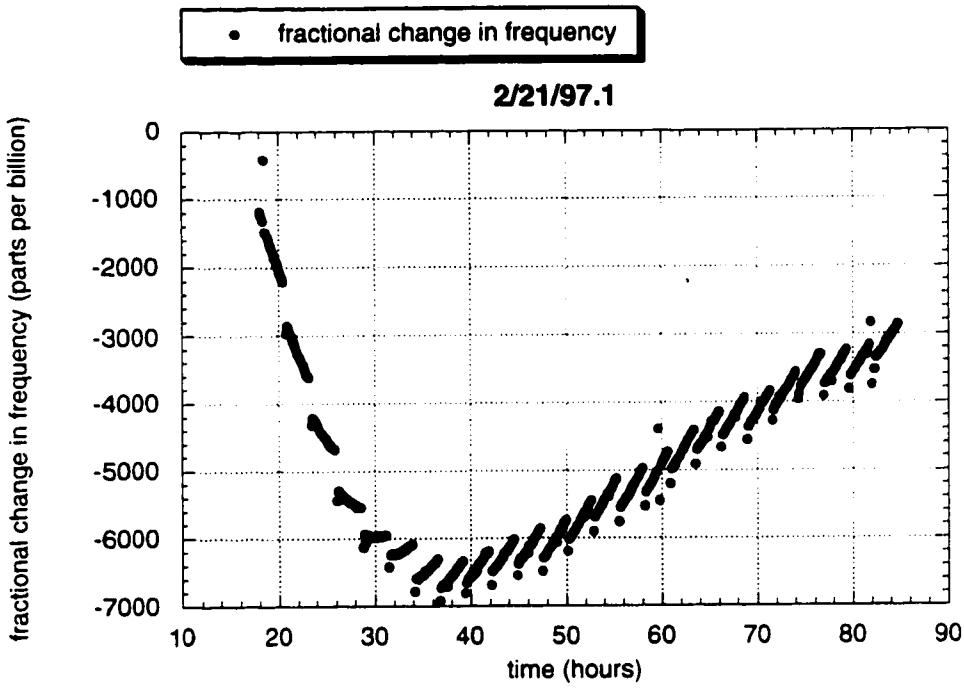

Figure 5.11. Fractional variation in frequency for data run 2/21/97.1. To detect a signal using the frequency method, a magnitude of one part per billion is roughly comparable to one nanoradian using the second harmonic method. Compare to Figure 5.9.

The large secular variation in frequency of about 6000 parts per billion is due to a variation in the fiber temperature of roughly 30 milliKelvin. The data run 2/21/97.1 was the first run we took after fully re-assembling the apparatus, and we were not patient enough to wait for over a week for the apparatus to thermally equilibrate. An $m = 1$ signal of 4 parts per billion using the old frequency method (at 105 degree amplitude) is equal to an $m = 1$ signal of 3 nanoradians using the new second harmonic method (at 230 degree amplitude), and so a 1 part per billion factional change in frequency is roughly comparable to a nanoradian of second harmonic. Instead of a variation of 6000 parts per billion, the total variation of the second harmonic amplitude in Figure 5.9 is bounded

within a range of 200 nanoradians, and the secular drift in the second harmonic is imperceptible. Using the old frequency method, a data run with a temperature variation like that of 2/21/97.1 would simply not be useable, but with the new second harmonic method, the data run 2/21/97.1 is perfectly adequate. Thus, the temperature variation problem has been suppressed. In Figure 5.11, there is also a change in frequency within each 21-period stretch of data due to the amplitude dependence of the frequency. These variations are caused by non-linearities in the fiber discussed in Section 4.1, and they would persist even if there were perfect fiber temperature control. Although these amplitude-induced linear drifts in frequency are larger in magnitude than the temperature-induced linear drifts in frequency, they are much less of a concern for producing false $m = 1$ signals because the amplitude-induced drifts are very reproducible from one 21-period stretch of data to the next.

To determine the magnitude of the $m = 1$ signal, the second harmonic is plotted as a function of the equilibrium position of the fiber, ϕ, in Figure 5.12. The equilibrium positions, ϕ, for each of the 10-parameter fits can be obtained from the $\hat{\theta}_1$, $\hat{\theta}_2$, and $\hat{C}$ estimates. The second harmonic estimates, $\hat{A}_{2lf}$, for each of the eight equilibrium positions (corresponding to the eight faces of the edge-reflector) are averaged together and plotted as a single point in Figure 5.12. Error bars calculated from the scatter within these averages (i.e., $(\text{variance}/(\text{number of points} - 1))^{1/2}$) are also plotted in Figure 5.12. Looking at those error bars, the reader can clearly start to see how nanoradian precision can be extracted from a 3-day run such as 2/27/97.1.

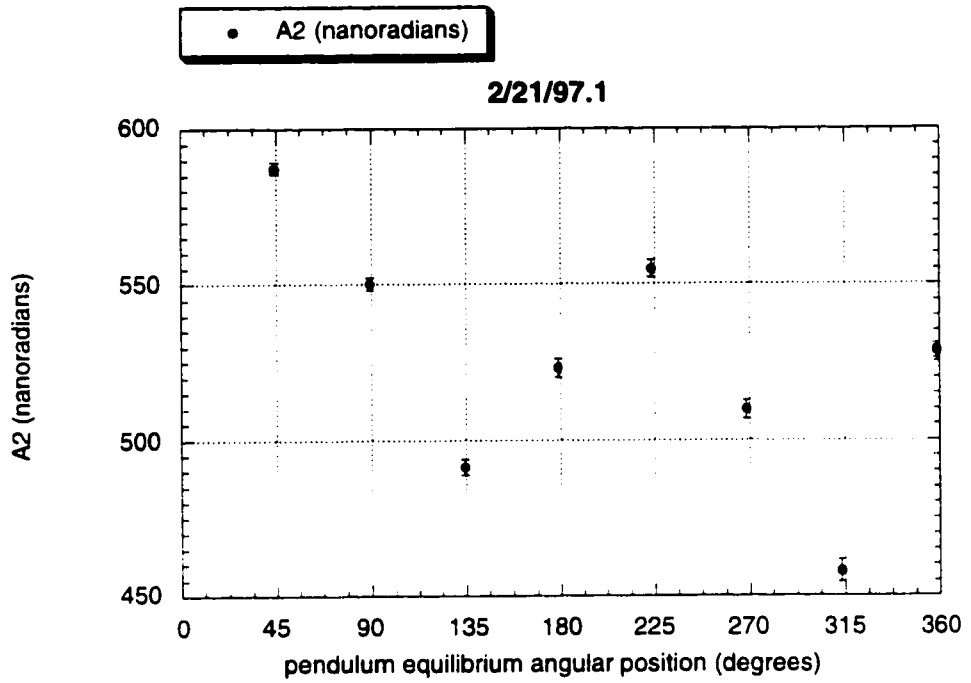

Figure 5.12. Plot of second harmonic amplitude versus equilibrium position (A_{2lf} vs. ϕ). In each of the eight positions, all of the fits have been averaged into a single point, and error bars have been calculated from the scatter within these averages.

When a fit of the form,

$$A_2(\phi) = a_0 + a_1\cos(\phi) + b_1\sin(\phi) + a_2\cos(2\phi) + b_2\cos(2\phi) \tag{5.12}$$

is done, the following values for the parameters are obtained,

$$\begin{aligned} a_0 &= 527.5 \pm 1.0 \text{ nanoradians} \\ a_1 &= 2.5 \pm 1.5 \text{ nanoradians} \\ b_1 &= 26.2 \pm 1.5 \text{ nanoradians} \\ a_2 &= 0.0 \pm 1.4 \text{ nanoradians} \\ b_2 &= 55.3 \pm 1.4 \text{ nanoradians} \end{aligned} \tag{5.13}$$

where the "±" signs indicate the one-sigma confidence levels in the parameter estimates assuming that the errors of the $\hat{A}_{2lf}$ estimates plotted in Figure 5.9 are

statistically independent. For additive "white" noise or thermal noise, the assumption of statistical independence is a valid one. Empirically, no statistically significant correlation between the "fixed mirror" fits and the "moveable mirror" fits is found which confirms the statistical independence of the fits. The a_0 parameter indicates the magnitude of the second harmonic due to fiber nonlinearities (see Section 4.1) whereas the a_1 and b_1 parameters indicate the magnitude of the second harmonic due to an external $m=1$ potential, $U_{ext}(\theta)=|U_1|\cos(\theta-\psi_1)$, and the a_2 and b_2 parameters indicate the magnitude of the second harmonic due to an external $m=2$ potential, $U_{ext}(\theta)=|U_2|\cos(2(\theta-\psi_2))$. The physical origin of these external potentials will be discussed once the results from the other 9 data runs have been presented.

First, however, I must confess that I have slightly misled the reader in the interest of simplicity. The results of Equation 5.13 do not derive from a fit of the form in Equation 5.12 to the eight points in Figure 5.12. Although the basic concept is correct, a more complicated fit of both amplitude and fiber support position,

$$\begin{aligned} A_2(\phi,A) = {} & f_0(A)a_0 + f_1(A)(a_1\cos(\phi)+b_1\sin(\phi)) \\ & + f_2(A)(a_2\cos(2\phi)+b_2\cos(2\phi)), \end{aligned} \tag{5.14}$$

to the points in Figure 5.9 is needed to accurately account for the amplitude dependence of the second harmonic and for the higher harmonics not explicitly included in the 10-parameter fit (see Section 4.3). The function

$$f_0(A)=\frac{A^2}{A_o^2} \tag{5.15}$$

accounts for the A^2 dependence of the second harmonic due to the fiber, and it effectively normalizes the $m=0$ contribution of each data point to what it would be at some nominal amplitude A_o. This prevents an $m=1$ variation in the amplitude from producing a false $m=1$ second harmonic signal by means of the amplitude dependence of the fiber second harmonic. For analyzing the data run 2/27/97.1, a nominal amplitude of $A_o = 233°$ was chosen because it is in the middle of the amplitude range of the data (see Figure 5.7). Similarly, the function

$$f_1(A) = \frac{J_2(A)}{J_2(A_o)} + \frac{3}{15}\frac{J_4(A)}{J_2(A_o)}\mathbf{s}\left(\hat{A}_2\right)\bullet\cos(4\omega_o t)\Big|_{A=A_o} + \frac{3}{35}\frac{J_6(A)}{J_2(A_o)}\mathbf{s}\left(\hat{A}_2\right)\bullet\cos(6\omega_o t)\Big|_{A=A_o} + \ldots \tag{5.16}$$

corrects for the $J_2(A)$ amplitude dependence of the $m=1$ signal and effectively subtracts off the error propagation of the fourth ($\propto J_4(A)$), sixth ($\propto J_6(A)$), and higher harmonics not in the 10-parameter fit. The $m=2$ function,

$$f_2(A) = \frac{J_2(2A)}{J_2(2A_o)} + \frac{3}{15}\frac{J_4(2A)}{J_2(2A_o)}\mathbf{s}\left(\hat{A}_2\right)\bullet\cos(4\omega_o t)\Big|_{A=A_o} + \frac{3}{35}\frac{J_6(2A)}{J_2(2A_o)}\mathbf{s}\left(\hat{A}_2\right)\bullet\cos(6\omega_o t)\Big|_{A=A_o} + \ldots, \tag{5.17}$$

is of the same form as $f_1(A)$ but with the $J_n(A)$ amplitude dependencies replaced with $J_n(2A)$. Since terms such as $\mathbf{s}\left(\hat{A}_2\right)\bullet\cos(4\omega_o t)\Big|_{A=A_o}$ involve the inversion of 10x10 matrices, $f_1(A)$ and $f_2(A)$ are calculated for several amplitudes prior to analysis, and interpolating functions for $f_1(A)$ and $f_2(A)$ are defined in Mathematica so that data analysis time is considerably reduced.

Table 5.1. Magnitude of the second harmonic amplitude due to the $m = 1$ potential. The parameter a_1 is proportional to cosine component of the potential, and b_1 is proportional to the sine component. The change in sign between the "0 degree" runs and the "180 degree" runs indicates that the observed $m = 1$ potential rotates with the vacuum can.

Data run	Position	a_1 (nanoradians)	b_1 (nanoradians)
2/21/97.1	0 degree	2.5 ± 1.5	26.2 ± 1.5
2/25/97.1	0 degree	6.1 ± 1.5	27.2 ± 1.5
2/28/97.1	0 degree	8.0 ± 1.8	30.7 ± 1.7
3/3/97.1	0 degree	7.7 ± 1.7	25.5 ± 1.5
3/6/97.1	180 degree	-5.5 ± 1.8	-25.7 ± 1.8
3/28/97.4	0 degree	4.6 ± 1.4	29.9 ± 1.3
4/1/97.2	180 degree	-6.9 ± 1.4	-27.5 ± 1.4
4/4/97.2	180 degree	-4.5 ± 1.4	-29.8 ± 1.4
4/7/97.2	180 degree	-4.8 ± 1.4	-26.0 ± 1.5
4/10/97.4	180 degree	-5.5 ± 1.1	-27.6 ± 1.1
average		0.18 ± 0.47	0.29 ± 0.47

In order to distinguish forces acting between the interior of the vacuum chamber and the pendulum from forces acting between cliff mass and the pendulum, the entire vacuum chamber can be rotated in a circular track about the nominal fiber axis, and data is taken in one of two diametrically opposed angular positions designated "0 degree" and "180 degree". Of the ten data runs in the set, five are in the "0 degree" position and five are in the "180 degree" position. The results for the $m = 1$ parameters, a_1 and b_1, are listed for each of the

ten data runs in Table 5.1. These results are depicted graphically in Figure 5.13. The error bars of the various runs differ because the runs are not all of the same duration and because the ground vibration from falling water in the back of the cave subsides as the spring runoff declines.

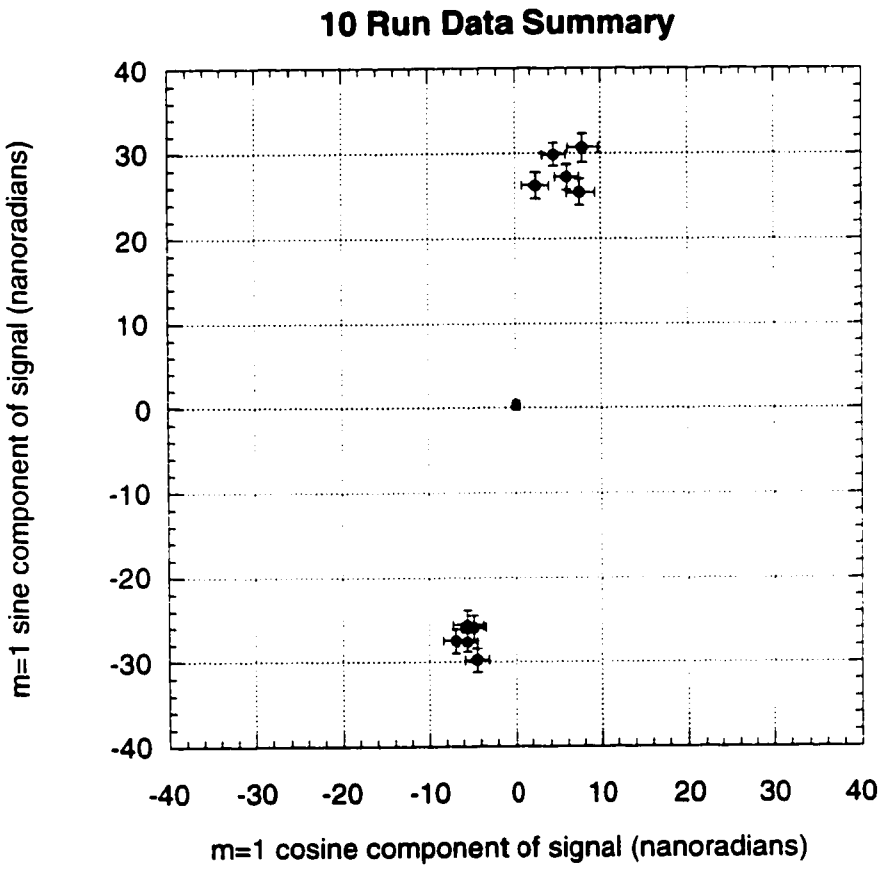

Figure 5.13. Graphical representation of the $m = 1$ results listed in Table 5.1.

Qualitatively, most of the $m = 1$ potential appears to rotate with the vacuum can as the results from the five "0 degree" runs and the five "180 degree" runs clus-

ter on opposite sides of the origin. To quantitatively assess what portion of the potential arises from the cliff or the Earth, these runs can be averaged together to subtract off the coupling from the vacuum can. That average result is depicted as a small cross at the origin of Figure 5.13, and it is more clearly shown in Figure 5.14.

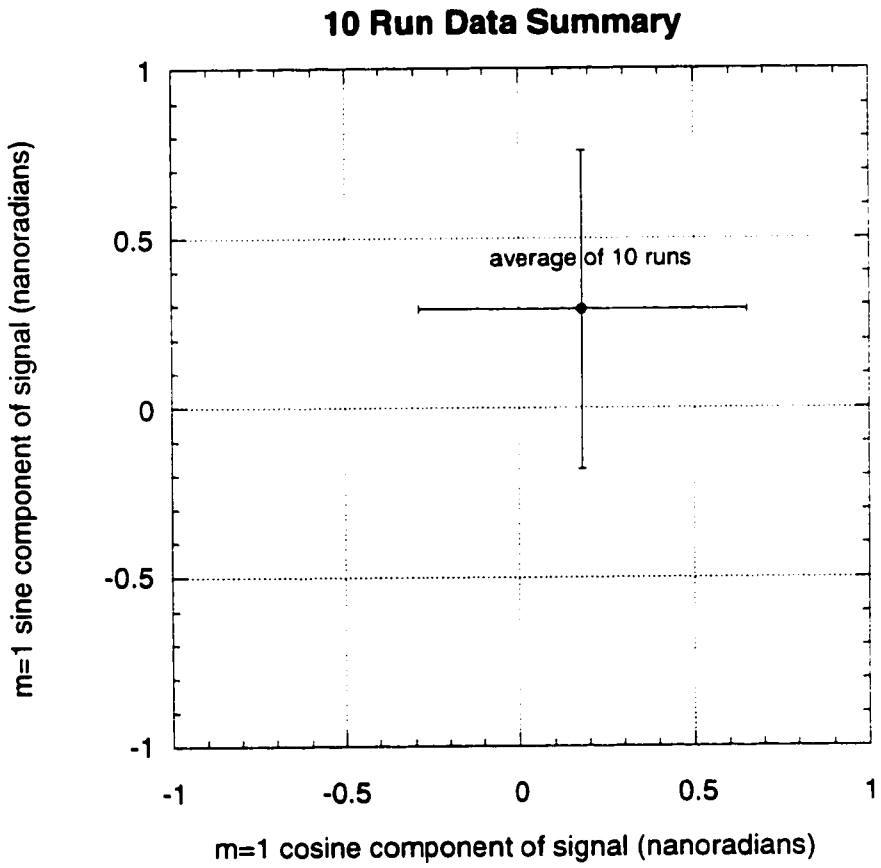

Figure 5.14. Area around the origin of Figure 5.13 magnified to more clearly display the average of all 10 runs which represents the strength of the composition-dependent force coupling to the cliff or Earth.

Thus for this experiment of 24 days of data, we measured the $m = 1$ variation in the second harmonic amplitude to a precision of 0.47 nanoradians (1σ confidence level), and the measured composition-dependent coupling to the cliff or Earth was consistent with zero. For the Index IV pendulum and fiber and the oscillation amplitude, $A = 233°$, of the data set, 0.47 nanoradians of second harmonic corresponds to a differential acceleration of

$$|\Delta a| = |a_{Be} - a_{Mg}| < 4.0 \times 10^{-12} \text{ cm / sec}^2 \tag{5.18}$$

between the magnesium and the beryllium. Given the latitude of the Index IV experiment, the horizontal acceleration of the materials has been measured to a fractional precision of

$$\frac{\Delta a}{a} = \frac{\Delta a}{g_\perp} < 2.3 \times 10^{-12}. \tag{5.19}$$

This places an upper limit on baryon-baryon coupling of

$$\xi(\lambda > R_{Earth}) = \frac{\Delta a}{g_\perp \Delta b} < 1.2 \times 10^{-9} \tag{5.20}$$

for ranges longer than the radius of the Earth. A plot of the upper limit $\xi(\lambda)$ as a function of λ would provide a more complete description of the class of excluded forces, but as this data set was originally intended to be a diagnostic run, I wish to emphasize the performance of the instrument and the second harmonic method rather than making strong claims about excluded forces. Moreover, the original numerical integration of the Index site source mass was done by Prof. Carrick Talmadge for Prof. Boynton and was used for previous Index experiments. Since then, we know that better geophysical data has be-

come available, and we would like to re-calculate the source mass integration for the Index site before presenting any new exclusion plots.

Although the coupling to the cliff or Earth produces a signal that is smaller than a nanoradian of second harmonic, the signal that rotates with the vacuum chamber (see Figure 5.13) is much larger, about 28 nanoradians. The question naturally arises, "What is that?" One possible response is "Who cares? Whatever it is, it rotates with the vacuum chamber and can be subtracted away." However, as this signal is 60 times larger than the noise limit of 0.47 nanoradians, I do not think the vacuum chamber coupling should be so glibly dismissed. Before one can have reasonable confidence that the signal from vacuum chamber coupling is perfectly equal and opposite in the 0 degree and 180 degree positions, one would like to know the physical origin of that signal. If the strength of the force is constant with time, and if the force's source is rigidly attached to the vacuum chamber, then a knowledge of the deviation of the vacuum chamber rotation axis from true vertical will allow one to place an upper limit on a difference in magnitude between the "0 degree" and "180 degree" couplings. More problematic are those forces that have a slow temporal variation. We observed an example of this in our initial data run with the composition-dipole pendulum. Outgassing from the vacuum chamber wall produced a time-varying signal. A naïve attempt to simply average the "0 degree" and "180 degree" runs of this initial data set produced a 7σ non-null signal. Only on closer inspection was it apparent that the vacuum chamber coupling was not constant in time and would therefore not subtract away. By placing a cylindrical copper insert inside the vacuum chamber to block the outgassing, this coupling was

removed, and the results of the ten data runs presented in this section are confirmation of that.

This still leaves an apparently constant 28 nanoradians that needs to be explained. Gravitational interactions are ruled out because otherwise we would have seen much larger signals with the exaggerated 2-1 and exaggerated 3-1 pendula (see Section 5.2). Likewise, the magnetic field can be exaggerated by a factor of at least 10,000 by dropping the magnetic shield and turning off the Helmhotz coils. Since we only see a signal of 10,000 nanoradians in the Earth's magnetic field, any magnetic interaction must be less than a nanoradian with the magnetic shield up and the Helmhotz coils on. We also investigated the possibility of laser pressure producing a false signal by taking data runs with the laser intensity reduced by one-half. The 28 nanoradian signal did not change. Next, we considered the possibility that imperfect gold coating on the pendulum might expose electrostatic contact potentials between the magnesium, beryllium, and gold that could interact with the contact potentials from dissimilar metals in the vacuum chamber. In particular, the gold coating on the interior surfaces of the pendulum was not very good. We tried placing a gold-coated foil annulus over the holes in the top endcap of the pendulum so that the interior was not directly exposed to the mirrors and brass tubes above the pendulum, and the 28 nanoradian signal went away. However, when we repeated the run with a lighter mesh annulus, that result was not reproducible. During our investigations we broke a fiber and had to re-hang the pendulum. The plug on the new fiber used to attach the pendulum turned out to be magnetically contaminated. With this contaminated plug, we detected a large signal even with the magnetic shield up and the Helmholtz coils on. Upon further investi-

gation we discovered that three screws inside the vacuum chamber that were supposed to be made of non-magnetic material were in fact made of steel. These have been replaced, but we do not have data yet to know whether they were the source of the 28 nanoradian signal. If this is the case, it will be a rather mundane explanation. However, careless errors can produce problems just as grave as those caused by conceptual misunderstandings. In fact, they are often harder to identify since you believe you have already accounted for those type of effects. Unfortunately, Mother Nature rarely awards partial credit for getting the experiment almost right.

5.4 Conclusion

Having read this far, the reader might be inclined to comment, "Yes, this is a cleaver innovation in the use of the torsion balance, but isn't that similar to making a retractable buggy whip? After all, it is almost the 21st century, and you guys should be using SQUID's, atomic force microscopes, and other modern developments rather than trying to resuscitate a centuries-old technology." To answer this, let us suppose that we have an atomic force microscope (AFM), and further let us suppose that the rim of our pendulum is so perfectly machined that we could count individual atoms as they passed by the AFM. How would that angular resolution compare to what we achieved with our Index IV apparatus? We have resolved the second harmonic amplitude to 0.47 nanoradians (see Table 5.1). Given the one inch radius of our torsion pendulum, 0.47 nanoradians corresponds to measuring the position of a point on the pendulum' rim to 0.12 Å. Since the spacing between atoms in a metal are typically a few Å, the AFM would have to resolve to better than a tenth of an atomic spacing in order to equal what we have done with the Index IV apparatus. In a re-

cent article (Peters et al. 1999), a group using atomic interferometry measured g to a precision of 3×10^{-6} cm/sec^2 and stated, "The absolute relative uncertainty $\Delta g/g$ of 3 parts in 10^9 achieved in the current work demonstrates that this type of interferometer can be used to make absolute measurements comparable with the most sensitive measurement tools in physics." They are correct because they restrict their claim to "absolute measurements", meaning they can count over 500,000 interference fringes and measure the total magnitude of g. But often it is only differential measurements that are required to test physical theories, and if we compare the atomic fountain's performance to that of the Index IV apparatus, its fractional acceleration precision is more than a factor of 1000 worse than Index IV's $\Delta a/a = 2.3\times10^{-12}$ (see Eq. 5.19), and its acceleration precision is a factor of 750,000 worse than Index IV's $\Delta a = 4.0\times10^{-12}$ cm / sec^2 (see Eq. 5.18).

Nor has our group exhausted the ability of the torsion balance/pendulum. Other groups have pushed the performance of the torsion balance even further. Consider the Eot-Wash group's uranium source mass experiment (Gundlach et al. 1997) in which they measured the differential acceleration to a precision of $\Delta a = 5.8\times10^{-13}$ cm / sec^2. How small an acceleration is that? To get a physical appreciation for that number, let us calculate the vertical gravity gradient at the Earth's surface,

$$\frac{\partial g_z}{\partial z} = -\frac{2g_z}{R_{Earth}} = -\frac{2\left(-980\ \text{cm/sec}^2\right)}{6.4\times10^8\ \text{cm}} = 3.1\times10^{-6}\ \text{sec}^{-2} = 3100\ \text{Eot}, \quad (5.21)$$

and ask what height difference, Δz, corresponds to $\Delta a = 5.8\times10^{-13}$ cm / sec^2.

$$\Delta z = \frac{\Delta a}{\partial g_z/\partial z} = \frac{5.8\times10^{-13}\ \text{cm / sec}^2}{3.1\times10^{-6}\ \text{sec}^{-2}} = 1.9\times10^{-7}\ \text{cm} = 19\ \text{Å}. \quad (5.22)$$

The width of a strand of DNA is about 20 Å, and so if you were to place it horizontally in the Earth's gravitational field, measuring a differential acceleration of $\Delta a = 5.8 \times 10^{-13}$ cm / sec^2 is equivalent to measuring the difference in g between the bottom edge and the top edge of the DNA molecule. The torsion balance is more than weekend toy for hobbyists; it is the premiere tool for measuring weak, macroscopic forces, and as the field of physics can be fairly described as the study of the forces of Nature, the ability to measure weak forces accurately is central to the pursuit of experimental physics. As Riley Newman is fond of saying, torsion balance/pendulum experiments are "very-low energy physics", and they provide a necessary complement to the more technologically impressive accelerators of high-energy physics.

No discussion of torsion balance performance is complete without mentioning Braginskii's and Panov's solar source mass test of the weak equivalence principle (Braginskii & Panov 1972) in which they achieved an acceleration precision of $\Delta a = 3 \times 10^{-13}$ cm / sec^2. It is instructive to investigate the scaling laws of thermal noise as they apply to this experiment. The signal of a CDF experiment is directly proportional to the pendulum composition-dipole moment and inversely proportional to the fiber constant, κ. If the two materials for the two halves of the pendulum already have been chosen (in Braginskii's and Panov's experiment, platinum and aluminum), then the signal of a modulated deflection method experiment, C_{mod}, scales as

$$C_{mod} \propto CDF\ signal \propto \frac{MR}{\kappa}, \tag{5.23}$$

where M is the mass of the pendulum and R is the radius of the pendulum. From discussions of thermal noise in Section 3.3 and in the Appendix, we know that the thermal noise error in measuring C_{mod} scales as

$$\begin{aligned} \text{stddev}_{th}\left(\hat{C}_{mod}\right) &\propto \frac{T^{1/2}}{Q^{1/2}\kappa^{1/2}(\text{number of periods})^{1/2}} \\ &\propto \frac{T^{1/2}}{Q^{1/2}\kappa^{1/2}(\omega_o\tau)^{1/2}} \propto \frac{T^{1/2}M^{1/4}R^{1/2}}{Q^{1/2}\tau^{1/2}\kappa^{3/4}}, \end{aligned} \tag{5.24}$$

where T is the absolute temperature of the fiber, Q is the quality factor of the fiber, and τ is the total integration time of observation. The signal-to-noise ratio for a thermal noise limited experiment therefore scales as

$$(S/N)_{th}[C_{mod}] \propto \frac{Q^{1/2}\tau^{1/2}M^{3/4}R^{1/2}}{T^{1/2}\kappa^{1/4}}. \tag{5.25}$$

Once a torsion fiber material is chosen (such as tungsten), the torsion fiber constant scales as $\kappa \propto d^4/\ell$ where d and ℓ are the diameter and length of the torsion fiber. With this substitution, the signal-to-noise ratio is

$$(S/N)_{th}[C_{mod}] \propto \frac{Q^{1/2}\tau^{1/2}M^{3/4}R^{1/2}\ell^{1/4}}{T^{1/2}d}. \tag{5.26}$$

From Equation 5.26, it is evident that in order to optimize the signal-to-noise, one would like the make the mass, M, as large as possible and the diameter of the fiber, d, as small as possible. However, one is going to be limited by the tensile strength of the torsion fiber material, and so for maximally weighted fibers, $d \propto M^{1/2}$. Under this limitation, both the signal,

$$C_{mod} \propto \frac{R\ell}{M}, \tag{5.27}$$

and the noise,

$$\text{stddev}_{th}\left(\hat{C}_{mod}\right) \propto \frac{T^{1/2}R^{1/2}\ell^{3/4}}{Q^{1/2}\tau^{1/2}M^{5/4}}, \tag{5.28}$$

become smaller with increasing mass rather than becoming larger with increasing mass as in Equations 5.23 and 5.24. The signal-to-noise ratio is

$$(S/N)_{th}[C_{mod}] \propto \frac{Q^{1/2}\tau^{1/2}M^{1/4}R^{1/2}\ell^{1/4}}{T^{1/2}}. \tag{5.29}$$

From Equation 5.29, it begins to become clear why Braginskii and Panov wanted to make their pendulum so big ($R = 10$ cm) and their fiber so long ($\ell = 290$ cm) although it is a little hard to see why they would go to such pains for a 3 meter vacuum chamber when the payback is only $\ell^{1/4}$. Making their pendulum so light ($M = 4$ grams) appears to have hurt them somewhat, but making the signal large enough to detect (see Eq. 5.27) was apparently a more important consideration than the thermal noise limit for their choice of pendulum mass.

Equation 5.29, however, was not the scaling law that drove the design of Braginskii's and Panov's experiment. Using an incorrect viscosity model of internal fiber losses, they erroneously believed that the quality factor of the fiber scaled as $Q \propto 1/\omega_o$, and that the signal-to-noise ratio would therefore scale as

$$(S/N)_{th,Q\propto 1/\omega_o}[C_{mod}] \propto \frac{\tau^{1/2}M^{1/4}R^{1/2}\ell^{1/4}}{\omega_o^{1/2}T^{1/2}} \propto \frac{\tau^{1/2}R\ell^{1/2}}{T^{1/2}}. \tag{5.30}$$

From Equation 5.30, it would seem there is no penalty for having a light mass, and the signal-to-noise to increases as R and $\ell^{1/2}$ providing a much stronger motivation to increase R and ℓ than the $R^{1/2}$ and $\ell^{1/4}$ scalings in Equation 5.29.

Prof. Peter Saulson (Gonzalez & Saulson 1995) has done much work showing that a $1/\tau_{int}$ spectrum of Maxwell units (see Sec. 4.2) provide a much better model for fiber losses. This model predicts that the quality factor, Q, is a constant of the fiber material, and it is not increased by decreasing the oscillation frequency, ω_o. If Panov and Braginsky were using incorrect scalings to optimize their experiment, why was their design so successful? Well, another consequence of the $1/\tau_{int}$ spectrum fiber loss model is that the thermal noise torque power spectrum is not "white" as it would be for simple, "dashpot" damping, but instead the thermal noise torque power has a $1/f$ spectrum. There is not room here for a detailed derivation, but the main effect is to add a factor of $(\omega_{mod}/\omega_o)^{1/2}$ to the simple "dashpot" signal-to-noise of Equation 5.29. When this is done,

$$\begin{aligned}(S/N)_{th,1/f}[C_{mod}] &\propto \frac{Q^{1/2}\tau^{1/2}M^{1/4}R^{1/2}\ell^{1/4}}{T^{1/2}}\left(\frac{\omega_{mod}}{\omega_o}\right)^{1/2} \\ &\propto \frac{Q^{1/2}\tau^{1/2}R\ell^{1/2}\omega_{mod}^{1/2}}{T^{1/2}},\end{aligned} \tag{5.31}$$

it is seen that the correct signal-to-mass scaling of Equation 5.31 has the same $M^0R\ell^{1/2}$ dependence as the incorrectly derived signal-to-mass scaling of Equation 5.30. Sometimes it is just as good to be lucky as right.

From their incorrect model, Braginskii and Panov predicted a damping time due to fiber losses of $\tau^* = 1/\gamma \cong 8\times10^9$ sec. When they attempted to measure the damping time of their oscillator, they claimed,

> "After three days the amplitude of the oscillations of the balance had changed at most $\approx 3\times10^{-3}$ of their initial magnitude; from this result we derive the inequality $\tau^* > 6\times10^7$ sec. It was not possible to determine τ^*

more accurately. The oscillatory period τ^o was 1.92×10^4 sec (5 hours 20 minutes)."

The "lower limit" of $\tau^* = 6\times10^7$ sec corresponds to a quality factor of $Q = 9800$ which is a fairly typical value for tungtsen. Most likely, their "lower limit" of the damping time was fairly close to the actual value. Despite their protestation that "It was not possible to determine τ^* more accurately", the simple expedient of increasing the oscillation amplitude comes to mind ($\text{stddev}_{th}(\hat{\gamma}) \propto 1/A$). However, I don't think Braginskii and Panov were terribly motivated to produce irrefutable evidence that their predicted value of $\tau^* = 1/\gamma \cong 8\times10^9$ sec was two orders of magnitude too large. When they calculated the thermal noise limit using the "lower limit" of $\tau^* = 6\times10^7$ sec, it was a factor of two smaller than their measured noise, and thus they believed they were not thermal-noise limited. They were genuinely puzzled by this because they thought they had been very careful in eliminating other sources of error, and they could not account for this excess error. In fact, the true thermal noise limit was a factor of $(\tau_{mod}/\tau_o)^{1/2} = (24\text{ hour}/5.33\text{ hour})^{1/2} \cong 2$ larger than the value they had predicted from an erroneous "dashpot" model, and thus there probably were not other sources of excess error. They were more successful than they believed themselves to be for they most likely had conducted a thermal-noise limited experiment. This is also a powerful rebuke to those who insinuate that Braginskii and Panov could not have really done as well as they had reported or that they somehow massaged their data to make it look better than it was because this is precisely the type of trap an unscrupulous experimentalist would have fallen into. It would have been the easiest thing in the world to shave off another factor of two so that the noise would be where they "knew" the thermal noise limit

should be. Instead, they reported their results exactly as they measured them, and as it turns out in hindsight, exactly where the correct theory predicted it should be.

Giving in to the temptation to be a Monday morning quarterback, I have one more mild criticism. Braginskii and Panov did not measure the M_{22} quadrupole moment of their torsion balance using an exaggerated local source mass, nor did they verify the magnitude of the diurnal variations in the V_{22} gravity gradient using an exaggerated M_{22} torsion balance. If they had made these type of empirical exaggerations, as more recent experimental groups have done, they would not have been so glib in dismissing gravitational interactions as a source of error. They did make an attempt to calculate what the magnitude of these gravitational interactions were, and although they were not as conservative as they thought themselves to be, they were not so grossly wrong that the gravitational errors were an order of magnitude larger than the thermal noise limit because otherwise that would have become apparent in their data. If Braginskii and Panov were so successful, why hasn't modern torsion balance design followed in their footsteps? The answer is that more recent experiments have not been solely solar source mass experiments but instead have also been testing for shorter range forces using the Earth or local lab masses as a source mass. Because of this, local gravity gradient couplings have been much more of a concern, and the pendula have been smaller than Braginskii's and Panov's $R = 10$ cm. The question then is not "How could Braginskii and Panov have done so well?", but rather "How could the Eot-Wash group's uranium source mass experiment have come within a factor two of Braginskii and Panov in terms of differential acceleration precision given the Eot-Wash apparatus'

smaller R and shorter ℓ?" The answer lies in the one factor in Equation 5.31 of which Braginskii and Panov were unaware, the dependence of the signal-to-noise ratio on $\omega_{mod}^{1/2}$. By rotating the uranium source mass around the torsion balance once every 1000 seconds instead of once every 24 hours, the Eot-Wash group made up for its smaller R and shorter ℓ, and the thermal noise limit on differential acceleration is about the same for the two experiments.

Although comparable to the present performance of the Index IV apparatus, the Eot-Wash's Earth/hillside source mass experiments (Su et al. 1994) have not yet achieved the acceleration precision of their uranium source mass experiment. The primary reason for this is that the Earth/hillside source mass experiments have been conducted at higher pressure, and thus the viscous air damping lowers the quality factor to a value of $Q = 25$ rather than the fiber-limited $Q = 9000$ of the uranium source mass experiment. Also, the modulation frequency, ω_{mod}, of the Earth/hillside source mass experiments have been not been as rapid as those employed in the uranium source mass experiment because there are more stringent requirements on the smoothness of rotation when the torsion balance is being rotated than when an external source mass is rotated. Neither of these are fundamental limits, however, and both are targeted for improvement in Eot-Wash's next generation of the Earth/hillside source mass experiments. Indeed, they want to push ω_{mod} past ω_o, and then the response of the torsion balance is qualitatively different. For resonant modulation, $\omega_{mod} = \omega_o$, the signal is a shift in either ω or γ depending on whether the source mass rotation is in phase or 90° degrees out of phase with the pendulum oscillation. If starting from $A = 0$, one observes a linear increase in amplitude (at least for $\omega_o \tau << Q$), and this method has been employed by

Prof. Cowsik's group in India (Cowsik et al. 1990). When limited by additive "white" noise, both Cowsik's method and the frequency method share the advantage of having their signal-to-noise increase as $\tau^{3/2}$ whereas for the deflection and second harmonic methods, the signal-to-noise increases only as $\tau^{1/2}$. For $\omega_{mod} > \omega_o$, the response of the oscillator becomes dominated by the inertia of the torsion balance, and the signal scales approximately as

$$C_{mod,\omega_{mod}>\omega_o} \propto \frac{R\ell}{M}\left(\frac{\omega_o}{\omega_{mod}}\right)^2 \propto \frac{1}{R\omega_{mod}^2}. \tag{5.32}$$

The thermal noise, however, is also proportionally smaller,

$$\text{stddev}_{th,1/f}\left(\hat{C}_{mod,\omega_{mod}>\omega_o}\right) \propto \frac{T^{1/2}}{Q^{1/2}\tau^{1/2}R^2\ell^{1/2}\omega_{mod}^{5/2}}, \tag{5.33}$$

so that the signal-to-noise ratio,

$$(S/N)_{th,1/f}\left[C_{mod,\omega_{mod}>\omega_o}\right] \propto \frac{Q^{1/2}\tau^{1/2}R\ell^{1/2}\omega_{mod}^{1/2}}{T^{1/2}}, \tag{5.34}$$

continues to improve as $\omega_{mod}^{1/2}$. The difference now is that each factor of 10 increase in the signal-to-noise ratio requires a factor of 10,000 improvement in detector sensitivity. This is a steep price to pay, but it points out that a fiber thermal-noise limit is not a fundamental limit for it can be improved upon by increasing ω_{mod}, and it also points out that there is no such thing as "excess" detector sensitivity. Any new technology that improves detector sensitivity is a welcome addition which can be immediately put to use to increase the signal-to-noise of a fiber thermal-noise limited experiment.

With the application of our second harmonic method to the Index IV apparatus, we are already, in a certain sense, operating in the $\omega_{mod} > \omega_o$ regime

because ω_{mod} is effectively $2\omega_o$. However, it is not quite equivalent to an $\omega_{mod} = 2\omega_o$ deflection method in which the torque signal is entirely in the second harmonic because in a large-amplitude method, the pendulum oscillation through the sinusoidal potential scatters the torque signal into the deflection, frequency, and all the higher harmonic channels (see Figure 2.3) so that at $A = 230$ degrees $= 4.01$ radians, only $2J_2(4.01)/3 = 0.24$ of the torque signal is in the second harmonic. Also, as discussed in Section 4.2, the move-and wait strategy of the fiber support excites exponential transients in the fiber that reduce the effective duty cycle of our data collection. On the plus side, we don't have to contend with the rumble from a turntable or with tilt-induced deflections. The quality factor, $Q = 4000$, of the Index IV apparatus is fiber limited, but we do not enjoy the high-Q thermal noise advantage because we are presently limited by the crossing-time errors that result from the seismically-induced rocking motions of the pendulum. It is possible that better optical alignment will remedy this problem of the Index IV apparatus. If not, our group's next generation inverse square law violation experiment has 512 pixel photodiode arrays that will most definitely allow us to filter out the rocking motion and become fiber thermal noise limited. For fiber thermal noise limited experiments, the scaling of a second harmonic method experiment is slightly different from a modulated deflection experiment because ω_{mod} is not a separate degree of freedom, and the $(\omega_{mod}/\omega_o)^{1/2}$ term in Equation 5.31 can not be altered from $2^{1/2}$. Thus the second harmonic signal-to-noise scales as

$$(S/N)_{th}[A_2] \propto \frac{Q^{1/2}\tau^{1/2}M^{1/4}R^{1/2}\ell^{1/4}}{T^{1/2}} \tag{5.35}$$

which identical to the naïve "dashpot" thermal noise scaling of Equation 5.29. One notable difference of the second harmonic signal-to-noise (see Eq. 5.35) from the modulated deflection signal-to-noise (see Eqs. 5.31 and 5.34) is the appearance of a mass dependence. One can improve the signal-to-noise ratio by increasing the mass because this requires a thicker fiber which increase ω_o and hence effectively increases ω_{mod}. The increase is modest, $(S/N)_{th}[A_2] \propto M^{1/4}$, whereas the decrease in signal,

$$A_2 \propto \frac{R\ell}{M}, \tag{5.36}$$

is inversely proportional to the mass, and so similar to the ω_{mod} scaling of the modulated deflection method, each factor of 10 increase in the signal-to-noise ratio requires a factor of 10,000 improvement in detector sensitivity. There is no fundamental limit to how much one can increase ω_{mod} using a modulated deflection method, but because of the finite densities of the pendulum materials, there is a limit to how much one can increase the mass of the pendulum for a given R, which itself is generally constrained by gravity gradient considerations. For a fiber thermal noise limited large-amplitude experiment, there is another approach to increase the effective ω_{mod}, and that is to increase the oscillation amplitude, A, and then use not only the second harmonic, $A_2(\phi)$, as a signal but all the higher harmonics, $A_n(\phi)$, as well. We have only done very preliminary calculations, but it appears that the signal amplitude decreases roughly as $1/A^2$ whereas the signal to noise increases roughly as $A^{1/2}$. Once again, each factor of 10 increase in the signal-to-noise ratio requires a factor of 10,000 improvement in detector sensitivity, but there is no inherent limit to how much one can increase A. All other things being equal, it would seem that in-

creasing the oscillation amplitude, A, in a large-amplitude method is technically less challenging than maintaining the required smoothness of rotation with an increased turntable speed in a modulated deflection method. On the other hand, the Eot-Wash group has a formidable track record of success, and if the past is any guide, it is most probable that they shall continue to improve the performance of their turntable in the future.

Yet another approach is that adopted by Prof. Newman's group at UC Irvine (Newman et al. 1996). Instead of trying to cheat thermal noise by increasing ω_{mod}, they are tackling the thermal noise problem head on by drastically reducing the temperature of the system with liquid helium. Cryogenic technology is a mature field in which experience has been gained from its application in several different areas of physics. Part of that hard won knowledge is that using cryogenic technology introduces many difficulties and headaches that are absent from room-temperature experiments. Prof. Newman, who probably has more experience with torsion balance/pendulum experiments than anyone else, has determined that the time has come to "bite the bullet" and see what improvements can be gained in torsion balance/pendulum performance by going to cryogenic temperatures. Prof. Newman's group has already done valuable empirical studies of beryllium-copper fibers at room temperature, liquid nitrogen temperature, and liquid helium temperature (Bantel & Newman 1998). They fit for the higher harmonic amplitudes, A_n, for oscillation amplitudes up to $A = 100$ radians in order to determine the nature of the fiber's non-linearities. They intend to use the frequency method at cryogenic temperatures, and one of their first applications is a measurement of the gravitational constant, G (Newman & Bantel 1999). Prof. Jens Gundlach, of the Eot-Wash group, is also con-

ducting a measurement of G (Gundlach et al. 1996) using a clever application of their turntable that makes the measurement almost entirely insensitive to fiber properties. Both intend to measure G to an accuracy of at least a part in 10^5, an order of magnitude better than anyone else has achieved, and as far as I know, no other groups besides these two are seriously attempting such accuracy. Prof. Newman's choice of the frequency method might seem to be a refutation of all the arguments in this thesis I have put forward championing the superiority of the second harmonic method relative to the frequency method, but my comparison was based on the temperature coefficient of the shear modulus and the temperature stability that can be achieved at room temperature. At liquid helium temperature, both the temperature coefficient of the shear modulus and typical variations in temperature are much smaller which greatly reduces the disadvantages of the frequency method. Furthermore, the frequency method's ability to decrease the "white" noise limit as $\tau^{3/2}$ becomes a much more valuable attribute once thermal noise has been greatly reduced. Besides, both the frequency and second harmonic methods are large-amplitude crossing-time methods, and it would require very little modification if Prof. Newman's group desired to switch over to a second harmonic method, or an even higher harmonic method, in the future. Previously, Prof. Newman's group had used a move-and-wait deflection method for his Earth/hillside source mass experiments (Beilby et al. 1994). Because they magnetically "clamped" the torsion balance during the moves, they did not suffer from the move-induced exponential transients, but because at least one period of data is required in each position and because some time is used up for the moves, they could not modulate the signal as quickly as they would have liked. In particular, they were dis-

turbed by reproducible temperature-induced variations in the optical path that they believed were caused by temperature gradients in their laboratory. Although they never implemented it, they did consider using a thick, rotating cork thermal insulation barrier around the instrument to minimize these external temperature gradients. Encouraged by our success in implementing large-amplitude crossing-time methods, Prof. Newman's group has become the only other group beside ourselves, of whom we are aware, to seriously pursue large-amplitude methods.

Regardless of whether zero-amplitude, continuous-sampling deflection methods or large-amplitude, crossing-time methods ultimately prove to be superior for data collection, both have proven their worth as diagnostic tools. Because the diagnostic strengths of the two methods complement one another, it would be wise to design future torsion balance/pendulum experiments so that they have the capability to collect data in both modes. The main advantage of continuous sampling is the ability to determine all the various vibration modes of the pendulum that bleed into the signal. Continuous sampling allow these vibrations to be filtered out from the data in analysis, but it is also a useful diagnostic to identify the physical origins of those vibrations and to evaluate the effectiveness of various physical methods that either passively or actively suppress those vibrations. More generally, continuous sampling allows one to observe any strange, unexpected behavior of the system. When pushing the performance of the apparatus into new territory, the emergence of previously undetected and unanticipated phenomena is not uncommon. Because of the simpler, more direct data analysis of continuous sampling, one is more likely determine the physical origin of these new phenomena than if one were to rely

solely on the more abstract inference of crossing-time fits. The main diagnostic advantage of the large-amplitude methods is their ability to directly measure the coupling between the pendulum and the vacuum can by rotating the fiber support to various positions in both a "0 degree" and "180 degree" vacuum can position. One can not do this when using a deflection method because rotating the fiber support destroys all information in the deflection channel. By directly measuring the vacuum can coupling, one is more likely to determine the physical origin of that coupling, and also one can evaluate the effectiveness of various efforts to remove or minimize that coupling. Although in theory one does subtract off the vacuum can coupling from the external signal by adding the results "0 degree" and "180 degree" runs, it is always preferable to physically remove the coupling than to solely rely on subtraction in the data analysis because at some level the coupling may not perfectly rotate. In addition, any unanticipated couplings between the vacuum can pendulum will become readily apparent.

Another useful diagnostic of large-amplitude methods is the ability to take data at various oscillation amplitudes in order to determine the amplitude dependence of the signal. Prior to taking the Index IV apparatus up to Index, we were testing it in the old Physics Building using the frequency method as we had not yet developed the second harmonic method. On one occasion, after moving the instrument across the lab, we did not carefully re-level the instrument. Subsequently, we observed a fairly large $m=1$ signal, $|\Delta\omega(\phi)|/\omega_o = 7.2\times10^{-5}$, and we could not think of a coupling that would produce such a large force. We then decided to take data at an oscillation amplitude of $A = 220$ degrees $= 3.83$ radians which is the first zero of the $J_1(A)$ Bessel

function. If the $|\Delta\omega(\phi)|/\omega_o = 7.2\times10^{-5}$ signal at $A = 105$ degrees were due to an $m = 1$ potential, its signal strength should go to zero at $A = 220$ degrees. In fact, the $|\Delta\omega(\phi)|/\omega_o$ signal remain unchanged at $A = 220$ degrees from which we concluded that the $|\Delta\omega(\phi)|/\omega_o$ signal was not produced by an $m = 1$ potential. Upon further investigation, we determined that a combination of a tilted fiber support and a slightly bent upper fiber in the magnetic damper mechanism conspired to physically change the effective length of the fiber when the fiber support was rotated to different positions. This would cause the shift in oscillation frequency, $\Delta\omega(\phi)/\omega_o$, to vary sinusoidally with fiber support position but in a manner that was independent of oscillation amplitude, which precisely described the phenomena we observed. Upon re-leveling the apparatus and replacing the bent upper wire, the large $\Delta\omega(\phi)/\omega_o$ signal went away.

What fundamental impediments are there to the future improvement of torsion balance/pendulum performance? As mentioned above, even the fiber thermal noise limit is not insurmountable provided one can continue to improve the sensitivity of one's detector. Improving detector sensitivity is also useful in attacking another severe limitation, gravity errors. By using exaggerated source masses and pendula, one can empirically measure and then trim non-zero potential derivatives and non-zero mass moments order by order, but for this to be done in a reasonable amount of time, one requires sufficient detector sensitivity to measure the increasingly more difficult higher moments and potential derivatives. Of course, this only works provided the gravity gradients are static. For temporally varying gravitational fields, and particularly for the most troublesome V_{xz} and V_{yz}, one can adopt a strategy of real-time correction using exaggerated "2-1" pendula in a closed feedback loop with computer-

controlled water pumps that pump water back and forth between water tanks to trim the local gravity gradient. Although this scheme is fairly straight forward in theory, no group has yet implemented this strategy. Another possible fundamental limitation is the rotational seismic noise. The effect of vertical and horizontal seismic rotations can be isolated in theory, but if the lab frame one is using to define one's co-ordinate frame is rotating, this places a limit on how small a rotational acceleration one measure. The technology of ring laser gyros (Stedman 1997) and potentially even more sensitive atomic beam devices (Gustavson et al. 1997) may soon become sensitive enough to measure the seismic rotation relative to an inertial frame so that one's torsion balance/pendulum data can be appropriately corrected. And ultimately there is the fundamental quantum limit of a harmonic oscillator, but that is still many orders of magnitude away. If the torsion balance/pendulum community ever gets to the point where they are replacing k_bT with $\hbar\omega_o$ as their leading noise source, then they will most definitely deserve to congratulate themselves on a job well done.

Bibliography

M.K. Bantel and R.D. Newman. Measurements of torsion anelastic properties in preparation for a new measurement of G. *1998 Conference on Precision Electromagnetic Measurements Digest (Cat. No. 98C?H36254).* IEEE, New York, NY. pp. 149-150. (1998)

M.A. Beilby, N. Krishnan, and R.D. Newman. A rotatable torsion balance for a new test of the equivalence principle. *Experimental Gravitation. Proceedings of the International Symposium on Experimental Gravitation.* Nathiagali, Pakistan, 26 June – 2 July 1993, eds., M. Karim and A. Qadir. pp. A277-A284. (1994)

V.B. Braginskii and V.I. Panov. Verification of the equivalence of inertial and gravitational mass. *Soviet Physics JETP.* **Vol. 34**, no. 3, pp. 463-466. (1972)

S. Carusotto, V. Cavasinni, A. Mordacci, F. Perrone, E. Polacco, and G. Zavattini. Preliminary Results from the GAL Experiment. *Progress in Atominc Physics Neutrinos and Gravitation, proceedings of the XIIth Moriond Workshop.* Les Arcs, France, January 1992, eds., G. Chardin, O. Fackler and J. Tran Thanh Van (Editions Frontières), pp. 463-469. (1992)

Y.T. Chen, A.H. Cook, and A.J.F. Metherell. An experimental test of the inverse square law of gravitation at range of 0.1 m. *Proceedings of the Royal Society of London, Series A (Mathematical and Physical Sciences).* **Vol. 394**, no. 1806, pp. 47-68. (1984)

R. Cowsik, N. Krishnan, S. Unnikrishnan, and S.N. Tandon. Strength of intermediate-range forces coupling to isospin. *Physical Review Letters.* **Vol. 64**, no. 4, pp. 336-339. (1990)

E. Fischbach, D. Sudarsky, A. Szafer, C. Talmadge, and S.H. Aronson. Reanalysis of the Eotvos experiment. *Physical Review Letters.* **Vol. 56**, no. 1, pp. 3-6. (1986)

G.I. Gonzalez and P.R. Saulson. Brownian motion of a torsion pendulum with internal friction. *Physics Letters A.* **Vol. 201**, no. 1, pp. 12-18. (1995)

J.H. Gundlach, E.G. Adelberger, B.R. Heckel, and H.E. Swanson. New technique for measuring Newton's constant G. *Physical Review D (Particles, Fields, Gravitation, and Cosmology).* **Vol. 54**, no. 2, pp. R1256-R1259. (1996)

J.H. Gundlach, G.L. Smith, E.G. Adelberger, B.R. Heckel, and H.E. Swanson. Short-range test of the equivalence principle. *Physical Review Letters.* **Vol. 78**, no. 13, pp. 2523-2526. (1997)

T.L. Gustavson, P. Bouyer, and M. Kasevich. Precision rotation measurements with an atom interferometer gyroscope. *Physical Review Letters.* **Vol. 78**, no. 11, pp. 2046-2049. (1997)

Walter Clark Hamilton. *Statistics in Physical Science; Estimation, Hypothesis Testing, and Least Squares.* Ronald Press Co. (1964)

Carl W. Helstrom. *Statistical Theory of Signal Detection.* Pergamon Press, second edition. (1968)

J.K. Hoskins, R.D. Newman, R. Spero, and J. Schultz. Experimental tests of the gravitational inverse-square law for mass separations from 2 to 105 cm. *Physical Review D (Particles and Fields).* **Vol. 32**, no. 12, pp. 3084-3089. (1985)

Y.L. Huang and P.R. Saulson. Dissipation mechanisms in pendulums and their implications for gravitational wave interferometers. *Review of Scientific Instruments.* **Vol. 69**, no. 2, pp. 544-553. (1998)

P.T. Keyser, J.E. Faller, and K.H. McLagan. New laboratory test of the equivalence principle. *Precision Measurement and Fundamental Constants II. Proceedings of the Second International Conference (NBS-SP-617).* NBS, Washington, DC. Pp. 639-641. (1984)

K. Kuroda. Does the time-of-swing method give a correct value of the Newtonian gravitational constant? *Physical Review Letters.* **Vol. 75**, no. 15, pp. 2796-2798. (1995)

S.K. Lamoreaux. Demonstration of the Casimir force in the 0.6 to 6 mu m range. *Physical Review Letters.* **Vol. 78**, no. 1, pp. 5-8. (1997)

G.G. Luther and W.R. Towler. Redetermination of the Newtonian gravitational constant 'G'. *Precision Measurement and Fundamental Constants II. Proceedings of the Second International Conference (NBS-SP-617).* NBS, Washington, DC. Pp. 573-576. (1984)

M.W. Moore, A. Boudreaux, M. DePue, G. Guthrie, R. Legere, A. Yan, and P.E. Boynton. Testing the inverse-square law of gravity: a new class of torsion pendulum null experiments. *Classical and Quantum Gravity.* **Vol. 11**, no. 6A, pp. A97-A117. (1994)

J. Muller and K. Nordtvedt. Lunar laser ranging and the equivalence principle signal. *Physical Review D (Particles and Fields).* **Vol. 58**, no. 6, pp. 062001/1-13. (1998)

P.G. Nelson, D.M. Graham, and R.D. Newman. Search for an intermediate-range composition-depedndent force coupling to N-Z. *Physical Review D (Particles and Fields).* **Vol. 42**, no. 4, pp. 963-976. (1990)

R.D. Newman and M.K. Bantel. On determining G using a cryogenic torsion pendulum. *Measurement Science & Technology.* **Vol. 10**, no. 6, pp. 445-453. (1999)

R.D. Newman, M.K. Bantel, and Z.R. Wang. Prospects for gravitational physics experiments with cryogenic torsion balances. *Dark Matter in Cosmology, Quantum Measurements, Experimental Gravitation, proceedings of the XVIth Moriond Workshop.* Gif-sur-Yvette, France, January 1996, eds., G. Chardin, O. Fackler and J. Tran Thanh Van (Editions Frontières), pp. 409-416. (1996)

A. Peters, K.Y. Chung, and S. Chu. Measurement of gravitational acceleration by dropping atoms. *Nature.* **Vol. 400**, pp. 849-852. (26 Aug 1999)

P.G. Roll, R. Krotkov, and R.H. Dicke. The equivalence of inertial and passive gravitational mass. *Annals of Physics.* **Vol. 26**, p. 442-517. (1964)

G.E. Stedman. Ring-laser tests of fundamental physics and geophysics. *Reports on Progress in Physics.* **Vol. 60**, no. 6, pp. 615-687. (1997)

C.W. Stubbs, E.G. Adelberger, F.J. Raab, J.H. Gundlach, B.R. Heckel, K.D. McMurray, H.E. Swanson, and R. Watanabe. Search for an intermediate-range interaction. *Physical Review Letters.* **Vol. 58**, no. 11, pp. 1070-1073. (1987)

C.W. Stubbs, E.G. Adelberger, B.R. Heckel, W.F. Rogers, H.E. Swanson, R. Watanabe, J.H. Gundlach, and F.J. Raab. Limits on composition-dependent interactions using a laboratory source: Is there a 'fifth force' coupled to isospin? *Physical Review Letters.* **Vol. 62**, no. 6, pp. 609-612. (1989)

Y. Su, B.R. Heckel, E.G. Adelberger, J.H. Gundlach, M. Harris, G.L. Smith, and H.E. Swanson. New tests of the universality of free fall. *Physical Review D (Particles, Fields Gravitation, and Cosmology).* **Vol. 50**, no. 6, pp. 3614-3636. (1994)

Appendix: Optimal Thermal-Noise Limited Fit of the Parameters of a Damped Harmonic Oscillator

A.1. Introduction

A.1.1. Motivation

Five parameters are required to specify the free oscillation of a damped harmonic oscillator. The purpose of this paper is to derive and describe the optimal method of fitting for those parameters when thermal fluctuations of the oscillator is the leading source of noise. More specifically, the paper will the address the case of a short duration (i.e., a few periods) continuous time series of a lightly damped oscillator whose amplitude is large compared to thermal fluctuations.

The original motivation for this work came from our precision gravitational experiments in which an oscillating torsion balance is used to measure the possible existence of extremely weak external torques, and so our interest in this problem is more than academic. The torsion balance, however, is not the only physical system that has been successfully modeled as a damped harmonic oscillator, and given the ubiquity of thermal noise, the optimal method of data analysis may be of general interest to any experimentalist. Furthermore, intuition would suggest that such a simple, canonical problem should have a straightforward, easily understandable solution.

As it turns out, the answer is indeed simple, but the problem is sufficiently subtle that it does not readily yield to "cookbook" methods. The mathematical tools to solve this problem certainly do exist (Helstrom 1968). These methods were intensely developed for radar applications during and following World

War II. Having a formal mathematical solution, however, does not necessarily translate quickly into a usable solution for experimentalists because even the simplest of statistical problems can generate a mountain of tedious algebra if an exact, closed form solution is sought. Unfortunately, the appropriate approximations and simplifications that make the solution tractable are often only apparent in hindsight.

This mathematical frustration can tempt one to adopt a standard analysis technique, such as least squares minimization of the time series residue, which although not optimal may seem good enough. This course is not to be recommended for the narrowband thermal noise of a high Q oscillator because the penalty can be quite severe—the variance in parameter estimates can be on the order of Q times larger than those of the optimal method!

A.1.2. Approximations and Symbols Used

Although the original motivation for this problem came from experience with torsion pendula, the results are applicable to any damped harmonic oscillator; thus, our discussion is phrased in terms of the more familiar position, velocity, force, and mass rather than in terms of angle, angular velocity, torque, and rotational inertia. The following symbols will be used:

Data

$x(t)$.....instantaneous position of oscillator

$v(t)$.....instantaneous velocity of oscillator

Constants

K.....Boltzmann's constant

T.....absolute temperature

M.....mass

$\kappa = -f_{spring}/x$ .....spring constant

$\beta = -f_{friction}/v$ .....damping constant

$\gamma = \beta/(2M)$.....decay constant (inverse of damping time)

$\omega_o = (\kappa/M)^{1/2}$ .....natural frequency

$\omega_d = (\omega_o^2 - \gamma^2)^{1/2}$.....damped frequency

$\omega_r = (\omega_o^2 - 2\gamma^2)^{1/2}$.....driven resonant frequency

$Q = \omega_r / (2\gamma) \cong \omega_d / (2\gamma)$ .....quality factor

τ.....duration of data sample

$t_i = -\tau/2$.....initial time of data sample

$t_f = +\tau/2$ .....final time of data sample

$N = \tau/(2\pi/\omega_d)$.....length of data sample in periods

A_o .....quadrature amplitude at t=0

ϕ_o.....phase at t=0

$\chi_{th} = (KT/\kappa)^{1/2}$ .....rms thermal fluctuation in position

Γ .....equilibrium position of oscillator

Parameters

(treated as variables rather than physical constants)

$a = A_o \cos(\phi_o)$ .....cosine amplitude

$b = A_o \sin(\phi_o)$.....sine amplitude

$c = \Gamma$ .....equilibrium position parameter

$g = \gamma$.....damping parameter

$w = \omega_d$.....frequency parameter

Parameterization of damped harmonic oscillator motion:

$$x(t)\{a,b,c,g,w\} = a\exp(-gt)\cos(wt) + b\exp(-gt)\sin(wt) + c$$

Additional symbols will be introduced at the beginning of the sections in which they are first used.

The derivations in this paper are for a perfectly linear, damped harmonic oscillator; any non-linearities or frequency dependence in the spring constant and damping constant are assumed to be negligible, and the damping is considered to be purely resistive with no reactive component. The motion of the pendulum is then entirely determined by the macroscopic spring and damping forces along with the microscopic fluctuations of the gaussian thermal driving force. Additive measurement error and the effects of a finite sampling rate are assumed negligible, leaving thermal noise to provide the only source of error in estimating the parameters. Because of the non-linear dependence on g and w, the derivation will be for large amplitude oscillations, $\alpha>>1$, so that linearization of the fit will be a valid approximation.

This paper will be devoted to high Q oscillators because the minimum variance in the estimates of c, g , and w all decrease as $1/Q$, and hence choosing a high Q system is clearly advantageous for a thermal noise limited experiment. This tends to conflict with the mathematical requirement that $N>>Q$ if standard Fourier space techniques are to be used. (Otherwise, the discrete Fourier components of the noise are not statistically independent). The main goal of this paper is to demonstrate how to proceed when the standard Fourier techniques fail. The opposite assumption will be invoked, $N<<Q$, so that results can be reasonably approximated to leading order in $1/Q$. Also in the interest of simplicity, the duration of the data sample will chosen to be an integer number of periods. Of course, requiring N to be exactly an integer value is equivalent to

requiring a perfect knowledge of the frequency, and so all that is strictly required is that N = integer $\pm$ $(1/Q)$; this level of *a priori* knowledge of the frequency can be easily obtained provided that the requirement of a large amplitude is satisfied.

A.1.3. Outline of Discussion

Section A.2 will briefly discuss the Fourier representation of stationary noise processes. Given the estimator function for a single parameter, it will be shown how the expected variance in that parameter estimate can be calculated using the noise power spectrum. Finally, the optimal estimator for the equilibrium position of the oscillator in thermal equilibrium will be introduced to provide a concrete example to illustrate these Fourier methods.

Section A.3 will address some of the statistical approximations that are used in the derivation: linearization of non-linear fits, neglecting third and higher moments of the noise ensemble, and assuming uniform *a priori* probabilities in parameter space. There is nothing unusual about these approximations–all of them are routinely invoked for problems with a large signal to noise ratio–but it is better to lay one's assumptions out on the table rather than sweep them under a rug.

Calculating the variance of a parameter estimate for a given estimator function is useful, but ideally one wants to know what estimator provides the optimal (minimum variance) estimate of that parameter for a particular noise process. Section A.4 reviews the theory of matched filters for "white" noise, and then generalizes the method for thermal noise. The optimal filters for single parameter estimates of a, b, c, g, and w are then derived.

An actual fit, however, must estimate all the parameters simultaneously. Section A.5 reviews the matrix formulation of optimal multi-parameter fits for discrete data. An alternate formulation optimal discrete data fits is presented whereby the optimal multi-parameter estimators are obtained from optimal single parameter filters. This method is extended to multi-parameter fits on a continuous time series, and finally these ideas are used to obtain the optimal simultaneous fit for the five parameters of a damped harmonic oscillator from the optimal single parameter fits derived in Section A.4.

A.2. Stationary Noise Processes and Linear Parameter Estimators

A.2.1 Approximations and Symbols Used

$x(t)$ ..... data variable (particular realization)

$X(t)$ ..... random data variable (represents ensemble)

$\mathbf{x}$ ..... entire data time series (as vector in Hilbert space)

$\mathbf{X}$ ..... time series ensemble

$\langle X(t) \rangle$ ..... expectation of random variable

$\mathrm{var}(X(t)) = \langle X^2(t) \rangle - \langle X(t) \rangle^2$ ..... variance of random variable

$\mathrm{stddev}(X(t)) = \sqrt{\mathrm{var}(X(t))}$ ..... standard deviation of random variable

$\mathrm{cov}(X(t_1), X(t_2)) = \langle X(t_1)X(t_2) \rangle - \langle X(t_1) \rangle \langle X(t_2) \rangle$ ..... covariance of two random variables

$\delta x(t) = x(t) - \langle X(t) \rangle$ ..... noise error

$\delta \mathbf{X} = \mathbf{X} - \langle \mathbf{X} \rangle$ ..... noise ensemble

p ..... parameter variable

ρ ..... true value of parameter (constant)

$x(t)\{p\}$ .....parameterized signal

$x(t)\{\rho\} = \langle X(t) \rangle$ .....true signal

$\hat{p}[\mathbf{x}]$ .....estimate of parameter

$f_{\hat{p}}(t)$ .....filter function (not normalized)

$e_{\hat{p}}(t)$ .....estimator function (normalized)

For linear fits, a parameter estimate, $\hat{p}[\mathbf{x}]$, can be expressed in terms of an estimator function, $e_{\hat{p}}(t)$, such that $\hat{p}[\mathbf{x}] = \int_{-\infty}^{+\infty} e_{\hat{p}}(t)x(t)dt$.

$\hat{P}[\mathbf{X}]$ .....estimate as random variable

$F_A[\mathbf{x}](\nu) = \int_{-\infty}^{+\infty} x(t)\cos(2\pi\nu t)dt$ ....cosine Fourier component of $\mathbf{x}$

$F_B[\mathbf{x}](\nu) = \int_{-\infty}^{+\infty} x(t)\sin(2\pi\nu t)dt$ .....sine Fourier component of $\mathbf{x}$

$F^2\left[\mathbf{e}_{\hat{p}}\right](\nu) =$

$\left(F_A\left[\mathbf{e}_{\hat{p}}\right](\nu)\right)^2 + \left(F_B\left[\mathbf{e}_{\hat{p}}\right](\nu)\right)^2$ .....spectral power density of estimator, $\mathbf{e}_{\hat{p}}$

$F^2[\delta\mathbf{X}](\nu) = \mathrm{var}(F_A[\delta\mathbf{X}](\nu)) + \mathrm{var}(F_B[\delta\mathbf{X}](\nu))$ .....spectral power density of noise ensemble, $\delta\mathbf{X}$

wh.....subscript indicating "white" noise

th .....subscript indicating thermal noise

op.....superscript indicating optimal fit

$F^2[\delta\mathbf{X}_{wh}](\nu) = \text{constant} = \eta_{wh}^2$ ....."white" noise spectral power density

$F^2[\delta\mathbf{X}_{th}](\nu) =$

$\dfrac{4KT\beta}{M^2\left(\left((2\pi\nu)^2 - \omega_o^2\right)^2 + (4\pi\gamma\nu)^2\right)}$ ...thermal noise spectral power density

Although this notation might appear somewhat pedantic, it is best initially to err on the side of specificity in order to avoid simple misunderstandings that subsequently could create confusion. Later, some of the notation that explicitly

denotes dependence on other variables will be dropped. In this section, signals are characterized by a single parameter. Fitting signals of several parameters will be covered in Section A.5. Also, the spectral power density of noise ensembles is assumed to be known; this paper will not address Student t type problems in which information about both the mean and variance of the ensemble is extracted simultaneously from the data.

A.2.2 Fourier Representation of Stationary Noise Processes

A data time series ensemble, **X**, can be decomposed into a reproducible part which is designated as the signal, $x(t)\{\rho\} = \langle X(t) \rangle$, and a random, fluctuating part which is designated as the noise, $\delta X(t) = X(t) - \langle X(t) \rangle$. If this is done, the noise is then, by definition, unbiased (i.e., $\langle \delta X(t) \rangle = 0$ for all t). The signal is parameterized; Roman letters, such as p, will denote the parameter as a variable in the fitting process, and Greek symbols, such as ρ, will denote the true, physical value (a constant). The fact that the continuous time series of the signal can be characterized by a single parameter (or ultimately, in Section A.5, a finite set of parameters) depends on having an accurate and complete physical model of the system. As mentioned earlier, this will be assumed. Nor will the physical interpretation of the parameter(s) be directly addressed because this goes beyond questions of precision into the realm of accuracy wherein all sources of systematic error that can bias the value of the parameter(s) have to be properly accounted for.

If a noise process has no special, preferred point in time, it is called a stationary noise process. One property of a stationary noise process is the time-translation invariance of all two-point time correlations:

$$\langle \delta X(0) \delta X(t) \rangle = \langle \delta X(\Delta t) \delta X(t + \Delta t) \rangle \text{ for all } t \text{ and } \Delta t. \qquad \text{(A.1)}$$

However, for our purposes, a more important property is that the correlations between pairs of different Fourier components are identically zero. For mathematical manipulations, particularly integration in the complex plane, defining a complex Fourier basis with both positive and negative frequencies is convenient, but as the reader will be spared from most of these mathematical details, we will adopt the engineering convention of real sine and cosine Fourier components with frequencies (in Hz rather than rad/sec) going from 0 to positive infinity (see definition of $F_A[\mathbf{x}](\nu)$ and $F_B[\mathbf{x}](\nu)$ above in Section A.2.1). By presenting the results entirely in real quantities, there are fewer ambiguities as to how they are to be employed in numerical calculations. Because there are no correlations between Fourier components (in matrix terminology, there are no off-diagonal elements), the spectral power density, $F^2[\delta\mathbf{X}](\nu)$, provides a complete description of the second moments of a stationary noise process.

$$\langle F_A[\delta\mathbf{X}](\nu)\rangle = \langle F_B[\delta\mathbf{X}](\nu)\rangle = 0 \quad \text{(unbiased noise ensemble)} \tag{A.2}$$

$$\left.\begin{aligned} &\langle F_A[\delta\mathbf{X}](\nu_1)F_B[\delta\mathbf{X}](\nu_2)\rangle = 0 \\ &\langle F_A[\delta\mathbf{X}](\nu_1)F_A[\delta\mathbf{X}](\nu_2)\rangle = 0 \quad \nu_1 \neq \nu_2 \\ &\langle F_B[\delta\mathbf{X}](\nu_1)F_B[\delta\mathbf{X}](\nu_2)\rangle = 0 \quad \nu_1 \neq \nu_2 \end{aligned}\right\} \text{(Fourier components uncorrelated)} \tag{A.3}$$

$$\mathrm{var}(F_A[\delta\mathbf{X}](\nu)) = \mathrm{var}(F_B[\delta\mathbf{X}](\nu)) \equiv F^2[\delta\mathbf{X}](\nu)/2 \quad \text{(random phase)} \tag{A.4}$$

A special ideal case of stationary noise processes is "white" noise, so called because it has equal amounts of all frequencies, $F^2[\delta\mathbf{X}_{wh}](\nu) = \text{constant} = \eta_{wh}^2$. This results in the elimination of all two-point time correlations, $\langle \delta X_{wh}(0)\delta X_{wh}(t)\rangle = 0$ for all $t \neq 0$. This type of noise if generally a good model for a succession of identical measurements whose errors are uncorrelated with

each other. "White" noise has infinite power (i.e., the integral, $\int_0^\infty \mathrm{F}^2[\delta \mathbf{X}_{wh}](\nu)d\nu$, does not converge); in any physical system, there is typically a high-frequency cutoff above which the noise is attenuated. For the derivations in this paper, however, we will be able to use the mathematically ideal "white" noise without generating any non-physical results.

The other stationary noise process in which we are interested is thermal noise on a damped harmonic oscillator. According to the fluctuation-dissipation theorem, the force power density exerted by the thermal bath is given by $4KT\beta$. The spectral power density in position and velocity can then be directly derived from the response function of the oscillator.

$$\mathrm{F}^2[\delta \mathbf{X}_{th}](\nu) = \frac{4KT\beta}{M^2\left(\left((2\pi\nu)^2 - \omega_o^2\right)^2 + (4\pi\gamma\nu)^2\right)} \tag{A.5}$$

$$\mathrm{F}^2[\delta \mathbf{V}_{th}](\nu) = \frac{4KT\beta(2\pi\nu)^2}{M^2\left(\left((2\pi\nu)^2 - \omega_o^2\right)^2 + (4\pi\gamma\nu)^2\right)} \tag{A.6}$$

Because this noise process is produced as the mechanical response to a "white" thermal driving force, Helstrom would call it a leucogenic noise process. In Section A.4.3, it will be shown that it is quite simple to find optimal filters when the noise process is leucogenic. Unlike the "white" thermal driving force which mathematically has infinite power, the integrals of the position and velocity noise power densities converge quite nicely, and they are related to the well-known expectation values for the potential and kinetic energy of a damped harmonic oscillator.

$$\int_0^\infty \mathrm{F}^2[\delta \mathbf{X}_{th}](\nu)d\nu = \frac{2\langle P.E.\rangle}{\kappa} = \frac{KT}{\kappa} \equiv \chi_{th}^2 \tag{A.7}$$

$$\int_0^\infty \mathrm{F}^2[\delta \mathrm{V}_{th}](\nu)d\nu = \frac{2\langle K.E.\rangle}{M} = \frac{KT}{M} = \frac{\chi_{th}^2}{\omega_o^2} \tag{A.8}$$

A.2.3 Variance of Linear Parameter Estimates

Given the spectral power density of a noise process, how is the variance of a linear parameter estimate, $\mathrm{var}\left(\hat{P}[\mathbf{X}]\right)$, calculated? A linear parameter estimate can be expressed in terms of a estimator function, $e_{\hat{p}}(t)$. For each realization of the data ensemble, $\mathbf{x}$, there is a parameter estimate, $\hat{p}[\mathbf{x}] = \int_{-\infty}^{+\infty} e_{\hat{p}}(t)x(t)dt$. First, calculate the variance in $\hat{P}[\mathbf{X}]$ introduced by a single Fourier component of unit amplitude and arbitrary phase, φ.

$$\begin{aligned} &\frac{1}{2\pi}\int_0^{2\pi}\left[\int_{-\infty}^{+\infty} e_{\hat{p}}(t)\cos(2\pi\nu t - \varphi)dt\right]^2 d\varphi = \\ &\frac{1}{2\pi}\int_0^{2\pi}\left[\mathrm{F_A}\left[\mathbf{e}_{\hat{p}}\right](\nu)\cos\varphi - \mathrm{F_B}\left[\mathbf{e}_{\hat{p}}\right](\nu)\sin\varphi\right]^2 d\varphi = \mathrm{F}^2\left[\mathbf{e}_{\hat{p}}\right](\nu)/2 \end{aligned} \tag{A.9}$$

To calculate the total variance, the contribution from each frequency component needs to be multiplied by the noise spectral power density at that frequency, and then all these contributions need to be integrated. Because there are no covariances between the various noise Fourier components, the variances from each of the components can be summed together.

$$\mathrm{var}\left(\hat{P}[\mathbf{X}]\right) = \int_0^\infty \mathrm{F}^2\left[\mathbf{e}_{\hat{p}}\right](\nu)\mathrm{F}^2[\delta\mathbf{X}](\nu)d\nu/2 \tag{A.10}$$

It should pointed out that any function, $f_{\hat{p}}(t)$, can be used as a filter function to produce an unbiased parameter estimate provided that it is properly normalized (define normalization as $e_{\hat{p}}(t) = \lambda f_{\hat{p}}(t)$):

$$\begin{aligned}\left\langle \hat{P}[\mathbf{X}] \right\rangle &= \int_{-\infty}^{+\infty} e_{\hat{p}}(t)(x(t)\{\rho\})dt = \rho \\ &= \int_{-\infty}^{+\infty} \lambda f_{\hat{p}}(t)(\rho * x(t)\{1\})dt = \rho \qquad \text{(A.11)} \\ \lambda = \frac{1}{\int_{-\infty}^{+\infty} f_{\hat{p}}(t)(x(t)\{1\})dt} \quad &\Rightarrow \quad e_{\hat{p}}(t) \equiv \frac{f_{\hat{p}}(t)}{\int_{-\infty}^{+\infty} f_{\hat{p}}(t)(x(t)\{1\})dt}\end{aligned}$$

The only exception is if $f_{\hat{p}}(t)$ is perfectly orthogonal to the signal in which case no information about the parameter can be extracted. Although $\left\langle \hat{P}[\mathbf{X}] \right\rangle$ does not depend on the choice of $f_{\hat{p}}(t)$, $\mathrm{var}\left(\hat{P}[\mathbf{X}]\right)$ does:

$$\mathrm{var}\left(\hat{P}[\mathbf{X}]\right) = \frac{\int_0^{\infty} \mathrm{F}^2\left[\mathbf{f}_{\hat{p}}\right](\nu)\mathrm{F}^2[\delta\mathbf{X}](\nu)d\nu/2}{\left[\int_{-\infty}^{+\infty} f_{\hat{p}}(t)(x(t)\{1\})dt\right]^2} \qquad \text{(A.12)}$$

Finding the optimal filter, $f_{\hat{p}}(t)$, that minimizes $\mathrm{var}\left(\hat{P}[\mathbf{X}]\right)$ is thus ultimately a problem in the calculus of variations. Furthermore, in order to have a well-posed minimization problem, there are typically constraints on the duration of the data sample in the time domain that are difficult to express in a Fourier basis which is the natural basis in which to calculate the parameter estimate variances. The solution to this dilemma for leucogenic noise processes is presented in Section A.4.3.

Finally, some remarks on calculation. The thermal noise spectral power density, $\mathrm{F}^2[\delta\mathbf{X}_{th}](\nu)$, is a meromorphic function (i.e., it only has isolated poles in the complex plane), and therefore most of the integrals involving thermal noise can be evaluated by the method of residues. For "white" noise processes, the variance in a parameter estimate can be calculated in the time domain as well as in a Fourier basis.

$$\begin{aligned}\mathrm{var}_{wh}\left(\hat{P}[\mathbf{X}]\right) &= \int_0^{\infty} \mathrm{F}^2\left[\mathbf{e}_{\hat{p}}\right](\nu)\mathrm{F}^2[\delta\mathbf{X}_{wh}](\nu)d\nu/2 = \frac{\eta_{wh}^2}{2}\int_0^{\infty}\mathrm{F}^2\left[\mathbf{e}_{\hat{p}}\right](\nu)d\nu \\ &= \frac{\eta_{wh}^2}{4}\int_{-\infty}^{+\infty}\mathrm{F}^2\left[\mathbf{e}_{\hat{p}}\right](\nu)d\nu = \frac{\eta_{wh}^2}{4}\int_{-\infty}^{+\infty} e_{\hat{p}}(t)^2 dt\end{aligned} \tag{A.13}$$

The last step above invokes Parseval's relation. Although it is generally easier to compute the parameter estimate variance in the time domain, the Fourier basis method will be emphasized because it can be generalized to non-"white" noise processes.

A.2.4 Boxcar vs. Optimal Estimator of Equilibrium Position

In order to illustrate the use of these Fourier methods and also to familiarize the reader with some aspects of the thermal noise problem, let us look at the determination of the equilibrium position of an oscillator, c, that is nominally at rest (i.e., $A_0 = 0$). One obvious method is to simply average the position, sometimes referred to as a "boxcar" estimator function. In the case where "white" measurement noise dominates, this is indeed the optimal estimator function (as will be explained in Section A.4.2 on matched filters), and we shall refer to it as the "white" noise optimal estimator, $\hat{c}_{wh}^{op}[\mathbf{x}]$. For a data sample of duration τ,

$$\hat{c}_{wh}^{op}[\mathbf{x}] = (1/\tau)\int_{-\tau/2}^{+\tau/2} x(t)dt \qquad \mathrm{F}^2\left[\mathbf{e}_{\hat{c}_{wh}^{op}}\right](\nu) = \frac{\sin^2(\pi\nu\tau)}{(\pi\nu\tau)^2}, \tag{A.14}$$

and the variance in the presence of "white" noise is,

$$\mathrm{var}_{wh}\left(\hat{C}_{wh}^{op}[\mathbf{X}]\right) = \int_0^{\infty}\mathrm{F}^2\left[\mathbf{e}_{\hat{c}_{wh}^{op}}\right](\nu)\mathrm{F}^2[\delta\mathbf{X}_{wh}](\nu)d\nu/2 = \frac{\eta_{wh}^2}{4\tau}. \tag{A.15}$$

When thermal noise dominates, the "boxcar" estimate has a different variance:

$$\begin{aligned}\mathrm{var}_{th}\left(\hat{C}_{wh}^{op}[\mathbf{X}]\right) &= \int_0^\infty \mathrm{F}^2\left[\mathbf{e}_{\hat{c}\,wh}^{op}\right](\nu)\mathrm{F}^2\left[\delta\mathbf{X}_{th}\right](\nu)d\nu/2 \\ &= \frac{2KT}{M\omega_d\omega_o^6\tau^2}\left(-3\gamma^2\omega_d+\omega_d^3+2\gamma^3\omega_d\tau+2\gamma\omega_d^3\tau+\right. \\ &\quad 3\gamma^2\omega_d e^{-\gamma\tau}\cos(\omega_d\tau)-\omega_d^3\exp(-\gamma\tau)\cos(\omega_d\tau)+ \\ &\quad \left.\gamma^3\exp(-\gamma\tau)\sin(\omega_d\tau)-3\gamma\omega_d^2\exp(-\gamma\tau)\sin(\omega_d\tau)\right).\end{aligned} \tag{A.16}$$

Even with this fairly simple problem, an exact closed form of the result is already becoming unwieldy; since, the multi-parameter problem will involve the inversion of 5x5 matrices of such terms, it is evident that some approximation of the results will be necessary to make the algebra manageable. Figure A.1 is a log-log plot of $\mathrm{var}_{th}\left(\hat{C}_{wh}^{op}[\mathbf{X}]\right)$ vs. $N=\tau/(2\pi/\omega_d)$ for $Q=10$ and $Q=100$.

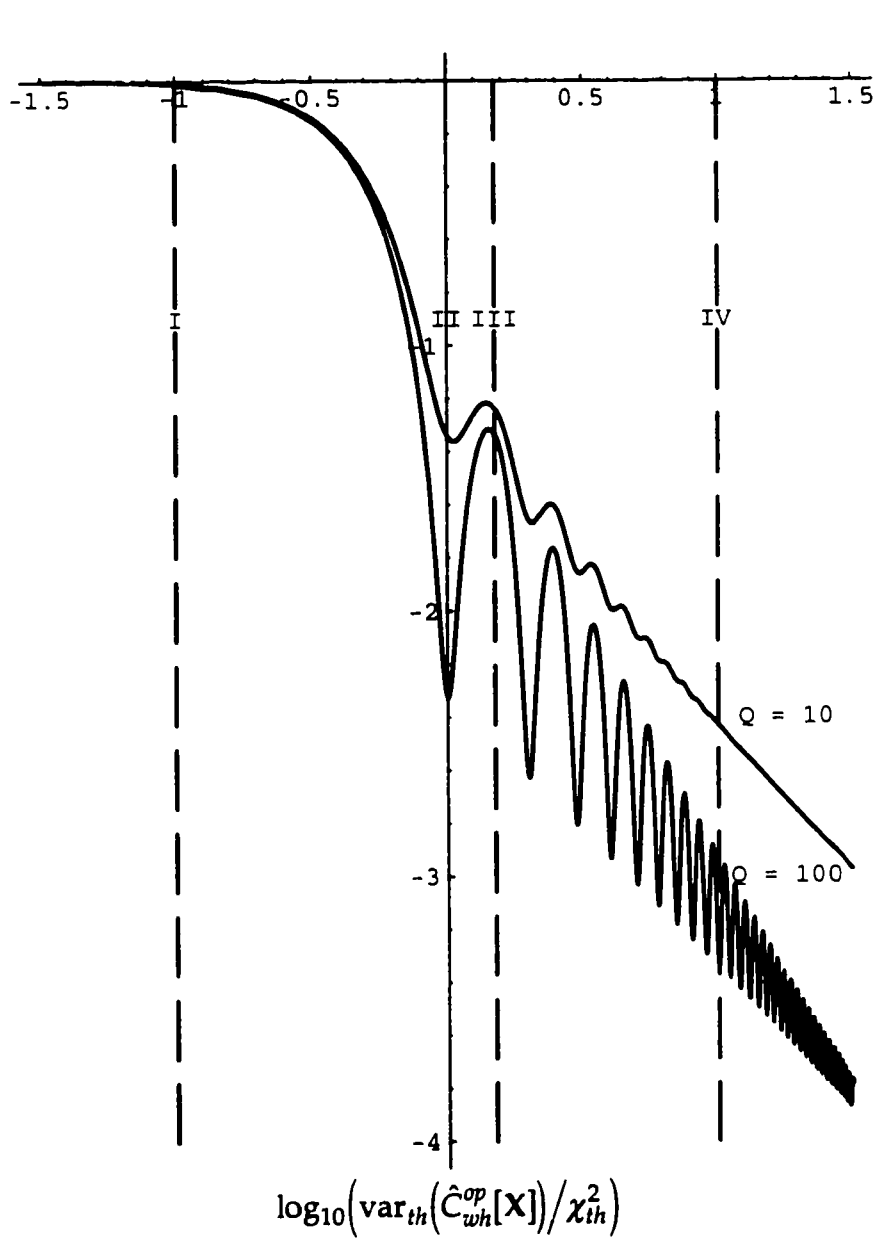

Figure A.1. Variance in "boxcar" estimate of deflection as a function of duration of integration expressed in number of oscillation periods, N. Variance is indicated for both a $Q = 10$ and $Q = 100$ oscillator. The vertical lines I, II, III, and IV correspond to frames in Figure A.2.

Looking at Figure A.1, it is apparent that the "boxcar" estimator is not optimal for thermal noise because $\mathrm{var}_{th}\left(\hat{C}^{op}_{wh}[\mathbf{X}]\right)$ is not a monotonically decreasing func-

tion of N. Adding more data should never degrade your ability to estimate a parameter. To qualitatively understand the structure of $\mathrm{var}_{th}\left(\hat{C}_{wh}^{op}[\mathbf{X}]\right)$, four cases (corresponding to $N = 0.1$, $N = 1$, $N = 1.5$, and $N = 10$) have been indicated in Figure A.1 and displayed as Fourier plots of $\mathrm{F}^2\left[\mathbf{e}_{\hat{c}wh}^{op}\right]$ and $\mathrm{F}^2[\delta\mathbf{X}_{th}]$ in Figure A.2. In all four plots of Figure A.2, the Lorentzian $\mathrm{F}^2[\delta\mathbf{X}_{th}]$ is shown for both $Q = 10$ and $Q = 100$. Most of the noise power is concentrated in the resonant peak; the $Q = 100$ peak, although much narrower than the $Q = 10$ peak, is much taller (both peaks are well above the top of the plots), and the area under both curves is 1 in the dimensionless units of the plot. In the low frequency ($\mathrm{F}^2[\delta\mathbf{X}_{th}] \propto \nu^0$) and high frequency ($\mathrm{F}^2[\delta\mathbf{X}_{th}] \propto \nu^{-4}$) regimes, the noise power is inversely proportional to Q.

For $N = 0.1$, $\mathrm{F}^2\left[\mathbf{e}_{\hat{c}wh}^{op}\right]$ is nearly unity throughout the resonant peak, and so $\mathrm{var}_{th}\left(\hat{C}_{wh}^{op}[\mathbf{X}]\right) \cong \chi_{th}^2$ regardless of the value of Q. Unlike "white" noise, the finite power of thermal noise means there is a reasonable instantaneous limit, $\mathrm{var}_{th}\left(\hat{C}[\mathbf{X}]\right) = \chi_{th}^2$, as $N \to 0$. For $N = 1$, the first notch in $\mathrm{F}^2\left[\mathbf{e}_{\hat{c}wh}^{op}\right]$ filters out most of the noise in the resonant peak. The greater Q is, the more narrowband the noise, and the more dramatic the reduction in $\mathrm{var}_{th}\left(\hat{C}_{wh}^{op}[\mathbf{X}]\right)$. For $N = 1.5$, the first and second notch of $\mathrm{F}^2\left[\mathbf{e}_{\hat{c}wh}^{op}\right]$ straddle the resonant peak causing $\mathrm{var}_{th}\left(\hat{C}_{wh}^{op}[\mathbf{X}]\right)$ to increase and losing the $1/Q$ advantage. As $N > Q$, the oscillations in $\mathrm{var}_{th}\left(\hat{C}_{wh}^{op}[\mathbf{X}]\right)$ die away because the notches and peaks in $\mathrm{F}^2\left[\mathbf{e}_{\hat{c}wh}^{op}\right]$ become narrower than the resonant peak. Also, the contribution from the very low frequencies, where $\mathrm{F}^2[\delta\mathbf{X}_{th}]$ is relatively flat, begins to dominate the contribution from the resonant peak, and thus $\mathrm{var}_{th}\left(\hat{C}_{wh}^{op}[\mathbf{X}]\right)$ adopts the $1/N$ dependence characteristic of "white" noise.

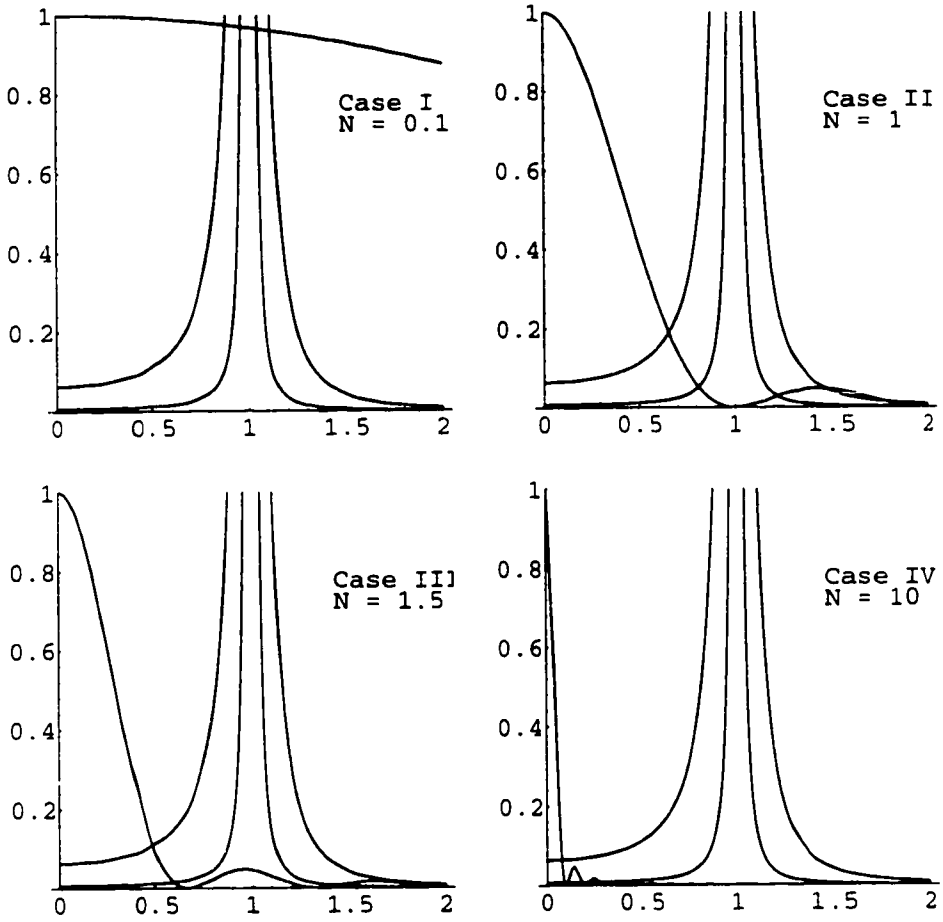

$$F^2\left[\mathbf{e}_{\hat{c}wh}^{op}\right],\ \frac{F^2[\delta X_{th}]_{Q=10}}{(2\pi/\omega_d)\chi_{th}^2},\ \text{and}\ \frac{F^2[\delta X_{th}]_{Q=100}}{(2\pi/\omega_d)\chi_{th}^2}\ \text{vs.}\ \frac{\nu}{(\omega_d/2\pi)}$$

Figure A.2. Lorentzian thermal noise displacement power spectrum for both a $Q = 10$ and $Q = 100$ oscillator is plotted along with $F^2\left[\mathbf{e}_{\hat{c}wh}^{op}\right]$ which quantifies how much a particular Fourier component of noise propagates into the "boxcar" estimate of deflection. $F^2\left[\mathbf{e}_{\hat{c}wh}^{op}\right]$ is plotted for a "boxcar" of 0.1 period, 1 period, 1.5 periods, and 10 periods of duration.

For the $N >> Q$ regime, it turns out that a "boxcar" average does provide an optimal, minimum variance estimate of c, and for $N = 1.5$, it obviously does not. How about the $N = 1$ case? It turns out that the "boxcar" is reasonably

good but not perfect. A factor of 2/3 reduction in $\mathrm{var}_{th}\left(\hat{C}[\mathbf{X}]\right)$ can be gained by using:

$$\hat{c}_{th}^{op}[\mathbf{x}]_{N=1} = \frac{v(t_f) - v(t_i)}{2\pi\omega_d} + \left(\frac{1}{\tau}\right)\int_{-\tau/2}^{+\tau/2} x(t)dt \qquad \text{(A.17)}$$

A Fourier plot comparison of $\mathrm{F}^2\left[\mathbf{e}_{\hat{c}wh}^{op}\right]_{N=1}$ to $\mathrm{F}^2\left[\mathbf{e}_{\hat{c}th}^{op}\right]_{N=1}$ is shown in Figure A.3. The main advantage of the thermal noise optimal estimator over the boxcar estimator is that it has a quartic rather than just a quadratic notch at the resonant frequency. The increased susceptibility to high frequency noise makes the thermal noise optimal estimator inferior to the "boxcar" for a "white" noise process. Figure A.3 demonstrates that this new estimator provides a reduction in $\mathrm{var}_{th}\left(\hat{C}[\mathbf{X}]\right)$, but it does not provide a compelling argument why it is the optimal estimator for thermal noise. That will be done in Section A.4.

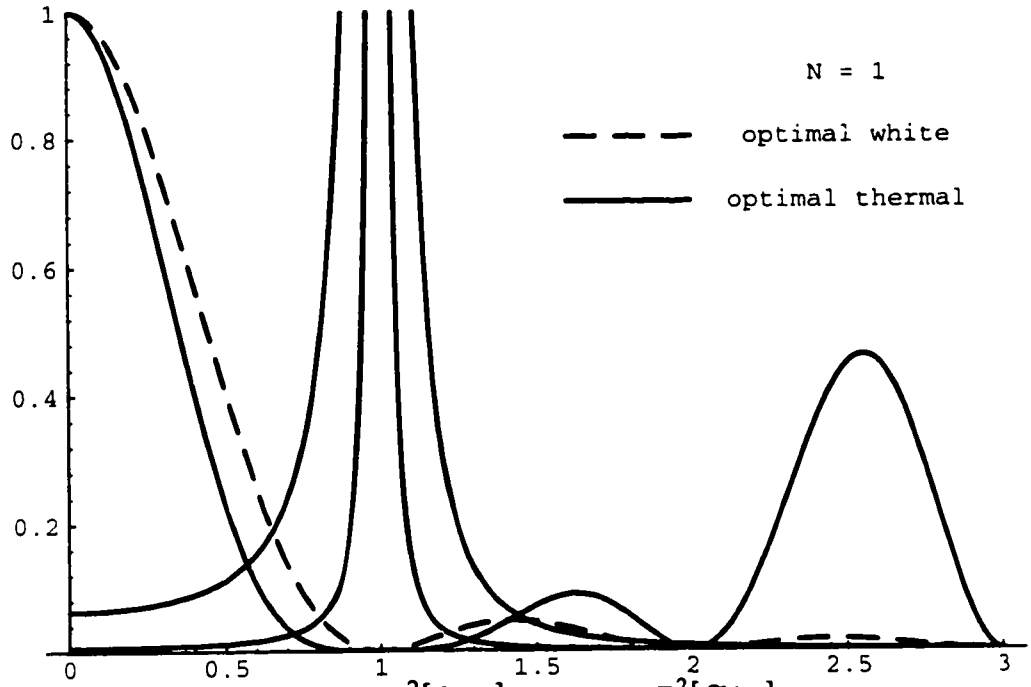

$F^2\left[\mathbf{e}_{\hat{c}_{wh}^{op}}\right]_{N=1}$, $F^2\left[\mathbf{e}_{\hat{c}_{th}^{op}}\right]_{N=1}$, $\dfrac{F^2[\delta X_{th}]_{Q=10}}{(2\pi/\omega_d)\chi_{th}^2}$, and $\dfrac{F^2[\delta X_{th}]_{Q=100}}{(2\pi/\omega_d)\chi_{th}^2}$ vs. $\dfrac{\nu}{(\omega_d/2\pi)}$

Figure A.3. Comparison of the error propagation of Fourier components of noise for both the "boxcar" estimate, which is optimal for "white" noise, and the optimal deflection estimate for thermal noise which incoporates the initial and final velocities as well as a "boxcar" average. Notice that although it allows in more high frequencies, which are not really a problem for thermal noise, it has a quartic rather than simply quadratic notch at the resonant frequency.

A.3. Linearization of Non-Linear Fits

A.3.1 Approximations and Symbols Used

$\delta x(t)\{\rho\} = x(t) - x(t)\{\rho\} =$
$\delta x(t) = x(t) - \langle X(t) \rangle$ .....true noise error

$\delta x(t)\{p\} = x(t) - x(t)\{p\}$ .....residue (estimated noise error)

$f_{\hat{p}}(t)\{p\}$ .....linearized filter function (not normalized)

$e_{\hat{p}}(t)\{p\}$ .....linearized estimator (normalized)

$\delta\hat{p}\left[\delta\mathbf{x}\{p\}\right]\{p\} = \int_{-\infty}^{+\infty} e_{\hat{p}}(t)\{p\}\delta x(t)\{p\}dt$ .....first-order correction of parameter estimate

$\delta\hat{p}\left[\delta\mathbf{x}\{\hat{p}[\mathbf{x}]\}\right]\{\hat{p}[\mathbf{x}]\} = 0$ .....convergence limit for non-linear fits

$\text{bias}\left(\hat{P}[\mathbf{X}]\right) = \left\langle \hat{P}[\mathbf{X}] \right\rangle - \rho$ .....bias of non-linear fit parameter estimate

A.3.2 Linearization of Fits

The results of Section A.2 are valid for signals whose dependence on its parameter(s) is entirely linear. Since the motion of a damped harmonic oscillator depends non-linearly on the parameters g and w, the methods of Section A.2 must be generalized to non-linear fits. In a linear fit, an estimator, $e_{\hat{p}}(t)$, is applied to the data, $x(t)$, to produce a parameter estimate, $\hat{p}[\mathbf{x}]$. For a non-linear fit, an initial value for the parameter, p, is assumed, the hypothesized signal is subtracted from the data to give a residue, $\delta x(t)\{p\} = x(t) - x(t)\{p\}$, and an estimator, $e_{\hat{p}}(t)\{p\}$, is applied to that residue to produce a first-order correction to the initial parameter estimate, $\delta\hat{p}\left[\delta\mathbf{x}\{p\}\right]\{p\}$.

$$\underset{\text{(linear)}}{\hat{p}[\mathbf{x}] = \int_{-\infty}^{+\infty} e_{\hat{p}}(t)x(t)} \quad \Rightarrow \quad \underset{\text{(non - linear)}}{\delta\hat{p}\left[\delta\mathbf{x}\{p\}\right]\{p\} = \int_{-\infty}^{+\infty} e_{\hat{p}}(t)\{p\}\delta x(t)\{p\}dt} \tag{A.18}$$

$$e_{\hat{p}}(t) \equiv \frac{f_{\hat{p}}(t)}{\int_{-\infty}^{+\infty} f_{\hat{p}}(t)(x(t)\{1\})dt} \quad \Rightarrow \quad e_{\hat{p}}(t)\{p\} \equiv \frac{f_{\hat{p}}(t)\{p\}}{\int_{-\infty}^{+\infty} f_{\hat{p}}(t)\{p\}\dfrac{\partial x(t)}{\partial p}\{p\}dt} \tag{A.19}$$

The estimator, $e_{\hat{p}}(t)\{p\}$, is normalized with respect to the derivative of the signal, $(\partial x(t)/\partial p)\{p\}$, and so this derivative must exist in the neighborhood of

the true signal, $x(t)\{\rho\}$, in order for the linearization of the fit to work. Indeed the major assumption is that the first-order Taylor series approximation,

$$x(t)\{p\} \cong x(t)\{\rho\} + \frac{\partial x(t)}{\partial p}\{\rho\} * (p - \rho), \tag{A.20}$$

is a good one, and then, to the extent to which it is possible, treat the fit as a perfectly linear one in $(p - \rho)$.

The explicit dependence on p of the estimator, $e_{\hat{p}}(t)\{p\}$, however, creates a qualitative difference between linear and non-linear fits; non-linear fits are, in general, iterative. The linear estimator is applied once, and repeating the process will not provide an improved parameter estimate. In a non-linear fit, the first application of the estimator, $e_{\hat{p}}(t)\{p\}$, to the residue, $\delta x(t)\{p\}$, provides an improved parameter estimate, p', and this generates an improved residue and estimator, $\delta x(t)\{p'\}$ and $e_{\hat{p}}(t)\{p'\}$ that provide a second improved parameter estimate, p''. This is repeated until the correction to the parameter estimate returned by the estimator converges to zero.

$$\begin{aligned} p' &= p + \delta\hat{p}'\left[\delta \mathbf{x}\{p\}\right]\{p\} \\ p'' &= p' + \delta\hat{p}''\left[\delta \mathbf{x}\{p'\}\right]\{p'\} \\ &\vdots \end{aligned} \qquad \begin{aligned} &\text{define } \hat{p}[\mathbf{x}] \text{ such that} \\ &\delta\hat{p}\left[\delta \mathbf{x}\{\hat{p}[\mathbf{x}]\}\right]\{\hat{p}[\mathbf{x}]\} = 0 \end{aligned} \tag{A.21}$$

The awkwardness of the $\delta\hat{p}\left[\delta \mathbf{x}\{p\}\right]\{p\}$ notation is intentional because it reflects an awkward concept. The notation emphasizes the dependence of both the estimator and the residue on the assumed value p, and since both are using p rather than the true value ρ, there is a certain sense in which you are trying to pull yourself up by your own bootstraps. Usually this iterative fit process is fairly robust, but there is no absolute guarantee that it will necessarily work.

Since the non-linear fit parameter estimate is not defined as a simple function but as the limit of an iterative fit, there are mathematical questions of the existence and uniqueness of that limit that need to be answered before the iterative fit method can be employed with confidence. For our purposes, the damped harmonic oscillator signal is simple and smooth enough that such mathematical pathologies do not present a problem, particularly for large amplitude oscillations which have large signal-to-noise ratios. As with all oscillatory functions though, the initial parameter estimate of the frequency can not be outrageous, it should be within a factor of two of the true value to ensure that it will converge properly.

The variance in the parameter estimate, $\mathrm{var}\left(\hat{P}[\mathbf{X}]\right)$, arises from two sources: 1) the true noise error, $\delta X(t) = X(t) - x(t)\{\rho\}$, propagating into the parameter estimate, and 2) errors arising from the use of p rather than ρ in the estimator and residue. For large signal-to-noise, the second source is much smaller than the first source, and so the first can be used as a reasonable approximation to the total variance.

$$\mathrm{var}\left(\hat{P}[\mathbf{X}]\right) \cong \mathrm{var}\left(\delta\hat{P}[\delta\mathbf{X}]\{\rho\}\right) = \int_0^\infty \mathrm{F}^2\left[\mathbf{e}_{\hat{p}}\{\rho\}\right](\nu)\mathrm{F}^2[\delta\mathbf{X}](\nu)d\nu \Big/ 2 \qquad \text{(A.22)}$$

A more insidious effect of the use of p rather than ρ in the estimator and residue is the introduction of a bias in the parameter estimate, $\hat{P}[\mathbf{X}]$, even though the noise ensemble, $\delta X(t)$, is perfectly unbiased. By using ρ as the initial value and calculating the expectation value of the second iterative fit, it can be shown that, to leading order, the bias is

$$\mathrm{bias}\left(\hat{P}[\mathbf{X}]\right) \cong \mathrm{var}\left(\hat{P}[\mathbf{X}]\right)\int_{-\infty}^{+\infty} \frac{\partial x(t)}{\partial p}\{\rho\}\frac{\partial e_{\hat{p}}(t)}{\partial p}\{\rho\}dt. \qquad \text{(A.23)}$$

For large signal-to-noise, $\text{bias}\left(\hat{P}[\mathbf{X}]\right) << \text{stddev}\left(\hat{P}[\mathbf{X}]\right)$, and this bias can usually be ignored, but it is a consideration to be kept in the back of your mind when averaging together the results of a multitude of fits because it is useless to average the standard deviation down to a value smaller than the bias of an individual fit unless the above bias is calculated and an appropriate correction is made to the averaged parameter estimate.

For linear fits, an improperly normalized estimator will result in a biased parameter estimate. If, for example, the estimator is 20% too large, the parameter estimate will be 20% too large. For iterative non-linear fits, however, this is not a source of bias because an improperly normalized estimator will still converge to the same value as a properly normalized one. Similarly, the variance of the estimate will not be affected. Provided that the normalization constant is between 0 and 2 times the true normalization, the estimator will converge, and the closer it is to 1 the quicker will be the convergence. This dependence of speed of convergence on proper normalization is not a property of the noise ensemble but of the non-linear character of the fit.

A.3.3 "White" Noise Decay Constant Example

As a simple example of a single parameter non-linear fit, consider fitting for the decay constant, g, of an exponentially decreasing sample in the presence of additive "white" noise, $\mathrm{F}^2[\delta \mathbf{X}_{wh}](\nu) = \eta_{wh}^2$. As a single parameter fit is desired, we'll make the artificial assumption that the initial concentration at $t = 0$, A_o, is exactly known *a priori* and only g is being fit for, $x(t)\{g\} = A_o \exp(-gt)$. Additionally, a real problem would have a finite duration of the data sample, $t = 0$ to $t = \tau$, but for mathematical simplicity, we'll take the limit as $\tau \to +\infty$. Because there is only a finite amount of information in an exponentially de-

creasing signal, $\mathrm{var}_{wh}\left(\hat{G}[\mathbf{X}]\right)$ will yield an interesting non-zero value even though the data sample is semi-infinite in duration.

As will be further discussed in Section A.4.2, the optimal single parameter matched filter for a non-linear fit in the presence of "white" noise is proportional to the derivative of the signal with respect to that parameter.

$$f_{\hat{g}_{wh}}^{op}(t)\{g\} = \partial A_o \exp(-gt)/\partial g = -A_o t \exp(-gt) \tag{A.24}$$

This just has to be properly normalized to yield the optimal estimator.

$$\begin{aligned} e_{\hat{g}_{wh}}^{op}(t)\{g\} &= \frac{f_{\hat{p}_{wh}}^{op}(t)\{g\}}{\int_0^{+\infty} f_{\hat{p}_{wh}}^{op}(t)\{g\}\dfrac{\partial x(t)}{\partial g}\{g\}dt} = \frac{-A_o t\exp(-gt)}{\int_0^{\infty}\left(-A_o t\exp(-gt)\right)^2 dt} \\ &= \frac{-4g^3 t\exp(-gt)}{A_o} \\ \delta\hat{g}_{wh}^{op}\left[\delta\mathbf{x}\{g\}\right]\{g\} &= \int_0^{+\infty}\frac{-4g^3 t\exp(-gt)}{A_o}\left(x(t) - A_o\exp(-gt)\right)dt \end{aligned} \tag{A.25}$$

The variance in the estimate, $\mathrm{var}_{wh}\left(\hat{G}_{wh}^{op}[\mathbf{X}]\right)$, can then be calculated from $\mathbf{e}_{\hat{g}_{wh}}^{op}\{\gamma\}$. Normally, this would be done in Fourier space, but for "white" noise it is easier to calculate in the time domain (as mentioned in Section A.2.3).

$$\begin{aligned} \mathrm{var}_{wh}\left(\hat{G}_{wh}^{op}[\mathbf{X}]\right) &= \int_0^{\infty}\mathrm{F}^2\left[\mathbf{e}_{\hat{g}_{wh}}^{op}\{\gamma\}\right](\nu)\mathrm{F}^2[\delta\mathbf{X}_{wh}](\nu)d\nu\Big/2 \\ &= \frac{\eta_{wh}^2}{4}\int_0^{\infty}\left(e_{\hat{g}_{wh}}^{op}(t)\{\gamma\}\right)^2 dt = \frac{\eta_{wh}^2}{4}\int_0^{\infty}\left(\frac{-4\gamma^3 t\exp(-\gamma t)}{A_o}\right)^2 dt \\ &= \frac{\gamma^3\eta_{wh}^2}{A_o^2} \end{aligned} \tag{A.26}$$

Notice that, unlike a linear fit, $\mathrm{var}_{wh}\left(\hat{G}_{wh}^{op}[\mathbf{X}]\right)$, depends upon the amplitude of the signal, A_o. A similar $1/A_o^2$ decrease in the optimal variance of the estimates

Notice that, unlike a linear fit, $\mathrm{var}_{wh}\left(\hat{G}^{op}_{wh}[\mathbf{X}]\right)$, depends upon the amplitude of the signal, A_o. A similar $1/A_o^2$ decrease in the optimal variance of the estimates of g and w will be seen in the thermal noise limited damped harmonic oscillator (see Sections A.4.4 and A.5.5).

The expected bias can be calculated, and as asserted above, it is indeed negligible provided the signal-to-noise is large (i.e., $\gamma/\mathrm{stddev}_{wh}\left(\hat{G}^{op}_{wh}[\mathbf{X}]\right) >> 1$).

$$\begin{aligned}\mathrm{bias}_{wh}\left(\hat{G}^{op}_{wh}[\mathbf{X}]\right) &\equiv \mathrm{var}_{wh}\left(\hat{G}^{op}_{wh}[\mathbf{X}]\right)\int_0^{+\infty}\frac{\partial x(t)}{\partial g}\{\gamma\}\frac{\partial e_{\hat{g}^{op}_{wh}}(t)}{\partial g}\{\gamma\}dt \\ &= \frac{3\gamma^2\eta^2_{wh}}{2A_o^2} \end{aligned} \tag{A.27}$$

$$\frac{\mathrm{bias}_{wh}\left(\hat{G}^{op}_{wh}[\mathbf{X}]\right)}{\mathrm{stddev}_{wh}\left(\hat{G}^{op}_{wh}[\mathbf{X}]\right)} = \frac{3\gamma^{3/2}\eta_{wh}}{2A_o} = \frac{3}{2}*\frac{\mathrm{stddev}_{wh}\left(\hat{G}^{op}_{wh}[\mathbf{X}]\right)}{\gamma} \tag{A.28}$$

A.3.4 Higher Moments of Noise Ensemble

For a stationary noise process, whose Fourier components are necessarily uncorrelated, the spectral power density, $\mathrm{F}^2[\delta\mathbf{X}](\nu)$, provides a complete description of its second moments. Is a knowledge of the third and higher moments of the noise ensemble required to determine the minimum variance fit? The answer is no, and indeed the higher moments need not even exist (that is, their expectation can be infinite), and the least-squares method will still work. (Hamilton 1964)

Often, the higher Fourier moments are assumed to be of a gaussian distribution, and for thermal noise–being the result of an extremely large number of microscopic interactions–this is usually a very reasonable assumption. If the higher moments are gaussian, then the optimum least-squares fit is not only a

minimum variance estimate but also a maximum likelihood estimate. The gaussian distribution also justifies the traditional interpretation of the variance as a 1 sigma (68%) confidence level.

Strictly speaking, it is only for perfectly linear fits that the variance in the parameter estimate is independent of the third and higher moments. Just as the variance causes a very small first moment shift, the bias of the estimate, the third moment "bleeds in" and causes a very small (usually negligible) shift in the variance. Fits can be viewed geometrically as projections of probability distributions in data space down to distributions in the subspace of possible signals that could occur without noise. For a linear fit, these subspaces are flat, multi-dimensional "planes", and the data-space gaussians project down to pure gaussians in these "planes." For a non-linear fit, these "planes" have some curvature which distorts the projection of the gaussian distributions causing the higher moments to "bleed in" and shift the value of the lower moments.

A.3.5 Bayesian Statistics

In the above subsection, it was pointed out that to interpret the variance of the parameter estimate as a confidence level, some assumptions had to be made about the higher moments of the distribution. However, an even more fundamental assumption is necessary to be able to interpret the variance, and that is the nature of the *a priori* probability distribution reflecting one's prior knowledge about the parameter. This consideration usually comes under the heading of Bayesian statistics.

The traditional interpretation is that one has no prior knowledge about the parameter, and so the *a priori* probability distribution is uniform. A measurement is then taken, and the *a posteriori* probability distribution is a gaussian

with a mean given by the fit from the measured data and the variance given by the known error propagation of the fit. If the *a priori* probability distribution is other than uniform, the formulas of Bayesian statistics dictate how to compute the appropriate *a posteriori* probability distribution.

There is a prejudice that the uniform probability distribution is the only one that a self-respecting experimentalist would use, and more advanced Bayesian statistics is only for unscrupulous types who want to adjust their results to get what they want. But fundamentally, there is no "natural" choice for an *a priori* distribution because it depends upon how the signal is parameterized which is itself arbitrary. As an example, you can have a uniform frequency distribution or you can have a uniform period distribution, but they are different distribution and you have to make a choice between the two. For large signal-to-noise, it doesn't make much difference in the results, but mathematically you can not avoid making an arbitrary decision about the *a priori* probability distribution.

A.4. Optimal Filters for Single Parameter Fits

A.4.1 Approximations and Symbols Used

$\Omega_{th} = M\frac{d^2}{dt^2} + \beta\frac{d}{dt} + \kappa$ .....equation of motion operator

$\Omega_{th}^{T} = M\frac{d^2}{dt^2} - \beta\frac{d}{dt} + \kappa$ .....transpose operator (time inverted)

$\Omega_{th}(x(t))$ .....thermal driving force

$z_{\hat{p}}(t)\{p\}$ .....linearized filter function (not normalized) in thermal driving force basis

$\theta(t-t_o) = \begin{cases} 1 \text{ for } t \geq t_o \\ 0 \text{ for } t < t_o \end{cases}$ .....Heavyside function

$\left(\theta(t-t_i) - \theta(t-t_f)\right)x(t)$ .....data set

$\delta(t-t_o)=\frac{d}{dt}\theta(t-t_o)$.....Dirac delta function

$\delta'(t-t_o)=\frac{d}{dt}\delta(t-t_o)$ .....Dirac delta time derivative

ε.....infinitesimal time

Useful Statistics

$\delta x_i\{p\}=x(t_i)-x(t_i)\{p\}$ .....initial position residue

$\delta x_f\{p\}=x(t_f)-x(t_f)\{p\}$.....final position residue

$\delta v_i\{p\}=v(t_i)-v(t_i)\{p\}$.....initial velocity residue

$\delta v_f\{p\}=v(t_f)-v(t_f)\{p\}$ .....final velocity residue

$\delta x_m\{p\}=\frac{1}{\tau}\int_{-\tau/2}^{+\tau/2}x(t)-x(t)\{p\}dt$...boxcar average of position residue

There is an unfortunate overuse of the symbol, δ. When used by itself with a time argument, it stands for the Dirac delta function; when used in front of data, it stands for noise or residue; and when used in front of a parameter estimate, it stands for a first-order correction to that estimate. In Section A.4.2, it will be used briefly as a functional derivative for a calculus of variations derivation of matched filters.

A.4.2 Optimal Filters for White Noise

In Section A.2, it was shown that if a filter function, $f_{\hat{p}}(t)$, is used to fit for a linearly parameterized signal, $x(t)\{p\}$, in the presence of a noise ensemble, $\delta\mathbf{X}$, the variance in the parameter estimate is

$$\mathrm{var}\left(\hat{P}[\mathbf{X}]\right)=\frac{\int_0^{\infty}\mathrm{F}^2\left[\mathbf{f}_{\hat{p}}\right](v)\mathrm{F}^2[\delta\mathbf{X}](v)dv\Big/2}{\left[\int_{-\infty}^{+\infty}f_{\hat{p}}(t)(x(t)\{1\})dt\right]^2}. \qquad (A.29)$$

For "white" noise, the numerator can be evaluated in the time domain,

$$\mathrm{var}_{wh}\left(\hat{P}[\mathbf{X}]\right) = \frac{\eta_{wh}^2 \int_{-\infty}^{+\infty} f_{\hat{p}}(t)^2 dt \Big/ 4}{\left[\int_{-\infty}^{+\infty} f_{\hat{p}}(t)(x(t)\{1\})dt\right]^2}. \tag{A.30}$$

In this section, we want to find the filter that minimizes $\mathrm{var}_{wh}\left(\hat{P}[\mathbf{X}]\right)$ for a given parameterized signal, $x(t)\{p\}$. In order to have to have a well-posed optimization problem, the duration of the data sample must be constrained to have a finite length, τ. The arbitrary filter function, $f_{\hat{p}}(t)$, can still vary over the entire Hilbert space of real functions provided that it is multiplied by appropriate "boxcar" Heavyside functions, $\left(\theta(t-t_i)-\theta\left(t-t_f\right)\right)f_{\hat{p}}(t)$, so that it has zero weight for those times before or after the data sample. This has the effect of changing the time limits of integration to $t_i = -\tau/2$ and $t_f = +\tau/2$.

$$\begin{aligned}\mathrm{var}_{wh}\left(\hat{P}[\mathbf{X}]\right) &= \frac{\eta_{wh}^2 \int_{-\infty}^{+\infty} \left(\left(\theta(t-t_i)-\theta\left(t-t_f\right)\right)f_{\hat{p}}(t)\right)^2 dt \Big/ 4}{\left[\int_{-\infty}^{+\infty} \left(\theta(t-t_i)-\theta\left(t-t_f\right)\right)f_{\hat{p}}(t)(x(t)\{1\})dt\right]^2} \\ &= \frac{\eta_{wh}^2 \int_{-\tau/2}^{+\tau/2} f_{\hat{p}}(t)^2 dt \Big/ 4}{\left[\int_{-\tau/2}^{+\tau/2} f_{\hat{p}}(t)(x(t)\{1\})dt\right]^2}\end{aligned} \tag{A.31}$$

The calculus of variations minimization of $\mathrm{var}_{wh}\left(\hat{P}[\mathbf{X}]\right)$ is simplified if we restrict ourselves to normalized estimator functions,

$$\mathrm{var}_{wh}\left(\hat{P}[\mathbf{X}]\right) = \frac{\eta_{wh}^2}{4} \int_{-\tau/2}^{+\tau/2} e_{\hat{p}}(t)^2 dt, \tag{A.32}$$

and introduce a Lagrange multiplier, λ, to impose the constraint of normalization,

$$\int_{-\tau/2}^{+\tau/2} e_{\hat{p}}(t)(x(t)\{1\})dt = 1. \tag{A.33}$$

When this is done,

$$\begin{aligned}\delta \mathrm{var}_{wh}\left(\hat{P}[\mathbf{X}]\right) &= \delta\left(\frac{\eta_{wh}^2}{4}\int_{-\tau/2}^{+\tau/2} e_{\hat{p}}(t)^2\,dt - \lambda\left(\int_{-\tau/2}^{+\tau/2} e_{\hat{p}}(t)(x(t)\{1\})dt - 1\right)\right) = 0 \\ &= \int_{-\tau/2}^{+\tau/2}\left(\frac{\eta_{wh}^2}{4}2e_{\hat{p}}(t) - \lambda x(t)\{1\}\right)\delta e_{\hat{p}}(t)dt,\end{aligned} \tag{A.34}$$

it can be seen that the expression in parentheses in the last line above must be zero if the variation in the variance, $\delta \mathrm{var}_{wh}\left(\hat{P}[\mathbf{X}]\right)$, is to be zero for any first-order variation in the estimator, $\delta e_{\hat{p}}(t)$. From this derives the main result of this section–the optimal "white" noise filter function (not normalized) for a linear, single-parameter signal, $x(t)\{p\}$, is simply the unit amplitude signal itself, $x(t)\{1\}$.

$$\begin{aligned}&\frac{\eta_{wh}^2}{4}2e_{\hat{p}_{wh}}^{op}(t) - \lambda x(t)\{1\} = 0 \\ &\Rightarrow \quad e_{\hat{p}_{wh}}^{op}(t) = \frac{2\lambda x(t)\{1\}}{\eta_{wh}^2} \quad \Rightarrow \quad f_{\hat{p}_{wh}}^{op}(t) = x(t)\{1\}\end{aligned} \tag{A.35}$$

The optimal "white" noise filter is often referred to as a matched filter because the filter is matched to the signal for which you are fitting. To get the optimal estimator, $e_{\hat{p}_{wh}}^{op}(t)$, the optimal filter must be normalized.

$$e_{\hat{p}_{wh}}^{op}(t) = \frac{\left(\theta(t-t_i) - \theta\left(t-t_f\right)\right)x(t)\{1\}}{\int_{-\tau/2}^{+\tau/2}\left(x(t)\{1\}\right)^2 dt} \tag{A.36}$$

The Heavyside functions are put there to remind the reader that they must be included if Fourier techniques are to be used (such as calculating $\mathrm{F}^2\left[\mathbf{e}_{\hat{p}_{wh}}^{op}\right](\nu)$).

The above results can be generalized to non-linear fits by replacing $x(t)\{1\}$ with $(\partial x(t)/\partial p)\{p\}$.

$$f_{\hat{p}_{wh}}^{op}(t)\{p\} = \Big(\theta(t-t_i) - \theta\big(t-t_f\big)\Big)\frac{\partial x(t)}{\partial p}\{p\} \tag{A.37}$$

$$e_{\hat{p}_{wh}}^{op}(t)\{p\} = \frac{\Big(\theta(t-t_i) - \theta\big(t-t_f\big)\Big)\frac{\partial x(t)}{\partial p}\{p\}}{\int_{-\tau/2}^{+\tau/2}\left(\frac{\partial x(t)}{\partial p}\{p\}\right)^2 dt} \tag{A.38}$$

A.4.3 Optimal Filters for Thermal Noise

Now that we have the optimal filter for "white" noise, we would like to find the optimal filter, $f_{\hat{p}_{th}}^{op}(t)$, when thermal noise is the dominant noise process. More specifically, we want to filter the Lorentzian spectral power density, $\mathrm{F}^2[\delta\mathbf{X}_{th}](\nu)$, characteristic of thermal noise on a damped harmonic oscillator. Once again, the data sample duration, τ, must be specified which then requires calculating $\mathrm{var}_{th}\big(\hat{P}[\mathbf{X}]\big)$ in the time domain.

$$\mathrm{var}_{th}\big(\hat{P}[\mathbf{X}]\big) = \int_{-\tau/2}^{+\tau/2}\int_{-\tau/2}^{+\tau/2} e_{\hat{p}}(t_1)\,\mathrm{cov}_{th}\big(X(t_1),X(t_2)\big)e_{\hat{p}}(t_2)dt_1dt_2 \tag{A.39}$$

Even without detailed calculations, we know that $\mathrm{cov}_{th}\big(X(t_1),X(t_2)\big)$ is not diagonal in the time domain because data that are separated by one period will be highly correlated whereas data that are separated by one-half of a period will be highly anti-correlated. In contrast, the covariance of "white" noise is diagonal,

$$\mathrm{cov}_{wh}\big(X(t_1),X(t_2)\big) = \big\langle \delta X_{wh}(t_1)\delta X_{wh}(t_2)\big\rangle = \eta_{wh}^2\,\delta(t_2-t_1)/4, \tag{A.40}$$

and the double integral convolution collapses nicely to a single integral.

Since $\mathrm{cov}_{th}\big(X(t_1),X(t_2)\big)$ is not diagonal, a direct calculus of variations derivation of $f_{\hat{p}_{th}}^{op}(t)$ would require an inversion of the operator, $\mathrm{cov}_{th}\big(X(t_1),X(t_2)\big)$. Although there are direct algorithms for inverting a discrete

matrix, an operator can not generally be inverted without first diagonalizing it, but diagonalization is even more difficult than inversion unless you have some *a priori* knowledge about the noise process that allows you to guess at a diagonal basis. For thermal noise, however, we do have such *a priori* knowledge because the fluctuation-dissipation theorem states that the thermal driving force is a "white" noise process with a spectral power density of $4KT\beta$. The thermal driving force can be extracted from the data time series, $x(t)$, by applying the equation of motion operator,

$$\Omega_{th} = M\frac{d^2}{dt^2} + \beta\frac{d}{dt} + \kappa. \tag{A.41}$$

$\Omega_{th}(x(t))$ then has the same diagonal covariance operator as "white" noise but with η_{wh}^2 replaced by $4KT\beta$.

$$\begin{aligned} \mathrm{cov}_{th}\left(\Omega_{th}(X(t_1)),\Omega_{th}(X(t_2))\right) &= \left\langle \Omega_{th}(\delta X_{th}(t_1))\Omega_{th}(\delta X_{th}(t_2))\right\rangle \\ &= KT\beta\delta(t_2 - t_1) \end{aligned} \tag{A.42}$$

The results of optimal "white" filters are therefore valid in the thermal driving force basis. In analogy with $f_{\hat{p}}(t)$, define $z_{\hat{p}}(t)$ as a filter (not normalized) in the thermal driving force basis which is applied to $\Omega_{th}(x(t))$ to extract a parameter estimate,

$$\hat{p}[\mathbf{x}] = \frac{\int_{-\infty}^{+\infty} z_{\hat{p}}(t)\Omega_{th}(x(t))dt}{\int_{-\infty}^{+\infty} z_{\hat{p}}(t)\Omega_{th}(x(t)\{1\})dt}. \tag{A.43}$$

The denominator above properly normalizes the parameter estimate. The optimal filter in the presence of "white" force noise is a matched filter of unit amplitude,

$$z_{\hat{p}_{th}}^{op}(t) = \Big(\theta(t-t_i) - \theta\big(t-t_f\big)\Big)\Omega_{th}(x(t)\{1\}). \tag{A.44}$$

Once again, Heavyside functions are explicitly included to denote the finite time duration of the filter. Note that care must be taken to place the Heavyside functions before the equation of motion operator because if the Ω_{th} operator were to act on the Heavyside functions it would create non-physical spikes in the force basis.

Although we have the optimal driving-force basis filter, $z_{\hat{p}_{th}}^{op}(t)$, it would be more convenient to find the optimal position basis filter, $f_{\hat{p}_{th}}^{op}(t)$, that could be applied directly to the raw data, $x(t)$. Given an arbitrary $z_{\hat{p}}(t)$, does there exist an equivalent $f_{\hat{p}}(t)$ that returns the same value when applied to $x(t)$ that $z_{\hat{p}}(t)$ does when applied to $\Omega_{th}(x(t))$? That is,

$$\int_{-\infty}^{+\infty} f_{\hat{p}}(t)x(t)dt = \int_{-\infty}^{+\infty} z_{\hat{p}}(t)\Omega_{th}(x(t))dt, \tag{A.45}$$

for any $x(t)$. Such an $f_{\hat{p}}(t)$ does exist, and it can be derived by integration by parts.

$$\int_{-\infty}^{+\infty} z_{\hat{p}}(t)\Omega_{th}(x(t))dt = \int_{-\infty}^{+\infty} z_{\hat{p}}(t)\left(M\frac{d^2x(t)}{dt^2} + \beta\frac{dx(t)}{dt} + \kappa x(t)\right)dt =$$

$$\left[z_{\hat{p}}(t)\left(M\frac{dx(t)}{dt} + \beta x(t)\right)\right]_{t=-\infty}^{t=+\infty} -$$

$$\int_{-\infty}^{+\infty}\frac{dz_{\hat{p}}(t)}{dt}\left(M\frac{dx(t)}{dt} + \beta x(t)\right)dt + \int_{-\infty}^{+\infty}\kappa z_{\hat{p}}(t)x(t)dt =$$

$$\left[z_{\hat{p}}(t)\left(M\frac{dx(t)}{dt} + \beta x(t)\right) - M\frac{dz_{\hat{p}}(t)}{dt}x(t)\right]_{t=-\infty}^{t=+\infty} +$$

$$\int_{-\infty}^{+\infty}\left(M\frac{d^2z_{\hat{p}}(t)}{dt^2} - \beta\frac{dz_{\hat{p}}(t)}{dt} + \kappa z_{\hat{p}}(t)\right)x(t)dt = \tag{A.46}$$

$$0 + \int_{-\infty}^{+\infty}\Omega_{th}^{T}\left(z_{\hat{p}}(t)\right)x(t)dt = \int_{-\infty}^{+\infty} f_{\hat{p}}(t)x(t)dt$$

Since $z_{\hat{p}}(t) = 0$ for $t < t_i$ and $t > t_f$, the terms in square brackets above vanish. The transpose or time-inverted equation of motion operator is defined as

$$\Omega_{th}^{T} = M\frac{d^2}{dt^2} - \beta\frac{d}{dt} + \kappa, \tag{A.47}$$

and from inspection of the last line above, it can be seen that $f_{\hat{p}}(t) = \Omega_{th}^{T}\left(z_{\hat{p}}(t)\right)$. Thus,

$$f_{\hat{p}_{th}}^{op}(t) = \Omega_{th}^{T}\left(z_{\hat{p}_{th}}^{op}(t)\right) = \Omega_{th}^{T}\left(\left(\theta(t-t_i) - \theta\left(t-t_f\right)\right)\Omega_{th}(x(t)\{1\})\right). \tag{A.48}$$

Here, Ω_{th}^{T} does act on the Heavyside functions, and so $f_{\hat{p}_{th}}^{op}(t)$ generally will include terms such as $\delta(t-t_i)$, $\delta\left(t-t_f\right)$, $\delta'(t-t_i)$, and $\delta'\left(t-t_f\right)$.

The optimal thermal noise estimator, $e_{\hat{p}_{th}}^{op}(t)$, is obtained by normalizing $f_{\hat{p}_{th}}^{op}(t)$.

$$e_{\hat{p}_{th}}^{op}(t) = \frac{\Omega_{th}^T\Big(\big(\theta(t-t_i)-\theta(t-t_f)\big)\Omega_{th}(x(t)\{1\})\Big)}{\int_{-\tau/2-\varepsilon}^{+\tau/2+\varepsilon} x(t)\{1\}\Omega_{th}^T\Big(\big(\theta(t-t_i)-\theta(t-t_f)\big)\Omega_{th}(x(t)\{1\})\Big)dt} \tag{A.49}$$

The limits of integration include the infinitesimal time increment, ε, in order to avoid any ambiguity as to how the Dirac delta functions at $t=t_i$ and $t=t_f$ are to be evaluated in the integral. As before, the optimal filters and estimators can be generalized to non-linear fits by replacing $x(t)\{1\}$ with $(\partial x(t)/\partial p)\{p\}$.

$$f_{\hat{p}_{th}}^{op}(t)\{p\} = \Omega_{th}^T\Big(z_{\hat{p}_{th}}^{op}(t)\{p\}\Big) = \Omega_{th}^T\left(\big(\theta(t-t_i)-\theta(t-t_f)\big)\Omega_{th}\left(\frac{\partial x(t)}{\partial p}\{p\}\right)\right) \tag{A.50}$$

$$e_{\hat{p}_{th}}^{op}(t)\{p\} = \frac{\Omega_{th}^T\left(\big(\theta(t-t_i)-\theta(t-t_f)\big)\Omega_{th}\left(\frac{\partial x(t)}{\partial p}\{p\}\right)\right)}{\int_{-\tau/2-\varepsilon}^{+\tau/2+\varepsilon}\frac{\partial x(t)}{\partial p}\{p\}\Omega_{th}^T\left(\big(\theta(t-t_i)-\theta(t-t_f)\big)\Omega_{th}\left(\frac{\partial x(t)}{\partial p}\{p\}\right)\right)dt} \tag{A.51}$$

A.4.4 Offset, Frequency and Damping

This section shall apply the above results to derive the optimal thermal noise parameter estimates for the three parameters, c, g, and w. The amplitude parameters, a and b, are handled differently and will be treated in Section A.4.5. We are only prepared to derive single-parameter optimal estimators, and they may vary from the optimal multi-parameter fits to be derived in Section A.5. Thus, when fitting for c, the artificial single-parameter signal,

$$x(t)\{c\} = A_o\exp(-\gamma t)\cos(\omega_d t - \phi_o) + c \tag{A.52}$$

shall be used in which the constants A_o, ϕ_o, γ, and ω_d are assumed to be known *a priori*, and c is the only unknown parameter to be estimated. Like-

wise, when fitting for g or w, the artificial single-parameter signals, $x(t)\{g\}$ and $x(t)\{w\}$ shall be used.

$$x(t)\{g\} = A_o \exp(-gt)\cos(\omega_d t - \phi_o) + \Gamma \tag{A.53}$$

$$x(t)\{w\} = A_o \exp(-\gamma t)\cos(wt - \phi_o) + \Gamma \tag{A.54}$$

In Section A.3.2, it was noted that non-linear fits are like "pulling yourself up by your own bootstraps" because, in calculating the residue, $\delta x(t)\{p\}$, and the estimator, $e_{\hat{p}}(t)\{p\}$, the assumed value of the parameter, p, is used rather than the true value, ρ. For optimal thermal noise fits, there is a further "bootstrap" issue because the equation of motion operator, Ω_{th}, is itself a function of the parameters g and w.

$$\Omega_{th}\{g,w\} = M\frac{d^2}{dt^2} + 2Mg\frac{d}{dt} + M\left(w^2 + g^2\right) \tag{A.55}$$

However, for large signal-to noise iterative fits, the use of g or w instead of γ or ω_d is a second-order effect that creates an entirely insignificant increase in the parameter estimate variances above their optimum minimum value.

So, without further ado, let us calculate the optimal thermal noise filters. Although the fit for c is a linear one, non-linear fit notation will be used to make it consistent with the g and w fits.

$$f_{\hat{c}_{th}}^{op}(t)\{c\} = \Omega_{th}^{T}\{\gamma,\omega_d\}\left(\left(\theta(t-t_i) - \theta\left(t-t_f\right)\right)\Omega_{th}\{\gamma,\omega_d\}\left(\frac{\partial x(t)}{\partial c}\{c\}\right)\right) \cong \tag{A.56}$$
$$M^2\omega_d^4\left(\theta(t-t_i) - \theta\left(t-t_f\right)\right) + M^2\omega_d^2\left(\delta'(t-t_i) - \delta'\left(t-t_f\right)\right)$$

$$f_{\hat{g}_{th}}^{op}(t)\{g\} = \Omega_{th}^{T}\{g,\omega_d\}\left(\left(\theta(t-t_i)-\theta(t-t_f)\right)\Omega_{th}\{g,\omega_d\}\left(\frac{\partial x(t)}{\partial g}\{g\}\right)\right) \cong$$
$$4M^2\omega_d^2 A_o\cos(\omega_d t-\phi_o)\left(\delta(t-t_i)-\delta(t-t_f)\right)+ \qquad (A.57)$$
$$2M^2\omega_d A_o\sin(\omega_d t-\phi_o)\left(\delta'(t-t_i)-\delta'(t-t_f)\right)$$

$$f_{\hat{w}_{th}}^{op}(t)\{w\} = \Omega_{th}^{T}\{\gamma,w\}\left(\left(\theta(t-t_i)-\theta(t-t_f)\right)\Omega_{th}\{\gamma,w\}\left(\frac{\partial x(t)}{\partial w}\{w\}\right)\right) \cong$$
$$4M^2w^2A_o\sin(wt-\phi_o)\left(\delta(t-t_i)-\delta(t-t_f)\right)- \qquad (A.58)$$
$$2M^2wA_o\cos(wt-\phi_o)\left(\delta'(t-t_i)-\delta'(t-t_f)\right)$$

The $\cong$ symbol is used because the results are only calculated to leading order in γ/ω_d since it is assumed that $Q>>1$. In fact, the correct leading order results are obtained by setting $\gamma\to 0$ in the signal and the equation of motion operator prior to calculation.

By normalization of the optimal filters, the optimal single-parameter estimators, $e_{\hat{p}}(t)\{p\}$, are obtained, and by applying the optimal estimators to the residues, $\delta x(t)\{p\} = x(t)-x(t)\{p\}$, the optimal first-order correction of the parameter estimates, $\delta\hat{p}\left[\delta x\{p\}\right]\{p\}$, are obtained. For simplicity, these are calculated only for the case of N being an integer number of periods and for $N<<Q$.

$$\delta\hat{c}_{th}^{op}\left[\delta x\{c\}\right]\{c\}_N = \int_{-\tau/2-\varepsilon}^{+\tau/2+\varepsilon} e_{\hat{c}th}^{op}(t)\{c\}_N\left(x(t)-x(t)\{c\}\right)dt$$
$$\cong \delta x_m\{c\}+\frac{\delta v_f\{c\}-\delta v_i\{c\}}{2\pi N\omega_d} \qquad (A.59)$$

$$\delta\hat{g}_{th}^{op}\left[\delta\mathbf{x}\{g\}\right]\{g\}_N = \int_{-\tau/2-\varepsilon}^{+\tau/2+\varepsilon} e_{\hat{g}_{th}}^{op}(t)\{g\}_N\left(x(t)-x(t)\{g\}\right)dt \equiv$$
$$(-1)^{N+1}\left(\frac{\cos(\phi_o)\omega_d\left(\delta x_f\{g\}-\delta x_i\{g\}\right)}{2\pi NA_o}+\frac{\sin(\phi_o)\left(\delta v_f\{g\}-\delta v_i\{g\}\right)}{2\pi NA_o}\right) \quad \text{(A.60)}$$

$$\delta\hat{w}_{th}^{op}\left[\delta\mathbf{x}\{w\}\right]\{w\}_N = \int_{-\tau/2-\varepsilon}^{+\tau/2+\varepsilon} e_{\hat{w}_{th}}^{op}(t)\{w\}_N\left(x(t)-x(t)\{w\}\right)dt \equiv$$
$$(-1)^{N}\left(\frac{\sin(\phi_o)w\left(\delta x_f\{w\}-\delta x_i\{w\}\right)}{2\pi NA_o}-\frac{\cos(\phi_o)\left(\delta v_f\{w\}-\delta v_i\{w\}\right)}{2\pi NA_o}\right) \quad \text{(A.61)}$$

Since the signal is much larger than noise, the $\gamma \to 0$ approximation can not be used when calculating the residues without introducing a significant systematic bias. For Section A.5, which is about multi-parameter fits, it will be important to note that $\delta\hat{c}_{th}^{op}\left[\delta\mathbf{x}\{c\}\right]\{c\}_N$, $\delta\hat{g}_{th}^{op}\left[\delta\mathbf{x}\{g\}\right]\{g\}_N$, and $\delta\hat{w}_{th}^{op}\left[\delta\mathbf{x}\{w\}\right]\{w\}_N$ can be expressed as linear combinations of the five statistics $\delta x_i\{p\}$, $\delta x_f\{p\}$, $\delta v_i\{p\}$, $\delta v_f\{p\}$, and $\delta x_m\{p\}$.

A.4.5 Cosine and Sine Amplitude

The derivation of the optimal thermal noise filters in Section A.4.3 implicitly assumed the existence of an external force signal, $\Omega_{th}\left(x(t)\{\rho\}\right) = \left\langle\Omega_{th}\left(X(t)\right)\right\rangle$, that would create the signal, $x(t)\{p\} = \left\langle X(t)\right\rangle$, in the position time series. The force time series ensemble is then the sum of the force signal and the "white" force noise, $\Omega_{th}(\delta\mathbf{X}_{th})$.

$$\Omega_{th}(\mathbf{X}) = \Omega_{th}\left(\mathbf{x}\{\rho\}\right) + \Omega_{th}(\delta\mathbf{X}_{th}) \quad \text{(A.62)}$$

The optimal force filter, $z_{\hat{p}_{th}}^{op}(t)$, searches for the existence of $\Omega_{th}\left(x(t)\{p\}\right)$ in the presence of $\Omega_{th}(\delta\mathbf{X}_{th})$.

This picture breaks down when applied to the amplitude parameters, a and b. Consider the two-parameter signal

$$x(t)\{a,b\} = a\exp(-\gamma t)\cos(\omega_d t) + b\exp(-\gamma t)\sin(\omega_d t) + \Gamma . \tag{A.63}$$

The application of the equation of motion operator yields zero.

$$\Omega_{th}\{\gamma,\omega_d\}\left(\frac{\partial x(t)}{\partial a}\{a,b\}\right) = \Omega_{th}\{\gamma,\omega_d\}(x(t)\{1,0\}) = 0 \tag{A.64}$$

$$\Omega_{th}\{\gamma,\omega_d\}\left(\frac{\partial x(t)}{\partial b}\{a,b\}\right) = \Omega_{th}\{\gamma,\omega_d\}(x(t)\{0,1\}) = 0 \tag{A.65}$$

This gives the nonsensical result that $z_{\hat{a}th}^{op}(t) = 0$ and $z_{\hat{b}th}^{op}(t) = 0$. What went wrong?

The explanation is that the transformation from the position basis to the driving force basis is not bijective (i.e., reversible). In order to reconstruct $x(t)$, one needs not only the driving force, $\Omega_{th}(x(t))$, but also the initial conditions, $x_i = x(t_i)$ and $v_i = v(t_i)$. Actually, any two boundary conditions will do, but since we want a statistically independent "white" basis, we choose X_i and V_i because causality dictates that they are statistically independent of $\Omega_{th}(X(t))$ for $t > t_i$. The zero's above indicate that there is no information about the parameters a or b in $\Omega_{th}(x(t))$. By process of elimination, the information about a and b must be in x_i and v_i.

$$\delta\hat{a}_{th}^{op}[\delta\mathbf{x}\{a,b\}]\{a,b\}_N \equiv (-1)^N \delta x_i\{a,b\} \tag{A.66}$$

$$\delta\hat{b}_{th}^{op}[\delta\mathbf{x}\{a,b\}]\{a,b\}_N \equiv (-1)^N \delta v_i\{a,b\}/\omega_d \tag{A.67}$$

Here again, the $\equiv$ symbol indicates the results are only calculated to leading order in γ/ω_d.

This begs the question as to whether there is any information about c, g, or w which is not in the force basis? To leading order in $1/Q$, the answer is no. Anyway, even if there were, it would not change the more important fact (as far as Section A.5 is concerned) that all five first-order correction to the parameter estimates– $\delta\hat{a}_{th}^{op}[\delta\mathbf{x}\{a\}]\{a\}_N$, $\delta\hat{b}_{th}^{op}[\delta\mathbf{x}\{b\}]\{b\}_N$, $\delta\hat{c}_{th}^{op}[\delta\mathbf{x}\{c\}]\{c\}_N$, $\delta\hat{g}_{th}^{op}[\delta\mathbf{x}\{g\}]\{g\}_N$, and $\delta\hat{w}_{th}^{op}[\delta\mathbf{x}\{w\}]\{w\}_N$–can be expressed as linear combinations of the five statistics $\delta x_i\{p\}$, $\delta x_f\{p\}$, $\delta v_i\{p\}$, $\delta v_f\{p\}$, and $\delta x_m\{p\}$.

The use of instantaneous position and velocity residues, such as $\delta x_i\{p\}$ and $\delta v_i\{p\}$, might seem problematic, but for mathematically pure thermal noise, the variances of these residues are finite.

$$\mathrm{var}_{th}\left(\delta X_i\{p\}\right) \equiv \mathrm{var}_{th}\left(\delta X_{th}(t)\right) = KT/\kappa = \chi_{th}^2 \tag{A.68}$$

$$\mathrm{var}_{th}\left(\delta V_i\{p\}\right) \equiv \mathrm{var}_{th}\left(\delta V_{th}(t)\right) = KT/M = \chi_{th}^2/\omega_o^2 \equiv \chi_{th}^2/\omega_d^2 \tag{A.69}$$

A.5. Simultaneous Fit for All Parameters

A.5.1 Approximations and Symbols Used

Matrix Notation

$\overline{\mathbf{m}}$ .....overbar indicating matrix (tensor)

$\overline{\mathbf{m}^T}$ .....transpose of matrix

$\bar{\mathbf{i}}$ .....square identity matrix

$\overline{\mathbf{m}^{-1}}$ .....inverse of square matrix

$\mathbf{u} \bullet \mathbf{v} = \sum_{j=1}^{n} u_j v_j$ .....inner (scalar) product

$\overline{\mathbf{u} \otimes \mathbf{v}} = \begin{pmatrix} u_1 v_1 & \cdots & u_1 v_n \\ \vdots & \ddots & \vdots \\ u_m v_1 & \cdots & u_m v_n \end{pmatrix}$ .....outer (tensor) product

Discrete Matrix Linear Least-Squares

x_j .....discrete datum

$\mathbf{x} = \{x_1, x_2, \ldots x_n\}$ .....data vector

$\mathbf{X} = \{X_1, X_2, \ldots X_n\}$ .....data vector ensemble

$\delta\mathbf{X} = \mathbf{X} - \langle \mathbf{X} \rangle$ .....noise ensemble

$\mathbf{p} = \{p_1, p_2, \ldots p_n\}$ .....parameter vector

$\mathbf{x}\{\mathbf{p}\}$ .....discrete multi-parameter signal

$\overline{\mathbf{e}_{\hat{\mathbf{p}}}}$ .....multi-parameter estimator matrix (in general, not square)

$\hat{\mathbf{p}}[\mathbf{x}] = \overline{\mathbf{e}_{\hat{\mathbf{p}}}} \bullet \mathbf{x}$ .....linear parameter vector estimate

$\overline{\mathbf{q}_{\mathbf{p}}^{T}} = \overline{\frac{\partial}{\partial \mathbf{p}} \otimes \mathbf{x}\{\mathbf{p}\}}$ .....transpose of design matrix (in general, not square)

$\overline{\mathbf{q}_{\mathbf{p}}}$ .....design matrix (in general, not square)

or in component form,

$$q_{\mathbf{p}\,jk} = \frac{\partial x_j\{\mathbf{p}\}}{\partial p_k} \qquad q^{T}_{\mathbf{p}\,jk} = \frac{\partial x_k\{\mathbf{p}\}}{\partial p_j}$$

$\overline{\mathbf{m}_{\mathbf{X}}} = \mathrm{cov}\left(\overline{\mathbf{X} \otimes \mathbf{X}}\right) = \left\langle \overline{\delta\mathbf{X} \otimes \delta\mathbf{X}} \right\rangle$ .....data covariance matrix

$\overline{\mathbf{m}_{\hat{\mathbf{P}}}} = \mathrm{cov}\left(\overline{\hat{\mathbf{P}}[\mathbf{X}] \otimes \hat{\mathbf{P}}[\mathbf{X}]}\right)$
$= \overline{\mathbf{e}_{\hat{\mathbf{p}}}} \bullet \overline{\mathbf{m}_{\mathbf{X}}} \bullet \overline{\mathbf{e}^{T}_{\hat{\mathbf{p}}}}$ .....parameter covariance matrix

$\overline{\mathbf{f}_{\hat{\mathbf{p}}}}$ .....filter matrix (not normalized) of single parameter filters

$\overline{\mathbf{n}}$ .....square normalization matrix (i.e., $\overline{\mathbf{e}_{\hat{\mathbf{p}}}} = \overline{\mathbf{n}} \bullet \overline{\mathbf{f}_{\hat{\mathbf{p}}}}$)

$\bar{\mathbf{r}}$ .....arbitrary square recombination matrix

Linear Continuous Time-Series Multi-Parameter Fits

$x(t)\{\mathbf{p}\}$ .....multi-parameter signal

$\mathbf{q}_{\mathbf{p}}(t) = \partial x(t)\{\mathbf{p}\}/\partial \mathbf{p}$ .....design vector of partial derivative functions

$\mathbf{f}_{\hat{\mathbf{p}}}(t)$ .....vector of filter functions (not normalized)

$\mathbf{e}_{\hat{\mathbf{p}}}(t) = \bar{\mathbf{n}} \bullet \mathbf{f}_{\hat{\mathbf{p}}}(t)$ .....vector of estimator functions (normalized)

$\hat{\mathbf{p}}[\mathbf{x}] = \int_{-\infty}^{+\infty} \mathbf{e}_{\hat{\mathbf{p}}}(t) x(t) dt$ .....linear parameter vector estimate

$$\overline{\mathbf{m}_{\hat{\mathbf{p}}}} = \mathrm{cov}\left(\hat{\mathbf{P}}[\mathbf{X}] \otimes \hat{\mathbf{P}}[\mathbf{X}]\right)$$

$$= \int_{-\infty}^{+\infty}\int_{-\infty}^{+\infty} \overline{\mathbf{e}_{\hat{\mathbf{p}}}(t_1) \otimes \mathbf{e}_{\hat{\mathbf{p}}}(t_2)} \times \mathrm{cov}\left(X(t_1)X(t_2)\right) dt_1 dt_2$$

.....parameter covariance matrix

No notational distinction is made between "row" and "column" vectors since the use of the vector is generally evident from its context. As such, the matrix transpose superscript, ^{T}, will not be applied to vectors.

A.5.2 Linear Multi-Parameter Fits for Discrete Data

To extend the concept of optimal filters and estimators to multi-parameter fits, let us look first at the case of discrete data in this section. Multi-parameter fits of continuous time series will be addressed in Section A.5.3. For discrete data, a particular realization of the data, $\mathbf{x}$, is not a function in Hilbert space but rather a data vector with a finite number of components.

$$\mathbf{x} = \{x_1, x_2, \ldots x_n\} \tag{A.70}$$

For multi-parameter signals, the parameters are collected into a vector as well,

$$\mathbf{p} = \{p_1, p_2, \ldots p_m\}. \tag{A.71}$$

The partial derivatives of the data with respect to each of the parameters constitutes the design matrix, $\overline{\mathbf{q_p}}$, and, for linear fits, the contraction of the design matrix with the parameter vector produces the multi-parameter signal, $\mathbf{x}\{\mathbf{p}\}$.

$$q_{\mathbf{p}jk} = \frac{\partial x_j\{\mathbf{p}\}}{\partial p_k} \qquad \mathbf{x}\{\mathbf{p}\} = \overline{\mathbf{q_p}} \bullet \mathbf{p} \tag{A.72}$$

Since the number of parameters is usually less than the number of data, the design matrix is generally rectangular. Estimation of the parameter vector, $\mathbf{p}$, makes use of another rectangular matrix, the estimator matrix, $\overline{\mathbf{e}_{\hat{\mathbf{p}}}}$.

$$\hat{\mathbf{p}}[\mathbf{x}] = \overline{\mathbf{e}_{\hat{\mathbf{p}}}} \bullet \mathbf{x} \tag{A.73}$$

The data ensemble, $\mathbf{X}$, consists of the true signal, $\langle \mathbf{X} \rangle = \mathbf{x}\{\rho\}$, plus a fluctuating noise ensemble, $\delta\mathbf{X} = \mathbf{X} - \mathbf{x}\{\rho\}$. The second moments of the noise ensemble are characterized by the data covariance matrix,

$$\overline{\mathbf{m}_\mathbf{X}} = \mathrm{cov}(\overline{\mathbf{X} \otimes \mathbf{X}}) = \langle \overline{\delta\mathbf{X} \otimes \delta\mathbf{X}} \rangle. \tag{A.74}$$

Note that, by construction, $\overline{\mathbf{m}_\mathbf{X}}$ is necessarily a symmetric matrix. The optimal estimator matrix, $\overline{\mathbf{e}_{\hat{\mathbf{p}}}}^{op}$, that returns minimum variance estimates of all the parameters in the presence of $\delta\mathbf{X}$ is given by

$$\overline{\mathbf{e}_{\hat{\mathbf{p}}}}^{op} = \left(\overline{\mathbf{q}_\mathbf{p}^T} \bullet \overline{\mathbf{m}_\mathbf{X}^{-1}} \bullet \overline{\mathbf{q}_\mathbf{p}}\right)^{-1} \bullet \overline{\mathbf{q}_\mathbf{p}^T} \bullet \overline{\mathbf{m}_\mathbf{X}^{-1}}. \tag{A.75}$$

This will not be proved here; the proof can be found in most treatments of least-squares fitting (Hamilton 1964), and it is mathematically similar to the proof of optimal matched filters in Section A.4.2. For linear fits, the parameter estimates

returned by the above optimal estimator matrix are the same as those found by a maximum likelihood least-squares method. The parameter covariance matrix can be obtained directly from the data covariance matrix and the estimator matrix.

$$\overline{\mathbf{m}_{\hat{\mathbf{P}}}} = \mathrm{cov}\left(\overline{\hat{\mathbf{P}}[\mathbf{X}] \otimes \hat{\mathbf{P}}[\mathbf{X}]}\right) = \overline{\mathbf{e}_{\hat{\mathbf{P}}}} \bullet \overline{\mathbf{m}_{\mathbf{X}}} \bullet \overline{\mathbf{e}_{\hat{\mathbf{P}}}^{T}} \tag{A.76}$$

Although the design matrix and the optimal estimator matrix are, in general, rectangular matrices which, therefore, can not be inverted, they do form what are called pseudo-inverses. That is,

$$\overline{\mathbf{e}_{\hat{\mathbf{P}}}^{op}} \bullet \overline{\mathbf{q}_{\mathbf{P}}} = \left(\overline{\mathbf{q}_{\mathbf{P}}^{T}} \bullet \overline{\mathbf{m}_{\mathbf{X}}^{-1}} \bullet \overline{\mathbf{q}_{\mathbf{P}}}\right)^{-1} \bullet \left(\overline{\mathbf{q}_{\mathbf{P}}^{T}} \bullet \overline{\mathbf{m}_{\mathbf{X}}^{-1}} \bullet \overline{\mathbf{q}_{\mathbf{P}}}\right) = \bar{\mathbf{i}}. \tag{A.77}$$

This orthonormality condition is required of linear fits if the parameter estimates are to be unbiased. Iterative, non-linear fits are not biased but their convergence is degraded if the orthonormality condition is not met. This is especially important for many parameter fits because it only takes one eigenvalue of $\overline{\mathbf{e}_{\hat{\mathbf{P}}}} \bullet \overline{\mathbf{q}_{\mathbf{P}}}$ to differ significantly from 1 in order to slow down the convergence of the entire fit.

A.5.3 Multi-Parameter Fits for Continuous Data

Now, let us look at an alternate formulation that allows the optimal multi-parameter estimators to be derived from the optimal single parameter filters without an explicit inversion of the data covariance matrix. This method will prove to be easier to generalize to continuous time series. Consider the case of a single parameter fit to discrete data. The design "matrix" and estimator "matrix" then become vectors, and the optimal estimator vector is

$$\mathbf{e}_{\hat{\mathbf{p}}}{}^{op} = \left(\mathbf{q}_{\mathbf{p}} \bullet \overline{\mathbf{m}_{\mathbf{X}}^{-1}} \bullet \mathbf{q}_{\mathbf{p}}\right)^{-1} \bullet \mathbf{q}_{\mathbf{p}} \bullet \overline{\mathbf{m}_{\mathbf{X}}^{-1}}. \tag{A.78}$$

The term $\left(\mathbf{q}_{\mathbf{p}} \bullet \overline{\mathbf{m}_{\mathbf{X}}^{-1}} \bullet \mathbf{q}_{\mathbf{p}}\right)^{-1}$ is no longer a matrix but a simple multiplicative constant. Thus an unnormalized optimal single parameter filter can be defined as

$$\mathbf{f}_{\hat{p}}{}^{op} \equiv \mathbf{q}_p \bullet \overline{\mathbf{m}_{\mathbf{X}}^{-1}}. \tag{A.79}$$

Note that for the case of "white" noise, $\overline{\mathbf{m}_{\mathbf{X}}} = \bar{\mathbf{i}}$, this definition of a filter gives

$$\mathbf{f}_{\hat{p}}{}^{op} = \mathbf{q}_p = \frac{\partial \mathbf{x}\{p\}}{\partial p} \tag{A.80}$$

which is consistent with the optimal matched filters derived for time series in Section A.4.2.

It is not immediately clear how the concept of an optimal filter should be extended to multi-parameter fits, but let us provisionally define the optimal multi-parameter filter matrix as

$$\overline{\mathbf{f}_{\hat{\mathbf{p}}}}^{op} \equiv \overline{\mathbf{q}_{\mathbf{p}}^{T}} \bullet \overline{\mathbf{m}_{\mathbf{X}}^{-1}} \tag{A.81}$$

where each row of the filter matrix is the optimal single parameter fit filter for one of the parameters. Further, let us assume that the optimal estimator matrix can be obtained from this filter matrix by multiplying it by some square matrix, $\bar{\mathbf{n}}$. That is, assume that

$$\overline{\mathbf{e}_{\hat{\mathbf{p}}}}^{op} = \bar{\mathbf{n}} \bullet \overline{\mathbf{f}_{\hat{\mathbf{p}}}}^{op}. \tag{A.82}$$

Since we know that the optimal estimator matrix and the design matrix are pseudo-inverses,

$$\overline{\mathbf{e}_{\hat{\mathbf{p}}}}^{op} \bullet \overline{\mathbf{q}_{\mathbf{p}}} = \bar{\mathbf{i}} = \bar{\mathbf{n}} \bullet \overline{\mathbf{f}_{\hat{\mathbf{p}}}}^{op} \bullet \overline{\mathbf{q}_{\mathbf{p}}}, \tag{A.83}$$

then the matrix $\bar{\mathbf{n}}$ can have only one possible value,

$$\bar{\mathbf{n}} = \left(\overline{\mathbf{f}_{\hat{\mathbf{p}}}}^{op} \bullet \overline{\mathbf{q}_{\mathbf{p}}}\right)^{-1}. \tag{A.84}$$

Substituting this value back into the equation for the estimator matrix, one gets

$$\overline{\mathbf{e}_{\hat{\mathbf{p}}}}^{op} = \bar{\mathbf{n}} \bullet \overline{\mathbf{f}_{\hat{\mathbf{p}}}}^{op} = \left(\overline{\mathbf{q}_{\mathbf{p}}^{T}} \bullet \overline{\mathbf{m}_{\mathbf{X}}^{-1}} \bullet \overline{\mathbf{q}_{\mathbf{p}}}\right)^{-1} \bullet \overline{\mathbf{q}_{\mathbf{p}}^{T}} \bullet \overline{\mathbf{m}_{\mathbf{X}}^{-1}}, \tag{A.85}$$

which is indeed the optimal estimator matrix obtained in Section A.5.2, and thus the assumption that $\overline{\mathbf{e}_{\hat{\mathbf{p}}}}^{op} = \bar{\mathbf{n}} \bullet \overline{\mathbf{f}_{\hat{\mathbf{p}}}}^{op}$ is justified. More importantly, we now have an equation for the optimal estimator matrix,

$$\overline{\mathbf{e}_{\hat{\mathbf{p}}}}^{op} = \left(\overline{\mathbf{f}_{\hat{\mathbf{p}}}}^{op} \bullet \overline{\mathbf{q}_{\mathbf{p}}}\right)^{-1} \bullet \overline{\mathbf{f}_{\hat{\mathbf{p}}}}^{op}, \tag{A.86}$$

that does not require an explicit knowledge of $\overline{\mathbf{m}_{\mathbf{X}}^{-1}}$.

It turns out that the normalization of the filter matrix defined by $\overline{\mathbf{f}_{\hat{\mathbf{p}}}}^{op} \equiv \overline{\mathbf{q}_{\mathbf{p}}^{T}} \bullet \overline{\mathbf{m}_{\mathbf{X}}^{-1}}$ is too restrictive. Only the linear space spanned by the filter matrix is important, not its particular normalization. Define a new filter matrix that is the old filter matrix, $\overline{\mathbf{f}_{\hat{\mathbf{p}}}}^{op}_{old} = \overline{\mathbf{q}_{\mathbf{p}}^{T}} \bullet \overline{\mathbf{m}_{\mathbf{X}}^{-1}}$, multiplied by an arbitrary, invertible matrix $\bar{\mathbf{r}}$.

$$\overline{\mathbf{f}_{\hat{\mathbf{p}}}}^{op}_{new} = \bar{\mathbf{r}} \bullet \overline{\mathbf{f}_{\hat{\mathbf{p}}}}^{op}_{old} \tag{A.87}$$

The equation, $\overline{\mathbf{e}_{\hat{\mathbf{p}}}}^{op} = \left(\overline{\mathbf{f}_{\hat{\mathbf{p}}}}^{op} \bullet \overline{\mathbf{q}_{\mathbf{p}}}\right)^{-1} \bullet \overline{\mathbf{f}_{\hat{\mathbf{p}}}}^{op}$, returns the same estimator matrix with the new filter matrix as it did with the old filter matrix.

$$\begin{aligned}\overline{\mathbf{e}}^{op}_{\hat{\mathbf{p}}\,new} &= \left(\overline{\mathbf{f}}^{op}_{\hat{\mathbf{p}}\,new} \bullet \overline{\mathbf{q}_{\mathbf{p}}}\right)^{-1} \bullet \overline{\mathbf{f}}^{op}_{\hat{\mathbf{p}}\,new} = \left(\bar{\mathbf{r}} \bullet \overline{\mathbf{f}}^{op}_{\hat{\mathbf{p}}\,old} \bullet \overline{\mathbf{q}_{\mathbf{p}}}\right)^{-1} \bullet \bar{\mathbf{r}} \bullet \overline{\mathbf{f}}^{op}_{\hat{\mathbf{p}}\,old} \\ &= \left(\overline{\mathbf{f}}^{op}_{\hat{\mathbf{p}}\,old} \bullet \overline{\mathbf{q}_{\mathbf{p}}}\right)^{-1} \bullet \overline{\mathbf{f}}^{op}_{\hat{\mathbf{p}}\,old} = \overline{\mathbf{e}}^{op}_{\hat{\mathbf{p}}\,old}\end{aligned} \tag{A.88}$$

This method can be readily extended to linear, multi-parameter fits on continuous time series. The design "matrix" becomes a vector of functions that can be contracted with the parameter vector to get the multi-parameter signal.

$$x(t)\{\mathbf{p}\} = \mathbf{q}_{\mathbf{p}}(t) \bullet \mathbf{p} \tag{A.89}$$

The estimator "matrix" also becomes a vector of functions.

$$\hat{\mathbf{p}}[\mathbf{x}] = \int_{-\infty}^{+\infty} \mathbf{e}_{\hat{\mathbf{p}}}(t) x(t) dt \tag{A.90}$$

The design vector of functions and the optimal estimator vector of functions satisfy an orthonormality condition,

$$\int_{-\infty}^{+\infty} \mathbf{e}_{\hat{\mathbf{p}}}(t)^{op} \otimes \mathbf{q}_{\mathbf{p}}(t) dt = \bar{\mathbf{i}}. \tag{A.91}$$

In analogy with the discrete data case, the optimal estimator vector of functions can be obtained from the vector of optimal single parameter filter functions and the design vector of functions.

$$\mathbf{e}_{\hat{\mathbf{p}}}{}^{op}(t) = \left(\int_{-\infty}^{+\infty} \mathbf{f}_{\hat{\mathbf{p}}}{}^{op}(t) \otimes \mathbf{q}_{\mathbf{p}}(t) dt\right)^{-1} \bullet \mathbf{f}_{\hat{\mathbf{p}}}{}^{op}(t) \tag{A.92}$$

The parameter covariance matrix can then be calculated.

$$\overline{\mathbf{m}}^{op}_{\hat{\mathbf{p}}} = \int_{-\infty}^{+\infty}\int_{-\infty}^{+\infty} \overline{\mathbf{e}_{\hat{\mathbf{p}}}{}^{op}(t_1) \otimes \mathbf{e}_{\hat{\mathbf{p}}}{}^{op}(t_2)} \operatorname{cov}\left(X(t_1)X(t_2)\right) dt_1 dt_2 \tag{A.93}$$

Except for the simple case of "white" noise, the parameter covariance matrix elements are usually not calculated in the time basis as a double integral, but

rather the Fourier basis techniques discussed in Section A.2 are easier to employ.

The generalization of these methods to non-linear fits is straightforward. The design, optimal filter, and estimator vectors of functions become dependent on the choice of parameters, and this dependence should be indicated by appending a $\{\mathbf{p}\}$ symbol. A simple example of a non-linear, multi-parameter fit is presented in the next sub-section.

A.5.4 "White" Noise Multi-Parameter Example: Simultaneous Fit of Amplitude and Decay Constant

As a concrete example of these optimal multi-parameter fit methods, let us extend the single parameter example of Section A.3.3 in which the decay constant of a damped exponential was fit for in the presence of "white" noise, $F^2[\delta\mathbf{X}_{wh}](\nu) = \eta_{wh}^2$, to the example of fitting simultaneously for both the decay constant and the amplitude in the presence of "white" noise. Once again, the data sample will extend from $t = 0$ to $t \to +\infty$.

First, let us review the single parameter case. In Section A.3.3, we fit for the g in the single parameter signal,

$$x(t)\{g\} = A_o \exp(-gt). \tag{A.94}$$

For completeness, let us also consider the case of fitting for the amplitude, a, with γ known *a priori*.

$$x(t)\{a\} = a\exp(-\gamma t) \tag{A.95}$$

For non-linear, "white" noise, single parameter fits, the optimal filters are the partial derivatives of the signal with respect to the parameter.

$$f_{\hat{a}_{wh}}^{op}(t)\{a\} = \theta(t)\frac{\partial x(t)}{\partial a}\{a\} \qquad f_{\hat{g}_{wh}}^{op}(t)\{g\} = \theta(t)\frac{\partial x(t)}{\partial g}\{g\} \qquad (A.96)$$
$$= \theta(t)\exp(-\gamma t) \qquad = -\theta(t)A_o t\exp(-gt)$$

The Heavyside functions are included because the filters can only be applied to data after $t = 0$. The optimal estimators are obtained by normalizing the optimal filters,

$$e_{\hat{a}_{wh}}^{op}(t)\{a\} = \frac{\theta(t)\exp(-\gamma t)}{2\gamma} \qquad e_{\hat{g}_{wh}}^{op}(t)\{g\} = -\frac{\theta(t)4g^3 t\exp(-gt)}{A_o}, \qquad (A.97)$$

and the variances in the parameter estimates can be calculated from the estimators.

$$\mathrm{var}_{wh}\left(\hat{A}_{wh}^{op}[\mathbf{X}]\right) = \frac{\gamma\eta_{wh}^2}{2} \qquad \mathrm{var}_{wh}\left(\hat{G}_{wh}^{op}[\mathbf{X}]\right) = \frac{\gamma^3\eta_{wh}^2}{A_o^2} \qquad (A.98)$$

In the two parameter example, both a and g are free parameters.

$$\mathbf{p} = \{a, g\} \qquad x(t)\{\mathbf{p}\} = a\exp(-gt) \qquad (A.99)$$

The partial derivatives of the signal are combined into the design vector of functions,

$$\mathbf{q}_{\mathbf{p}}(t)\{\mathbf{p}\} = \begin{pmatrix} \frac{\partial x(t)}{\partial a}\{\mathbf{p}\} \\ \frac{\partial x(t)}{\partial g}\{\mathbf{p}\} \end{pmatrix} = \begin{pmatrix} \exp(-gt) \\ -at\exp(-gt) \end{pmatrix}, \qquad (A.100)$$

and the single parameter matched filters are combined into the multi-paramter optimal filter vector of functions,

$$\mathbf{f}_{\hat{\mathbf{p}}_{wh}}^{op}(t)\{\mathbf{p}\} = \theta(t)\mathbf{q}_{\mathbf{p}}(t)\{\mathbf{p}\} = \begin{pmatrix} \theta(t)\exp(-gt) \\ -\theta(t)at\exp(-gt) \end{pmatrix}. \qquad (A.101)$$

The optimal estimator vector of functions can then be calculated.

$$\begin{aligned}
\mathbf{e}_{\hat{\mathbf{p}}_{wh}}^{op}(t)\{\mathbf{p}\} &= \left(\int_{+\infty}^{-\infty} \mathbf{f}_{\hat{\mathbf{p}}_{wh}}^{op}(t)\{\mathbf{p}\} \otimes \mathbf{q}_{\mathbf{p}}(t)\{\mathbf{p}\}dt\right)^{-1} \bullet \mathbf{f}_{\hat{\mathbf{p}}_{wh}}^{op}(t)\{\mathbf{p}\} \\
&= \begin{pmatrix} \int_0^\infty \exp(-2gt)dt & -\int_0^\infty at\exp(-2gt)dt \\ -\int_0^\infty at\exp(-2gt)dt & \int_0^\infty a^2t^2\exp(-2gt)dt \end{pmatrix}^{-1} \bullet \begin{pmatrix} \theta(t)\exp(-gt) \\ -\theta(t)at\exp(-gt) \end{pmatrix} \\
&= \begin{pmatrix} \theta(t)4g(1+gt)\exp(-gt) \\ \theta(t)4g^2(1+2gt)\exp(-gt)/a \end{pmatrix}
\end{aligned} \tag{A.102}$$

Note that these estimator functions are different from the single parameter fit estimators because not only must they be sensitive to the parameter which they are trying to estimate, they must also be insensitive (i.e., orthogonal) to the other parameter. The first-order correction to the parameter estimates are obtained by applying the estimator functions to the multi-parameter residue, $\delta x(t)\{\mathbf{p}\} = x(t) - a\exp(-gt)$.

$$\begin{aligned}
\delta\hat{\mathbf{p}}_{wh}^{op}[\delta\mathbf{x}\{\mathbf{p}\}]\{\mathbf{p}\} &= \begin{pmatrix} \delta\hat{a}[\delta\mathbf{x}\{a,g\}]\{a,g\} \\ \delta\hat{g}[\delta\mathbf{x}\{a,g\}]\{a,g\} \end{pmatrix} \\
&= \begin{pmatrix} \int_0^{+\infty} \left(4g(1+gt)\exp(-gt)\right)\left(x(t) - a\exp(-gt)\right)dt \\ \int_0^{+\infty} \left(4g^2(1+2gt)\exp(-gt)/a\right)\left(x(t) - a\exp(-gt)\right)dt \end{pmatrix}
\end{aligned} \tag{A.103}$$

The residue and both estimators depend on both of the parameters, a and g. Thus it makes no sense to talk of the fit being linear in a and non-linear in g. Once one of the parameters has a non-linear dependence, the entire fit becomes an iterative, non-linear process.

The parameter covariance matrix can be calculated from the optimal multi-parameter estimators. For this calculation, the true physical values of the parameters, A_0 and γ, are used, and since the noise is "white", each of the pa-

rameter covariance matrix elements can be evaluated as an integral in the time domain.

$$\overline{\mathbf{m}}^{op}_{\hat{\mathbf{P}}\,wh} = \mathrm{cov}\left(\overline{\hat{\mathbf{P}}^{op}_{wh}[\mathbf{X}] \otimes \hat{\mathbf{P}}^{op}_{wh}[\mathbf{X}]}\right)$$

$$\equiv \mathrm{cov}\left(\overline{\delta\hat{\mathbf{P}}^{op}_{wh}[\delta\mathbf{X}_{wh}]\{A_o,\gamma\} \otimes \delta\hat{\mathbf{P}}^{op}_{wh}[\delta\mathbf{X}_{wh}]\{A_o,\gamma\}}\right)$$

$$= \begin{pmatrix} \frac{\eta^2_{wh}}{4}\int_{-\infty}^{+\infty}\left(e^{op}_{\hat{a}wh}(t)\{A_o,\gamma\}\right)^2 dt & \frac{\eta^2_{wh}}{4}\int_{-\infty}^{+\infty} e^{op}_{\hat{a}wh}(t)\{A_o,\gamma\}e^{op}_{\hat{g}wh}(t)\{A_o,\gamma\}dt \\ \frac{\eta^2_{wh}}{4}\int_{-\infty}^{+\infty} e^{op}_{\hat{a}wh}(t)\{A_o,\gamma\}e^{op}_{\hat{g}wh}(t)\{A_o,\gamma\}dt & \frac{\eta^2_{wh}}{4}\int_{-\infty}^{+\infty}\left(e^{op}_{\hat{g}wh}(t)\{A_o,\gamma\}\right)^2 dt \end{pmatrix}$$

$$= \begin{pmatrix} \frac{\eta^2_{wh}}{4}\int_0^{+\infty} 16\gamma^2(1+\gamma t)^2\exp(-2\gamma t)dt & \frac{\eta^2_{wh}}{4}\int_0^{+\infty}\frac{16\gamma^3(1+\gamma t)(1+2\gamma t)\exp(-2\gamma t)}{A_o}dt \\ \frac{\eta^2_{wh}}{4}\int_0^{+\infty}\frac{16\gamma^3(1+\gamma t)(1+2\gamma t)\exp(-2\gamma t)}{A_o}dt & \frac{\eta^2_{wh}}{4}\int_0^{+\infty}\frac{16\gamma^4(1+2\gamma t)^2\exp(-2\gamma t)}{A_o^2}dt \end{pmatrix}$$

$$= \begin{pmatrix} \gamma\eta^2_{wh} & \frac{\gamma^2\eta^2_{wh}}{A_o} \\ \frac{\gamma^2\eta^2_{wh}}{A_o} & \frac{\gamma^3\eta^2_{wh}}{A_o^2} \end{pmatrix} \qquad (A.104)$$

Looking at the diagonal elements of $\overline{\mathbf{m}}^{op}_{\hat{\mathbf{P}}\,wh}$, it can be seen that the variances in the parameter estimates are twice as large for the multi-parameter fit as compared to the single parameter fits. The non-zero off-diagonal element indicates that the errors in the two parameter estimates are correlated, and therefore a knowledge of one parameter helps reduce the variance in the estimate of the other.

A.5.5 Optimal Thermal Noise Limited Parameter Estimates for a Damped Harmonic Oscillator

The primary question of this paper can now be addressed: what are the optimal estimators for the parameters of a damped harmonic oscillator in the

presence of thermal noise? The possible motions of the oscillator are parameterized by five parameters,

$$\begin{aligned}&\mathbf{p} = \{a,b,c,g,w\}\\ &x(t)\{\mathbf{p}\} = a\exp(-gt)\cos(wt) + b\exp(-gt)\sin(wt) + c,\end{aligned} \tag{A.105}$$

and the corresponding design vector of functions has five components,

$$\mathbf{q}_{\mathbf{p}}(t)\{\mathbf{p}\} = \begin{pmatrix} (\partial x(t)/\partial a)\{\mathbf{p}\} \\ (\partial x(t)/\partial b)\{\mathbf{p}\} \\ (\partial x(t)/\partial c)\{\mathbf{p}\} \\ (\partial x(t)/\partial g)\{\mathbf{p}\} \\ (\partial x(t)/\partial w)\{\mathbf{p}\} \end{pmatrix} \equiv \begin{pmatrix} \cos(wt) \\ \sin(wt) \\ 1 \\ -at\cos(wt) - bt\sin(wt) \\ bt\cos(wt) - at\sin(wt) \end{pmatrix}. \tag{A.106}$$

To simplify calculations, the above is calculated in the undamped limit of $\gamma \to 0$ which it turns out is sufficient to get results to leading order in $1/Q$.

In Section A.4, it was shown that the optimal thermal noise single parameter estimates were all linear combinations of the five statistics, $\delta x_i\{p\}$, $\delta x_f\{p\}$, $\delta v_i\{p\}$, $\delta v_f\{p\}$, and $\delta x_m\{p\}$. Since normalization and recombination of the rows of a multi-parameter filter are unimportant as long as the rows remain linearly independent, a simple choice for the component functions of the optimal thermal noise multi-parameter filter are the five functions that extract the five statistics $\delta x_i\{\mathbf{p}\}$, $\delta x_f\{\mathbf{p}\}$, $\delta v_i\{\mathbf{p}\}$, $\delta v_f\{\mathbf{p}\}$, and $\delta x_m\{\mathbf{p}\}$.

$$\mathbf{f}_{\hat{\mathbf{p}}_{th}}^{op}(t)\{\mathbf{p}\}_N \equiv \begin{pmatrix} \delta(t-t_i) \\ \delta(t-t_f) \\ \delta'(t-t_i) \\ \delta'(t-t_f) \\ \big(\theta(t-t_i) - \theta(t-t_f)\big)/(t_f - t_i) \end{pmatrix} \tag{A.107}$$

The N subscript is included to remind the reader that the above optimal filter is only valid for a data sample duration, $\tau = t_f - t_i$, that is an integer number of periods, N.

The optimal estimator vector of functions can then be calculated.

$$\mathbf{e}_{\hat{\mathbf{p}}_{th}}^{op}(t)\{\mathbf{p}\}_N = \left(\int_{+\infty}^{-\infty} \mathbf{f}_{\hat{\mathbf{p}}_{th}}^{op}(t)\{\mathbf{p}\}_N \otimes \mathbf{q}_{\mathbf{p}}(t)\{\mathbf{p}\}dt\right)^{-1} \bullet \mathbf{f}_{\hat{\mathbf{p}}_{th}}^{op}(t)\{\mathbf{p}\}_N$$

$$\equiv \begin{pmatrix} (-1)^N & 0 & 1 & (-1)^N\left(\frac{\pi Na}{w}\right) & (-1)^N\left(\frac{-\pi Nb}{w}\right) \\ (-1)^N & 0 & 1 & (-1)^N\left(\frac{-\pi Na}{w}\right) & (-1)^N\left(\frac{\pi Nb}{w}\right) \\ 0 & (-1)^N w & 0 & (-1)^N(-a+\pi Nb) & (-1)^N(\pi Na+b) \\ 0 & (-1)^N w & 0 & (-1)^N(-a-\pi Nb) & (-1)^N(-\pi Na+b) \\ 0 & 0 & 1 & (-1)^N\left(\frac{b}{w}\right) & (-1)^N\left(\frac{a}{w}\right) \end{pmatrix}^{-1} \bullet \mathbf{f}_{\hat{\mathbf{p}}_{th}}^{op}(t)\{\mathbf{p}\}_N \quad \text{(A.108)}$$

The above 5x5 matrix is inverted to give the coefficients that go in front of $\delta(t-t_i)$, $\delta(t-t_f)$, $\delta'(t-t_i)$, $\delta'(t-t_f)$, and $\left(\theta(t-t_i)-\theta(t-t_f)\right)/(t_f-t_i)$ in the estimator functions. The optimal estimators are then applied to the residue, $\delta x(t)\{\mathbf{p}\} = x(t) - x(t)\{\mathbf{p}\}$, to get the optimal first-order correction to the parameter estimate vector, $\delta\hat{\mathbf{p}}_{th}^{op}[\delta\mathbf{x}\{\mathbf{p}\}]\{\mathbf{p}\}_N$.

$$\delta\hat{\mathbf{p}}_{th}^{op}\left[\delta\mathbf{x}\{\mathbf{p}\}\right]\{\mathbf{p}\}_N = \begin{pmatrix} \delta\hat{a}_{th}^{op}\left[\delta\mathbf{x}\{\mathbf{p}\}\right]\{\mathbf{p}\}_N \\ \delta\hat{b}_{th}^{op}\left[\delta\mathbf{x}\{\mathbf{p}\}\right]\{\mathbf{p}\}_N \\ \delta\hat{c}_{th}^{op}\left[\delta\mathbf{x}\{\mathbf{p}\}\right]\{\mathbf{p}\}_N \\ \delta\hat{g}_{th}^{op}\left[\delta\mathbf{x}\{\mathbf{p}\}\right]\{\mathbf{p}\}_N \\ \delta\hat{w}_{th}^{op}\left[\delta\mathbf{x}\{\mathbf{p}\}\right]\{\mathbf{p}\}_N \end{pmatrix}$$

$$= \int_{-\tau/2+\varepsilon}^{+\tau/2+\varepsilon} \begin{pmatrix} e_{\hat{a}th}^{op}(t)\{\mathbf{p}\}_N \\ e_{\hat{b}th}^{op}(t)\{\mathbf{p}\}_N \\ e_{\hat{c}th}^{op}(t)\{\mathbf{p}\}_N \\ e_{\hat{g}th}^{op}(t)\{\mathbf{p}\}_N \\ e_{\hat{w}th}^{op}(t)\{\mathbf{p}\}_N \end{pmatrix} \left(x(t) - x(t)\{\mathbf{p}\}\right)dt$$

$$= \begin{pmatrix} (-1)^N\left(\dfrac{\delta x_i\{\mathbf{p}\} + \delta x_f\{\mathbf{p}\}}{2} - \dfrac{\delta v_f\{\mathbf{p}\} - \delta v_i\{\mathbf{p}\}}{2\pi N w} - \delta x_m\{\mathbf{p}\}\right) \\ (-1)^N\left(-\dfrac{\delta x_f\{\mathbf{p}\} - \delta x_i\{\mathbf{p}\}}{2\pi N} + \dfrac{\delta v_f\{\mathbf{p}\} + \delta v_i\{\mathbf{p}\}}{2w}\right) \\ \dfrac{\delta v_f\{\mathbf{p}\} - \delta v_i\{\mathbf{p}\}}{2\pi N w} + \delta x_m\{\mathbf{p}\} \\ (-1)^N\left(-\dfrac{aw\left(\delta x_f\{\mathbf{p}\} - \delta x_i\{\mathbf{p}\}\right)}{2\pi N\left(a^2+b^2\right)} - \dfrac{b\left(\delta v_f\{\mathbf{p}\} - \delta v_i\{\mathbf{p}\}\right)}{2\pi N\left(a^2+b^2\right)}\right) \\ (-1)^N\left(\dfrac{bw\left(\delta x_f\{\mathbf{p}\} - \delta x_i\{\mathbf{p}\}\right)}{2\pi N\left(a^2+b^2\right)} - \dfrac{a\left(\delta v_f\{\mathbf{p}\} - \delta v_i\{\mathbf{p}\}\right)}{2\pi N\left(a^2+b^2\right)}\right) \end{pmatrix} \tag{A.109}$$

Although the $\gamma \to 0$ approximation was used in the estimators, it can not be used when calculating the residue, $\delta x(t)\{\mathbf{p}\} = x(t) - x(t)\{\mathbf{p}\}$, without introducing a systematic bias in the parameter estimates.

The optimal parameter estimation method has now been prescribed. What are the variances in these parameter estimates? For thermal noise, it is easiest to calculate the variance of a parameter estimate in the Fourier basis. Let us review the Fourier calculation method described in Sections A.2.3 and A.3.2.

Given an estimator $e_{\hat{p}}(t)\{p\}$, the true physical value of the parameter, ρ, is inserted and its spectral power density, $\mathrm{F}^2\left[\mathbf{e}_{\hat{p}}\{\rho\}\right](\nu)$, is calculated.

$$\mathrm{F}^2\left[\mathbf{e}_{\hat{p}}\{\rho\}\right](\nu)=\left(\int_{-\infty}^{+\infty}e_{\hat{p}}(t)\{\rho\}\cos(2\pi\nu t)dt\right)^2+\left(\int_{-\infty}^{+\infty}e_{\hat{p}}(t)\{\rho\}\sin(2\pi\nu t)dt\right)^2 \quad \text{(A.110)}$$

This is multiplied by the spectral power density of the thermal noise ensemble, $\mathrm{F}^2[\delta\mathbf{X}_{th}](\nu)$, and then integrated over ν to get the variance in the parameter estimate.

$$\begin{aligned}
&\mathrm{var}_{th}\left(\hat{P}[\mathbf{X}]\right)\equiv\mathrm{var}_{th}\left(\delta\hat{P}[\delta\mathbf{X}_{th}]\{\rho\}\right)=\int_0^\infty\mathrm{F}^2\left[\mathbf{e}_{\hat{p}}\{\rho\}\right](\nu)\mathrm{F}^2[\delta\mathbf{X}_{th}](\nu)d\nu\Big/2\\
&=\frac{2KT\beta}{M^2}\int_0^\infty\frac{\mathrm{F}^2\left[\mathbf{e}_{\hat{p}}\{\rho\}\right](\nu)d\nu}{\left((2\pi\nu)^2-\omega_o^2\right)^2+(4\pi\gamma\nu)^2} \qquad \text{(A.111)}\\
&\equiv\frac{2\chi_{th}^2\omega_d^3}{Q}\int_0^\infty\frac{\mathrm{F}^2\left[\mathbf{e}_{\hat{p}}\{\rho\}\right](\nu)d\nu}{(2\pi\nu-\omega_d-i\gamma)(2\pi\nu-\omega_d+i\gamma)(2\pi\nu+\omega_d-i\gamma)(2\pi\nu+\omega_d+i\gamma)}
\end{aligned}$$

In the last line above, the denominator has been factored to indicate that the integral can be readily evaluated in the complex plane using the method of residues provided that $\mathrm{F}^2\left[\mathbf{e}_{\hat{p}}\{\rho\}\right](\nu)$ is analytic. The expressions $\chi_{th}^2=KT/\kappa$ and $Q=2\omega_r/\gamma\equiv2\omega_d/\gamma$ have been introduced because they provide a convenient form to in which to express the final results.

When this Fourier method for calculating the variance of a parameter estimate is applied to the diagonal elements of the parameter covariance matrix, the following optimal (i.e., minimum) variances are obtained for the five parameters.

$$\mathrm{var}_{th}\left(\hat{A}_{th}^{op}[\mathbf{X}]_N\right) \equiv \chi_{th}^2 \qquad \mathrm{var}_{th}\left(\hat{B}_{th}^{op}[\mathbf{X}]_N\right) \equiv \chi_{th}^2$$

$$\mathrm{var}_{th}\left(\hat{C}_{th}^{op}[\mathbf{X}]_N\right) \equiv \frac{\chi_{th}^2}{\pi NQ} \tag{A.112}$$

$$\mathrm{var}_{th}\left(\hat{G}_{th}^{op}[\mathbf{X}]_N\right) \equiv \frac{\omega_d^2}{2\pi NQ}\left(\frac{\chi_{th}^2}{A_o^2}\right) \qquad \mathrm{var}_{th}\left(\hat{W}_{th}^{op}[\mathbf{X}]_N\right) \equiv \frac{\omega_d^2}{2\pi NQ}\left(\frac{\chi_{th}^2}{A_o^2}\right)$$

The variance of all the parameter estimates is directly proportional to χ_{th}^2 and hence to the absolute temperature as well. The variance in the estimates of the amplitude parameters, a and b, is simply χ_{th}^2 which is the variance in the instantaneous measurement of position, $\mathrm{var}_{th}(X(t))$. Notice that increasing the number of periods of measurement, N, does not reduce the variance in the amplitude parameter estimates because their uncertainty is dominated by fluctuations that occurred before the data sample began. The uncertainty in the other three parameters, c, g, and w, is dominated by non-resonant fluctuations during the data sample. Therefore the variance in these three parameters decreases as $1/N$ because the noise can be averaged over a longer time period, and these variances decrease as $1/Q$ because the position noise power outside of the resonant peak decreases as $1/Q$. The variances in the parameter estimates g and w are proportional to $1/A_o^2$, and this arises from the amplitude dependence of $(\partial x(t)/\partial g)\{\mathbf{p}\}$ and $(\partial x(t)/\partial w)\{\mathbf{p}\}$ in the design vector of functions, $\mathbf{q_p}(t)\{\mathbf{p}\}$. Essentially, the change in the signal, $x(t)\{\mathbf{p}\}$, as g or w is varied becomes proportionally larger as the amplitude of the signal is increased, and therefore the ability to detect small changes in these parameters is correspondingly increased. Also note that although the functional form of the estimators for g and w depends on the phase of the signal, the variances in the estimates

of these parameters is independent of phase for the case of the data sample being an integer number of periods. There is no preferred phase of the signal that optimizes the determination of the parameters.

With a little modification, the calculation of the off-diagonal elements of the parameter covariance matrix can also be done using Fourier methods. If expanded, the covariance of two random variables, X_1 and X_2, can be expressed in terms of variances.

$$\begin{aligned} \mathrm{cov}(X_1X_2) &= \langle \delta X_1 \delta X_2 \rangle = \frac{1}{2}\left\langle (\delta X_1 + \delta X_2)^2 - (\delta X_1)^2 - (\delta X_2)^2 \right\rangle \\ &= \frac{1}{2}\left(\mathrm{var}(X_1 + X_2) - \mathrm{var}(X_1) - \mathrm{var}(X_2)\right) \end{aligned} \tag{A.113}$$

The covariances of the different parameter estimates can thus be decomposed into variances and calculated in the same manner as the diagonal elements were. When this is done, it turns out all off-diagonal elements are zero to leading order in $1/Q$. More specifically, the correlation coefficients, defined as

$$\mathrm{corr}(X_1X_2) = \frac{\mathrm{cov}(X_1X_2)}{\mathrm{stddev}(X_1)\mathrm{stddev}(X_2)}, \tag{A.114}$$

are at most of order $1/Q^{1/2}$ and therefore go to zero in the high Q limit.

As a final note, the $\left(\delta x_f\{\mathbf{p}\} - \delta x_i\{\mathbf{p}\}\right)$, $\left(\delta v_f\{\mathbf{p}\} - \delta v_i\{\mathbf{p}\}\right)$, and $\delta x_m\{\mathbf{p}\}$ terms in $\delta\hat{a}_{th}^{op}[\delta\mathbf{x}\{\mathbf{p}\}]\{\mathbf{p}\}_N$ and $\delta\hat{b}_{th}^{op}[\delta\mathbf{x}\{\mathbf{p}\}]\{\mathbf{p}\}_N$ can be dropped without increasing the variances in the estimates of a and b to leading order in $1/Q$. One might question whether these terms should be included in the leading order formulation, but their presence is required to maintain the orthogonality of the fit to leading order in $1/Q$. If these terms are dropped, it will be the speed of convergence of the fit that will be degraded.

Vita

1979.....Received Regents' Scholarship from UCLA.

1984.....Graduated with B.S. in Physics, Magna cum Laude from UCLA.

1984.....Commissioned as Officer in United States Navy.

1984-1988.....Instructor at the Naval Nuclear Power School in Orlando FL. Two years in the Enlisted Heat Transfer and Fluid Flow Division and two years in the Officer Heat Transfer and Fluid Flow Division.

1989.....Received Honorable Mention in National Science Foundation Fellowship competition.

1992.....Presented "Proposed inverse square law test of gravity" at Progess in Aomic Physics, Netrinos, and Gravitation, XXVIIth Rencontre de Moriond in Les Arcs, Savoie, France.

1993.....Received Dahlstrom Prize from University of Washington Physics Department for developing concept for design of Gravitational Inverse Square Law Violation experiment.

1993.....Presented "Testing the inverse square law of gravity: a new class of torsion pendulum null experiments" at International Symposium on Experimental Gravitation in Nathiagali, Pakistan.

1994.....Presented "Detection of non-newtonian forces" at Seventh Marcel Grossmann Meeting at Stanford University in Palo Alto, CA.

1996.....Received Dahlstrom Prize from University of Washington Physics Department for developing second harmonic method for torsion pendulum experiment.

1996.....Presented "Precision measurements of small forces" at Dark Matter in Cosmology, Quantum Measurements, and Experimental Gravitation, XXXIst Rencontre de Moriond in Les Arcs, Savoie, France.

1999.....Presented "Status of oscillating torsion pendulum test of the inverse square law of gravity" at Symposium on Experimental Gravitation in Samarkand, Uzbekistan.

2000.....Received Ph.D. in Physics from University of Washington.